



## City Research Online

### City, University of London Institutional Repository

---

**Citation:** Margnelli, A. (2019). Influence quantification of non-stationary frequency content of earthquake ground motions to performance-based earthquake engineering. (Unpublished Doctoral thesis, City, University of London)

This is the accepted version of the paper.

This version of the publication may differ from the final published version.

---

**Permanent repository link:** <https://openaccess.city.ac.uk/id/eprint/24802/>

**Link to published version:**

**Copyright:** City Research Online aims to make research outputs of City, University of London available to a wider audience. Copyright and Moral Rights remain with the author(s) and/or copyright holders. URLs from City Research Online may be freely distributed and linked to.

**Reuse:** Copies of full items can be used for personal research or study, educational, or not-for-profit purposes without prior permission or charge. Provided that the authors, title and full bibliographic details are credited, a hyperlink and/or URL is given for the original metadata page and the content is not changed in any way.

---

---

---

City Research Online:

<http://openaccess.city.ac.uk/>

[publications@city.ac.uk](mailto:publications@city.ac.uk)

---

# **Influence Quantification of Non-Stationary Frequency Content of Earthquake Ground Motions to Performance-Based Earthquake Engineering**

*Thesis by*

ALESSANDRO MARGNELLI

*In partial fulfilment for the degree of  
Doctor of Philosophy*



CITY, UNIVERSITY OF LONDON

*School of Mathematics, Computer Science & Engineering*

*Department of Civil Engineering*

*Research Centre for Civil Engineering Structures*

JULY 2019





CITY, UNIVERSITY OF LONDON

School of Mathematics,

Computer Science & Engineering

Department of Civil Engineering

*Research Centre for Civil*

*Engineering Structures*

**Influence quantification of non-stationary  
frequency content of earthquake ground motions  
to performance-based earthquake engineering**

Doctoral Candidate: *Alessandro Margnelli*

Supervisor: *Dr. Agathoklis Giaralis*

Co-Supervisor: *Dr. Dimitrios Vamvatsikos*

London, July 2019



“Quid est ergo tempus?

Si nemo ex me quaerat, scio;

si quaerenti explicare velim, nescio”

*“What then is time?*

*If no one asks me, I know;*

*If I wish to explain it to one that ask, I know not”*

St. Augustine (354 AD - 430 AD)



# Contents

Contents	i
Acknowledgements	vi
Declaration	viii
Abstract	x
List of Figures	xii
List of Tables	xix
List of Symbols	xxi
List of Operations	xxv
Glossary of Acronyms	xxvii
<b>Chapter 1</b>	<b>30</b>
Introduction	30
1.1 Motivation, Aims, and Objectives	31
1.2 Thesis Organisation	34
<b>Chapter 2</b>	<b>37</b>
State-of-Art Review on Frequency Content Signal Characterisation in Performance Based Earthquake Engineering	37
2 Preliminary remarks	38
2.1 Overview of Performance-Based Earthquake Engineering (PBEE) framework	38
2.1.1 Methodological steps of the PBEE framework	38
2.1.2 Establishing statistical IM-EDP relationships	42
2.1.3 GM record selection criteria in deriving IM-EDP relationships	46
2.2 Fourier transform-based time-histories characterisation in PBEE	47
2.3 Non-stationary signal attributes in earthquake engineering: Physical considerations, signal representation tools, and applications	49
2.3.1 Physical considerations	49
2.3.2 Qualitative overview of joint time-frequency signal analysis tools	51

2.3.3	The continuous wavelet transform (CWT)	53
2.3.4	Indicative applications of wavelet transform signal analysis in earthquake engineering	55
2.4	Research gaps and needs	58
<b>Chapter 3</b>		<b>62</b>
	Morlet Wavelet-Based Mean Instantaneous Period and moving resonance of yielding structures under recorded GMs	62
3	Preliminary remarks	63
3.1	Energy distribution of continuous-time functions on the time-frequency plane	63
3.2	CWT-based signal analysis on the time-period plane using complex Morlet wavelets	66
3.2.1	Complex Morlet wavelets: definition and properties	66
3.2.2	Computation of CWT using complex Morlet wavelets	68
3.3	Instantaneous Frequency and Wavelet Ridge analysis for non-stationary mono-harmonic signals	70
3.3.1	The instantaneous frequency of non-stationary signals	70
3.3.2	The ridges of the CWT spectrogram	72
3.3.3	Illustrative applications of Morlet CWT ridge extraction	74
3.4	Wavelet-based Mean Instantaneous Period (MIP) of recorded GMs	78
3.5	MIP of seismic inelastic structural response time-histories and illustration of moving resonance	82
3.6	Concluding Remarks	89
<b>Chapter 4</b>		<b>92</b>
	“Alpha” ( $\alpha$ ): A Novel Wavelet-based Scalar Capturing the Average Non-Stationary Frequency Content of Recorded GMs	92
4	Preliminary remarks	93
4.1	Mathematical Definition of the $\alpha$ Property of Recorded GMs	94
4.2	Statistical relationships of $\alpha$ with seismological parameters, local soil conditions, and GM properties	97

4.3	Non-sufficiency of PGA and PGV against $\alpha$ for Peak Inelastic Response Prediction	103
4.4	Concluding Remarks	106
<b>Chapter 5</b>		109
	Influence of Non-Stationary Frequency Content of GMs to Seismic Demands of Inelastic Single-Degree-of-Freedom Systems	109
5	Preliminary Remarks	110
5.1	Description and modelling of adopted inelastic SDOF systems	110
5.2	Numerical direct integration scheme	117
5.3	Selection of Intensity Measures	117
5.4	Comparisons of IDA curves using different IMs	119
5.5	Regression Analysis of IMs against $\alpha$ and statistical quantification of the influence of $\alpha$	126
5.6	Concluding Remarks	138
<b>Chapter 6</b>		140
	Influence of Non-Stationary Frequency Content of GMs to Seismic Demands of Inelastic Multi-Degree of Freedom System	140
6	Preliminary Remarks	141
6.1	Description and modelling of adopted inelastic MDOF systems	141
6.1.1	Nonlinear modelling considerations of flexible benchmark 7-storey reinforced concrete building	142
6.1.2	3-storey Concentrically-Braced Frame Building	144
6.2	Construction of spectrally-equivalent GM ensembles with different range of $\alpha$ values	145
6.3	Quantification of $\alpha$ influence on IDA curves statistics from the spectrally-equivalent GM sets	149
6.3.1	7-storey building: Numerical results	149
6.3.2	3-storey building: Numerical results	156
6.3.3	IDA curves comparison between 7-storey and 3-storey benchmark building models	157
6.4	Concluding Remarks	159

<b>Chapter 7</b>	161
Concluding Remarks	161
7 Introduction	162
7.1 Summary of Work, Contributions and Major Findings	162
7.2 Recommendations for Future Research	166
<b>Appendix A</b>	170
Ground Motions (GMs) sets	170
A1 GMs SET 1 - 20 GMs	171
A2 GMs SET 2 - 611 GMs	172
A3 GMs SET 3 – 2 x 611 GMs	175
<b>Appendix B</b>	178
Brief notes on Energy-Based methodology	178
B1 Introduction	179
B1.1 Energy Based methodology	179
B1.2 Elasto-Perfectly Plastic material and the effect on the Energy Actions	181
<b>Appendix C</b>	189
Brief notes on Regression Analysis	189
<b>Appendix D</b>	193
Significance Testing	193
D1 Hypothesis testing	194
D2 Confidence interval	195
D3 Type I and II errors	196
D4 P-value of a Hypothesis test	196
D5 Regression analysis and Hypothesis test	197
<b>Appendix E</b>	200
Implementation of Hysteretic Material in OpenSees	200
<b>Bibliography</b>	205



# Acknowledgements

First and foremost, I would like to thank Dr Agathoklis Giaralis, my thesis supervisor, for his support during these years of our collaboration. He constantly inspired and supported my ideas with invaluable advices and profound knowledge. His intuitions and determination have been the key factors for this thesis.

I am also particularly grateful to Dr Dimitrios Vamvatsikos, my thesis co-supervisor, for constantly providing his enthusiastic support and scientific knowledge.

Special thanks are also expressed to my colleague and friend Davide Spano' for our evening discussions "after work" which have been an invaluable source of inspiration mixed with pragmatism.

Finally, I would like to thank my wife Ottavia and my daughter Alice for their love, support and patience throughout the course of this work. Without them, the last years would have been impossible.



# Declaration

I grant powers of discretion to the University Librarian to allow the thesis to be copied in whole or in part without further reference to the author. This permission covers only single copies made for study purposes, subject to normal conditions of acknowledgement.



# Abstract

Typical recorded acceleration traces of seismic ground motions (GMs) exhibit a time-varying frequency composition due to the dispersion of different types of seismic waves having different amplitudes and pre-dominant frequencies and arriving at the recording station at different time instants. However, none of the current GM properties used in earthquake engineering to quantify the structural damage potential of GMs account for the time-evolving trends of GM frequency content. Indeed, intensity measures (IMs) and record selection criteria adopted in the context of performance-based earthquake engineering (PBEE) do not account for the non-stationary frequency content of GMs. This lack of a metric to characterise non-stationary frequency content in recorded GMs has hindered, consequently, the systematic investigation of the influence of the evolutionary frequency content of recorded GMs to the inelastic response of different types of yielding structures. To address this gap in the current state-of-knowledge, this thesis puts forth a novel scalar quantity termed alpha, “ $\alpha$ ”, defined by the average slope (angle) of the wavelet-based mean instantaneous period (MIP) to characterize the temporal evolution of the mean frequency content of recorded GMs. Specifically, the MIP is the time-varying first-order average along the frequency or, equivalently, along the period axis of the wavelet-based GM spectrogram (squared magnitude of the GM wavelet transform) treated as a GM energy distribution on the time-frequency/period plane. Hence,  $\alpha$  captures the rate by which the mean frequency content of GMs changes in time.

Linear regression analyses involving 611 typical far-field recorded GMs from 30 seismic events of magnitude  $6.5 < M < 8$  and distance to rupture plane  $20\text{km} < R_{\text{rup}} < 120\text{km}$  demonstrate no significant correlation between  $\alpha$  and  $M$ ,  $R_{\text{rup}}$ , or peak ground acceleration (PGA). However, it is established that  $\alpha$  correlates with the average frequency content of GMs as captured by the mean Fourier-based period ( $T_m$ ) and with the peak ground velocity (PGV): the lower the average frequency content, the larger the value of  $\alpha$  tends to be, that is, the faster the time evolution (transition) of the average frequency content is from higher to lower frequencies. Further, linear regression between  $\alpha$  and shear wave velocity ( $V_{s30}$ ) dictates that GMs recorded on softer soils are more likely to have larger  $\alpha$ , a phenomenon that is attributed to the fact that soft soils under strong seismic shaking exhibit strong non-linear behaviour that enriches the low frequency content of recorded GMs at later time instants. The reported numerical data suggest that increased level of correlation between  $\alpha$ - $T_m$  and  $\alpha$ - $V_{s30}$  is exhibited for as PGA increases.

Next, the influence of the non-stationary GM frequency content as captured by  $\alpha$  to the peak inelastic response of hysteretic single-degree-of-freedom (SDOF) oscillators used as proxies of multi-storey yielding structures is assessed within the PBEE framework. First, it is shown that

PGA and PGV, treated as non-structure specific IMs in conducting incremental dynamic analysis (IDA), are non-sufficient in predicting the peak drift of a hysteretic oscillator with strength and stiffness degradation representing a benchmark 12-storey reinforce concrete frame exposed to the above set of 611 GMs. These results provide for an indirect indication of the significance of  $\alpha$  and, thus, of the non-stationary GM frequency content to peak inelastic structural response. Next, IDA results from two different benchmark SDOF systems corresponding to ductile and non-ductile structural inelastic behaviour with different pre-yielding natural periods are considered using advanced IMs accounting for spectral shape. It is found statistically that  $\alpha$  is increasingly important for close to collapse limit states irrespective of structural ductility and stiffness. As stiffness increases  $\alpha$  influences more substantially the ductile structure and it is mostly important for flexible ( $T_1=2s$ ) non-ductile structures and for intermediate stiffness ( $T_1=1s$  to  $1.5s$ ) ductile structures.

Finally, the concept of spectrally equivalent GMs is used in conjunction with a large database of 1222 far-field GMs to construct several sets of 50 and 25 GMs each having significantly different median  $\alpha$  values but closely matching mean response spectral shapes, as well as effective duration and  $T_m$  distributions. Numerical results obtained from IDA to lumped- plasticity multi-degree-of-freedom (MDOF) models of benchmark, 3-storey and 7-storey code-compliant structures demonstrate that median peak inter-storey drift ratio demand posed by the GM set with high  $\alpha$  values is significantly larger from the GM set with low- $\alpha$  values for the flexible 7-storey structure ( $T_1=1.6s$ ), but not for the stiffer 3-storey structure ( $T_1=0.55s$ ) confirming conclusions drawn for the case of inelastic SDOF structures. This is the true even for the case of a high-sufficiency and efficiency intensity measure accounting for spectral shape averaging over several spectral ordinates centered at  $T_1$ . Overall, findings suggest that the evolutionary frequency content of recorded GMs does influence peak inelastic structural response and should be accounted for in GM record selection used for seismic performance evaluation of structures with  $T_1 \geq 1s$ . To this aim, the herein proposed  $\alpha$  index can serve as a potent record selection criterion.

# List of Figures

Figure 2-1 PBEE performance levels, (Deierlein 2004), (SEAOC Vision 2000 1995)	39
Figure 2-2 Steps of PBEE Methodology, (PEER Report 2007/08 2008), (Porter 2003)	40
Figure 2-3 Components of PBEE Methodology, (Deierlein 2004)	42
Figure 2-4 IDA Curves with respect to $S_a(T_1)$ - (a) Individual IDA Curves; (b) normal distribution;(c) Median (Solid Lines) and $\pm 1 \sigma$ Standard Deviation (Broken Lines) Ensemble Curves.	44
Figure 2-5 An example of a recorded seismic accelerogram illustrating the time-varying frequency content, in terms of zero-crossings, and intensity of strong ground motions (Giaralis 2008).	50
Figure 2-6 Use of a wavelet-based damage sensitive factor (DSF) to derive fragility curves (Noh, et al. 2012)	57
Figure 3-1 Heisenberg box of a function $\psi(t)$ .	65
Figure 3-2 Heisenberg boxes for Morlet wavelets at different scales (Mallat 1998)	68
Figure 3-3 Contour Morlet wavelet spectrogram (power spectrum) of recorded GM #18 in Table A-1 (Appendix A).	69
Figure 3-4 Representation of an analytic mono-harmonic signal on the complex plane using the amplitude $A_y(t)$ and the phase $\phi_y t$ .	71
Figure 3-5 Wavelet spectrogram and ridge extraction for a stationary harmonic signal with $T=0.01s$ period.	73
Figure 3-6 Ridge extraction procedure step - MATLAB® script.	74
Figure 3-7 Morlet CWT analysis of a mono-harmonic signal with linearly increasing frequency (chirp) of the form $ft = A \cdot \cos(\omega t^2)$ . Top panel: time-history; Middle panel: Contour Morlet CWT with ridges indicated by thick black lines; Bottom panel: Morlet CWT.	75
Figure 3-8 Morlet CWT analysis of the signal in equation (3.30) with $t_1=0.1s$ , $t_2=0.3s$ , $t_3=0.7s$ , $\omega_0 = 32 \text{ rad/s}$ (period 0.196s), $\omega_1 = 64 \text{ rad/s}$ (period 0.392s), $N_1=0.05$ . Top panel: time-history; Middle panel: Contour Morlet CWT with ridges indicated by thick black lines; Bottom panel: Morlet CWT.	76
Figure 3-9 Morlet CWT analysis of the signal in equation (3.30) with $t_1=0.1s$ , $t_2=0.3s$ , $t_3=0.7s$ , $\omega_0 = 32 \text{ rad/s}$ (period 0.196s), $\omega_1 = 64 \text{ rad/s}$ (period 0.392s), $N_1=0.05$ . Top panel: time-history; Middle panel: Contour Morlet CWT with ridges indicated by thick black lines; Bottom panel: Morlet CWT.	77

## List of Figures

---

Figure 3-10 Ridge extraction process based on local CWT maxima for multi-harmonic signals.	78
Figure 3-11 Wavelet-based significant evolutionary frequency content characterisation of a typical recorded GM on the time-period plane. Left panel: ridge analysis- thick black curves denote local Morlet CWT ridges; Right panel: thick black curve is the mean instantaneous period (MIP) computed from equation (3.31).	79
Figure 3-12 Instantaneous CWT spectrogram across period axis.	80
Figure 3-13 Mean instantaneous period (MIP) in equation (3.31) (black thick curve) plotted on top of the contour Morlet CWT spectrogram. The window with broken white line indicates the limits of MIP calculation on the time-period plane.	81
Figure 3-14 Morlet CWT-based MIP of the 20 GMs in Appendix A (Table A-1). The broken blue curve is the ensemble MIP average and the red broken line indicates the average (linear) slope of the blue curve	81
Figure 3-15 Parametric definition of the capacity boundary curve of the Ibarra et al. (2005) hysteretic model.	82
Figure 3-16 Section and Plan view of the test building (Mwafy and Elnashai 2001)	84
Figure 3-17 Capacity Boundary curve as implemented in Opensees	85
Figure 3-18. MIPs of input and output signals considered in the IDA analysis for the Ground Motion No. 13 GM (Imperial Valley, 1979, Chihuahua (282) Station). The number of scaled curves in this case is 11.	87
Figure 3-19. MIPs of input and output signals considered in the IDA analysis for the No. 8 GM.	88
Figure 3-20. Morlet wavelet based MIRPs of response acceleration signals at immediate occupancy (after first yielding – blue line) and at near collapse limit states (red line), respectively, and average slope of the ensemble average MIPs. On the right input/output average slopes of the ensemble average MIPs	89
Figure 4-1 Definition of the mean slope $\alpha$ of the Morlet CWT-based MIP	94
Figure 4-2 Recorded GM component RSN122: Friuli, Italy (1976)- see GM set 2 description in Appendix A. Upper panel: acceleration time-history; middle panel: contour plot of Morlet CWT spectrogram with MIP; lower panel: GM property $\alpha$ (slope of mean MIP)	96
Figure 4-3 Recorded GM component RSN726: Superstition Hill, CA (1987) see GM set 2 description in Appendix A. Upper panel: acceleration time-history; middle panel: contour plot of Morlet CWT spectrogram with MIP; lower panel: GM property $\alpha$ (slope of mean MIP)	97
Figure 4-4 Linear regression analyses results of $\alpha$ against PGA, PGV, $T_m$ and $V_{s30}$ as indicated in the title of each panel for the GM data set of Table A-2 (Appendix A).	99

## List of Figures

---

Figure 4-5 Linear regression analyses results of $\alpha$ against $T_m$ and $V_{s30}$ as indicated in the title of each panel for the GM data set of Table A-2 (Appendix A) classified in 2 different PGA bins.	101
Figure 4-6 Linear regression analyses results of $\alpha$ against magnitude $M$ and fault distance $R_{up}$ as indicated in the title of each panel for the GM data set of Table A-2 (Appendix A) classified in 2 different PGA bins.	102
Figure 4-7 Adopted IM-EDP sufficiency testing.	104
Figure 4-8 (a): Regression analysis of $\varepsilon_{PGV}$ residuals with $\alpha$ (p-value=0.0186)	105
Figure 4-9 Regression analysis of $\varepsilon_{PGA}$ residuals with $\alpha$ (p-value=0.0096)	105
Figure 5-1 Force-Displacement capacity boundary and Hysteretic cycles with stiffness/strength degradation	111
Figure 5-2 Hysteretic behaviour for models with: (a) cyclic strength degradation; and (b) in-cycle degradation (FEMA 2009)	111
Figure 5-3 Generic force-displacement capacity boundary - (FEMA P440A 2009).	112
Figure 5-4 One-dimensional load-deformation response model (PEER 2003/10)	113
Figure 5-5 Unloading stiffness degradation and reloading stiffness degradation (PEER 2003/10)	114
Figure 5-6 Strength degradation (PEER 2003/10)	114
Figure 5-7 Illustration of energy calculation in the damage model adopted.	116
Figure 5-8 Force-Displacement capacity boundary and Hysteretic cycles with stiffness/strength degradation	116
Figure 5-9 Response effects of structural softening (Cordova, et al. 2000 )	118
Figure 5-10 16, 50, 84% fractiles incremental dynamic analysis (IDA) curves for $S_a(T1)$ – a) SDOF $T=0.5s$ Non-Ductile SDOF, b) SDOF $T=0.5s$ Ductile SDOF	120
Figure 5-11 16, 50, 84% fractiles incremental dynamic analysis (IDA) curves for $AvgS_a(T1)$ – a) SDOF $T=0.5s$ Non-Ductile SDOF, b) SDOF $T=0.5s$ Ductile SDOF	121
Figure 5-12 16, 50, 84% fractiles incremental dynamic analysis (IDA) curves for $S_a(T1)$ – a) SDOF $T=1s$ Non-Ductile SDOF, b) SDOF $T=1s$ Ductile SDOF	121
Figure 5-13 16, 50, 84% fractiles incremental dynamic analysis (IDA) curves for $AvgS_a(T1)$ – a) SDOF $T=1s$ Non-Ductile SDOF, b) SDOF $T=1s$ Ductile SDOF	122
Figure 5-14 16, 50, 84% fractiles incremental dynamic analysis (IDA) curves for $S_a(T1)$ – a) SDOF $T=1.5s$ Non-Ductile SDOF, b) SDOF $T=2s$ Ductile SDOF	122
Figure 5-15 16, 50, 84% fractiles incremental dynamic analysis (IDA) curves for $AvgS_a(T1)$ – a) SDOF $T=1.5s$ Non-Ductile SDOF, b) SDOF $T=1.5s$ Ductile SDOF	123
Figure 5-16 16, 50, 84% fractiles incremental dynamic analysis (IDA) curves for $S_a(T1)$ – a) SDOF $T=2s$ Non-Ductile SDOF, b) SDOF $T=2s$ Ductile SDOF	123

## List of Figures

---

Figure 5-17 16, 50, 84% fractiles incremental dynamic analysis (IDA) curves for AvgSa(T1) – a) SDOF T=2s Non-Ductile SDOF, b) SDOF T=2s Ductile SDOF	124
Figure 5-18 16, 50, 84% fractiles incremental dynamic analysis (IDA) curves for $R = Sa(T, 5\%)/Say(T, 5\%)$ – a) SDOF T=0.5s,1s,1.5, 2s Non-Ductile SDOF, b) SDOF T=0.5s,1s,1.5s, 2s Ductile SDOF	124
Figure 5-19 Influence of period on ductile force reduction and R definition (Paulay and Priestley 1992)	125
Figure 5-20 Post-yield behavior comparisons of SDOF T=1s Non-Ductile SDOF and 3b and the effect to the collapse capacity system	125
Figure 5-21 $\eta$ ratio (slope) of the linear regression curve	127
Figure 5-22 Linear regressions between the Sa(T1) and $\alpha$ of MIP for periods T=0.5s for Non-Ductile and Ductile. Sa(T1) is obtained interpolating the results at $\theta_{max}=6\%$ for Non-Ductile and $\theta_{max}=8\%$ for Ductile.	129
Figure 5-23 Linear regressions between the Sa(T1) and $\alpha$ of MIP for periods T=1s for Non-Ductile and Ductile. Sa(T1) is obtained interpolating the results at $\theta_{max}=6\%$ for Non-Ductile and $\theta_{max}=8\%$ for Ductile.	130
Figure 5-24 Linear regressions between the Sa(T1) and $\alpha$ of MIP for periods T=1.5s for Non-Ductile and Ductile. Sa(T1) is obtained interpolating the results at $\theta_{max}=6\%$ for Non-Ductile and $\theta_{max}=8\%$ for Ductile.	131
Figure 5-25 Linear regressions between the Sa(T1) and $\alpha$ of MIP for periods T= 2s for Non-Ductile and Ductile. Sa(T1) is obtained interpolating the results at $\theta_{max}=6\%$ Non-Ductile and $\theta_{max}=8\%$ for Non-Ductile and Ductile.	132
Figure 5-26 Linear regressions between the R and $\alpha$ of MIP for periods T=0.5s, Non-Ductile and Ductile. R is obtained interpolating the results at $\theta_{max}=6\%$ for Non-Ductile and $\theta_{max}=8\%$ for Ductile.	134
Figure 5-27 Linear regressions between the R and $\alpha$ of MIP for periods T=1s, Non-Ductile and Ductile. R is obtained interpolating the results at $\theta_{max}=6\%$ for Non-Ductile and $\theta_{max}=8\%$ for Ductile.	134
Figure 5-28 Linear regressions between the R and $\alpha$ of MIP for periods T=1.5s, for Non-Ductile and Ductile. R is obtained interpolating the results at $\theta_{max}=6\%$ for Non-Ductile and $\theta_{max}=8\%$ for Ductile.	134
Figure 5-29 Linear regressions between the R and $\alpha$ of MIP for periods T= 2s for Non-Ductile and Ductile. R is obtained interpolating the results at $\theta_{max}=6\%$ for Non-Ductile and $\theta_{max}=8\%$ for Ductile.	135
Figure 5-30 Comparison $\eta$ slope values, for different condition of T (s) and $\theta$ – 3D view	136
Figure 5-31 Comparison $\eta$ slope values, for different condition of T (s) – 2D view	136

## List of Figures

---

Figure 5-32 Comparison $\eta$ slope values, for different condition of $\theta$ – 2D view	137
Figure 6-1 Generic model idealization of the perimeter RCMRFs with typical plan view with perimeter stability frames (Kazantzi and Vamvatsikos 2015)	143
Figure 6-2 Case study 3-storey steel frame concentrically braced building (INNOSEIS, 2017)	144
Figure 6-3 Definition of curvature parameter $R(\xi)$ in Menegotto-Pinto Steel Model (Filippou, et al. 1983)	145
Figure 6-4 (b) Response Spectra of Two Spectrally Equivalent GMs (twins) with High And Low $\alpha$ Values from San Fernando 1971 (Station: la Hollywood Stor Ff) and Landers 1992 (Station: Silent Valley, Poppet Flat) events, respectively: Low- $\alpha$ GM Scaled by 4.52, (b) Individual and Ensemble Mean Response Spectra of High- $\alpha$ and Low- $\alpha$ Sets.	147
Figure 6-5 Histograms of the 50 high- $\alpha$ and 50 low- $\alpha$ sets for: (a) alpha, $\alpha$ , values and (b) effective duration $D_{S_{5-95}}$ .	148
Figure 6-6 Histograms of the 50 high- $\alpha$ and 50 low- $\alpha$ sets for $T_m$ , values.	148
Figure 6-7 IDA Curves with respect to $S_a(T_1)$ for High and Low $\alpha$ Spectrally Equivalent Ensembles of 50 GMs: (A) Individual Curves; (B) Median (Solid Lines) and Median $\pm 1$ Standard Deviation (Broken Lines) Ensemble Curves.	150
Figure 6-8 IDA Curves with respect to AvgSa for High and Low $\alpha$ Spectrally Equivalent Ensembles of 50 GMs: (A) Individual Curves; (B) Median (Solid Lines) and Median $\pm 1$ Standard Deviation (Broken Lines) Ensemble Curves.	151
Figure 6-9 Vertical stripes on IDA curves and boxplots for 50 High and Low $\alpha$ sets	152
Figure 6-10 Histograms of the 25 high- $\alpha$ and 25 low- $\alpha$ sets for: (a) alpha, $\alpha$ , values and (b) effective duration $D_{S_{5-95}}$ .	153
Figure 6-11 Histograms of the 25 high- $\alpha$ and 25 low- $\alpha$ sets for $T_m$ , values.	154
Figure 6-12 IDA curves comparisons for 25 High and Low $\alpha$ sets (median curves)	154
Figure 6-13 IDA COV (Coefficient of Variation) between 50 pairs and 25 max high alphas (two curves with 50L(red) and 50H(blue)), and one curve (25L+25H), black)	155
Figure 6-14 COV (Coefficient of Variation) between 50 pairs and 25 pairs with min alpha difference between pairs (two curves with 50L(red) and 50H(blue)), and one curve (25L+25H), black)	155
Figure 6-15 IDA curves for 50 High and Low $\alpha$ sets (A) Individual Curves; (B) Median (Solid Lines) and Median $\pm 1$ Standard Deviation (Broken Lines) Ensemble Curves.	156
Figure 6-16 Boxplots and IDA curves of R for 50 High and Low $\alpha$ sets for the 3-storey building	157
Figure 6-17 IDA curves comparisons of R for 50 High and Low $\alpha$ sets for the 3 and 7 storey building	158

## List of Figures

---

Figure 6-18 Median IDA curves comparison in terms of R for High- $\alpha$ and Low- $\alpha$ and ratio $R_{Low}/R_{High}$ for the 3-storey building.	158
Figure 6-19 Median IDA curves comparison in terms of R for High- $\alpha$ and Low- $\alpha$ and ratio $R_{Low}/R_{High}$ for the 7-storey building.	159
Figure A-1 Magnitude vs distance for the set of 611 GMs	172
Figure A-2 Magnitude vs distance for the set of 611 GMs	175
Figure B-1 Diagram of a SDOF	179
Figure B-2 Force Deformation Curve (Elastoplastic Behaviour) (Chopra 2007)	181
Figure B-3 ElCentro seismic action (Chopra 2007)	182
Figure B-4 Elastic response ( $f_y = 1$ )	182
Figure B-5 Elastic response ( $f_y = 0.5$ )	183
Figure B-6 Elastic response ( $f_y = 0.25$ )	183
Figure B-7 Comparison between various levels Force-deformation relations	184
Figure B-8 Comparison between various levels Energies (time variation of energy): a) Elastic SDOF $f_y=1$ , b) Elasto-plastic SDOF with $f_y=0.5$	185
Figure B-9 Comparison between various levels Energy indices (time variation of energy): a) Elasto-plastic SDOF $f_y=0.5$ , b) Elasto-plastic SDOF with $f_y=0.25$	186
Figure B-10 Comparison between various energy indices $\eta$ and $\lambda$ (time variation of energy): a) Elasto-plastic SDOF $f_y=0.5$ , b) Elasto-plastic SDOF with $f_y=0.25$	187
Figure C-1 Concepts of Regression Analysis	190
Figure D-1 Example of confidence intervals at significance levels $\alpha I = 5\%$ and $\alpha I = 1\%$	195
Figure D-2 Example of two-sided confidence intervals at significance levels $\alpha I/2$	195
Figure D-3 Example one-sided confidence intervals at significance levels $\alpha I$	196
Figure D-4 Example of one-sided hypothesis testing	197
Figure E-1 Force–Displacement capacity boundary and Hysteretic cycles principles as adopted in OpenSees	201



# List of Tables

Table 3-1 Parameters adopted in Opensees definition of the Ibarra et al. (2005) hysteretic model .....	83
Table 3-2 SDOF Properties (Mwafy and Elnashai 2001) – Normalised to the Yield values.....	85
Table 4-1 Regression analysis results between $\alpha$ and four different GM properties .....	98
Table 5-1 Force-Displacement Capacity Boundary .....	112
Table 5-2 $\Delta Sa(T1)$ results for $\Delta\alpha = 2^\circ$ .....	133
Table 5-3 $\Delta R$ results for $\Delta\alpha = 2^\circ$ .....	135
Table 6-1 Summary table of the GMs sets parameters .....	153
Table A-1 Properties of the 20 ground motions considered by (Vamvatsikos and Cornell, Incremental dynamic Analysis 2002) .....	171
Table A-2 Properties of the 611 ground motions considered .....	172
Table A-3 Properties of the 611 ground motions considered .....	175
Table E-1 Non-ductile SDOF Properties .....	201
Table E-2 Ductile SDOF Properties.....	202



# List of Symbols

$x_n$	Sequence, argument $n$ is an integer $n \in \mathbb{N}$
$x(t)$	Function, argument $t$ is continuous-valued $t \in \mathbb{R}$
$S_a(T_1)$	“First-Mode” Spectral acceleration
$avgS_a(T_1)$	“Multi-Modes” Average Spectral acceleration
$\phi_{xy}$	Phase of difference
$\Lambda(t)$	Ridge of the Wavelet transform
$C_\psi$	Admissibility constant
$\lambda(\cdot)$	Mean annual frequency of exceedance
$\varphi_{\omega 0}$	Mother wavelet (Morlet)
$W(s, n)$	Continuous Wavelet Transform, argument $s, n$ are integers $s, n \in \mathbb{R}$
$\Psi_{j,k}(\omega)$	Harmonic wavelet
$T_m$	Mean Period
$\bar{W}_{par}$	Averaged wavelet power spectrum
$\bar{W}_{taw}$	Time-averaged wavelet power spectrum
$S_{\ddot{u}_g}$	Kanai-Tajimi Power Spectral Density
$R_x$	Autocorrelation Function
$f_y$	Yield strength
$\bar{f}_y$	Normalised yield strength
$u_y$	Yield displacement
$R$	Force Reduction Factor
$\mu_M$	Ratio between Mean Instantaneous Period (MIP) of Response and Input
$V_{s,30}$	Shear wave velocity
$\alpha$	Variation of the Mean Instantaneous Period (MIP)
$\theta_{max}$	Maximum Interstory drift
$M$	Magnitude

## List of Symbols

---

$R_{rup}$	Distance to Rapture
$\varepsilon _{IM}$	Residuals of a regression analysis
$D_i$	Damage indices
$\eta$	Ratio (slope) of the linear regression curve
$\eta_s$	Ratio between the Low- $\alpha$ and High- $\alpha$ “First-Mode” Spectral accelerations
$E_i$	Energy Input
$E_k$	Kinematic Energy
$E_D$	Dissipated Energy
$E_S$	Restoring Strain Energy
$E_Y$	Hysteretic Energy
$\eta_E$	Ratio between the Hysteretic energy and the input energy
$\lambda_E$	Ratio between the Hysteretic energy and the maximum Hysteretic energy
$u_k^+$	Average number of zero-crossing with positive slope of a time-history
$\xi$	Damping ratio
$f_0$	Peak value of elastic strength
$u_0$	Peak value of elastic displacement
$u_m$	Peak value of ultimate displacement
$\mathcal{H}_0$	Null Hypothesis
$\mathcal{H}_a$	Alternative Hypothesis
$D_c$	Falsified Region (or Critical Region)
$T(x)$	Test statistic
$c$	Critical value
$a_g$	Ground Acceleration
$t_{05}$	Time instant at the 5% of the signal energy
$t_{95}$	Time instant at the 95% of the signal energy
$\delta_f$	Resolution in period (scaling)
$\delta_t$	Resolution in time

## List of Symbols

---

$\Delta t$	Time step
$T$	Period
$R^2$	Coefficient of Determination - Statistics
$c_v$	Coefficient of Variation
$D_{5-5-95}$	Effective Duration between 5%-95% of the signal's energy



# List of Operations

$x_n$	Sequence, argument $n$ is an integer $n \in \mathbb{N}$	
$x(t)$	Function, argument $t$ is continuous-valued $t \in \mathbb{R}$	
$\Re(\cdot)$	$\Re(a + ib) = a \quad a, b \in \mathbb{R}$	
$\Im(\cdot)$	$\Im(a + ib) = b \quad a, b \in \mathbb{R}$	
$x(t) \rightarrow X(\omega)$	$X(\omega) = \int_{-\infty}^{\infty} x(t)e^{-i\omega t} dt$	Fourier Transform
$X(\omega) \rightarrow x(t)$	$x(t) = \frac{1}{2\pi} \int_{-\infty}^{\infty} X(\omega)e^{i\omega t} d\omega$	Inverse Fourier Transform
$\text{floor}(\cdot)$	floor operator	
$\text{ceil}(\cdot)$	ceiling operator	
$H[\cdot]$	Hilbert transform	
$z(t)$	$x(t) + i \cdot H[z(t)]$	Analytical complex signal
$\bar{x}$	Complex conjugate of $x$	
$\mu$	Mean value	
$\sigma$	Standard Deviation	
$\sigma^2$	Variance	
$p\text{-value}$	Minimum significant level of a test	
$\beta$	Parameter estimator of a regression analysis	
$p_x(x, t)$	$\frac{1}{\sqrt{2\pi}\sigma_x(t)} \cdot e^{-\frac{(x-\mu_x(t))^2}{2\sigma_x^2(t)\sigma}}$	Probability Density function



# Glossary of Acronyms

ARMA	Autoregressive moving average
CDF	Cumulative distribution function
DFT	Discrete Fourier Transform
FFT	Fast Fourier transform
PDF	Probability Density Function
FT	Fourier transform
IDA	Incremental Dynamic Analysis
SDOF	Single Degree of Freedom
MDOF	Multi-Degree of Freedom
MIP	Mean Instantaneous Period
MIRP	Mean Instantaneous Response Period
PGA	Peak Ground Acceleration
PGV	Peak Ground Velocity
EDP	Engineering Demand Parameter
IM	Intensity Measure
PBEE	Performance Based Earthquake Engineering
DM	Damage Measure
MIDR	Maximum Interstorey Drift
WN	White Noise Signal
GM	Ground Motion
NRHA	Nonlinear Response History Analysis
IO	Immediate Occupancy
LS	Life Safety
CP	Collapse Prevention
PEER	Pacific Earthquake Engineering Research

## Glossary of Acronyms

---

HWT	Harmonic Wavelet Transform
SHM	Structural Health Monitoring
V-SHM	Vibration-Based Structural Health Monitoring
DI	Non-physical Data driven
WT	Wavelet Transform
STFT	Short-time Fourier transform
COV	Coefficient of Variation
DCH	Ductility Class High
DCL	Ductility Class Low
PSHA	Probabilistic Seismic Hazard Assessment



# Chapter 1

## Introduction

## 1 Motivation, Aims, and Objectives

Past and most of current codes of practice for earthquake resistant design of ordinary structures rely primarily on a force-based design approach usually for a single (nominal) design level of seismic action (e.g., Avramidis et al. 2016). The latter is defined in terms of seismic forces obtained from a (design) response spectrum with reduced spectral ordinates compared to the elastic seismic demands to allow for structures to yield and, thus, resist the design seismic action through ductile (energy dissipative) behaviour. Conveniently, in this approach, linear types of analyses suffice to estimate design seismic demands in line with structural design for all other types of loading (e.g., gravitational, wind loads, etc.), while relatively simple capacity design rules ensure sufficient ductility capacity to resist earthquakes even stronger than the nominal seismic design action without global collapse. However, one of the many limitations attributed to traditional force-based seismic design approach is the inability to assess, let alone account for in design, the actual performance of the structure for different levels of seismic action including those that are higher than the nominal design seismic action (Priestley et al. 2007). The latter consideration has become increasingly important in the past two decades in the wake of several major seismic events affecting large cities in developed countries and causing disproportionately high seismic loss such as Loma Prieta (1989), Northridge (1994), Kobe (1995), L'Aquila (2009), and Christchurch (2011) to name some. In this context, equally important is the development of tools for accurate seismic vulnerability assessment and (monetary) seismic loss prediction of existing structures which requires examining different levels of seismic action and accounting for their site-specific relative probability of occurrence or exceedance in a probabilistic/statistical context (McGuire 1995). Such tools facilitate decision making on allocating judicially limited funds/resources to mitigate seismic risk from the building owner level all the way up to Governmental decisions and public safety policies.

It is well-recognized that the Performance-Based Earthquake Engineering (PBEE) framework (e.g., Porter 2003) fulfils the above requirements both for the seismic design of new structures and for the vulnerability assessment of existing ones. This is achieved by implementing a number of methodological steps to link different (ideally all possible for a given site) levels of seismic action onto seismic performance represented through Engineering Demand Parameter (EDPs) (usually chosen to be peak seismic response quantities of interest to structural engineers such as inter-storey building drifts), which are well-representing structural damage and, thus, can ultimately, be readily mapped onto (monetary) seismic loss. Whilst it is possible to represent the seismic action within PBEE through stochastic seismological models (e.g., Boore 2003, Jalayer and Beck 2008, Rezaeian and Der Kiureghian 2008, Tsioulou, Taflanidis and Galasso 2019), such models are not commonly used currently for the task since they require specialist knowledge to

interpret and define their (seismological) input parameters (such as magnitude  $M$  and epicentre distance  $R$ ) while use of different stochastic models often lead to differences to seismic vulnerability analyses (Vetter and Taflanidis 2014). To this end, the seismic action is widely represented in PBEE applications via suites of recorded ground motions (GMs) appropriately selected to represent site-specific seismotectonic environment and local effects. These GMs are sometimes selected and, even, modified to match linear (i.e., non-reduced) response spectra for design (e.g., Katsanos et al. 2010, Smerzini et al. 2014) or, more generally, site-specific spectral shapes/ordinates (e.g., Baker and Cornell 2006). In most cases, GMs are amplitude scaled up/down through a scalar intensity measure (IM) to span different seismic intensity levels (Ebrahimian et al. 2015). This is the case of applying the so-called incremental dynamic analysis (IDA), arguably, the most widely used procedure, out of a number of alternatives, to derive a mapping of different levels of the input seismic action in terms of an IM onto an EDP obtained from non-linear response history analyses (NRHA) (Vamvatsikos and Cornell 2002, Vamvatsikos and Cornell 2004). IDA considers a set of judiciously selected recorded GMs which are amplitude scaled to span EDPs related to different limit states and, if so desired, all the way to collapse. Still, alternative approaches to IDA such as multi-stripe analysis (MSA) (Jalayer and Cornell 2009) and cloud analysis (Bazzurro et al. 1998) uses un-scaled GMs in conjunction with NRHA to span a certain range of EDP-IM plane (Jalayer et al. 2015).

Regardless of the NRHA-based procedure of choice, all the established procedures require accounting for aleatory uncertainty to seismic loss due to GM record-to-record variability within PBEE by considering an adequate number of GMs. Still, performing NRHA for large numbers of GMs is computationally onerous especially for large nonlinear finite element models. In this regard, on one hand much research effort has been devoted to define single degree of freedom (SDOF) inelastic structural systems and related EDPs used as proxies of more complex multi degree of freedom (MDOF) models in the context of PBEE. On the other hand, similarly significant research effort has been devoted in the past two decades by the earthquake engineering community to define IMs in conjunction with GM record selection criteria to facilitate the establishment of dependable IM-EDP relationships within a statistical/probabilistic context using as fewer as possible GMs (e.g. Baker and Cornell 2005, Baker and Cornell 2006, Kazantzi and Vamvatsikos 2015, Tothong and Cornell 2007 and Minas and Galasso 2019). Nevertheless, none of the current GM record selection criteria and IMs considered in the literature account for the time-dependent frequency content of recorded GMs due to the arrival of different types of seismic waves at different times at recording stations (e.g., Kramer 1996). This is so, despite the fact that several parametric stochastic models of the seismic ground motion, which account for non-stationary frequency content, have been developed over the past decades (Liu 1972, Yeh and Wen 1990, Conte and Peng 1997, Rezaeian and Der Kiureghian 2008). In this respect, the influence of

non-stationary frequency content, in establishing statistical IM-EDP relationships and, ultimately, fragility curves, is not accounted for in modern seismic risk quantification studies relying on recorded GMs. Moreover, the lack of a metric to characterise non-stationary frequency content in recorded GMs has hindered investigating the influence of the evolutionary frequency content of recorded GMs to the inelastic response of different types of yielding structures. This is the case, even though exist a number of studies demonstrating influence of non-stationary frequency content to peak inelastic demands where the seismic action is represented by stochastic models accounting for non-stationary frequency content (e.g., Wang et al. 2002, Vetter and Taflanidis 2014).

The above considerations and lack of knowledge motivate the present research work whose overarching aims are to:

- 1) Propose a novel scalar quantity, invariant to uniform GM scaling, that can effectively represent the time-evolving frequency content and its time-dependent relative significance/amplitude in recorded GMs.
- 2) Quantify the influence of the non-stationary frequency content of recorded GMs, as captured by the proposed scalar quantity, to the inelastic response of yielding structures and, ultimately, to delineate the range of importance of considering non-stationary frequency content attributes in establishing statistical IM-EDP relationships within the PBEE framework.

In this context, the research work reported in this thesis addresses the following objectives/tasks:

- (i) To undertake a detailed literature survey on time-frequency signal analysis tools and any previous successful applications in earthquake engineering capable of tracing the salient features of non-stationary frequency content time-series in time.
- (ii) To build on or tailor, as appropriate, the above identified tools to address the rich frequency content of recorded GMs and their transient characteristics leading, ultimately, to the definition of a scalar metric representative of the time-evolving frequency content of GMs and computationally efficient to compute.
- (iii) To establish statistical relationships between the novel metric of non-stationary frequency content and standard seismological parameters and GM properties widely used for record selection and/or as IMs in order to establish its relevance in earthquake engineering.
- (iv) To utilise this metric and the insights obtained from relationships with other parameters and IMs, to demonstrate and quantify the influence of non-stationary GM frequency content to the IM-EDP relationships governing inelastic single-degree-of-freedom (SDOF) oscillators widely used as proxies of yielding structures within the PBEE framework. Thus, ultimately, to establish the types of SDOF structures whose hysteretic

seismic response is most likely to be influenced by the non-stationary frequency content of recorded GMs.

- (v) To utilise the same metric to demonstrate and verify the influence of non-stationary frequency content of recorded GMs to the hysteretic seismic response of real-life/benchmark multi-storey yielding building structures modelled through detailed multi-degree-of-freedom FE models.

## 1.1 Thesis Organisation

The thesis is composed of seven chapters and five appendices. The current introductory chapter (*§1 - Introduction*) outlines the motivation of the present work in relation to PBEE and specifies overarching aims and objectives.

Chapter 2 (*§2 – State-of-Art Review on Frequency Content Signal Characterisation in Performance Based Earthquake Engineering*) offers a brief overview of the PBEE framework focusing on the concepts of intensity measures (IMs), engineering demand parameters (EDPs) as well as the use of incremental dynamic analysis (IDA) approach to derive statistical IM-EDP relationships which is a main computational tool used throughout the thesis to gauge the seismic inelastic response of structures to recorded ground motion accelerograms (GMs) using nonlinear response history analysis (NRHA) in a probabilistic context. Moreover, the Chapter highlights the need for characterising time-histories in earthquake engineering using time-frequency/period signal analysis tools and reviews the use of such tools with a focus on the continuous wavelet transform (CWT) spectrogram. Ultimately, research gaps are identified and approaches to fill them are put forth building on the presented literature review.

Chapter 3 (*§3 – Morlet Wavelet-Based Mean Instantaneous Period and moving resonance of yielding structures under recorded GMs*) discusses salient properties of CWT coupled with Morlet wavelets which facilitate significantly useful signal energy representation/distribution on the time-frequency/period plane. Ridge analysis of the CWT spectrogram is illustrated and its limitations for the case of recorded GMs is provided giving way to the concept of the mean instantaneous period (MIP) herein tailored as a bona fide tool to trace temporal changes of the average frequency content of recorded GMs relevant to structural earthquake engineering. MIP curves are derived for a small suite of GMs used as benchmark in developing IDA as well as for NRHA time-series aiming to demonstrate phenomenologically the relevance of the MIP to hysteretic response of simple yielding structures based on moving resonance and period elongation phenomena.

Chapter 4 (*§4 – “Alpha”(α): A Novel Wavelet-based Scalar Capturing the Average Non Stationary Frequency Content of Recorded GMs*) defines mathematically a novel scalar parameter

termed “alpha”,  $\alpha$ , extracted from the MIP of Morlet CWT spectrograms to quantify the non-stationary frequency content of GMs in a fashion expected to be relevant to hysteretic structural response. Further, statistical relationships of this novel scalar quantity,  $\alpha$ , with seismological parameters ( $M$ ,  $R$ ), local soil conditions (shear wave velocity  $V_{S30}$ ) and GM properties, PGA and PGV, are pursued. First statistical evidence identifying (but not quantifying) the influence of  $\alpha$  as a proxy of non-stationary frequency content of recorded GMs are further provided based on IDA results for the small benchmark suite of GMs used in Chapter 3.

Chapter 5 (*§5 - Influence of Non-Stationary Frequency Content of GMs to Seismic Demands of Inelastic Single-Degree-of-Freedom Systems*) undertakes novel numerical study to quantify the influence of  $\alpha$ , and thus of the average non-stationary GMs frequency content trends, to the response of SDOF ductile and non-ductile inelastic oscillators with various elastic periods widely used as proxies of yielding structures in undertaking seismic structural vulnerability and loss assessment within PBEE. This is pursued via gauging the influence of  $\alpha$  on widely used IMs adopted in undertaking IDA to propagate the seismic hazard onto peak inelastic seismic deformation used as EDP.

Chapter 6 (*§6 - Influence of Non-Stationary Frequency Content of GMs to Seismic Demands of Inelastic Multi-Degree of Freedom System*) quantifies the influence of the average non-stationary GM frequency content, as captured by  $\alpha$ , to peak inelastic seismic demands of MDOF inelastic models representing multi-storey building structures which yield under seismic excitation with progressively increasing intensity. In this regard, this chapter extends the numerical work of the previous chapter 5, by considering IDA results for MDOF inelastic systems as opposed to SDOF systems together with rigorous GM record selection to construct GM sets with same spectral shape and other GM properties known to influence EDP estimation but very different  $\alpha$  values.

Lastly, Chapter 7 (*§7 - Concluding Remarks*) summarises the contributions achieved by this doctoral thesis and highlights areas for future research.

The appendices provide the following supportive information and topics underpinning various chapters of the thesis. Appendix A contains catalogues of three different recorded GM suites used in various chapters to support the numerical work of this thesis. Appendix B provides a brief review of energy approach in the analysis of simple hysteretic oscillators under seismic excitation. Appendix C presents brief notes on linear regression analysis while Appendix D does the same for standard hypothesis statistical testing used in several instances in the thesis. Lastly, Appendix E provides input details for OpenSees modelling.



## Chapter 2

# State-of-Art Review on Frequency Content Signal Characterisation in Performance Based Earthquake Engineering

## 2 Preliminary remarks

This chapter begins with a brief outline of PBEE to highlight the importance of dependable statistical IM-EDP relationships in assessing seismic risk and loss in a probabilistic context. Then, a succinct review of different approaches for deriving IM-EDP relationships is offered utilising NRHA for recorded GMs. Special attention is focused on the IDA approach which is exclusively used in later chapters of this thesis to establish IM-EDP relationships and, ultimately, to demonstrate statistically the importance of accounting for the non-stationary frequency content of recorded GMs in estimating peak inelastic demands (EDPs) of seismically excited yielding structural models. Further, the chapter reviews studies adopting various joint time-frequency signal representation techniques, with emphasis given on the wavelet transform, to study the time-varying frequency content of typical signals encountered in earthquake engineering applications including recorded GMs and response time-histories of seismically excited structures. The chapter concludes with research gaps identified based on the provided state-of-the-art literature review.

### 2.1 Overview of Performance-Based Earthquake Engineering (PBEE) framework

#### 2.1.1 Methodological steps of the PBEE framework

PBEE is an approach which goes beyond the current seismic codes of practice, unifying seismic design (for new structures) and assessment (for existing structures) under a single probabilistic/statistical framework (Porter 2003). Its purpose is to facilitate decision making by various stakeholders (e.g. owners of civil infrastructure, insurance companies, Governments, etc.) on issues such as the achieved (targeted) level of seismic protection as a function of the seismic hazard and cost (FEMA P-58-1 2012) (FEMA-273 1997). PBEE aims to quantify seismic performance in terms of discrete quantifiable limit states expressed by means of an EDP as a function of the severity of seismic action which, for all practical reasons, is also discretised and expressed probabilistically in terms of an IM (e.g., probability that some critical IM is met or exceeded within a specific time window of exposure). Thus, for the design of new structures, PBEE renders the overall performance of the building as a function of the design process (Deierlein 2004), (FEMA-273 1997), (Porter 2003).

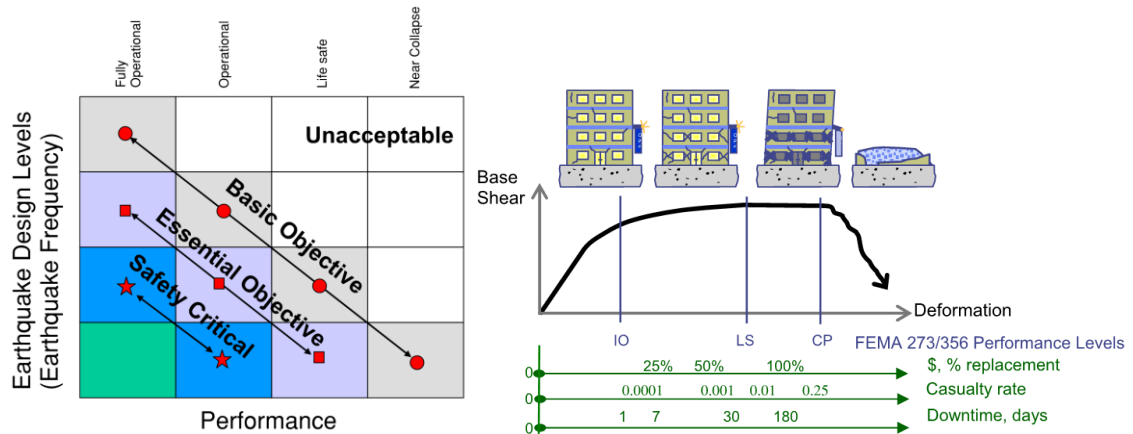


Figure 2-1 PBEE performance levels, (Deierlein 2004), (SEAOC Vision 2000 1995)

An early implementation of performance based design was made by (SEAOC Vision 2000 1995) and (FEMA-273 1997) in which analytical procedures for seismic performance quantification were formulated and the relation between performance (horizontal axes of the charts in Figure 2-1) and the severity of the seismic in terms of frequency of occurrence and/or in terms of total design base shear (vertical axes of the charts in Figure 2-1) were conceptually defined. Each cell represents a *performance objective*, which therefore is defined as a performance level at specific earthquake intensity. Stakeholders can then decide to implement different designs achieving different performance levels based on the type of infrastructure and/or capital available. For example, an owner may adopt the Basic Objective for an ordinary residential building, whereas a local borough may require that a hospital should meet safety-critical criteria.

Probabilistically, cost-effectiveness of different decisions within the PBEE framework may be expressed through the *mean annual frequency* (MAF) of exceedance,  $\lambda (DV)$ , of a judicially defined “decision variable” (DV) (e.g. repair cost) or vector of decision variables  $DV$ , given information about the structure (including its location) and a standard seismic hazard curve.

This is accomplished by considering the following steps with reference to the flowchart of Figure 2-2.

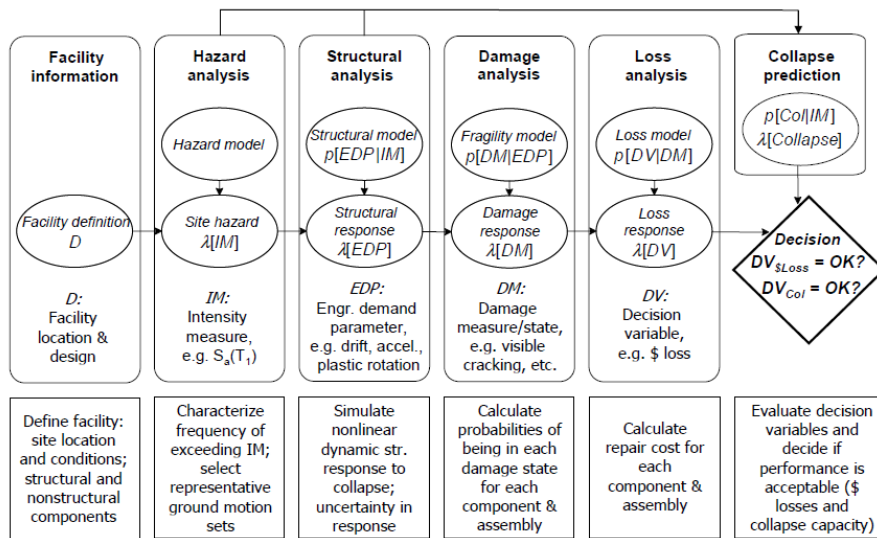


Figure 2-2 Steps of PBEE Methodology, (PEER Report 2007/08 2008), (Porter 2003)

Notably, the second step of PBEE involves hazard analysis to determine the MAF of exceedance  $\lambda(IM)$  of a seismic GM “intensity measure” (IM) which can be a single scalar IM or a vector  $IM$ . Examples of IMs are the peak ground acceleration (PGA), peak ground velocity (PGV), the spectral acceleration at the fundamental natural period  $T_l$  of the structure ( $S_a(T_1)$ ) and many others (e.g. Tothong and Cornell 2007, Kazantzi and Vamvatsikos 2015, Minas and Galasso 2019). The third step involves structural analysis to establish a statistical relationship between the IM and an “Engineering Demand Parameter” (EDP). The latter is chosen to be a (peak) response quantity of seismically excited structures such that it is representative of, and thus readily related to, a particular “Damage Measure” (DM). That is, the EDP needs to map well onto Damage limit states. For building structures, common EDPs are the peak inter-storey drift which is well-correlated to damage in structural and non-structural components and the peak floor acceleration which is well-correlated to damage in sensitive equipment, objects, and artefacts. It is noted that the PBEE framework allows for the treatment of both the “aleatoric” and the “epistemic” uncertainty (Der Kiureghian and Ditlevsen 2009). Aleatoric uncertainty is considered to be independent of our state of knowledge or number of experimental/simulation “runs”. Such uncertainty is possessed by the properties/characteristics of future earthquake induced GMs observing the same (or almost the same) seismological (e.g. Magnitude  $M$ , epicentral distance  $R$ , etc.) and site-specific characteristics (e.g. soil conditions). This uncertainty is practically accounted for by representing the seismic action with a suite of historic ground motion accelerograms recorded under the same (or almost the same) seismological and site-specific characteristics.

Therefore, the structural analysis step involves non-linear response history analysis (NRHA) of appropriate finite element (FE) models which capture the dynamic/hysteretic behaviour of the

structure under consideration. Further, epistemic uncertainty (e.g. due to lack of knowledge of the structural properties) can be accommodated by considering a Monte-Carlo based or a reliability based structural analysis step in which properties of the adopted FE model are treated as random variables (Liel et al. 2009, Vamvatsikos and Fragiadakis 2009).

In any case, the structure analysis step in PBEE needs to provide adequate statistical information to establish the conditional probability  $p\langle EDP|IM \rangle$ . The next (fourth) step involves damage-limit state analysis which seeks the quantification of the level of damage suffered by the structure in terms of a judiciously chosen DM for a particular EDP value. This is accomplished in a probabilistic/statistical sense by establishing fragility (survival probability) functions to obtain the conditional probability  $p\langle DM|EDP \rangle$ . The final step is the loss analysis involving DVs such as the repair costs and loss of lives, which is expressed via the conditional probability  $p\langle DV|DM \rangle$ . The following mathematical expression, using the same steps of Figure 2-2 and based on the total probability theorem, can be used to express the MAF of exceedance of a DV computed by means of the PBEE methodology considering the IM, EDP, DM, and DV (PEER Report 2007/08 2008).

$$MAF \text{ of exceedance} = \iiint (STRUCTURAL) \cdot (FRAGILITY) \cdot (LOSS) \cdot d(S, F, L) \quad (2.1)$$

or

$$\lambda(DV) = \iiint p\langle EDP|IM \rangle \cdot p\langle DM|EDP \rangle \cdot p\langle DV|DM \rangle \cdot d\lambda(IM) \cdot dIM \cdot dEDP \cdot dDM \quad (2.2)$$

Implied by the triple integral is that the assessment can be modelled as a Markov process, where the conditional probabilities are independent and can each be evaluated as such. While conceptually simple, there are many details associated with the implementation of each step of the framework that renders the procedure challenging. Some discussion is provided below on the development of statistical relationship between *IM* and *EDP*.

Process	Output Variable	Disciplines	Key Parameters
Seismic Hazard Analysis Site →IM	<b>IM: Intensity Measure</b> <ul style="list-style-type: none"> <li>• <math>S_a(T_1)</math></li> <li>• PGA, PGV</li> <li>• Aires intensity</li> <li>• Inelastic spectra</li> </ul>	Seismology; geotechnical engineering	<ul style="list-style-type: none"> <li>• fault location &amp; type</li> <li>• location &amp; length of rupture (M-R)</li> <li>• site &amp; soil conditions</li> </ul>
Structural Analysis IM →EDP	<b>EDP: Engrg. Demand Parameter</b> <ul style="list-style-type: none"> <li>• peak &amp; residual interstory drift</li> <li>• floor accelerations</li> <li>• component forces &amp; deformations</li> </ul>	structural & geotechnical engineering	<ul style="list-style-type: none"> <li>• foundation &amp; structural system properties</li> <li>• model parameters</li> <li>• gravity loads</li> </ul>
Damage Assessment EDP→DM	<b>DM: Damage Measure</b> <ul style="list-style-type: none"> <li>• component damage and repair states</li> <li>• hazards (falling, egress, chemical release, etc.)</li> <li>• collapse</li> </ul>	structural & construction engineering; architecture; loss modeling	<ul style="list-style-type: none"> <li>• structural &amp; components</li> <li>• HVAC &amp; plumbing systems</li> <li>• cladding &amp; partition details</li> <li>• contents</li> </ul>
Loss & Risk Analysis DM→DV	<b>DV: Decision Variable</b> <ul style="list-style-type: none"> <li>• casualties</li> <li>• closure issues (post EQ safety)</li> <li>• direct \$ losses</li> <li>• repair duration</li> </ul>	construction cost estimating; loss modeling; risk mgmt.	<ul style="list-style-type: none"> <li>• occupancy</li> <li>• time of earthquake</li> <li>• post-eq recovery resources</li> </ul>

Figure 2-3 Components of PBEE Methodology, (Deierlein 2004)

### 2.1.2 Establishing statistical IM-EDP relationships

Information for IM is conventionally obtained through probabilistic seismic hazard analyses and it is expressed as a mean annual frequency of exceedance  $\lambda(\text{IM})$ , which is specific to the location and potentially to the structure. On one hand, conventional IMs, such as PGA and  $S_a(T_1)$ , are simple to use as seismic hazard curves for these IMs are readily available. Since the aim of the structural analysis step of PBEE is the evaluation of conditional probability  $p(\text{EDP}|\text{IM})$ , the stronger the correlation between the selected **IM** to the predicted **EDP** is the higher the accuracy of the analysis becomes (Luco and Cornell 2007). In order to make this conditional probability estimation more effective and accurate the **IM** of choice should be both *sufficient* and *efficient* (Tothong and Cornell 2007). A sufficient **IM**, should be pursued among all the possible IMs which make the **EDP** conditionally independent, given **IM**, at least from the two most basic seismological parameters: fault distance, R, and earthquake magnitude, M. This enables the simplification  $p(\text{EDP} > x|\text{IM}, M, R) = p(\text{EDP} > x|\text{IM})$ . Then, the most efficient **IM** should be ideally sought among all sufficient IMs to minimise the variability between **EDP** for a given **IM** (Luco and Cornell 2007). In this regard, efficiency is the amount of variability of an **EDP** given an **IM** and the measure used to evaluate efficiency is the dispersion, defined as the standard deviation of the logarithm of the demand model residuals. An efficient demand model requires a smaller number of GMs and, therefore, of NRHAs to achieve a desired level of confidence in obtaining accurate statistical IM-EDP relationships (Shome and Cornell 1999).

Examples of IMs, beyond the obvious peak ground acceleration (PGA), include  $Sa(T_1)$  as well as the more advanced geometric mean of spectral ordinates, AvgSa, (e.g., Cordova et al. 2000, Kazantzi and Vamvatsikos 2015). In principle, quality IMs are those that can better reflect relations of GM properties to the structural response as well as to seismological parameters. An example of the former consideration would be that  $Sa(T_1)$  is a preferable IM over PGA since it accounts for structural natural period and inherent damping while PGA does not bring in any information about the structure (e.g., Vamvatsikos and Cornell 2002). An example of the latter consideration is AvgSa (a parameter, later defined, which captures the period shift effect) is an even more quality IM than  $Sa(T_1)$  as it accounts for the influence of GM spectral shape and not only on a single spectral ordinate (at  $T_1$ ). This aspect is important as it accounts for the influence of higher modes, in case structures are modelled as multi degree-of-freedom (MDOF) systems (e.g., Kazantzi and Vamvatsikos 2015), as well as of longer effective structural periods associated with period elongation phenomena of yielding (softening) structures (e.g., Katsanos et al. 2014). On the other hand, EDPs describe structural response in terms of deformation, acceleration or any other structural property which can characterise seismic demand of the structure and relate in a meaningful way to structural damage. To this end, a common EDP in building structures is the interstory drift ratio which monitoring the relative deformation of two consecutive floors. Considering the discrete nature of limiting states, statistical relationships between EDP and IM are typically obtained through conducting nonlinear response history analyses (NRHA) using inelastic structural models for GMs with increasing intensity expressed through the selected IM.

Currently there are several databases of GM records spanning large range of seismological parameters (such as magnitude, fault distance, etc) which helps to create the IM vector quantities generating IM-compatible input records. Even though these databases have developed in the last decades (PEER Database <https://ngawest2.berkeley.edu/> (Global), the European database <https://esm.mi.ingv.it/> (Europe and Middle east) and the Japanese <http://www.kyoshin.bosai.go.jp/>) there are still missing combination of parameters which may be important in constructing dependable statistics for the full range of  $p(\mathbf{EDP}|\mathbf{IM})$  probability. One approach to fill in missing data which is receiving increasing prominence in recent years is to consider artificial and/or simulated GMs consistent with stochastic models reflecting site-specific seismological environment (e.g., Tsioulou et al. 2018). Still, arguably, the most popular approach is to consider representative suites of GMs using certain GM selection criteria and to incrementally scale them up uniformly in time (i.e., by application of a multiplier different for each GM in the suite) to sufficiently high IM levels such that the structure reaches the limit state of interest (measured in terms of the EDP) which, if so desired, may be all the way to collapse (total structural instability). This is the essence of IDA (Vamvatsikos and Cornell 2002) resulting in an IDA curve for each GM on the IM-EDP plane. By using a collection of IDA curves, it is

possible to plot discrete IM conditioned on EDPs (i.e., vertical stripes on the IM-EDP plane), where each IDA contributes a single data point corresponding a particular GM. By convention IDA curves are limited to a maximum value of interstorey drift which depends on the ductility of structures, where they all terminate with a horizontal segment, referred to as “flatline.” Horizontal segments in IDA curves mean that large displacements occur at small increments in ground motion intensity, which is indicative of lateral dynamic instability. The intensity where IDA curves become horizontal is taken as the final (collapse) capacity of the system.

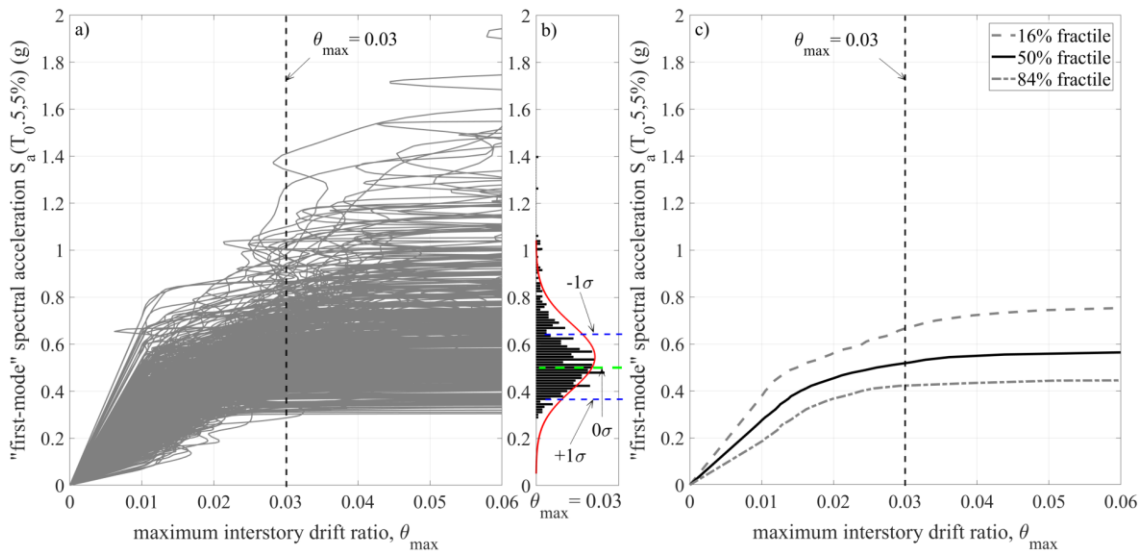


Figure 2-4 IDA Curves with respect to  $S_a(T_1)$  - (a) Individual IDA Curves; (b) normal distribution; (c) Median (Solid Lines) and  $\pm 1\sigma$  Standard Deviation (Broken Lines) Ensemble Curves.

Figure 2-4 provides an example of IDA analysis. It shows that the collapse capacity varies significantly from one GM record to another (record-to-record variability). Since their variability is quite substantial it is normal to use statistical tools to quantify the response of a suite of ground motions, such as the central tendency (median) and variability (dispersion) of the behaviour of a structural system. To this aim, typically, the 16<sup>th</sup>, 50<sup>th</sup> (median) and 84<sup>th</sup> percentile curves are used, which represent the fixed percentile at  $\mu \mp 1\sigma$ , mean  $\mp$  standard deviation (Figure 2-4 (b)). A percentile is the percentage transposition of the fractile which is the cut off point for a certain fraction of a sample. Knowing the probability distribution, the fractile becomes the cut-off point where the distribution reaches a certain probability. The 16<sup>th</sup>, 50<sup>th</sup> (median) and 84<sup>th</sup> percentile curves are therefore obtained, at each EDP value (i.e., vertical stripes on the IM-EDP plane), from a probability distribution function, constructed by fitting a normal distribution within the points extracted at the specific EDP values (Figure 2-4 (b)).

Importantly, the IDA curves are obtained through amplitude *scaling* of as-recorded GMs (after perhaps some pre-processed by seismologists), judiciously selected from large GM databanks. After selected the IM, the scaling process is carried out on the unscaled *vector* of accelerograms  $\mathbf{a} = [a_1, a_2, \dots, a_n]$  via a non-negative scalar factor  $\lambda \in [0, +\infty)$  such as  $\mathbf{a}_\lambda = \lambda \cdot \mathbf{a}$  (Vamvatsikos and Cornell, 2002). Commonly, and throughout this thesis, an algorithm is configured to use an initial first elastic run at 0.005 g, with a step increment of 0.01 g, to a maximum number of 32 scaling steps. The Collapse limit state (CP) is reached for a point of the IDA curve where the local tangent reached 20% of the elastic slope or  $\theta_{max} = 10\%$ . The Global Instability happens when the IDA curves are flat, where any increase of IM comports an infinitive increase of the EDP (i.e.  $\theta_{max}$ ) chosen (Vamvatsikos and Cornell, 2004).

As a closure to this section, it is noted in passing that despite the wide popularity of IDA, alternative NRHA-based procedures are available which circumvent GM amplitude scaling: arguably the main deficiency of IDA which received much criticism as excessive scaling may be inconsistent with seismological/physical considerations (Jalayer and Cornell 2009). The most well-known alternatives to IDA are *Cloud Analysis* and *Multi Strip Analysis* (MSA). The former is based on fitting a logarithmic linear regression to the pairs of structural response parameters (such as Maximum inter-storey drift) and IM for a set of recorded GMs (Jalayer et al. 2017). It is a well-known method for its simplicity but criticised for being very much sensitive to the selected suite of records, let alone to the lack of statistically significant number of records corresponding to large IM levels required to drive modern ductile structures to collapse in undertaking seismic collapse risk studies. On the other end, MSA carries out MRHAs at discrete set of IM levels each one having possibly a different GM set providing statistical information about structural demand over a wide range of spectral acceleration values. Thus, in contrast, to IDA approach, the MSA employs unique records with different intensities in lieu to the scaling approach (Jalayer and Cornell 2009). However, the requirement of varying GM records at different IMs adds a significant layer of complexity compared to IDA especially for routine/practical PBEE implementation. Further, as in the cloud analysis, lack of statistically significant number of records corresponding to large IM levels may again become an issue. Given the significant popularity of IDA among researchers and practitioners and the fact that the novelty of the herein pursued work should be independent of the tool used in deriving IM-EDP relationships, IDA is adopted throughout this work as the approach of choice in the establishing IM-EDP statistics using NRHA for recorded GMs.

### 2.1.3 GM record selection criteria in deriving IM-EDP relationships

Aleatory uncertainty in EDPs stemming from GM natural randomness (record-to-record variability), require the use of an adequate number of GMs in deriving IM-EDP relationships through NRHA-assisted procedures such as IDA, MSA, or cloud analysis. In order to reduce the computational cost of these procedures, GM record selection criteria beyond the standard seismological criteria of earthquake magnitude,  $M$ , and characteristic distance from the fault,  $R$ , are often employed. This is because carefully selected records reduce record-to-record variability thus relaxing the number of required GMs to establish statistically dependable IM-EDP relationships through NRHA. Further, they reflect better site-specific conditions resulting in more representative IM-EDP relationships for the site. Examples of GM record selection criteria, beyond the obvious  $M$  and  $R$  seismological parameters, include the GM pseudo-acceleration response spectrum shape or simply spectral shape. In this regard, the use of GMs with average response spectrum close to a given spectral shape has been widely considered in the literature to expedite IM-EDP derivations (see e.g., Katsanos et al. 2010). A common choice of a spectral shape is the one typically used by design seismic codes to specify design seismic action accounting for local soil conditions and seismicity. Alternatively, the conditional mean spectrum (Baker 2010) is taken as the target spectral shape. The latter is specified with the aid of the so-called epsilon “ $\epsilon$ ” parameter defined as the number of standard deviations by which the logarithm of the spectral acceleration,  $S_a(T_l)$ , of a recorded GM evaluated at the fundamental natural period  $T_l$  of a structure differs from the median logarithm of  $S_a(T_l)$  calculated from GM prediction relationships (Baker and Cornell 2006). The  $\epsilon$  parameter attracted much the interest of researchers as it relates well to spectral shape which, in turn, is closely correlated to the damage potential of a GM for structures with  $T_l$  pre-yield (elastic) fundamental period.

Other GM properties that were found to influence significantly peak inelastic seismic response demands of certain types of yielding structures is the effective GM duration (Trifunac and Brady 1975) and the mean Fourier-based GM period,  $T_m$ , (Rathje et al. 1998 and 2004). The former affects mostly the response of ductile structures close to collapse (Chandramohan et al. 2015), while the latter affects wider class of structures with  $T_l$  close to  $T_m$  (Kumar et al. 2011, Katsanos and Sextos 2015). In this regard, the previous works suggested that effective GM duration and  $T_m$  are used as record selection criteria in PBEE. Given the focus of this thesis in capturing the frequency content of GM and studying its impact to GM structural potential, more details on the  $T_m$  are provided in the following section since this is currently the most well-recognised frequency domain GM property to influence peak inelastic structural demands.

## 2.2 Fourier transform-based time-histories characterisation in PBEE

As in all engineering fields, standard Fourier or frequency domain time-series (signal) analysis is an indispensable signal representation tool in earthquake engineering which is widely used to resolve the significant frequencies included in recorded GMs and in structural response time-histories of earthquake excited structures (e.g., Kramer 1996). This is achieved by means of the Fourier transform (FT) which decomposes a signal on a basis of harmonically related sinusoidal functions. Effectively, the FT assigns a “weighting coefficient” (Fourier coefficient) to each harmonic, the modulus of which represents the total signal energy (or information) carried by each harmonic, or at each frequency.

Specifically, consider a band-limited time  $t$  signal  $x(t)$  (e.g., a recorded GM or a response time-history of an earthquake excited structure) of duration  $T_0$  and its discrete-time version  $x[n] = x(n \cdot \Delta t)$  with  $n = 0, 1, 2, \dots, N-1$  sampled at (at least) the Nyquist frequency with time step  $\Delta t$ , such that  $T_0 = N \cdot \Delta t$ . The discrete Fourier transform (DFT), defined as (e.g., Bracewell 1999)

$$\hat{X}[k] = \frac{1}{N} \sum_{n=0}^{N-1} x[n] e^{-i\omega_k n \Delta t} \quad (2.3)$$

decomposes/projects  $x[n]$  onto an orthogonal basis of harmonically related discrete-time sinusoidal functions with frequencies  $\omega_k = 2\pi k/T_0$  (in rad/s) for  $k \leq N/2$  assuming  $N$  is even and  $\omega_k = -2\pi k/T_0$  (in rad/s) for  $k > N/2$  with  $k=0, 1, 2, \dots, N-1$ . In the above equation and henceforth  $i = \sqrt{-1}$ . The magnitude of the complex-valued Fourier coefficients  $|\hat{X}[k]|$  can be viewed as a measure of similarity between the signal  $x(t)$  and a non-decaying in time sinusoidal function of frequency  $\omega_k$  (i.e., single frequency component). Therefore, the magnitude of the DFT achieves a representation of the *average over time frequency composition* of  $x(t)$  on a discretised domain (axis) of frequency  $\omega$  with discretisation step  $\Delta\omega = 2\pi/T_0$  and maximum frequency  $\pi/\Delta t$  or, equivalently, on the period  $T = 2\pi/\omega$  axis consistent with the above discretisation.

In this regard, the predominant frequency,  $\omega_p$  at which the magnitude DFT is maximised, that is,

$$\omega_p = \frac{2\pi p}{T_0} \quad \text{where } p = \underset{k}{\operatorname{argmax}}\{|\hat{X}[k]|\} \quad (2.4)$$

or, equivalently, the predominant period,  $T_p = 2\pi/\omega_p$ , is the simplest frequency domain metric to characterise the frequency content of recorded GMs in relation to their structural damage potential (Kramer 1996). The rationale of this consideration is that structures with  $T_l$  close to the  $T_p$  of a GM are expected to be mostly affected by the GM. Nevertheless, Rathje et al. (1998, 2004)

found that the most representative frequency-domain metric of GM structural damage potential is the Fourier-based mean period,  $T_m$ , over several other Fourier-based and response spectrum based metrics (see also Kumar et al. 2011). In detail,  $T_m$  is computed within a frequency range [0.25 20] Hz as (Rathje et al. 1998)

$$T_m = \frac{\sum_{k=K_1}^{K_2} |\hat{X}[k]|^2 T_k}{\sum_{k=K_1}^{K_2} |\hat{X}[k]|^2} \quad (2.5)$$

where  $K_1$  and  $K_2$  are the closest integers to  $0.25N\Delta t$  and  $20N\Delta t$ , respectively, and  $T_k = \frac{2\pi}{\omega_k}$ . It can be interpreted as the central GM period by noting that the DFT in equation (2.3) is energy preserving (i.e.,  $(x[n])^2 \propto |\hat{X}[k]|^2$ ) and, therefore, by treating the square magnitude of the Fourier coefficients as a distribution of the signal energy in the frequency domain. Indeed, several recent studies (Kumar et al. 2011, Katsanos et al. 2014, Katsanos and Sextos 2015) quantified statistically relationships (correlation) between standard EDPs (such as peak inelastic structural deformation),  $T_m$  and  $T_l$ .

Turning the attention to structural seismic response time-histories, Omori (1922) was the first to show almost a century ago that earthquake-induced damage elongates natural frequencies of buildings which, in turn, can be readily estimated by local “peak-picking” in the Fourier-transformed response acceleration time-histories (Brincker and Venutra 2015). The latter approach involves identifying the frequencies at which the DFT of structural response (vibrations) signals, measured by accelerometers installed in structures for health monitoring purposes, attain local maximum values for sufficiently broadband excitations (e.g., due to ambient noise). In this setting, several recent case-studies (e.g., Regnier et al. 2013, Vidal et al. 2013, Çelebi et al. 2016, Ubertini et al. 2017) quantified *period elongation* estimated from acceleration measurements before and after damaging earthquakes in various structures and related shifts of the period to the level of structural damage (see also Gkoktsi and Giaralis 2020). They verified, based on field recorded data, that the stronger the inelastic behaviour yielding structures exhibit under earthquake excitation (i.e., the heavier the damages structures suffer), the more flexible they become (i.e., the higher lateral stiffness degradation they sustain). Further, Goulet et al. (2015) developed a data-driven statistical learning framework for predicting, at city-scale, the safety state of buildings based on measured period elongation and a limited number of inspections. Moreover, Katsanos et al. (2014) quantified the period elongation in seismically excited single degree of freedom inelastic oscillators representing reinforced concrete building structures by monitoring the change of the predominant period,  $T_p$ , of response acceleration time-histories in the context of IDA. Ultimately, they found positive correlation between  $T_p$  of response time-histories with the  $T_m$  of GMs as GMs were scaled up in undertaking IDA. Importantly, note that the establishment

of such response  $T_p$  with excitation  $T_m$  for scaled GMs is enabled by the fact that  $T_m$  in equation (2.5) is invariable to signal (GM) scaling since FT is a linear transformation. More recently, Trevelopoulos and Guéguen (2016) showed positive correlation between period elongation and peak inter-storey drift in a number of typical inelastic multi-storey planar reinforced concrete structural models subject to MSA. They thus used period elongation as an EDP to represent cumulative seismic damage for sequences of earthquakes in seismic risk assessment of reinforced concrete structures within a PBEE context.

Collectively, the above reviewed works adopting FT-based metrics to relate GM excitation to structural damage represented by structural period elongation demonstrate clearly the usefulness of looking into the frequency composition of GMs and seismic response time-histories to inform PBEE. However, by definition, the FT cannot trace the time-varying (non-stationary) attributes of GMs and of response histories of inelastic seismically excited structures. This is because the sinusoidal functions employed by the transformation (signal projection) do not decay in time and, thus, the signal energy distribution in time is lost upon application of the FT. In other words,  $|\hat{X}[k]|$  is only a function of frequency. To this end, literature survey on the need and importance of representing transient time-histories encountered in earthquake engineering on the joint time-frequency plane is undertaken in the following section which reviews briefly signal analysis tools beyond the standard FT for joint time-frequency signal representation and their applications in earthquake engineering.

## 2.3 Non-stationary signal attributes in earthquake engineering: Physical considerations, signal representation tools, and applications

### 2.3.1 Physical considerations

Recorded acceleration GM signals are inherently non-stationary as their intensity and frequency content evolve with time. This is due to the dispersion of different types of seismic waves having different amplitudes and pre-dominant frequencies and arriving at the recording station at different time instants (Kramer 1996). Commonly, tension-compression (P-waves) characterised by relatively low amplitude and high frequencies arrive first as they tend to propagate faster than other seismic waves. Then, shear waves (S-waves) arrive and, in the case of far-field recording sites, various types of surface waves follow up which have typically lower frequencies and higher amplitudes than the P-waves. As a result, the intensity of typical GMs decay smoothly in time, after a short initial period of growth, while the dominant frequency content reduces in time. These GM attributes have been recognized since the early days of earthquake engineering (e.g. Housner,

1947; Housner, 1955; Thomson, 1959), and can be readily deduced by inspection of recorded GM time-histories. An example of a recorded acceleration time-history is given in Figure 2-5 where at different time segments different intensity levels are exhibited and radically different rates of zero-crossings occur (Giaralis 2008). The latter intuitively relates to the presence of time-evolving dominant frequencies.

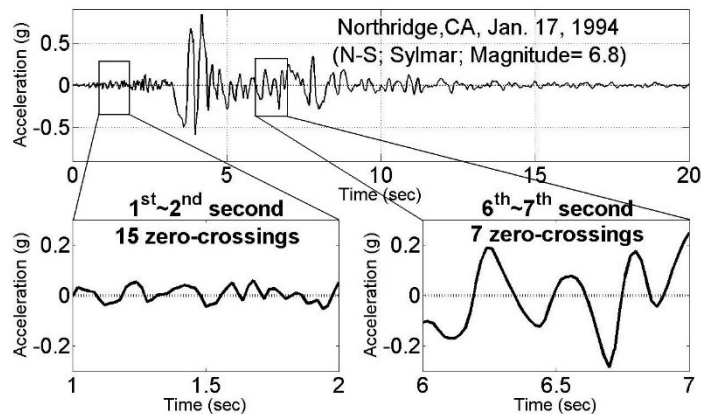


**Figure 2-5** An example of a recorded seismic accelerogram illustrating the time-varying frequency content, in terms of zero-crossings, and intensity of strong ground motions (Giaralis 2008).

Furthermore, response time-histories, such as floor displacements, accelerations, and inter-story drifts of buildings subject to seismic excitation, are also nonstationary signals whose evolving frequency content not only reflects, obviously, some characteristics of the input GM but also carries information about the structures and the possible level of potential structural damage. This information includes the onset of structural damage which phenomenologically leads to *transient apparent softening* of structures due to structural members stiffness degradation experienced during seismic excitation (e.g., DiPasquale and Cakmak 1990). Note that transient softening is a time-evolving phenomenon exhibited during the earthquake excitation and, thus, is different from the period elongation discussed in the previous section which is related to post-earthquake/residual stiffness degradation of members reflected, phenomenologically, to a shift of structural natural periods measured before and after a seismic event (see also Trevelopoulos and Guéguen 2016). Indeed, DiPasquale and Cakmak (1990) monitored the evolution of an *effective fundamental period* in field recorded seismic response acceleration time-histories across three stages: an initial period at the start of the ground shaking, a maximum (longest) period corresponding to the strong phase of shaking, and a final period corresponding to the damaged structure vibrating under low seismic excitation towards the end of the ground shaking and beyond (free vibration). This effective fundamental period was obtained by fitting a linear system,

following system identification techniques, to response time-history data during earthquake shaking delimited by a series of windows under known (measured) ground shaking.

In view of the above physical considerations, it is evident that joint time-frequency signal analysis is required to achieve a full picture of the energy distribution of recorded GM and of response time-histories in seismically excited structures, for it is clear that their time- dependent frequency content cannot be adequately represented by Fourier analysis which provides only the average spectral decomposition of a signal (Cohen, 1995; Qian, 2001). A qualitative overview of various time-frequency signal analysis tools considered over the years in earthquake engineering applications is provided in the following section before dwelling on the continuous wavelet transform (CWT) which is arguably the most widely considered of these tools by the earthquake engineering community.

### 2.3.2 Qualitative overview of joint time-frequency signal analysis tools

Gabor (1946) introduced historically the first joint time-frequency signal analysis approach by extending the application of the FT to signals with time-varying (non-stationary) properties. This was achieved by time-limiting the non-decaying sinusoidal function employed by the FT in equation (2.3) for signal decomposition by means of a window in time giving birth to what is known as windowed Fourier transform or short-time Fourier transform (STFT). The window is shifted in time (i.e., sliding along the time axis) as well as modulated in frequency (i.e., sliding along the frequency axis) without changing its width (or support) in time. These shifting and modulating operations results in the STFT of a signal being a two-variable function of both time (with reference to the window shifting in time) and frequency (with reference to the window modulating in frequency). Ultimately, the spectrogram, defined by the modulus of the STFT squared, emerges as a distribution of the signal energy on the time-frequency plane (Cohen 1995). Whilst intuitive and widely used for decades to gain an insight of the energy distribution of non-stationary signals on the time-frequency plane in engineering and applied physics, STFT has the limitation of an *a priori* fixed resolution in time and in frequency specified by the window properties, that is, its support in time and in frequency (Qian 2001). This becomes problematic for studying relatively broadband signals as high-frequency components (indicative of sudden changes in physical systems such as structural damage during earthquakes) tend to be well-localised in time (therefore finer time resolution is usually desired), while low-frequency components (e.g., characteristic pulses in near-field recorded GMs) tend to be well-spread in time (therefore finer frequency resolution is normally sought after).

The Wigner- Ville distribution (WVD) (Ville 1948) aims to circumvent some of the shortcomings of the STFT spectrogram by using a modulated and shifted window function which coincides

with the signal itself after being time-reversed. It can be shown mathematically that the STFT spectrogram is a smoothed version of the WVD, and thus the latter achieves better time-frequency resolution (Qian, 2001). However, the WVD lacks, to a certain degree, physical meaning since in several cases it yields negative values for the spectrum with obvious physical interpretation problems (Cohen 1995, Qian 2001).

Having emerged in 1980s, the wavelet transform (WT) has become a potent signal analysis tool as, among several other applications, was proved to be quite useful for representing signals on the time-frequency plane (e.g. Mallat 1998, Qian, 2001). Instead of windowed versions of sinusoidal functions used by STFT, WT decomposes signals using oscillatory wave-like functions, termed wavelets, generated by scaling the effective time duration of a single “mother wavelet” function and shifting its position in time. The scaling operation is key as it changes simultaneously the effective support of wavelets in time (duration) and in frequency (bandwidth) in a way that is consistent with practical requirements for joint time-frequency resolution for most physical phenomena described by non-stationary time-histories. Specifically, low wavelet scales correspond to very well-localised in time wavelets with high-frequency content capturing with high accuracy (resolution) in time high-frequency signal components which, as discussed before, are usually sudden (short-lived) in time. On the antipode, high wavelet scales correspond to stretched in time (large duration) wavelets with well-localised in the frequency domain low-frequency content which make them ideal to resolve accurately low frequency components of signals which are usually long-lived in time. Clearly, the above attributes rectify shortcomings of both the STFT and the WVD. At the same time, a plethora of analysing wavelet functions capable of achieving practically useful signal representations through the scaling operation have been developed to address different applications in science and engineering together with highly efficient algorithms for numerical implementation of the transformation founded on rigorous mathematical theory (see e.g., Daubechies 1988, Mallat 1998 and references therein). These facts endow WT with exceptional flexibility which is the main reason for gaining wide popularity in the past two decades in the fields of structural dynamics and vibrations-based damage detection (see e.g. Staszewski, 1998a; Spanos and Failla, 2005; Kijewski and Kareem, 2006; Gkoktsi and Giaralis 2015 and references therein).

More recent adaptive signal processing techniques for capturing local variations of non-stationary signals include the adaptive chirplet transform (ACT) and the empirical mode decomposition (EMD). The former combines signal decomposition on a special type of analysing functions called Gaussian chirplets (Mann and Haykin, 1995) with the WVD of the decomposed signal, which is positive everywhere for the case of Gaussian chirplets (Baraniuk and Jones, 1996), to give rise to signal time-frequency representations with additional flexibility (degrees of freedom) beyond wavelet scaling. The latter provides a case-specific data-driven decomposition of a signal

into non parametric mono-chromatic intrinsic mode functions (Huang et al., 1998; Flandrin and Gonçalves, 2004) which can be processed via the Hilbert transform (see e.g. Papoulis, 1977) to trace the time-evolution of the dominant frequency components of the original signal. The ACT has been used to process recorded GMs as well as response histories from NRHA in a number of works (Wang et al. 2002, Spanos et al. (2007a). The EMD has been employed for the same tasks by Kijewski-Correa and Kareem (2006) and Spanos et al. (2007a). It was found that the success of these adaptive methods rely on computationally intensive algorithms requiring the fine-tuning of certain parameters and thresholds, while the achieved time-frequency resolution do not compensate for the increased computational cost. In this regard, the remainder of this review focuses on the CWT which is the tool of choice used throughout this thesis.

### 2.3.3 The continuous wavelet transform (CWT)

The Continuous Wavelet Transform (CWT) originates from the work of the geophysicist Jean Morlet and the physicist Alex Grossman (Grossmann and Morlet 1984) who decomposed empirically seismic geophysical signals using what is now known as Morlet wavelets (Mallat, 1989). For a discrete-time signal  $x[n]$ , the CWT is defined as (e.g., Torrence and Compo 1997)

$$W[\tau, s] = \sqrt{\frac{\Delta t}{s}} \sum_{n=0}^{N-1} x[n] \psi^* \left( \frac{(n-\tau)\Delta t}{s} \right), \quad (2.6)$$

where  $\psi \left( \frac{(n-\tau)\Delta t}{s} \right)$  is a wavelet function generated by scaling a mother wavelet oscillatory function  $\psi(t)$  using the scaling parameter  $s > 0$  and by shifting the mother wavelet in time using the time parameter  $\tau = 0, 1, 2, \dots, N-1$ . In the last equation the superscript (\*) denotes complex conjugation as a wavelet function can be complex-valued, while the term  $\sqrt{\Delta t/s}$  is added to ensure that all scaled versions of  $\psi(t)$  have the same energy. A qualified (or admissible) wavelet function needs to be zero-mean and have finite support in frequency (finite bandwidth) acting effectively as a band-pass filter (see e.g. Mallat 1998).

Importantly, the scaling operation and the oscillatory form of the wavelets are the salient features that allow for interpreting the squared magnitude (spectrum) of the wavelet coefficients,  $|W(\tau, s)|^2$ , as an estimator of the signal energy distribution on the time-frequency or, equivalently, on the time-period plane. That is,

$$SP(t, \omega) = SP\left(\tau\Delta t, \frac{\omega_p}{s}\right) = |W[\tau, s]|^2. \quad (2.7)$$

This is because the scale parameter  $s$  is associated with frequency through a reciprocal relationship  $\omega = \omega_p / s$  where  $\omega_p$  is the predominant frequency of the unscaled (i.e.,  $s=1$ ) mother wavelet (e.g., Mallat 1998). Moreover, the CWT in equation 2.6 implies that  $N$  wavelet coefficients can be computed for each scale value which facilitates visually meaningful wavelet spectrograms,  $SP(t, \omega)$ , in equation 2.7. The so-called ridges of the wavelet spectrogram are salient features defined as collections of CWT local maxima along the time axis (Carmona et al. 1997). That is,

$$s_r(t) = \max_{\omega} \{SP(t, \omega)\} \quad \text{or} \quad s_r[\tau] = \max_s \{|W[\tau, s]|^2\}, \quad (2.8)$$

where  $r=1, 2, \dots, R$  and  $R$  is the total number of ridges (looking across different scales) at any given time instant. Intuitively, the ridges of the wavelet spectrogram signify local (in time) significant energy corresponding to a certain scale/frequency which can be attributed to the existence of a local in time signal frequency component picked up by the analysing wavelet scaled at the considered scale/frequency. For mono-harmonic signals, it can be analytically shown that the (single) ridge of the wavelet spectrogram coincides with the signal frequency component,  $\omega_p$ , at each time instant (instantaneous frequency) provided a suitable wavelet is used in computing the CWT (Lilly and Olhede 2009). Nevertheless, multi-harmonic non-stationary signals will have several different ridges at each time instant and wavelet ridge analysis becomes computationally challenging (Carmona et al. 1999) and, in the case of noisy signals, visually counter-intuitive and, ultimately, non-practical (as will be demonstrated later in Chapter 3 for typical recorded GMs). On the other hand, for the latter type of signals, it may be desired to know only the mean frequency in time which is likely not to coincide with any actual frequency component present in the signal. This gives rise to the (energy) mean instantaneous frequency defined as the geometric mean of all the frequencies present in the signal at each time instant. That is (e.g., Lilly and Olhede 2009),

$$MIF(t) = \frac{\int \omega SP(t, \omega) d\omega}{\int SP(t, \omega) d\omega} \quad \text{or} \quad MIF[\tau] = \frac{\int \frac{\omega_p}{s} |W[\tau, s]|^2 ds}{\int |W[\tau, s]|^2 ds}. \quad (2.9)$$

In the limiting case of mono-harmonic signals, the above *MIF* coincides with the signal instantaneous frequency (Boashash 1992a) as long as suitable analysis wavelet is used in computing the CWT as discussed by Lilly and Olhede (2009).

Despite its usefulness for meaningful time-frequency signal representations, it is noted in passing that the CWT in equation (2.6) is redundant in the sense that it generates  $N$  wavelet coefficients for each chosen scale level from an  $N$ -length discrete-time signal. In this regard, Daubechies (1988) showed how to efficiently construct families of orthogonal wavelets compactly supported in time domain or in frequency domain using digital filter-banks and allowed for non-redundant wavelet signal analysis and reconstruction of  $N$ -long discrete-time signal using  $N$  total number of wavelet coefficients across different scales giving birth to what is known as the discrete wavelet transform (DWT). Moreover, Mallat (1989) embedded DWT within a multi-resolution analysis framework (Mallat, 1998). Still, whilst DWT preserves signal energy, it is not particularly helpful in providing intuitive visualisations of signal energy distribution on the time-frequency plane. A conspectus of applications of the wavelet transform in earthquake engineering follows aiming to demonstrate the breadth of its usage and applicability without being, by any means, exhaustive.

### 2.3.4 Indicative applications of wavelet transform signal analysis in earthquake engineering

Basu and Gupta (1998) considered an early form of DWT, employing wavelets compactly supported in frequency domain and non-overlapping across scales, to compute spectral moments and, ultimately, peak structural responses of seismically excited single-degree-of-freedom (SDOF) oscillators. In this manner, they were able to correlate structural response to different frequency bands of seismic excitation. Further, Iyama and Kuwamura (1999) relied on DWT signal energy preservation to demonstrate that the square modulus of wavelet coefficients of recorded GMs is proportional to the seismic input instantaneous energy at different frequency bands. In addition, they found that seismic waves long periods have different velocities depending on the epicentral distance and that the peak wavelet instantaneous energy is proportional to the total input seismic energy. Moreover, Baker (2007) employed the DWT to identify and extract low-frequency large amplitude pulse-like content typical of near-field GMs and proposed widely adopted classification rules for pulse-like near-fault GMs. In addition, Montejo and Kowalsky (2008) used the CWT of recorded GMs to define frequency-dependent effective GM duration and gauged its influence for predicting damage in the context of PBEE using IDA.

Focusing next on applications considering treatment of structural response signals under seismic excitation, Pan and Lee (2002) examined the effectiveness of STFT, DWT and CWT to identify dynamic characteristics of bilinear elasto-plastic seismic response of SDOF and MDOF structures aiming to correlate signal frequency content variation with excursions of the yielding strength in time. Similarly, Basu (2005) used DWT with compactly supported in frequency domain and non-overlapping across scales wavelets to analyse response acceleration signals of bilinear non-hysteretic and of Bouc-Wen hysteretic SDOF structures subject to recorded GMs and successfully traced stiffness variations and temporal location of damage onset. More recently, Castellanos and Ordaz (2013) used DWT wavelet coefficients of yielding time-histories of bilinear elasto-plastic oscillators subject to seismic GMs (i.e., binary time-histories indicating time intervals that oscillator resisting force is above the yielding strength) to predict seismic ductility demand and, ultimately, the level of structural damage.

Independently of the above line of research, Ruzzene et al. (1997) were the first to suggest that the ridges of the CWT in equation (2.8) of response acceleration signals of MDOF linear structures can be viewed as representative signatures of vibration modes. They thus used CWT ridges to determine the structural natural frequencies of structures in a system identification context. More recently, Wang et al. (2013) extended the use of CWT ridge analysis for system identification of yielding structures under seismic excitation by interpreting CWT ridges as phenomenological time-evolving effective natural frequencies of the inelastic structures treated as linear time-varying dynamical systems (see also Staszewski 1998b). Further, Spanos et al. (2007a) extracted the MIF in equation (2.9) of response displacement time-histories obtained from NRHA to a 21-storey steel frame model subject to recorded GMs scaled at different intensities. They used wavelets compactly supported in frequency domain and non-overlapping across scales achieving high frequency resolution and demonstrated that the MIF decays faster in time (i.e., towards lower frequencies, thus longer periods) as GM intensity increase. They, thus, concluded that tracing the CWT MIF in time can be used as a seismic damage detection tool.

Further to the above use of CWT ridges and MIF time-histories for structural damage detection, Noh et al. (2011) defined scalar CWT-based damage sensitive indices for seismic damage characterisation of yielding structures. It was reported that the most efficient index for the task relies on the energy of wavelet coefficients (wavelet spectrogram) at scales corresponding to  $T_l$ . This index was used by Noh et al. (2012) as an EDP to perform full-fledge statistical seismic vulnerability analysis in the context of PBEE framework using IDA. The steps of the CWT-assisted PBEE are shown in (Figure 2-6). In Balafas and Kiremidjian (2015), the same CWT-based index was obtained for excitation time-histories (recorded GMs) as well as for response acceleration time-histories from experimental specimens of reinforce concrete columns progressively damaged under shaking table testing using the recorded GMs. The authors

demonstrated correlation between indices of response and excitation suggesting that the relationship between indices can be used for rapid data-driven structural damage characterisation in the aftermath of major seismic events in structures instrumented with accelerometers for health monitoring.

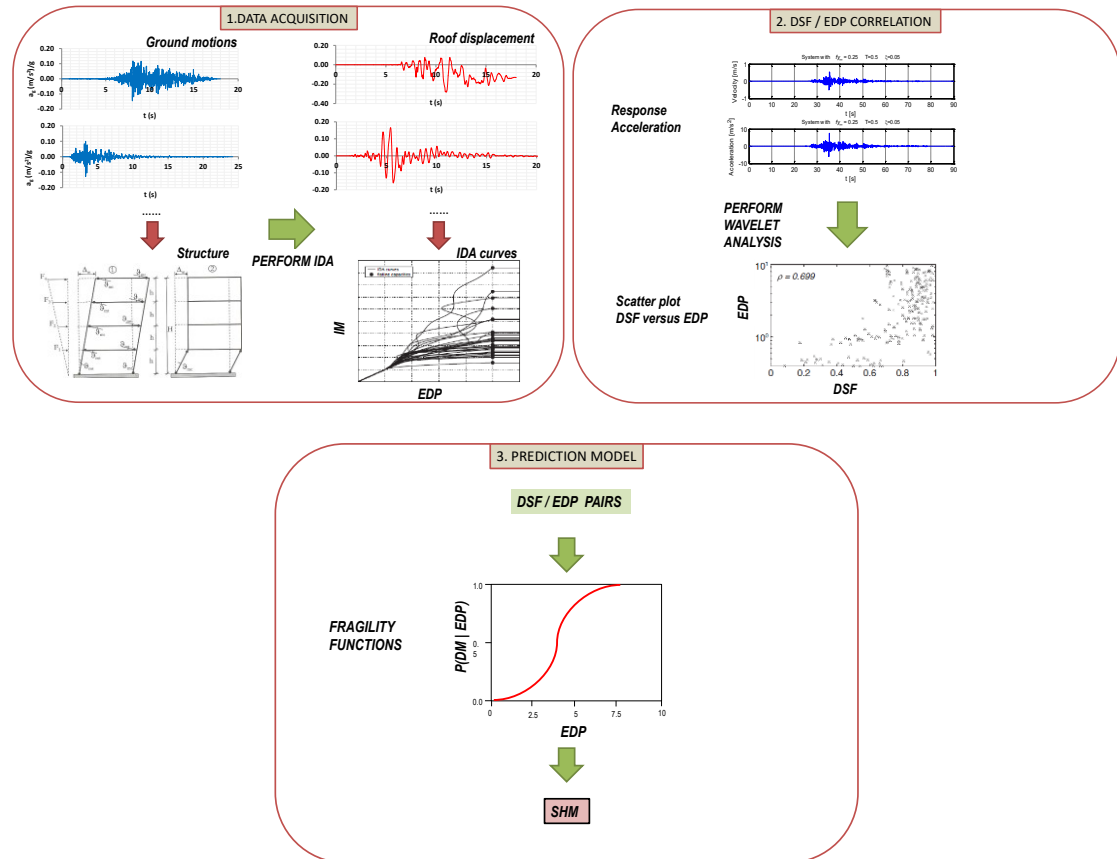


Figure 2-6 Use of a wavelet-based damage sensitive factor (DSF) to derive fragility curves (Noh, et al. 2012)

The effectiveness of various time-frequency signal analysis tools, including the CWT, to capture non-stationary features in response time-histories of seismically excited structures has been also demonstrated by various researchers using field recorded data from instrumented real-life structures. The main focus of such studies is to characterise earthquake-induced damage during seismic excitation. In this setting, Mucciarelli et al (2004) considered the STFT and the CWT, among other techniques, to demonstrate elongation of structural natural frequencies of an instrumented reinforced concrete building indicative of structural damage during a sequence of historic earthquake events occurred in central East Italy in 2002. Further, Todorovska and Trifunac (2010) successfully captured changes (elongation) to structural natural periods through ridge analysis to STFT-based spectrogram of seismic response acceleration time-series recorded in an instrumented building in California during the 1979 Imperial Valley seismic event. On a

different end, Michel and Gueguen (2011) studied the WVD of field recorded seismic response time-histories and concluded that changes of dominant frequency components in the signals are not necessarily due to structural damage but may actually be signatures of the excitation carried over to response time-series.

A final important application of time-frequency analysis tools used in conjunction with recorded seismic GMs is to facilitate the development of seismic GM stochastic models which, ideally, should account for non-stationarity in both amplitude and frequency content as recorded (natural) GMs do. Such models are used as input to analytical stochastic nonlinear dynamics techniques, such as statistical linearisation (e.g., Roberts and Spanos 1999), to obtain seismic response statistics of inelastic structures without undertaking NRHA. Alternatively, they are used to generate artificial seismic GMs used as input for NRHA to derive seismic response statistics in a Monte Carlo simulation-based context (e.g., Giaralis and Spanos 2012). To this aim, Conte and Peng (2007) applied the STFT to recorded GMs to calibrate a parametric non-stationary stochastic GM model. Further, Wang et al. (2002) defined a stochastic GM model using the average ACT-based spectrogram of recorded GMs. More recently, Jian et al. (2014) used a CWT-based signal analysis tool to find the evolutionary frequency content statistics including the mean and the variance instantaneous frequency from large suites of recorded GMs. These time-varying statistics were used to define a parametric stochastic GM model for simulation of artificial GMs achieved through filtering white noise through a linear time-varying filter.

### 2.4 Research gaps and needs

The above undertaken state-of-art survey reveals that the average (stationary) frequency content of recorded GMs, as captured by Fourier-based  $T_m$  (Rathje et al. 1998), influences the inelastic response of seismically excited yielding structures. The significance of this influence depends on the pre-yield structural stiffness, commonly expressed through  $T_l$ , (e.g. Kumar et al. 2011). Moreover, several studies considering both field recorded data and computer generated NRHA data reported that structural natural periods and primarily  $T_l$  change during seismic excitation (apparent softening) as well as elongate (permanent change) after damaging earthquakes compared to values attained before earthquakes (healthy state). It was further shown that this change of natural frequencies is dependent on the average stationary frequency content of recorded GMs (Katsanos et al. 2014). Moreover, stochastic dynamics approaches showed moving resonance in which the effective natural frequencies follow, with some delay, the time-varying frequency content of the excitation. A further indication of the influence of seismic evolving frequency content to inelastic structural response was demonstrated by using artificially generated

GMs from stochastic seismic GM models with varying frequency content Wang et al. (2002), Vetter and Taflanidis (2014).

However, a first major conclusion of the review is that no systematic study of non-stationary frequency content using recorded GMs have been undertaken in the open literature. This is an important gap in the current state-of-art research in earthquake engineering and applied inelastic structural dynamics since PBEE is commonly undertaken based on NRHA using recorded GMs. The undertaken literature review shows that such a systematic study is primarily hindered by the lack of a GM property that captures the evolutionary frequency content of GMs and can, perhaps, be used either as a record selection criterion or as an IM. Indeed, none of the current IMs and record selection criteria adopted in deriving IM-EDP relationships using recorded GMs within the PBEE framework accounts for the non-stationary (time-evolving) frequency content of GMs. Specifically, the Fourier-based average frequency  $T_m$  cannot discriminate time-evolving frequency composition in GM signals. Further, the spectral ordinate  $S_a(T_1)$  and, more generally, spectral shape does not uniquely represent the time-varying amplitude trends let alone frequency content of GMs. This can be deduced by the work of Giaralis and Spanos (2010, 2012) and Spanos and Giaralis (2013) who demonstrated that stationary stochastic processes with different durations and energy content as well as stochastic processes with different time-amplitude properties and effective durations but constant frequency content can fit in the mean sense any given spectral shape.

A second major conclusion is that non-stationary features of frequency content do affect the inelastic response of yielding structures and, therefore, EDPs as evidenced by stochastic dynamics approaches (e.g., Papadimitriou) which model seismic excitation by means of stochastic processes with non-stationary frequency content and by simulation-based approaches which model the seismic action by means of artificial time-histories compatible with stochastic processes with non-stationary frequency content (e.g., Wang et al. 2002, Taflanidis and Vetter 2014). In this regard, there is scope in investigating the influence of non-stationary frequency content to EDPs when seismic action is represented by suites of recorded GMs which is currently the mode of preference in deriving IM-EDP relationships within PBEE. However, gauging qualitatively as well as quantitatively this influence is hindered by the lack of a GM metric or property measuring or accounting for non-stationary frequency content. This consideration establishes the premises of the first overarching aim pursued this thesis, that is, to propose a novel GM metric representative of the non-stationary frequency content of GMs. Having such a metric at hand will enable the quantification of the influence of GM non-stationary frequency content by probing into statistical IM-EDP relationships for suites of judiciously selected GMs and for a variety of structural models with different properties.

To this aim, the following third major conclusion from the undertaken literature review is utilised. That is, the fact that CWT has been shown to be a most potent and widely used signal analysis tool to trace the time-evolving features of the energy composition of signals encountered in earthquake engineering on the joint time-frequency plane. In particular, the MIF introduced by Spanos et al. (2007) as a detection tool for earthquake induced structural damage is a concept that is reasonable to be used for characterising the evolution of the mean frequency content of GM signals. Apart from the well-recognized ability of the CWT for extracting time-varying frequency content in transient signals, a main justification behind choosing to explore the potential of MIF for the purpose at hand is the fact that  $T_m$  (the average in time mean frequency content of GMs) has already been seen to influence the response of the yielding structures (Kumar et al. 2011) as well as to characterise period elongation and, thus, the level of inelastic structural behaviour by application to response time-histories obtained through NRHA (Katsanos et al. 2014). In other words,  $T_m$  seems to relate excitation and response signals. One would expect that MIF of excitation and response may also be correlated and this hypothesis is addressed in this thesis.

To this end, the next chapter discusses CWT potential for the purpose at hand focusing on a particular analysing mother wavelet found to be rather efficient for treating recorded GMs and used throughout this work, and defines the WT-based mean instantaneous period (MIP) for GMs as a generalisation of the Fourier-based  $T_m$ .



## Chapter 3

Morlet Wavelet-Based Mean

Instantaneous Period and moving

resonance of yielding structures under

recorded GMs

### 3 Preliminary remarks

This chapter discusses salient properties of CWT coupled with Morlet wavelets which facilitate significantly useful signal energy representation/distribution on the time-frequency/period plane. Ridge analysis of the CWT spectrogram is illustrated and its limitations for the case of recorded GMs is provided giving way to the concept of the mean instantaneous period (MIP) herein tailored as a bona fide tool to trace temporal changes of the average frequency content of recorded GMs relevant to structural earthquake engineering. MIP curves are derived for a small suite of GMs used as benchmark in developing IDA as well as for NRHA time-series aiming to demonstrate phenomenologically the relevance of the MIP to hysteretic response of simple yielding structures based on moving resonance and period elongation phenomena.

#### 3.1 Energy distribution of continuous-time functions on the time-frequency plane

Any time-history or temporal signal is a function of time which carries information at different frequencies distributed as *energy* on the time- frequency plane (Cohen 1995). As detailed in Section 2.2, the concept of frequency and the underlying frequency domain analysis/interpretation of signals relies on the Fourier transform (FT) which decomposes any signal using sinusoidal functions. For the case of a continuous-time  $t$  signal, where  $\psi(t)$  are functions  $\in \mathcal{L}^2(\mathbb{R})$  (Hilbert space of square-integrable functions), of finite energy, that is

$$\|\psi\|^2 = \int_{-\infty}^{+\infty} |\psi(t)|^2 dt < \infty, \quad (3.1)$$

the FT is expressed by the Fourier integral (e.g., Bracewell 1999)

$$\hat{\Psi}(\omega) = \int_{-\infty}^{+\infty} \psi(t)e^{-i\omega t} dt. \quad (3.2)$$

where the symbol  $|\cdot|$  stands for absolute value for real functions and for magnitude for complex functions, while the symbol  $\|\cdot\|$  denotes the standard second norm (Cohen 1995). The above signal decomposition allows for writing the signal  $\psi(t)$  in terms of complex sinusoidal functions  $e^{i\omega t}$  of circular frequency  $\omega$  (in radians per second) using the so-called inverse Fourier transform integral as

$$\psi(t) = \frac{1}{2\pi} \int_{-\infty}^{+\infty} \hat{\Psi}(\omega)e^{i\omega t} d\omega. \quad (3.3)$$

The FT preserves the signal energy as seen by the equalities

$$\int_{-\infty}^{+\infty} |\psi(t)|^2 dt = \frac{1}{2\pi} \int_{-\infty}^{+\infty} |\hat{\Psi}(\omega)|^2 d\omega = \int_{-\infty}^{+\infty} |\hat{\Psi}(2\pi f)|^2 df \text{ or } \|\psi\|^2 = \frac{1}{2\pi} \|\hat{\Psi}\|^2 \quad (3.4)$$

where  $f = 2\pi/\omega = 1/T$  is the frequency in Hertz. In this regard, it is always possible to interpret  $|\psi(t)|^2/\|\psi\|^2$  and  $|\hat{\Psi}(\omega)|^2/\|\hat{\Psi}\|^2$  as probability density functions (pdfs) providing the energy distribution in the time and in frequency domain, respectively. Then, the mean and the variance of the former time-domain pdf, written as

$$\mu_{t,\psi} = \frac{1}{\|\psi\|^2} \int_{-\infty}^{+\infty} t |\psi(t)|^2 dt \quad (3.5)$$

and

$$\sigma_{t,\psi}^2 = \frac{1}{\|\psi\|^2} \int_{-\infty}^{+\infty} (t - \mu_{t,\psi})^2 |\psi(t)|^2 dt, \quad (3.6)$$

can be seen as proxies of signal central location in time and its “spread” in time with respect to this central location, respectively. Similarly, the mean and the variance of the latter frequency-domain pdf written as

$$\mu_{\omega,\hat{\Psi}} = \frac{1}{2\pi} \frac{1}{\|\hat{\Psi}\|^2} \int_{-\infty}^{+\infty} \omega |\hat{\Psi}(\omega)|^2 d\omega \quad (3.7)$$

and

$$\sigma_{\omega,\hat{\Psi}}^2 = \frac{1}{2\pi} \frac{1}{\|\hat{\Psi}\|^2} \int_{-\infty}^{+\infty} (\omega - \mu_{\omega,\hat{\Psi}})^2 |\hat{\Psi}(\omega)|^2 d\omega \quad (3.8)$$

can be seen as proxies of signal effective/central frequency and its spread (effective bandwidth) with respect to the central frequency, respectively.

The above proxies allow for localising the energy of any oscillatory wave-like function  $\psi(t)$  on the time-frequency plane  $(t,\omega)$  as depicted in Figure 3-1. In this setting, the time interval  $[\mu_{t,\psi} - \sigma_{t,\psi}; \mu_{t,\psi} + \sigma_{t,\psi}]$  with length (duration) of  $\sigma_t = 2\sigma_{t,\psi}$  and the frequency interval  $[\mu_{\omega,\hat{\Psi}} - \sigma_{\omega,\hat{\Psi}}; \mu_{\omega,\hat{\Psi}} + \sigma_{\omega,\hat{\Psi}}]$  with length (bandwidth)  $\sigma_\omega = 2\sigma_{\omega,\hat{\Psi}}$  define the stretch where the most significant part of the energy of functions  $\psi(t)$  and  $\hat{\Psi}(\omega)$  lie, respectively. Therefore, the rectangular box defined as

$$H := [\mu_{t,\psi} - \sigma_{t,\psi}; \mu_{t,\psi} + \sigma_{t,\psi}] \times [\mu_{\omega,\psi} - \sigma_{\omega,\psi}; \mu_{\omega,\psi} + \sigma_{\omega,\psi}] = \sigma_t \times \sigma_\omega \quad (3.9)$$

specifies a representative area of the time-frequency plane where most energy/information of function  $\psi(t)$  is located. This rectangle is called *Heisenberg box*

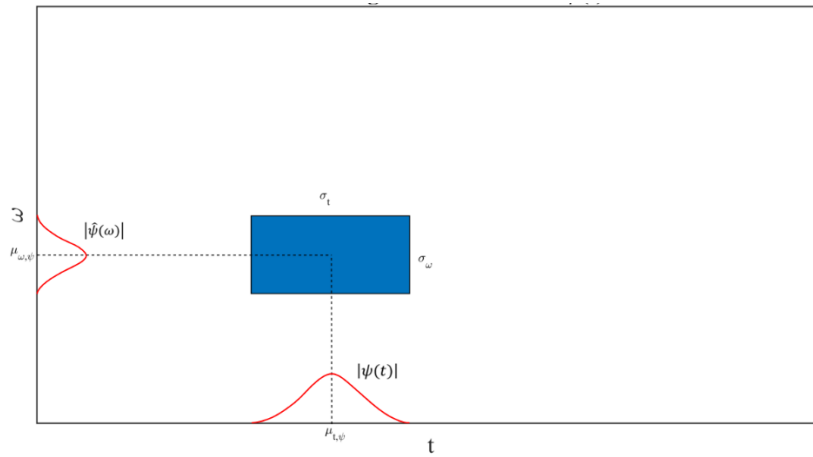


Figure 3-1 Heisenberg box of a function  $\psi(t)$ .

It can be mathematically shown (e.g., Cohen 1995, Mallat 1998) that the following relationship between the sides of Heisenberg box

$$\sigma_t \sigma_\omega \geq \frac{1}{2} \quad (3.10)$$

will always apply due to the property

$$\psi\left(\frac{t}{s}\right) \leftrightarrow |s| \widehat{\psi}(s\omega) \quad (3.11)$$

observed by all Fourier pair functions  $\psi(t) \leftrightarrow \widehat{\psi}(\omega)$ , where  $s > 0$  is a scaling factor. The last two expressions epitomise mathematically the so-called Heisenberg uncertainty principle which states that any time-history (or time-domain waveform) cannot be localised concurrently in the time and in the frequency domain with arbitrary precision: increasing time domain resolution (i.e., decreasing the Heisenberg box side  $\sigma_t$ ) results in reduced frequency domain resolution (i.e., increase of the Heisenberg box side  $\sigma_\omega$ ) and vice versa.

In this context, note that the FT in equation (3.2) uses sinusoidal functions which do not decay in time to decompose the signal  $\psi(t)$ . By virtue of the Heisenberg uncertainty principle, these functions have a sharpest possible resolution in frequency in the sense that their bandwidth is the minimum possible but, consequently, no time resolving (localisation) capabilities. In this respect,

the energy distribution in time is lost upon application of the FT. Thus, as discussed in Section 2.2, it becomes impossible to discern transient local time behaviour due to non-stationary attributes of earthquake accelerograms or due to non-linear behaviour/yielding of structural systems in applying the FT to input acceleration time-histories or to dynamic response signals of seismically excited yielding structures. Nevertheless, the CWT reviewed in Section 2.3.3 uses oscillatory functions that are localised simultaneously in time and in frequency to decompose a given signal allowing for signal energy representation on the time-frequency plane. A most popular wavelet family and, historically, the first to be used in conjunction with CWT, namely the Morlet wavelet, is briefly presented in the following section and used throughout this thesis.

## 3.2 CWT-based signal analysis on the time-period plane using complex Morlet wavelets

### 3.2.1 Complex Morlet wavelets: definition and properties

Given a discrete-time finite energy signal (e.g., a recorded GM or a structural response time-history obtained from NRHA) the CWT in equation (2.6) uses series of wavelet functions to localise the signal energy simultaneously in time and frequency as discussed in Section 2.3.3. These functions are generated by scaling and translating in time a mother wavelet,  $\psi(t)$ , which, at minimum, must satisfy the following so-called admissibility condition (e.g., Mallat 1998)

$$\int_{-\infty}^{\infty} \frac{|\hat{\Psi}(\omega)|^2}{\omega} d\omega < \infty. \quad (3.12)$$

Since the 1980s, a plethora of mother wavelets have been developed with different application-dependent properties (Mallat 1998). As mentioned in previous Chapters, the main aim of this thesis for using the CWT is to capture effectively the time-varying trends of the frequency content in recorded GMs. For this task, the complex Morlet wavelets, widely used in earthquake engineering and structural dynamics applications (e.g., Staszewski 1998a, Spanos and Failla 2005, Noh et al. 2011, 2012), is adopted throughout this thesis since it furnishes advantageous properties for the sought aim as discussed in this section.

The herein adopted unscaled (mother) Morlet wavelet is analytically expressed in time domain as (Torrence and Compo 1997)

$$\psi(t) = \pi^{-\frac{1}{4}} e^{i\omega_0 t} e^{-\frac{t^2}{2}}, \quad (3.13)$$

while the Fourier transform of a scaled version by  $s>0$  of the Morlet wavelet is given as

$$\hat{\Psi}(s\omega) = \pi^{-\frac{1}{4}} H(\omega) e^{-\frac{1}{2}(s\omega - \omega_0)^2} \text{ where } H(\omega) = \begin{cases} 1 & \omega > 0 \\ 0 & \omega \leq 0 \end{cases} \quad (3.14)$$

In the last two equations  $\omega_0$  is a characteristic frequency of the unscaled mother wavelet taken equal to 6 rad/s throughout this work as per Torrence and Compo (1997) which satisfies the admissibility condition in equation (3.12).

Morlet wavelets attain a number of desirable properties which are important for the purposes of this work (e.g. Conrانيا and Soares 2011). First of all, it is a complex (analytic) function since its Fourier transform vanishes at negative frequencies. This makes the CWT in equation (2.6) a complex function which can be written in terms of amplitude and phase enabling a rigorous definition of CWT ridges as detailed the following section. Further, Morlet wavelets facilitate an intuitive and straightforward mapping of scales onto frequencies and, thus, periods. This is because the characteristic frequency  $\omega_0=6$  rad/s of the (unscaled) mother wavelet coincides with its predominant frequency,  $\omega_p^{\hat{\Psi}}$ , defined in equation (2.4), with its central frequency  $\mu_{\omega, \hat{\Psi}}$  in equation (3.7) as well as with its instantaneous frequency,  $IF_{\psi}$  at  $t=0$ , defined as the first time derivative of the wavelet phase (see 3.3.1), that is,

$$\omega_p^{\hat{\Psi}} = \mu_{\omega, \hat{\Psi}} = IF_{\psi}(0) = \omega_0, \quad (3.15)$$

and, at the same time, for  $\omega_0=6$  rad/s the scale  $s$  almost equals the wavelet Fourier-based period  $T_{\psi}$ , that is, (Torrence and Compo 1997)

$$T_{\psi} = \frac{4\pi s}{\omega_0 + \sqrt{2 + \omega_0^2}} \cong s. \quad (3.16)$$

Lastly, Morlet wavelets have a small Heisenberg box area (Mallat 1998) which can be interpreted as striking a good balance between time and frequency resolution at different scales or frequencies as shown in Figure 3-2. Notably, the last figure demonstrates the ability of Morlet wavelets in the

context of the CWT discussed in Section 2.3.2 to achieve improved frequency resolution at lower frequencies and better time resolution at higher frequencies.

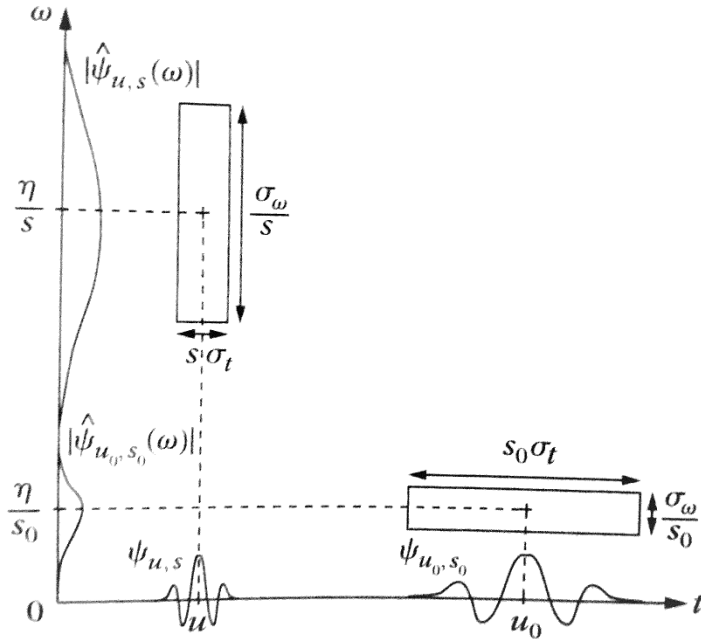


Figure 3-2 Heisenberg boxes for Morlet wavelets at different scales (Mallat 1998)

### 3.2.2 Computation of CWT using complex Morlet wavelets

Having defined the analysis (Morlet) wavelets, the next important step in CWT analysis of discrete-time signals is the numerical implementation of equation (2.6) which involves the selection of wavelet scale discretisation to support useful signal representations on the time-frequency plane via the wavelet spectrogram in equation (2.7). Herein, the Fourier convolution theorem is utilised to compute the CWT from its inverse DFT using the formula (Torrence and Compo 1997)

$$W[\tau, s] = \sqrt{\frac{2\pi s}{\Delta t}} \sum_{k=0}^{N-1} \hat{X}[k] \hat{\Psi}^*(s\omega_k) e^{i\omega_k \tau \Delta t}, \quad (3.17)$$

in which the term in front of the summation is added so that all scaled versions of the Morlet wavelet have the same energy with the unscaled mother wavelet which is equal to one (i.e.,  $\|\hat{\Psi}(\omega)\|^2=1$ ) and the angular frequency is defined as  $\omega_k = \frac{2\pi k}{N\Delta t}$  for  $k \leq \frac{N}{2}$  and  $\omega_k = -\frac{2\pi k}{N\Delta t}$  for  $k > \frac{N}{2}$ . This consideration ensures that the computed wavelet coefficients at different scales are comparable to each other and that the wavelet spectrogram  $|W[\tau, s]|^2$  in equation (2.7) provides

for a valid distribution of the signal energy on the time-frequency or time-period plane. From a computational viewpoint, equation (3.16) can be readily computed using a standard DFT algorithm (such as the "FFT" routine of MATLAB) to efficiently compute  $N$  wavelet coefficients spaced every  $\Delta t$  ( $\tau=0,1,2,\dots,N-1$ ) simultaneously for each chosen value of scale  $s$ .

For the choice of scales, after extensive experimentation with large databanks of recorded GMs (See Appendix A), it was found convenient to define scales as fractional power of 2 (Torrence and Compo 1997)

$$s_j = s_0 \cdot 2^{j\Delta_j}; j = 0,1, \dots, J \text{ and } J = \frac{\log_2(T_0/s_0)}{\Delta_j} \quad (3.18)$$

with  $\Delta_j=0.1$  and  $s_0=2\Delta t$ .

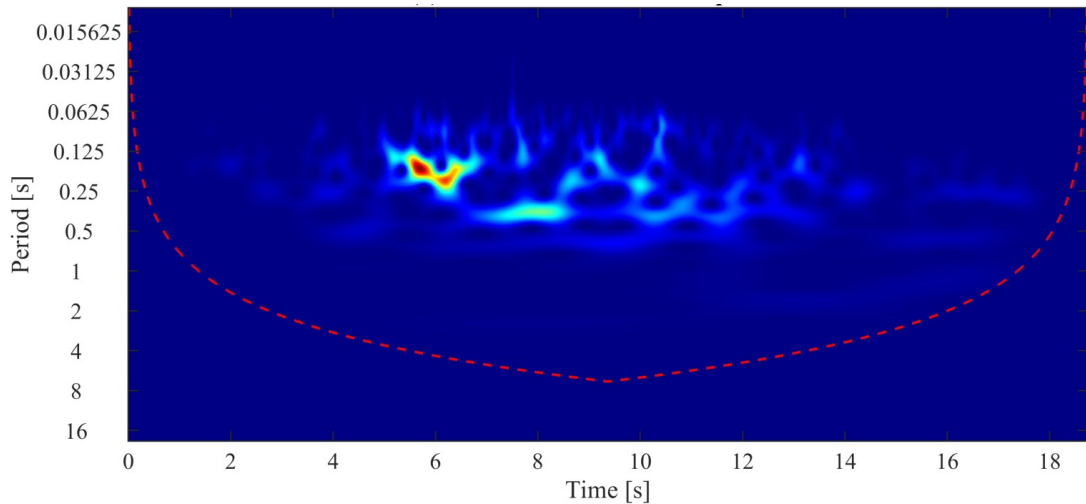


**Figure 3-3** Contour Morlet wavelet spectrogram (power spectrum) of recorded GM #18 in Table A-1 (Appendix A).

Figure 3-3 furnishes an illustrative example of the achieved energy distribution visualisation of recorded GMs on the time-period plane using the above CWT numerical scheme in conjunction with the adopted complex Morlet wavelets. It plots a contour of the Morlet wavelet spectrogram  $|W[\tau, s]|^2$  of the Plaster City (045) GM component (USGS Station 5052) recorded during the Imperial Valley seismic event on 15/10/1979 (record #18 in Table A-1 of Appendix A) in which warmer colours denote higher energy concentration. The herein employed CWT scheme achieves smooth visualisation of the energy distribution which is well-localised in time and in period/frequency.

Still, it is important to note that a significant part of the wavelet spectrogram, often times called *cone of influence* (COI), cannot be used with confidence due to the analysing wavelets located close to the beginning and to the end of a time-limited signal extending outside the time boundaries of the signal. In this regard, the size of COI is scale-dependent and, consequently, frequency and period dependent. This is because the effective duration of the analysing (Morlet) wavelets increases with decreasing scale or with decreasing central frequency as seen in Figure 3-2. To this end, the COI is approximated by a time window representing the effective support or duration of the analysis wavelet to the beginning of the time observation interval (e.g.,  $t=0$ ) and subtracting one same time window the end of the interval (e.g., at the end of the signal duration) with this time-window being different for each scale. Different criteria can be set to define the time-window and, thus, the COI. For the case of Morlet wavelets, the criterion adopted by Torrence and Campo (1997) is used throughout this thesis defined as the time it takes for the energy of a wavelet centred at  $t=0$  to drop by  $e^{-2}$  which can be shown to be

$$t_{COI}(s) = \frac{s}{\sqrt{2}} \quad (3.19)$$

The COI region is delimited in Figure 3-3 and hereafter by a red broken line: the part of the spectrogram below the red broken line is likely to be influenced by edge effects and should not normally be considered. Note, that as period (and thus scale) increases  $t_{COI}$  becomes larger and for some limiting period/scale  $2t_{COI}$  becomes larger than the observation time window which means that all wavelet coefficients at those scales should be discarded from the analysis.

### 3.3 Instantaneous Frequency and Wavelet Ridge analysis for non-stationary mono-harmonic signals

#### 3.3.1 The instantaneous frequency of non-stationary signals

Consider the class of mono-harmonic (or mono-chromatic) signals whose energy is carried by a single harmonic. For stationary mono-harmonic signals the concept of frequency is well-defined and the single time-invariant frequency can be readily retrieved through Fourier analysis (FT) discussed in section 2.2 for discrete-time signals and in section 3.1 for continuous-time signals. However, the study of non-stationary mono-harmonic signals with varying frequency content requires a formal definition of a time-varying frequency: the so-called *instantaneous frequency* (*IF*). To assist the definition of the *IF*, an arbitrary real mono-harmonic continuous-time signal is firstly written as

$$y(t) = A_y(t) \cos \phi_y(t) \quad (3.20)$$

where  $A_y(t)$  is the time-varying amplitude and  $\phi_y(t)$  is the time-varying phase of the signal  $y(t)$  as shown in Figure 3-4. Then, the so-called analytic version of the above signal with vanishing negative frequencies (that is with  $\hat{Y}(\omega)=0$  for  $\omega<0$ ) is always complex-valued and can be written as (Gabor 1946)

$$z(t) = y(t) + iH[y(t)] = A_y(t)e^{i\phi_y(t)}, \quad (3.21)$$

where  $H[y(t)]$  is the Hilbert transform of  $y(t)$  provided that time variation of the amplitude is much slower than time variations of the phase and, therefore, the amplitude changes little during one cycle of oscillation. Signals that meet this slowly varying amplitude condition are termed *asymptotic*. The *IF* is then defined as the time derivative of the phase (Boashash 1992)

$$IF_y(t) = \phi'(t) = \frac{d\phi}{dt} = \frac{d}{dt} [\arg z(t)] \quad (3.22)$$

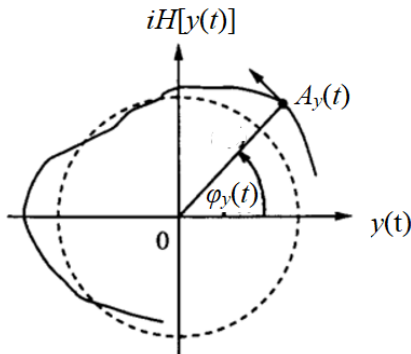


**Figure 3-4** Representation of an analytic mono-harmonic signal on the complex plane using the amplitude  $A_y(t)$  and the phase  $\phi_y(t)$ .

Notionally, the *IF* can be seen as a time-dependent function which provides an effective frequency of the non-stationary signal with time-varying frequency content in a (very) short time-interval.

### 3.3.2 The ridges of the CWT spectrogram

As previously discussed, the CWT of a real signal with complex-valued wavelets such as the complex Morlet wavelet in equation (3.13) is complex. In case the (real) signal  $y(t)$  and the analysing wavelet at scale  $s$  are both asymptotic, then the CWT of  $y(t)$  can be approximated by (Carmona et al. 1997)

$$W[\tau, s] \cong |W[\tau, s]|e^{i\phi_W[\tau, s]} \quad (3.23)$$

where the CWT amplitude is proportional to the product of the signal amplitude with the Fourier transform of the analysis wavelet, that is,

$$|W[\tau, s]| \propto A_y[\tau]\widehat{\Psi}^*(s\phi_W'[\tau, s]) \quad (3.24)$$

and  $\phi_W[\tau, s]$  is the CWT phase given as

$$\phi_W[\tau, s] = \phi_y(n\Delta t) - \phi_\psi\left(\frac{(n - \tau)\Delta t}{s}\right). \quad (3.25)$$

The ridge of the CWT in equation (2.8) along which the wavelet spectrogram or, equivalently, the CWT amplitude attain a local maximum is defined as the set points for which the *IF* of the CWT is equal to zero (e.g., Carmona et al. 1997). Using equations (3.25) and (3.22) the above definition yields the following relationship for a point belonging to a ridge located at  $n_o$  time index where a wavelet analysis function at scale  $s_r$  is centred ( $n_o = \tau$ )

$$\begin{aligned} \phi'_W[\tau = n_o, s] = 0 &\rightarrow \phi'_y(n_o\Delta t) - \frac{1}{s_r}\phi'_\psi\left(\frac{(n_o - n_o)\Delta t}{s_r}\right) = 0 \\ \rightarrow IF_y[\tau = n_o] &= \frac{1}{s_r}\phi'_\psi(0) = \frac{1}{s_r}IF_\psi(0) \end{aligned} \quad (3.26)$$

The above relationship shows that the *IF* time-history of a mono-harmonic signal can be retrieved from the ridge of its CWT. This result has been used in structural dynamics and earthquake engineering (Staszewski 1998, Wang et al. 2013) to trace changes the resonant (natural) structural frequencies of non-linear structures in time through the CWT of response acceleration time-series as mentioned in Section 2.3.4. To this aim, Morlet wavelets proved to be rather advantageous as discussed in Section 3.2.1 since the above relationship simplifies by making use of equation (3.15)

$$IF_y[\tau] = \frac{\omega_o}{s_r[\tau]}. \quad (3.27)$$

Still, use of equation (3.25) requires robust computational methods to extract the ridges of a wavelet spectrogram  $|W(\tau, s)|^2$  which can be viewed as “paths” of local maximum energy signal concentration on the time-period/frequency plane (see e.g., Figure 3-5 depicting the trivial case of ridge extraction of the wavelet spectrogram of a stationary harmonic signal with period  $T=0.01$ s). To this aim, numerous different optimisation formulations and algorithms have been proposed in the literature (e.g., Carmona et al. 1997, Staszewski 1998, Wang et al. 2013 and references therein).

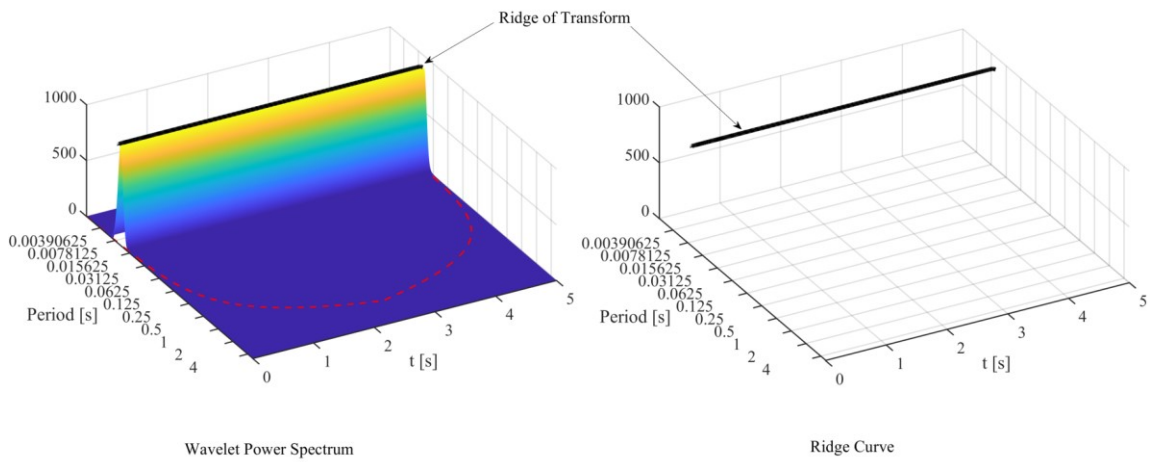


**Figure 3-5** Wavelet spectrogram and ridge extraction for a stationary harmonic signal with  $T=0.01$ s period.

Herein, an optimisation formulation detailed in Carmona et al. (1997) in conjunction with an algorithm proposed by Wang et al. (2013) are adopted for CWT ridges extraction. The formulation relies on a Lagrangian multiplier-style approach to define a penalty (objective) function  $\Lambda$  on the set of ridge candidates written in continuous-time as

$$\Lambda(t, s_r(t)) = - \int |W(t, s_r(t))|^2 dt + \lambda \int s_r'(t)^2 dt, \quad (3.28)$$

which needs to be minimised, where  $s_r(t)$  is a ridge candidate and  $\lambda$  is a penalty factor. Note that for  $\lambda = 0$ ,  $\Lambda$  is minimised by looking for the minimum of  $|W(t, s)|^2$  in the  $s_r(t)$  direction (Carmona et al. 1997). In this setting, the second term in the objective function is introduced to smoothen out the fluctuations of the extracted wavelet ridge in time by forcing the search towards less abruptly changing candidates (i.e., controls the discontinuity of the ridge).

For numerical implementation in discrete-time, equation (3.28) becomes

$$\Lambda[\tau, s_r[\tau]] = \sum_{\tau=1}^{N-1} \left\{ -|W[\tau, s_r[\tau]]|^2 + \lambda |s_r[\tau + 1] - s_r[\tau]| \right\}^2. \quad (3.29)$$

Then, the numerical algorithm in Wang et al. (2013) custom-coded script in MATLAB is used for ridge extraction. Figure 3-6 illustrates diagrammatically the ridge extraction algorithm which finds the minimum of  $\Lambda$  in equation (3.9) thus determining global maxima of  $|W[\tau, s]|^2$  at points  $(t_k, T_k), k=1,2,\dots$  on the time-period plane.

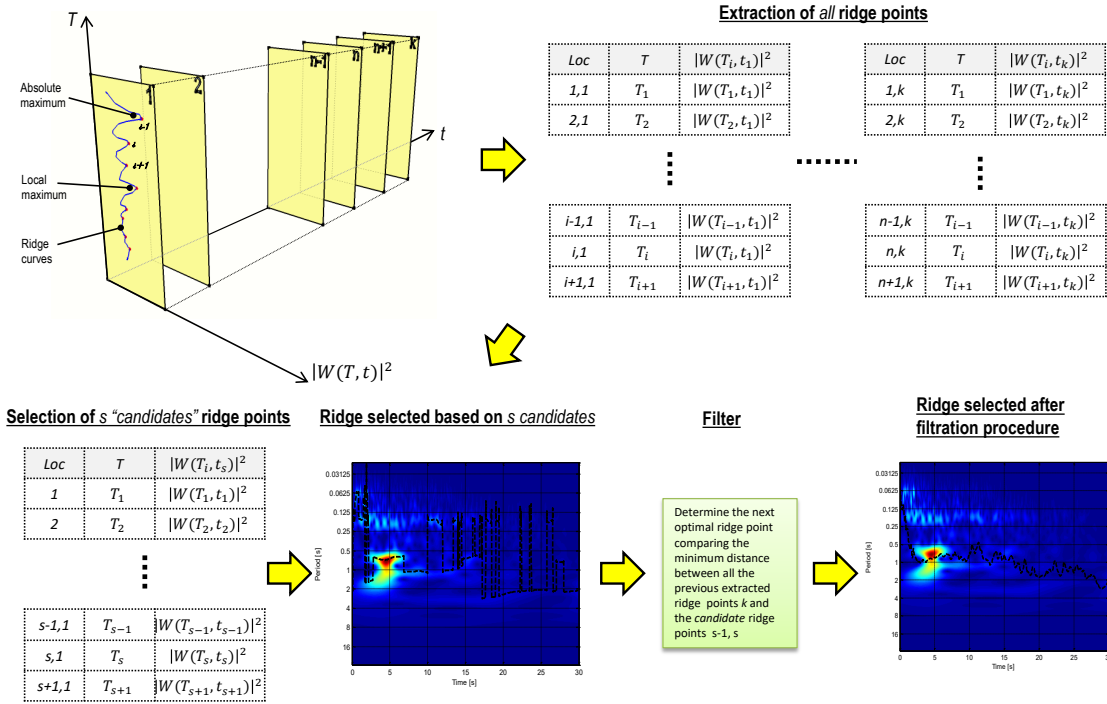


Figure 3-6 Ridge extraction procedure step - MATLAB® script.

### 3.3.3 Illustrative applications of Morlet CWT ridge extraction

In this sub-section, illustrative numerical examples are furnished to exemplify the accuracy of the ridge extraction algorithm and to delineate the concept of instantaneous frequency for mono-harmonic signals and its relevance to the ridges of the Morlet CWT. Figure 3-7 demonstrates the potential of the CWT ridge to accurately trace on the time-period plane the  $IF$  of a 5s long mono-harmonic signal with linearly varying frequency in time (linear chirp) having initial frequency of 2.5Hz or period 0.4s (analytical form:  $f(t) = A \cdot \cos(\omega t^2)$ ). Extracted ridges are marked by thick black line in the contour CWT plot. It is seen that outside the COI delimited by the red broken line the ridge follows accurately the signal  $IF$ .

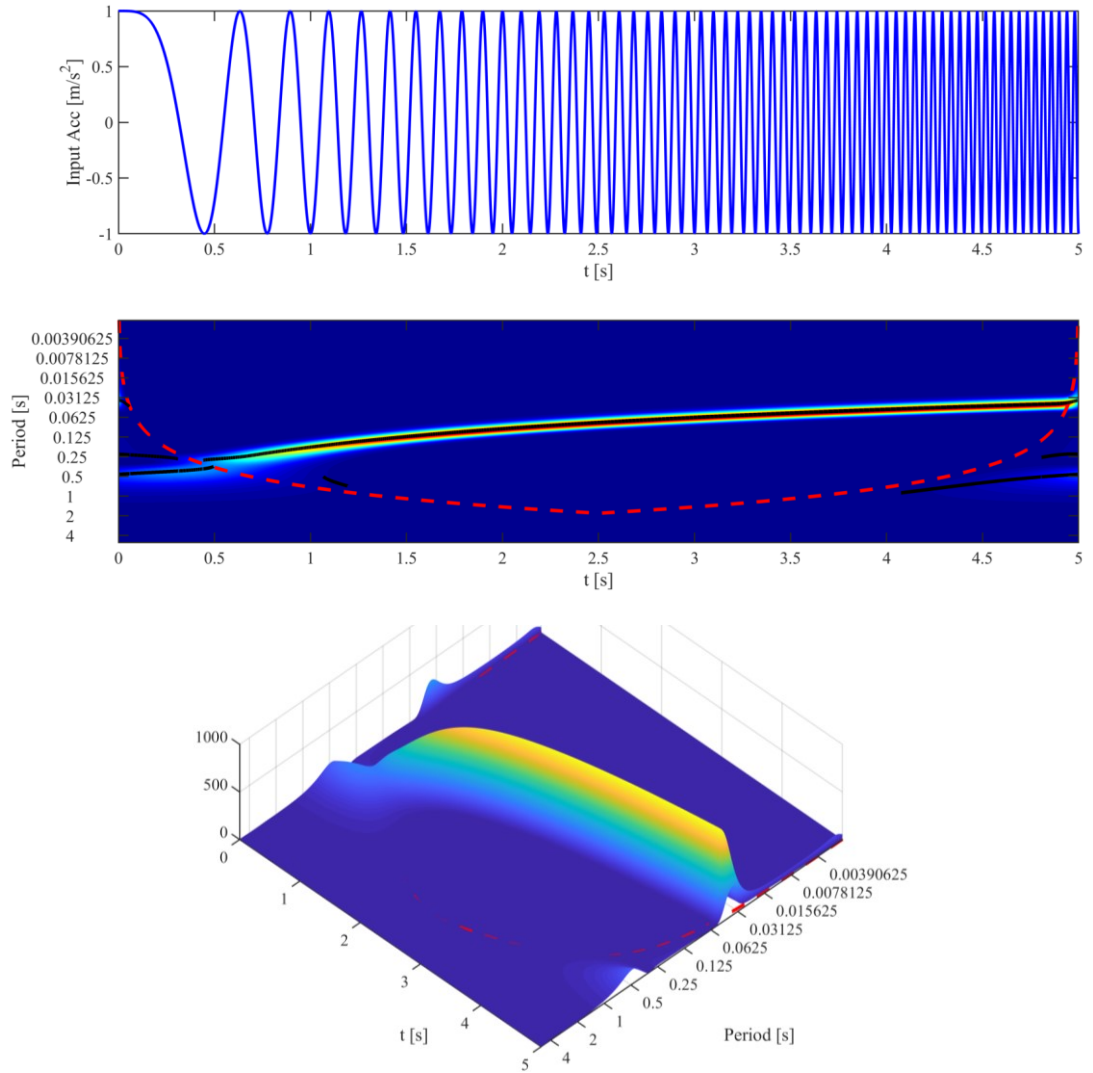


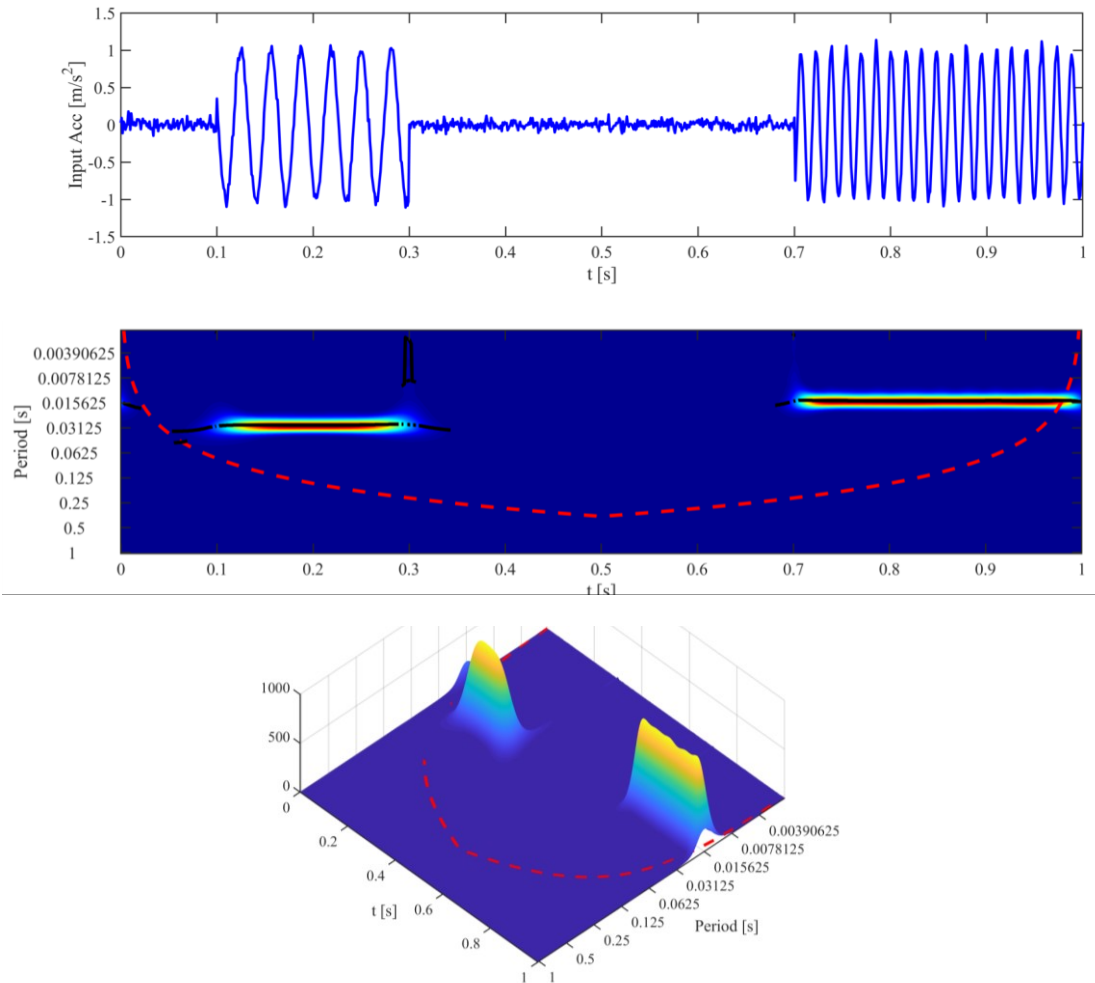
Figure 3-7 Morlet CWT analysis of a mono-harmonic signal with linearly increasing frequency (chirp) of the form  $f(t) = A \cdot \cos(\omega t^2)$ . Top panel: time-history; Middle panel: Contour Morlet CWT with ridges indicated by thick black lines; Bottom panel: Morlet CWT.

Figure 3-8 illustrates the potential of the Morlet CWT ridge to localise time-limited mono-harmonic signals in the presence of additive random noise. The test signal has the analytical form

$$f(t) = \begin{cases} \cos(2\pi\omega_0 t), & 0.1s \leq t < 0.3s \\ \sin(2\pi\omega_1 t), & t > 0.7s \end{cases} + N_1 \cdot e(t). \quad (3.30)$$

with  $t_1=0.1s$ ,  $t_2=0.3s$ ,  $t_3=0.7s$ ,  $\omega_0 = 32 \text{ rad/s}$  (period 0.196s),  $\omega_1 = 64 \text{ rad/s}$  (period 0.392s),  $N_1=0.05$ . In the last equation,  $e(t)$  are uniformly distributed random numbers in the interval  $[0,1]$ .

It is seen that CWT ridge analysis resolves frequencies  $\omega_0$  and  $\omega_1$  on the time-period plane with satisfactory time localisation while it is not affected by the additive random noise.



**Figure 3-8** Morlet CWT analysis of the signal in equation (3.30) with  $t_1=0.1s$ ,  $t_2=0.3s$ ,  $t_3=0.7s$ ,  $\omega_0 = 32 \text{ rad/s}$  (period 0.196s),  $\omega_1 = 64 \text{ rad/s}$  (period 0.392s),  $N_1=0.05$ . Top panel: time-history; Middle panel: Contour Morlet CWT with ridges indicated by thick black lines; Bottom panel: Morlet CWT.

Nevertheless, Figure 3-9 shows that CWT ridge analysis is affected by large level of additive noise. Specifically, a test signal following the analytical form in equation (3.30) with  $t_1=0$ ,  $t_2=1$ ,  $t_3=3s$ ,  $\omega_0 = 100 \text{ rad/s}$  (period 0.063s),  $\omega_1 = 64 \text{ rad/s}$  (period 0.098s), and  $N_I=0.30$  (i.e., noise amplitude equals 30% of signal amplitude) is considered in Figure 3-9(a). Evidently, extracted ridge lines become quite noisy and unreliable to resolve the signal frequencies from the noise as seen in Figure 3-9(b), even though frequencies  $\omega_0$  and  $\omega_1$  are visually seen in the contour Morlet CWT spectrogram. This observation demonstrates the limitations of CWT ridge analysis. This issue can be rectified by denoising first the test signal through standard low-pass filtering to eliminate the high-frequency noise. Figure 3-9(c) shows the contour CWT spectrograms of low-

pass filtered signal in which the ridges now coincide with the visually discernible wavelet energy maximised at frequencies and times corresponding to the two harmonic signal segments (see also the CWT plotted in three-dimensions in Figure 3-9(d)).

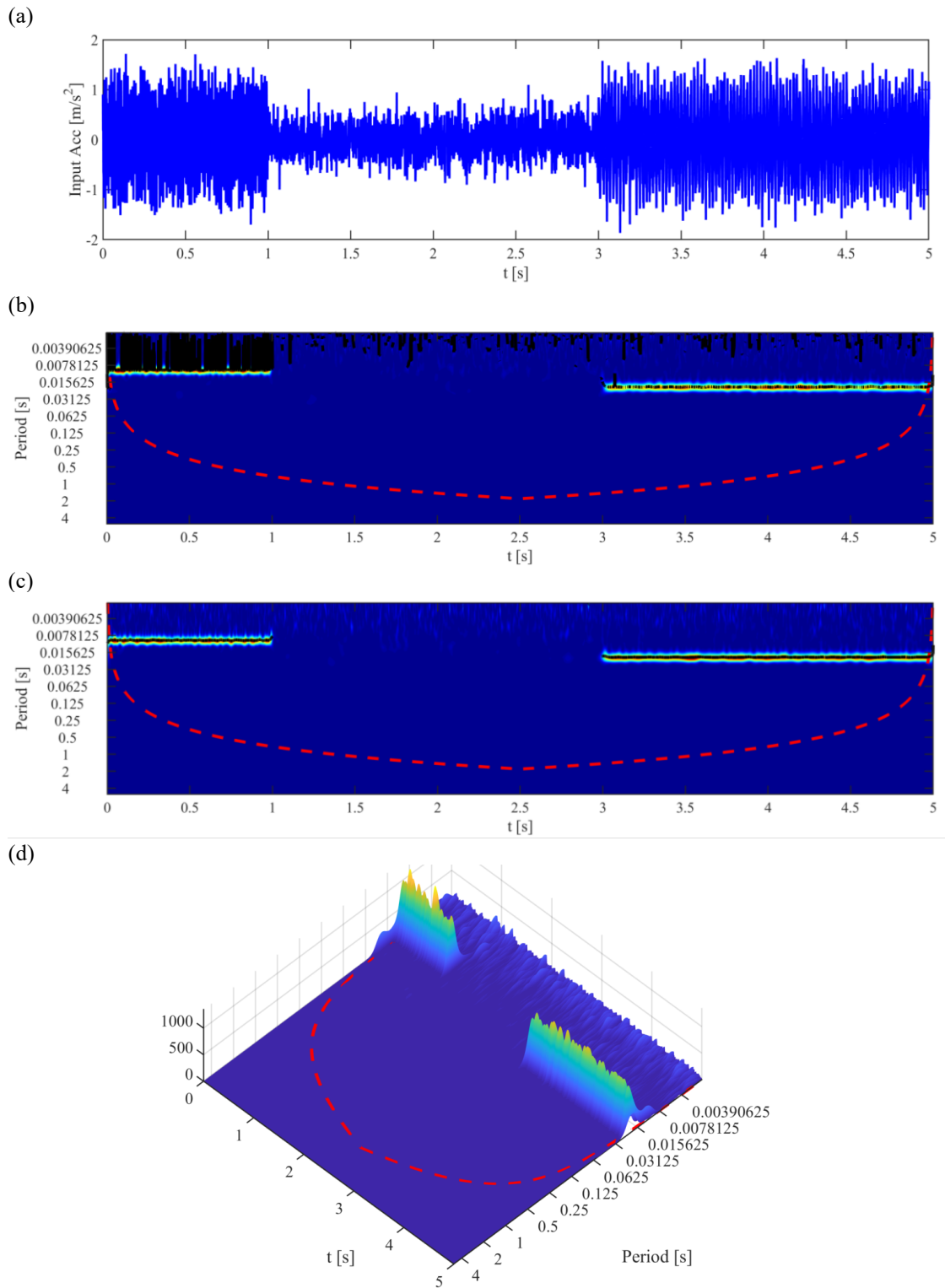


Figure 3-9 Morlet CWT analysis of the signal in equation (3.30) with  $t_1=0.1s$ ,  $t_2=0.3s$ ,  $t_3=0.7s$ ,  $\omega_0 = 32 \text{ rad/s}$  (period 0.196s),  $\omega_1 = 64 \text{ rad/s}$  (period 0.392s),  $N_1=0.05$ . Top panel: time-history; Middle panel: Contour Morlet CWT with ridges indicated by thick black lines; Bottom panel: Morlet CWT.

Overall, the herein reported numerical data support the capability of Morlet CWT spectrogram to visually discern the  $IF$  of mono-harmonic signals from the local wavelet energy concentration on the time-period plane. It was also seen that CWT ridges resolve signal  $IF$  as theory suggests for relatively low noise levels.

### 3.4 Wavelet-based Mean Instantaneous Period (MIP) of recorded GMs

Whilst the ridge analysis of the CWT spectrogram is a formidable approach to extract non-stationary frequency content of mono-harmonic signals, the approach becomes less advantageous for multi-harmonic signals (as seen in Figure 3-10) and, in general, for broadband signals with large numbers of harmonics at each time instant (Carmona et al. 1999). The first reason is because of the increased complexity and computational cost of ridge extraction algorithms for multi-harmonic signals increase significantly and their robustness to additive noise becomes an issue since high-pass filtering may actually eliminate parts of important signal information. The second reason is because knowledge of all (local) ridges becomes less important as those with low energy would most probably be less important/influential. Both the above reasons are particularly relevant for recorded GMs. Detailed ridge analysis of Morlet CWT for a large number of recorded GMs undertaken as part of this reaserch work (see left panel of Figure 3-11 for an example GM) showed that there usually exist tenths of ridges at each time instant while for higher frequencies (shorted periods) ridge curves tend to be too noisy to be meaningful. At the same time, previous published works demonstrated that the *average* frequency content rather than the *dominant* frequency characterises better the earhtquake damage potential of recorded GMs (Rathje et al. 1998, 2004) as it correlates mostly with the fundamental pre-yielding structural natural period (e.g., Kumar et al 2011).

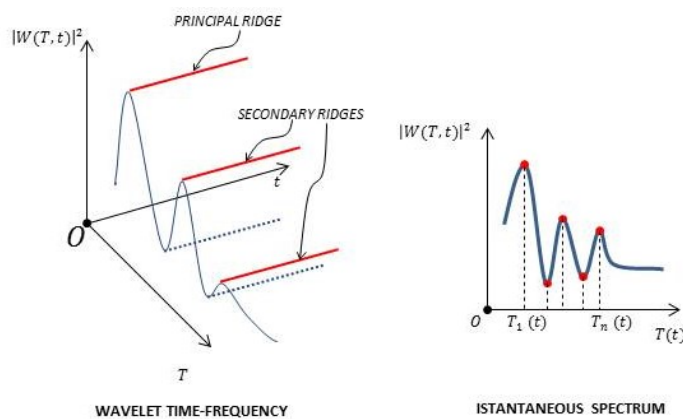
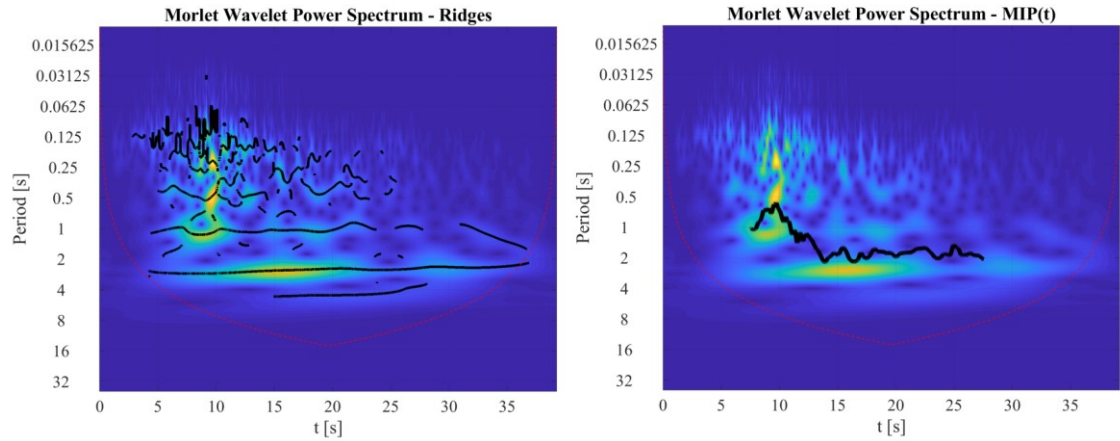


Figure 3-10 Ridge extraction process based on local CWT maxima for multi-harmonic signals.



**Figure 3-11** Wavelet-based significant evolutionary frequency content characterisation of a typical recorded GM on the time-period plane. Left panel: ridge analysis- thick black curves denote local Morlet CWT ridges; Right panel: thick black curve is the mean instantaneous period (MIP) computed from equation (3.31).

In view of the above, the mean instantaneous frequency of the Morlet CWT spectrogram,  $MIF$ , in equation (2.9) or, equivalently, the mean instantaneous period,  $MIP=2\pi/MIF$ , is herein considered as a tool to trace time-varying features of frequency components of recorded GMs in a practically meritorious manner over the CWT ridges. To facilitate a qualitative comparison, Figure 3-11 juxtaposes CWT ridges and the MIP time-history of the CWT spectrogram plotted as thick black curves on top of the Morlet CWT spectrogram for a typical recorded GM. In this junction, it is important to note that for mono-harmonic signals the  $MIF$  in equation (2.9) coincides with the  $IF$  in equation (3.22). However, for multi-harmonic signals the  $MIF$  may not coincide with any of the existing frequency components (see Giaralis 2008 for numerical illustrations) as it provides an average (geometric mean) of all frequency components present at a given time instant in the signal. Still, in case a GM has a single prominent frequency component at some time instant as captured by the CWT spectrogram, the MIP will lie close to this prominent frequency on the time-period plane as it will be “attracted” by it. This is because the  $MIP=2\pi/MIF$  is a weighted average of the frequency components at each time instant with weights being the energy of the wavelet coefficients. To illustrate further this point, Figure 3-12 provides sections of CWT spectrogram along the period axis at two different instants. At instant  $t_i$  the section has two prominent local peaks at periods  $T_o$  and  $T_l$  and therefore the  $MIP[t_i]$  will lie in between the two. At instant  $t_{i+1}$  the section has one dominant local peak at period  $T_o$  and therefore the  $MIP[t_{i+1}]$  will pass close through  $T_o$ . Consequently, the MIP curve in the right panel of Figure 3-11 is attracted by the warm colors of the CWT spectrogram corresponding to higher energy concentration (larger values of magnitude wavelet coefficients).

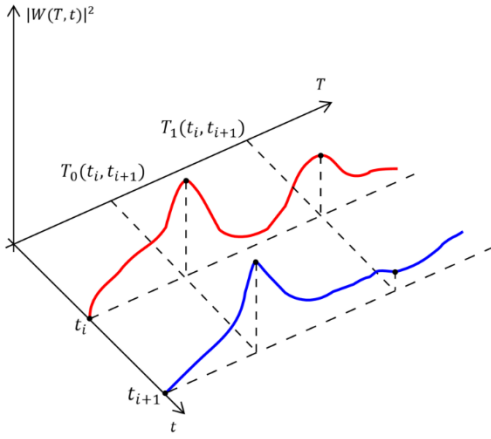


Figure 3-12 Instantaneous CWT spectrogram across period axis.

For the purposes of this work, the MIP of the Morlet CWT spectrogram is mathematically defined in discrete-time as

$$\text{MIP}[\tau] = \text{MIP}(\tau \Delta t) = \frac{\sum_{s=S_1}^{S_2} |W[\tau, s]|^2 T_\psi(s)}{\sum_{s=S_1}^{S_2} |W[\tau, s]|^2} \quad \text{for} \quad \frac{t_{05}}{\Delta t} \leq \tau \leq \frac{t_{95}}{\Delta t}, \quad (3.31)$$

where  $T_\psi$  is the wavelet Fourier-based period of the Morlet analysis wavelet at scale  $s$  given in equation (3.16),  $S_1$  and  $S_2$  are integers specifying scales with “effective” period  $T_\psi$  corresponding to frequencies 0.25Hz and 20Hz, respectively, and  $t_{05}$  and  $t_{95}$  are the time instants at which 5% and 95% of the total signal energy, respectively, has been accumulated in time. Three important practical considerations underpinning the above definition are in order in relation to recorded GMs. Firstly, the computation of the MIP circumvents the computationally involved for the case of recorded GMs CWT ridges. MIP only requires computing the standard CWT which can be efficiently done using equation (3.17) in conjunction with MATLAB “FFT” built-in command using the scale discretisation scheme in equation (3.18). Secondly, the MIP in equation (3.31) is band-limited to the same frequency interval as the Fourier-based mean period  $T_m$  in equation (2.5) specified by Rathje et al (1998) which is mostly relevant for structural earthquake engineering applications. Noting further the analogy between equations (2.5) and (3.31) it can be argued that the herein proposed MIP provides an estimate of the temporal evolution of the mean period  $T_m$  and, to this effect, it can be viewed as a generalization of  $T_m$ . Thirdly, the MIP is time-limited within a GM-dependent time-window in which the central 90% of the total signal energy lies. This time frame corresponds to the “effective duration” defined as (Trifunac and Brady 1975)

$$Ds_{5-95} = t_{95} - t_{05}, \quad (3.32)$$

which is the most widely used criterion to define the significant duration of recorded GMs relevant to their structural damage potential (Kramer 1996). Figure 3-13 plots the MIP of a typical recorded GM superimposed on the Morlet CWT spectrogram and indicating the window of MIP calculation (limits in time and in frequency/period).

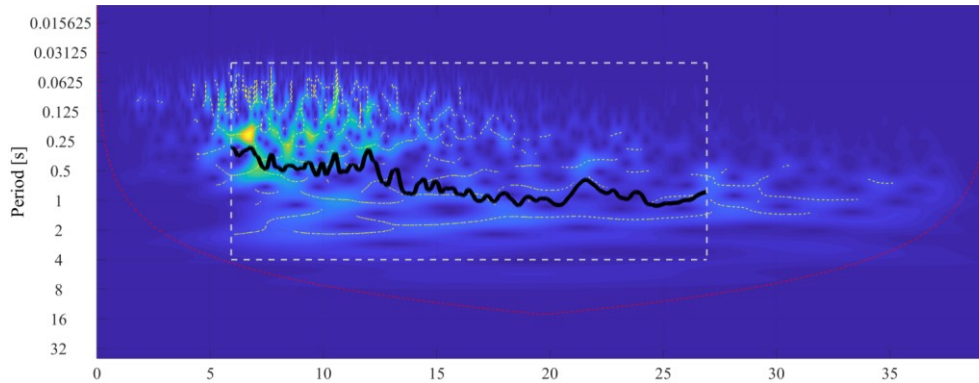


Figure 3-13 Mean instantaneous period (MIP) in equation (3.31) (black thick curve) plotted on top of the contour Morlet CWT spectrogram. The window with broken white line indicates the limits of MIP calculation on the time-period plane.

To further illustrate the potential of the herein proposed Morlet CWT-based MIP to represent the evolutionary trends of the average frequency content of recorded GMs, Figure 3-14 plots MIP time-histories of a small suite of 20 GMs listed in Table A-1 of the Appendix A and used by Vamvatsikos and Cornell (2002) to illustrate the application of IDA for a representative “scenario earthquake”. Significant dispersion is observed of the MIP values at every time instant and non-monotonic fluctuation of individual MIPs. However, the ensemble average MIP has a distinct monotonic trend towards longer periods (lower frequencies) in time which is in alignment with physical considerations discussed in Section 2.3.1 (see also Figure 2-4). This average trend of MIPs is well represented by the mean slope of the ensemble average MIP indicated by a red broken line in Figure 3-14 whose significance will be discussed in the next Chapter.

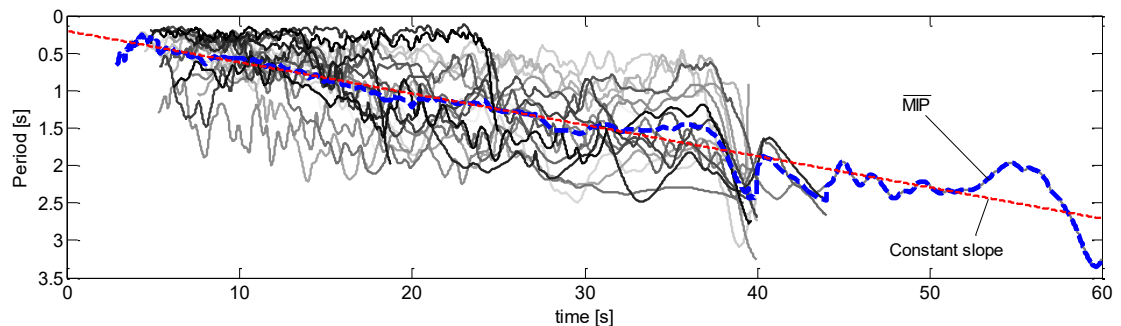
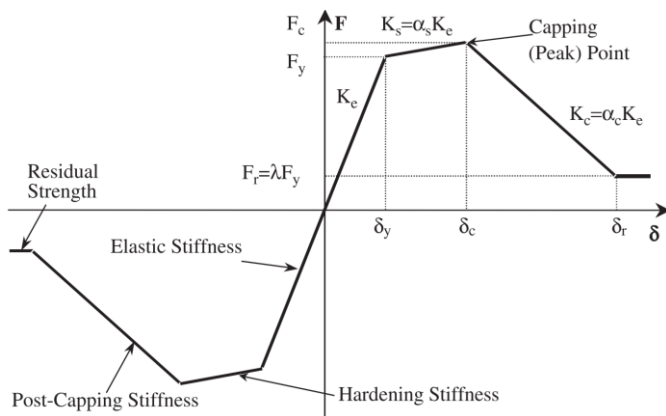


Figure 3-14 Morlet CWT-based MIP of the 20 GMs in Appendix A (Table A-1). The broken blue curve is the ensemble MIP average and the red broken line indicates the average (linear) slope of the blue curve

### 3.5 MIP of seismic inelastic structural response time-histories and illustration of moving resonance

The suite of 20 GMs considered in the previous section (Table A-1 of Appendix A) is used in this section to perform IDA and to compare MIPs of the input GMs and of the output inelastic response time-histories aiming to draw relationships between the two as well as with inelastic phenomena reported in the literature and reviewed in Section 2.3 including transient softening and period elongation. To this aim, a single-degree-of-freedom (SDOF) hysteretic oscillator with strength and stiffness degradation following the inelastic model of Ibarra et al. (2005) as implemented in the OpenSees finite element platform (McKenna and Fenves 2001) is considered. The model incorporates energy-based parameters that controls four cyclic deterioration modes: basic strength, post-capping strength, unloading stiffness, and accelerated reloading stiffness deterioration. The capacity boundary curve of the adopted model is shown in Figure 3-15 defined parametrically by the elastic (initial) stiffness  $K_e$ , the yield strength  $F_y$ , and the strain-hardening stiffness  $K_s = \alpha_s K_e$ . When deterioration is included, the softening branch initiates at the cap deformation ( $\delta_c$ ), which corresponds to the peak strength ( $F_c$ ) on the force axis. In the model there is the possibility to set the residual strength ( $F_r$ ), where the strength does not drop below this value.



**Figure 3-15** Parametric definition of the capacity boundary curve of the Ibarra et al. (2005) hysteretic model.

The values of the Ibarra et al. (2005) model parameters used in the Opensees structural model are reported in Table 3.1 together with their qualitative description. It should be noted that the ductility capacity becomes unimportant if the cyclic deterioration parameter is very small ( $\lambda_{S,C,A,K}=25$ ), i.e. cyclic deterioration effects overpower the effect of monotonic ductility Ibarra et al. (2005). For simplicity it is assumed that all the rates of cyclic deterioration are approximated by the same  $c_S$ ,  $c_K$ ,  $c_A$ , and  $C_c$  value and taken as 1 Ibarra et al. (2005).

Table 3-1 Parameters adopted in Opensees definition of the Ibarra et al. (2005) hysteretic model

Parameter	Value	Description
$f_y$	1	Normalised yield strength for positive and negative loading direction
$f_c$	1.02	Normalised peak strength for positive and negative loading direction
$f_r$	0	Normalised residual strength for positive and negative loading direction
$u_y$	1	Normalised first yield deformation
$u_c$	5	Normalised peak deformation
$u_r$	0	Normalised residual deformation
$k_0$	$\frac{f_y}{u_y}$	Initial stiffness
$k_s$	$\frac{(f_c - f_y)}{(u_c - u_y)}$	strain-hardening stiffness
as_plus, as_neg	$\mp \frac{k_s}{k_0}$	Strain hardening ratio after n modification
FprPos	0.4	Ratio of the force at which reloading begins to force corresponding to the absolute maximum historic deformation demand
A_Pinch	0.6	Ratio of reloading stiffness
$\lambda_s, \lambda_c, \lambda_A$	100	Cyclic deterioration parameter for strength, post-capping and acceleration reloading stiffness deterioration
$\lambda_K$	200	Cyclic deterioration parameter for unloading stiffness deterioration
c_S, c_K, c_A, c_C	1	Rate of strength deterioration, post-capping strength deterioration, acceleration reloading stiffness deterioration and unloading stiffness deterioration. The default value is 1.0

The bilinear backbone curve of the considered oscillator has been calibrated, using the N2 pushover method, against a regular benchmark 12-storey r/c frame with fundamental natural period of 0.715s designed according to the European seismic code of practice (EC8) for the high ductility class (Katsanos, Sextos and Elnashai 2014), (Mwafy and Elnashai 2001). The pre-yield natural period of the SDOF oscillator is equal to  $T_1=0.966s$  and a viscous damping of 5% has been assumed. The overall plan dimensions of the configuration considered is 15 m×20 m. The total height is 36m with storey heights of 3 m. The lateral force resisting system is moment frames

with a solid slab as floor system. Live loads and loading from floor finishes and partitions are both assumed to be 2.0 kN/m<sup>2</sup>. The building is assumed to be founded on medium soil type ‘B’ of EC8 (firm). The cross-section capacities are computed by considering a characteristic cylinder strength of 25 N/mm<sup>2</sup>, yield strength of 500 N/mm<sup>2</sup> for concrete and a characteristic for both longitudinal and transverse steel.

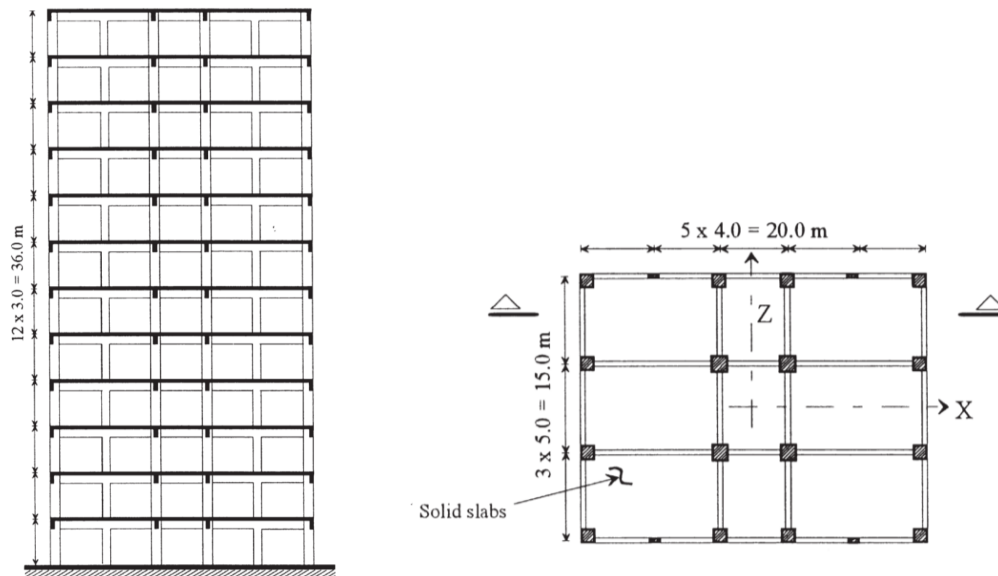


Figure 3-16 Section and Plan view of the test building (Mwafy and Elnashai 2001)

With the assumption that an SDOF equivalent systems would have similar elastic properties of the first period of the MDOF, an effective stiffness was introduced on the basis of the yield point of the bi-linear Standard Pushover (SPO):

$$T^* = 2\pi \sqrt{\frac{m^* \cdot D_y^*}{F_y^*}} \quad (3.33)$$

where  $F_y^*$  and  $D_y^*$  are, respectively, the yield strength point and displacement of the bi-linear standard pushover curve of which parameters are summarised in Table 3-2.

The spectral pseudo-acceleration at the fundamental pre-yield natural period,  $S_a(T1,5\%)$ , has been used as the intensity measure (IM) in conducting IDA, while the immediate occupancy (i.e. in terms of the peak deflection (or drift)  $\theta_{max} = 2\%$ , following the FEMA guidelines, (FEMA P-58-1 2012)) and the near collapse (or collapse prevention) limit states are defined in terms of the peak deflection of the oscillator (i.e.  $\theta_{max} = 8\%$  or when the IM-curve has a tangent slope equal to 20% of the elastic slope) following the recommendations of (Vamvatsikos and Cornell, 2002). In this study, the N2 method (P. Fajfar 2000) have been considered to substitute the above

five multi-storey structures by SDOF oscillators exhibiting a bilinear (envelope) pushover curve as shown in Table 3-2.

**Table 3-2** SDOF Properties (Mwafy and Elnashai 2001) – Normalised to the Yield values

SDOF	Deformation		Base Shear		Stiffness [kN/m]	
	Yield	Collapse	Yield	Collapse	Elastic	Post-Yield
12RFDCH	1	5	1	1.02	18260	76

Stability (bounded solution) and accuracy are the most important issues of time integration schemes. For this reasons a Newmark Average Acceleration where  $\alpha = 0.5$  and  $\beta = 0.25$  with a time step of  $\Delta t = 0.01$  s to avoid numerical instability. This model uses Rayleigh damping which formulates the damping matrix as a linear combination of the mass matrix and stiffness matrix:

$$[c] = a_0 \cdot [m] + a_1 \cdot [k] \tag{3.34}$$

where  $a_0$  is the mass proportional damping coefficient,  $a_1$  is the stiffness proportional damping coefficient and  $[m]$  and  $[k]$  are, respectively, the matrix of mass and stiffness.

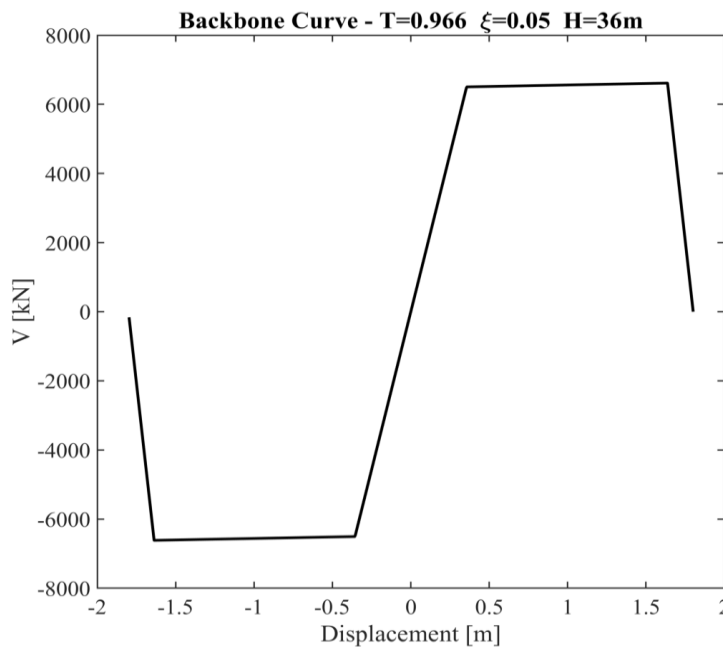


**Figure 3-17** Capacity Boundary curve as implemented in Opensees

In this junction, the same Morlet CWT-based MIP in equation (3.31) is used to treat acceleration structural response time-series, one for each limit state considered. Note that mathematically this

is a variation of the MIF introduced by Spanos et al. (2007a) obtained here in terms of period ( $MIP=2\pi/MIF$ ) using a significantly different analysis wavelets (Hamornic wavelets as opposed to Morlet) suited for damage detection purposes (see also Gkoktsi and Giaralis 2015) rather than for smooth time-varying frequency content tracing considered in this research. Here Morlet wavelet-based, named MIRP(t), time-histories are derived from zero-mean acceleration response (output) signals obtained from IDAs. It is important to note that this Mean Response Period is not the fundamental period of the structure as obtained from a forced response where the input frequency energy is present in the wavelet transform. At this stage, though, the MIPR(t) will give useful insight information capable to shed light into concepts and effects otherwise hidden, and for these reasons it has been used as comparative measure.

It is observed (Figure 3-18 and 3-19) for all individual GM records considered that the MIRP of the output signal tend to *converge* to the MIP of the GM in a *point-wise manner* within the strong ground motion duration as the IM increases, or equivalently as the structure approaches the near collapse limit state (see Figure 3-18 and 3-19 for illustrative examples). This is the “moving resonance” phenomenon firstly described by Beck and Papadimitriou (1993) in the context of stochastic dynamics. This is usually true (i.e., the MIRP of the output at near collapse state to trace closely the MIP of the input GM) after the first derivative (slope) of the input MIP attains locally in time a relatively large value or after the input MIP is close to  $T_1$  (Fundamental Period of the structure). Two representative examples are shown in Figures 3-18 and 3-19 for the No. 13 (Imperial Valley, 1979, Chihuahua (282) Station) and the No. 12 (Superstition Hills (1987), Wildlife Liquefaction Array (090) Station) GMs. For the former GM considered, the output MIRP(t) curve at near collapse state begins to trace closely the input MIP(t) curve after about  $t = 10$  s when a relatively steep slope in the input MIP(t) lasting for about 4s is observed. Here it is to note that a period of “strong” energy frequency content, imposed by the input (Figure 3-18), is suffered by the structure whose frequency follows the input frequency. At the end of this 4s period, it presents a local large deterioration “cycle” with a large step in the dissipated energy (about 25%) clear from the yielding energy ratio plots  $\lambda = E_y/E_{y_{max}}$  (Figure 3-18) (see Appendix B for a definition of this ratio). A change in the frequency content is clearly present in the so-called  $\nu(t) = MIRP_{LS}(t)/MIRP_{el}(t)$  ratio (the ratio between the MIRP(t) at different Limit States and the Elastic MIRP(t)) which shows a local increase right after the “damage” occurred with a “temporary shift” in period (Figure 3-18).

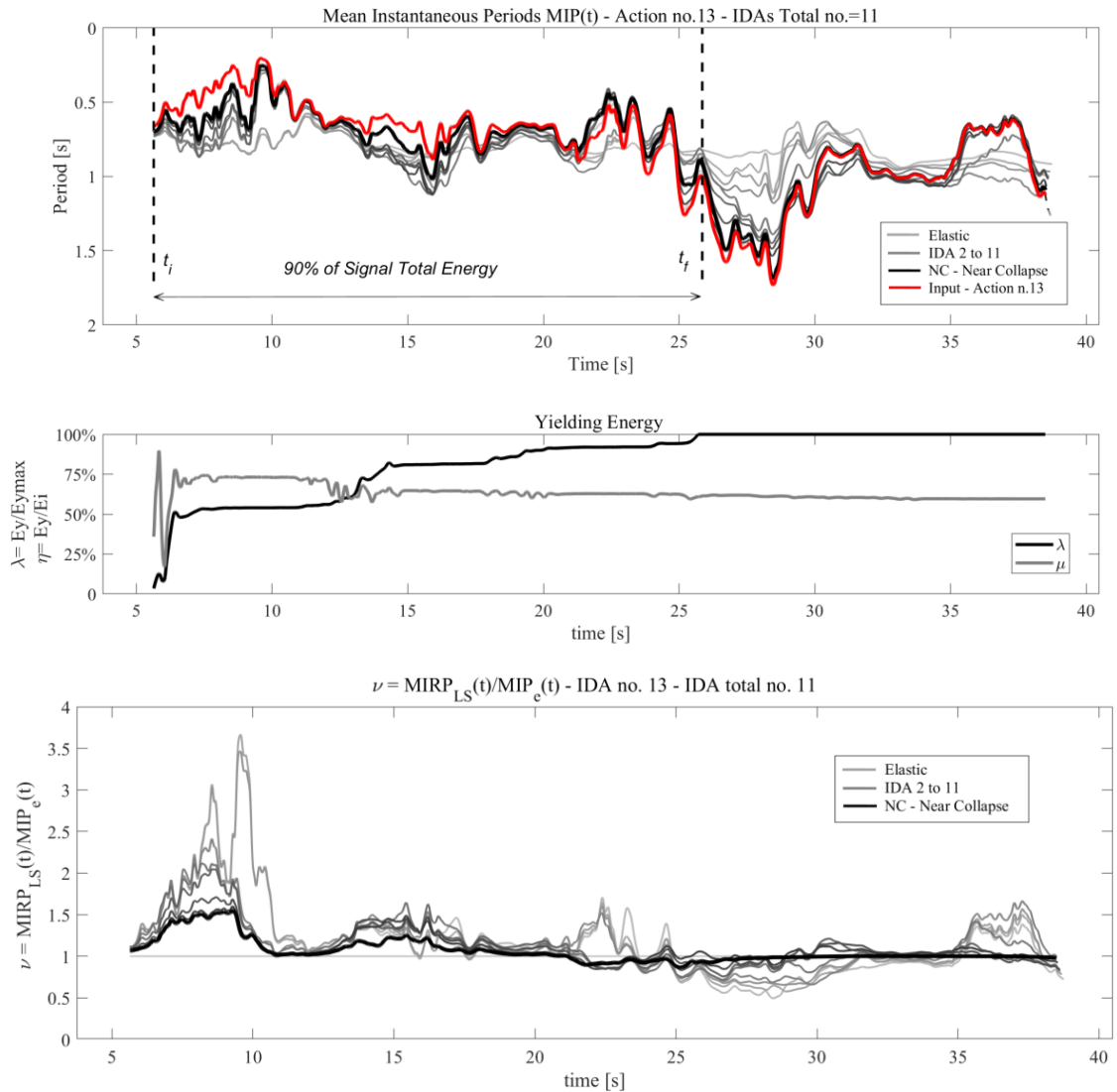


**Figure 3-18.** MIPs of input and output signals considered in the IDA analysis for the Ground Motion No. 13 GM (Imperial Valley, 1979, Chihuahua (282) Station). The number of scaled curves in this case is 11.

This important effect it is also visible a few seconds after (around 18s - Figure 3-18) when another “input energy push” is given by the GM, visible from the point-wise period convergence, followed again, with the presence of a large deteriorated cycle and a consequential “shift” in period. The final *point-wise “accordance”* in frequency happened after again a long local steep increasing in GM period with larger consequences suffered by the structure which reaches its dissipated maximum energy level and collapses. Here the MIPR(t) shows only the input energy associated with the GM’s MIP(t) as the energy frequency content of the structure isn’t enough to react to the GM influence.

For the latter considered GM (action n.8), the output MIRP(t) at near collapse state begins to trace closely the input MIP after about  $t = 9$  s when the input MIP tends to sharply increase in period for about 10s. The final frequency accordance between the input and the output happened after

80% circa of the energy is dissipated. Similar trends are observed for the input/output MIPs of the rest of the GMs considered not shown here for brevity.

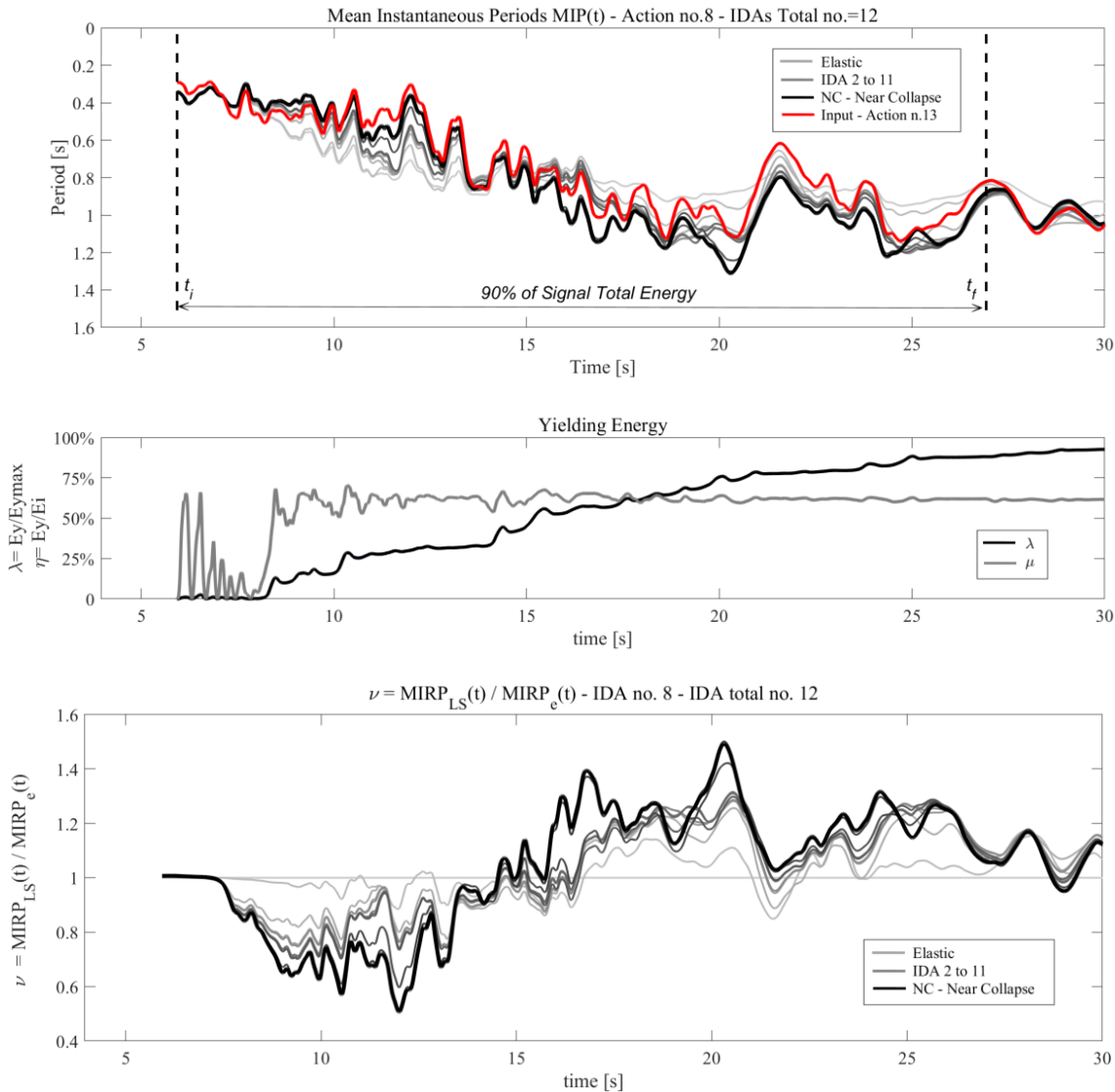


Figure 3-19. MIPs of input and output signals considered in the IDA analysis for the No. 8 GM.

Lastly, Figure 3-20 summarises and plots all the output MIPs for the “immediate occupancy” (or after first yielding) limit state and for the near collapse limit state, respectively. The most important observations pertain to the level of variability of the MIPs which is higher for the near collapse state and to the mean slope of the ensemble average MIP (shown in broken lines) which is steeper for the near collapse state. The latter observation relates mostly to the phenomenological “period elongation” phenomenon as indicated in Figure 3-20 which superposes the slopes of the mean ensemble average MIPs of GM’s input, with the MIRP(t) of the output- after first yielding, and the MIRP(t) of the output- near collapse limit state (Figure 3-20). As a final remark, Figure 3-20 (right panel) shows clearly that the slope of the output at near collapse limit state lies much closer to the input slope compared to the slope of the output after first yielding. This observation

suggests that the average slope of the MIP may be a useful record selection criterion/scalar in performing IDA.

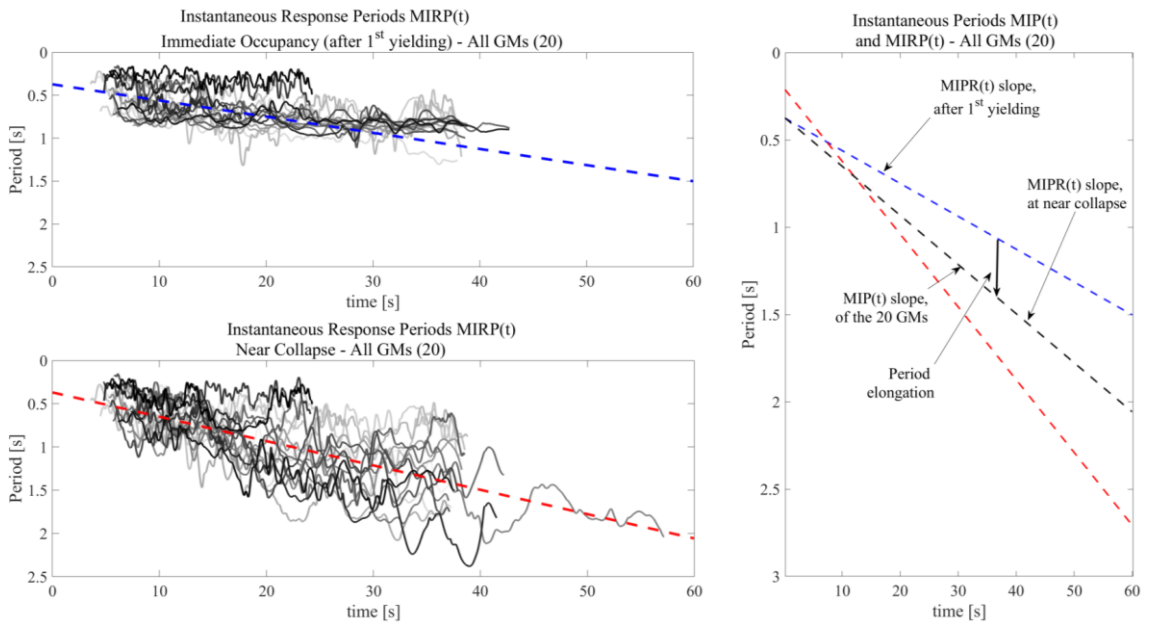


Figure 3-20. Morlet wavelet based MIRPs of response acceleration signals at immediate occupancy (after first yielding – blue line) and at near collapse limit states (red line), respectively, and average slope of the ensemble average MIPs. On the right input/output average slopes of the ensemble average MIPs

### 3.6 Concluding Remarks

A time-dependent wavelet-based mean instantaneous period (MIP) has been put forth as a numerical tool to characterize the time-varying frequency content of typical far-field recorded earthquake ground motions (GMs) and to probe into the hysteretic response of seismically excited yielding structures. The MIP captures well the temporal change of the average frequency content of GMs towards lower frequencies by considering the MIPs of 20 scenario earthquake GMs derived using two different wavelet families. It is further argued that the MIP can be viewed as a generalization of the Fourier-based mean period  $T_m$ . This argument is based on the observation that temporal averaged MIPs lie reasonably close to  $T_m$  for judiciously defined wavelet bases. Moreover, MIRPs of acceleration response signals are examined derived from incremental dynamic analysis applied to a hysteretic oscillator representing a benchmark 12-storey r/c frame for the above suite of GMs. It is observed that the response signal MIRPs tend to converge to the GM MIP in a point-wise manner as stronger inelastic behaviour is exhibited (moving resonance phenomenon). Further, it is shown that the slope of the ensemble average MIRP for the near-collapse limit state lies close to the ensemble average GM MIP, while it may also be treated as indicator of the so-called “period elongation” phenomenon for degrading inelastic structures. Overall, the herein reported numerical data suggest that the time-varying frequency content is an

important influence factor for hysteretic systems especially at the near collapse limit state and that the slope of the MIP might be used as a record selection criterion accounting for the influence of the time-varying frequency content of GMs to structural response within the performance-based earthquake engineering framework. The insights gained on the relationship between input GM MIP and hysteretic response MIP as well as the potential of the MIP to trace the average non-stationary frequency content of GMs motivates the definition of a scalar quantity related to the wavelet-based GM MIP detailed in the next Chapter in order to quantify the influence of the non-stationary excitation frequency content to the hysteretic structural response.

As a closure to this chapter, it is important to highlight the main difference of the proposed MIP with respect to the  $MIF=2\pi/MIP$  in Spanos et al. (2007). The usage and purpose of the MIP is different and, therefore, novel: In Spanos et al. (2007) MIF was used for earthquake induced damage detection. Here, MIP is ultimately used to trace the time-varying frequency content of GMs and, eventually, to define (chapter 4) a novel scalar metric quantifying the evolving frequency content of GMs.



## Chapter 4

“Alpha” ( $\alpha$ ): A Novel Wavelet-based  
Scalar Capturing the Average Non-  
Stationary Frequency Content of Recorded  
GMs

## 4 Preliminary remarks

The MIP of recorded GMs in equation (3.31) was found useful to visualize qualitatively the evolutionary trend of the mean frequency content of GMs as seen in Section 3.4. However, being a time-history on the time-period plane, it bears limited practical merit to serve as an index quantifying the evolving frequency content of GMs. For this task, defining a scalar quantity is desirable in alignment with all various GM properties currently used in PBEE either as IMs (e.g., PGA, PGV,  $Sa(T_1)$ ) or as record selection criteria (e.g.,  $M$ ,  $R$ ,  $\varepsilon$ ) to characterise recorded GMs (see Section 2.1 for detailed review and references). For this purpose, it is herein proposed to consider the mean slope of the MIP, henceforth termed “alpha”,  $\alpha$ , as a scalar that captures the evolutionary trend in time of the mean frequency content of recorded GMs. This consideration is motivated by the numerical evidence provided in Section 3.5 demonstrating that the slope of the ensemble mean MIP of inelastic response time-histories (output of NRHA) increases *and* gets closer to the slope of the ensemble mean MIP of the recorded GMs (input of NRHA) as the level of nonlinear behaviour (limit state) increase through amplitude GM scaling in the context of IDA. Though limited, this evidence showcases that, on the average, the mean slope of the output MIP correlates to period elongation of yielding structural systems which, in turn, was shown to be a potent EDP in the context of PBEE (Trevlopoulos and Guéguen 2016). At the same time, the input MIP mean slope correlates with the output MIP mean slope which, ultimately, implies that the MIP mean slope of GMs is a GM property that will relate to structural damage potential in a statistical context.

In this Chapter, the  $\alpha$  property of GMs is first defined mathematically and then statistical relationships of  $\alpha$  with seismological parameters ( $M, R$ ), local soil conditions (shear wave velocity  $V_{S30}$ ) as well as PGA and PGV (i.e., arguably the most commonly adopted non-structural IMs in IDA) are derived and discussed to gain physical insights on the significance of  $\alpha$ . This is achieved by means of standard linear regression analyses pertaining to a databank of 611 far-field GMs. Lastly, standard statistical sufficiency testing of PGA and PGV against  $\alpha$  is undertaken involving IDA for the inelastic SDOF system previously used in Section 3.5 subjected to the above large suite of GMs to verify that non-stationary GM frequency content, as captured by  $\alpha$ , does influence peak seismic inelastic ductility demands. This influence is quantified in subsequent Chapters.

### 4.1 Mathematical Definition of the $\alpha$ Property of Recorded GMs

The proposed scalar quantity  $\alpha$  of a given GM is the slope of the linear function fitted using standard least squares minimisation criterion to the CWT-based MIP determined by equation (3.31) as graphically shown in Figure 4-1.

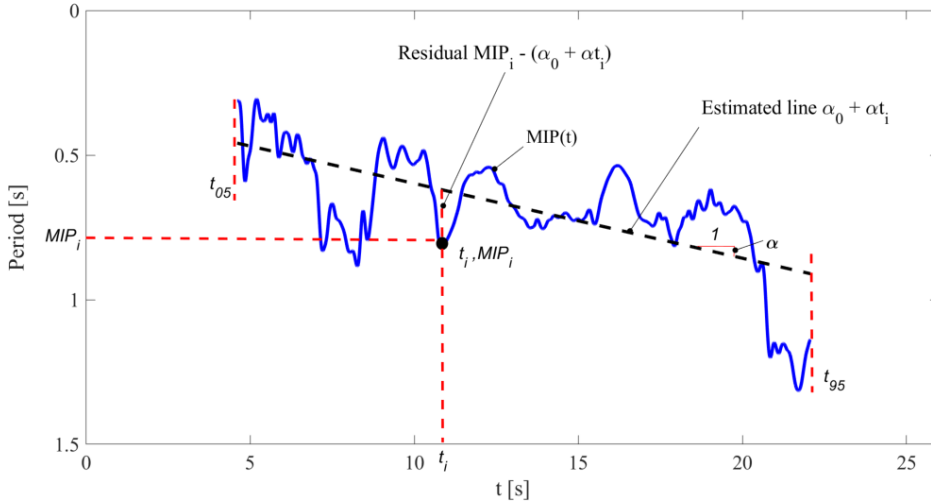


Figure 4-1 Definition of the mean slope  $\alpha$  of the Morlet CWT-based MIP

Specifically, assume that the MIP is given at discrete time instants with time step  $\Delta t$ , which, without loss of generality, can be taken equal to the time-step of the recorded GM. Introducing the notation  $MIP[\tau]=MIP_\tau$  and  $t_\tau=\tau\Delta t$ , the parameters  $\alpha_0$  and  $\alpha$  of the linear function are determined by minimising the objective function

$$\sum_{i=\tau_1}^{\tau_2} [MIP_i - (\alpha_0 + \alpha t_i)]^2, \tag{4.1}$$

where  $\tau_1 = \frac{t_{05}}{\Delta t}$  and  $\tau_2 = \frac{t_{95}}{\Delta t}$  following the definition of the MIP in equation 3.31.

This is achieved by satisfying simultaneously the following two conditions (e.g., Benjamin and Cornell (1970))

$$\frac{\partial}{\partial \alpha_0} \sum_{i=\tau_1}^{\tau_2} [MIP_i - (\alpha_0 + \alpha t_i)]^2 = \sum_{i=\tau_1}^{\tau_2} 2[MIP_i - (\alpha_0 + \alpha t_i)] \cdot (-1) = 0 \tag{4.2}$$

$$\frac{\partial}{\partial \alpha} \sum_{i=n_1}^{n_2} [MIP_i - (\alpha_0 + \alpha t_i)]^2 = \sum_{i=\tau_1}^{\tau_2} 2[MIP_i - (\alpha_0 + \alpha t_i)] \cdot (-t_i) = 0 \quad (4.3)$$

Further algebraic manipulation leads to the following system of linear equations in  $\alpha_0, \alpha$

$$\overline{MIP} - \alpha_0 - \alpha \bar{t} = 0 \quad (4.4)$$

$$\sum_{i=\tau_1}^{\tau_2} MIP_i \cdot t_i - (\tau_2 - \tau_1) \alpha_0 \bar{t} - \alpha \sum_{i=n_1}^{n_2} t_i^2 = 0 \quad (4.5)$$

where  $\overline{MIP}$ ,  $\bar{t}$ , are sample mean values (see also Appendix C). The solution of the above system of equations yields

$$\alpha_0 = \overline{MIP} - \alpha \bar{t} \quad (4.6)$$

$$\alpha = \frac{\sum_{i=\tau_1}^{\tau_2} MIP_i \cdot t_i - \overline{MIP} \cdot \bar{t}}{\sum_{i=\tau_1}^{\tau_2} t_i^2 - (\tau_2 - \tau_1) \cdot (\bar{t})^2} \quad (4.7)$$

Therefore, equation (4.7) provides for a mathematically rigorous definition of the  $\alpha$  GM property as well as a useful formula for its numerical evaluation given a discrete-time MIP time series and together with the vector of discrete time instants at which the MIP has been computed.

For the purposes of this work, the angle  $\alpha$  is measured in degrees and is assigned a positive value when the mean MIP increases with time (i.e., when the average GM frequency content evolves from shorter periods/higher frequencies to longer periods/lower frequencies as shown in the illustrative example in Figure 4-2), while is assigned a negative value when the mean MIP reduces in time (i.e., when the average GM frequency content evolves from longer periods/lower frequencies to shorter periods periods/higher frequencies as shown in the illustrative example in Figure 4-3). Further, it is important to note that the length of the observation time window (duration) spanning the fitted linear function assumed in the derivation of  $\alpha$  affects the value of  $\alpha$  in as much as it affects MIP trends. From a PBEE viewpoint, it is of interest to monitor MIP during the relatively strong part of the recorded GM. Thus, an observation time window equal to the effective duration  $D_{s5-95}$  in equation (3.32) is adopted throughout this study as indicated in equation (4.1). This definition of GM duration corresponds to the time window in which 90% of the central GM energy is released and is the most widely used metric to measure the duration of GMs of interest in earthquake engineering (Kramer 1996). As a final remark on the definition of  $\alpha$ , it is important to note that the  $\alpha$  index is invariable to GM amplitude scaling heavily considered

in deriving IM-EDP relationships within the PBEE context as discussed in Section 2.1. This is because the CWT is a linear transformation and any amplitude GM scaling factor cancels out by definition of the MIP in Eq.(3.31).

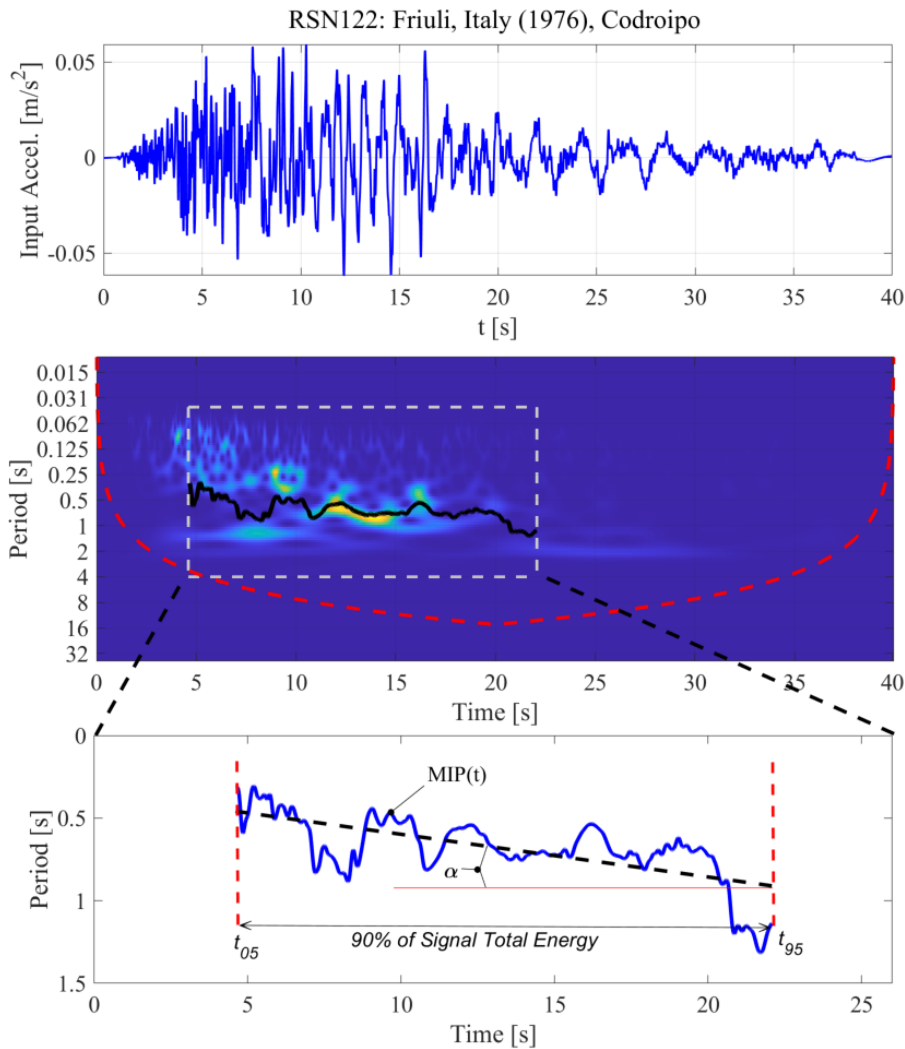


**Figure 4-2** Recorded GM component RSN122: Friuli, Italy (1976)- see GM set 2 description in Appendix A. Upper panel: acceleration time-history; middle panel: contour plot of Morlet CWT spectrogram with MIP; lower panel: GM property  $\alpha$  (slope of mean MIP)

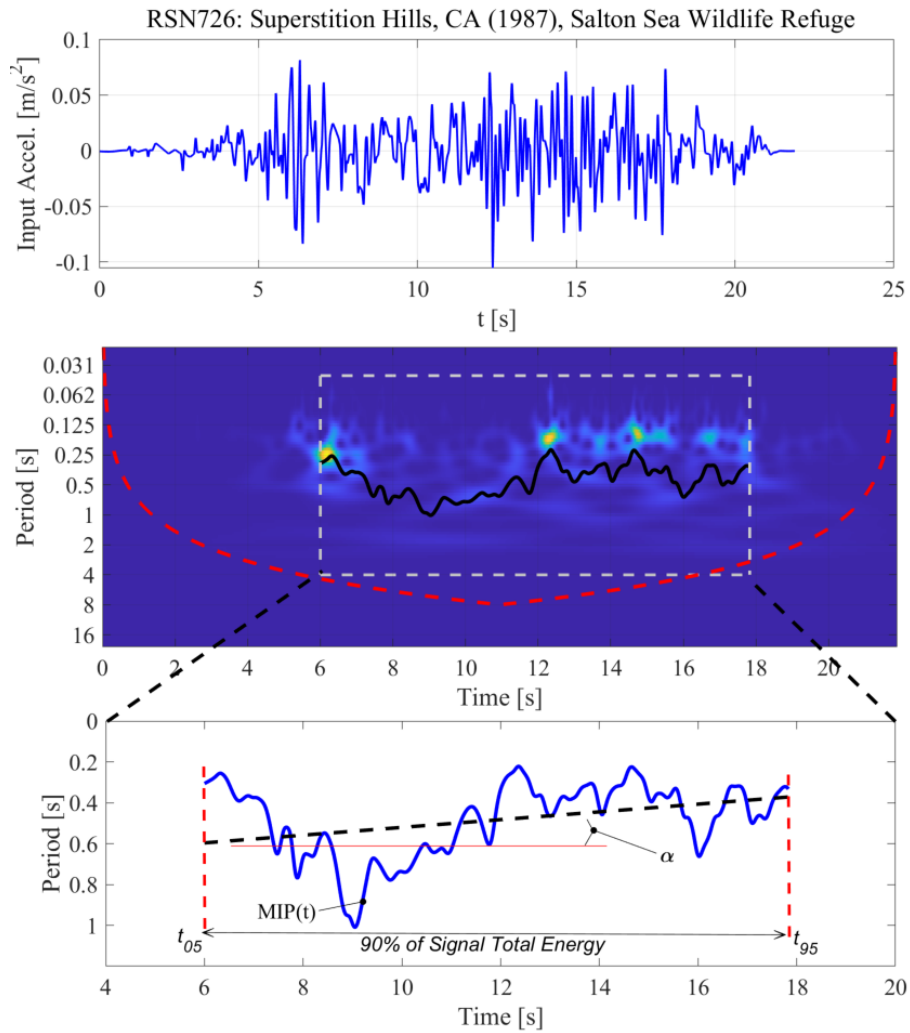


Figure 4-3 Recorded GM component RSN726: Superstition Hill, CA (1987) see GM set 2 description in Appendix A. Upper panel: acceleration time-history; middle panel: contour plot of Morlet CWT spectrogram with MIP; lower panel: GM property  $\alpha$  (slope of mean MIP)

## 4.2 Statistical relationships of $\alpha$ with seismological parameters, local soil conditions, and GM properties

To gain an intuition on non-stationary average frequency content trends of typical far-field recorded GMs, the angle  $\alpha$  defined in the previous section has been computed using equation (4.7) for 611 recorded GMs from 30 different seismic events with magnitude range  $6.5 < M < 8$  and distance to rupture plane range  $20\text{km} < R_{\text{rup}} < 120\text{km}$  with no “pulse-like” content as classified by Baker (2007). The considered GMs, listed in Table A-2 in Appendix A, have been downloaded from the PEER NGA-West2 Ground Motion Database and post-processed as detailed in Appendix A. They achieve a good spread on the  $M$ - $R_{\text{rup}}$  plane as shown in Figure A-1 which supports well the purpose of investigating statistically the  $\alpha$  values for a wide/inclusive range of

seismological parameters. In computing the  $\alpha$  for each GM, the Morlet CWT is first obtained using equation (3.17) and, next, the MIP of the Morlet CWT spectrogram is determined using equation (3.31). Finally, the  $\alpha$  is calculated for each record from equation (4.7).

Overall, visual record-by-record qualitative inspection of Morlet CWT spectrograms and MIPs of all the 611 GMs herein considered (not presented for obvious practical reasons) suggests that the obtained  $\alpha$  values of reflect well the actual average-in-time evolutionary trend of the mean frequency content as captured by the Morlet CWT. Following seismological considerations, it is expected that typical horizontal far-field GMs with no near-fault signatures would normally have a positive  $\alpha$  since the seismic waves that arrive first at a recording station are dominated by higher frequencies while lower frequencies kick in at later times (see e.g., Kramer 1996, Rezaeian 2008, Jian et al. 2014). Indeed, this is true for more than 90% of the 611 far-field GM components examined (see Figure 4-2 for a typical example). Nevertheless, there are also far-field GMs with  $\alpha < 0$ , as the recorded acceleration considered in Figure 4-3. Careful examination of the CWT spectrograms and the associated MIPs reveal that GMs with negative  $\alpha$  values are typically characterized by the late appearance of significant bursts of energy carried at slightly higher frequencies compared to the mean frequency content at the beginning of the GM.

Further to the above qualitative investigation of the  $\alpha$  values obtained, standard linear regression analysis is undertaken to establish statistical relationships between  $\alpha$  and three different GM properties, namely PGA, PGV, and  $T_m$ , widely used in PBEE as discussed in section 2.1. For each GM, the values of PGA and PGV reported in the PEER NGA-West2 database are used, while  $T_m$  is computed using equation (2.5). Further, a similar regression analysis is also undertaken between  $\alpha$  and the shear wave velocity  $V_{s30}$  value (a representative measure of the local soil site conditions) as defined and reported in the same database. The aim of these analyses is to quantify the regression slope coefficients between  $\alpha$  and PGA, PGV,  $T_m$ , and  $V_{s30}$  which, upon qualitative interpretation, can serve as evidence that  $\alpha$  is a valid index to capture the non-stationary frequency trends of GMs, based on phenomenological arguments, rather than a signal analysis artefact.

**Table 4-1** Regression analysis results between  $\alpha$  and four different GM properties

<b>Y</b>	<b>R<sup>2</sup></b>	<b>Standard error (SE)</b>	<b>Coefficient</b>	<b>Coefficient Value</b>	<b>95% confidence interval</b>		<b>p-value</b>
<b>PGA</b>	0.0038	0.646	$C_0$ (intercept)	1.16	1.019	1.318	$4.22 \cdot 10^{-18}$
			$C_I$ (slope)	0.97	-0.29	2.246	0.1304

<b>PGV</b>	0.103	0.004	$C_0$ (intercept)	0.72	0.565	0.872	$5.75 \cdot 10^{-18}$
			$C_1$ (slope)	0.036	0.0275	0.044	$3.5 \cdot 10^{-16}$
<b><math>T_m</math></b>	0.06	0.14	$C_0$ (intercept)	0.56	0.328	0.798	$3.2 \cdot 10^{-6}$
			$C_1$ (slope)	0.90	0.618	1.182	$6.52 \cdot 10^{-10}$
<b>Vs<sub>30</sub></b>	0.03	0.0002	$C_0$ (intercept)	1.70	1.482	1.925	$4.88 \cdot 10^{-18}$
			$C_1$ (slope)	-0.001	-0.0017	-0.0006	$1.95 \cdot 10^{-5}$

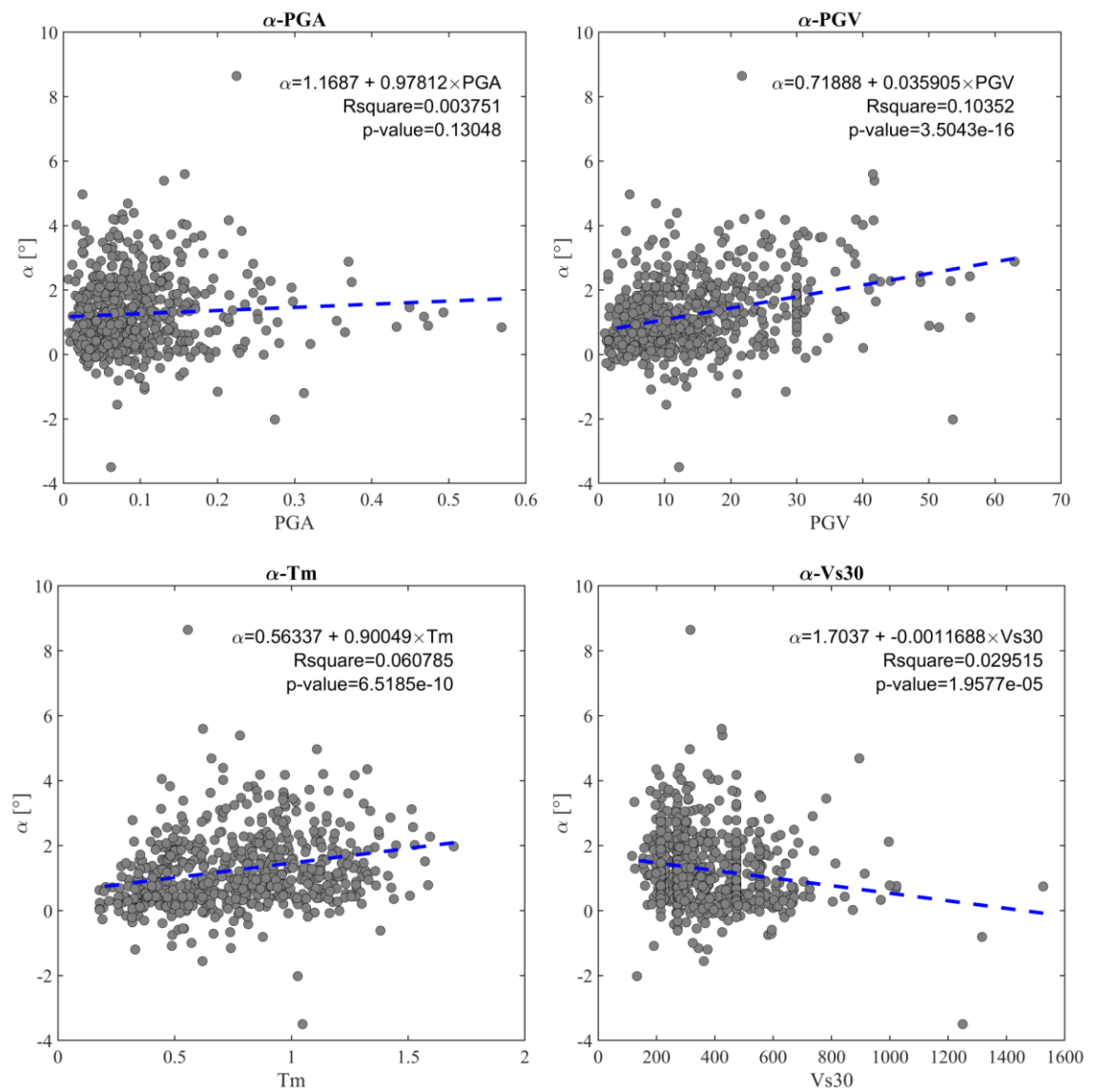


Figure 4-4 Linear regression analyses results of  $\alpha$  against PGA, PGV,  $T_m$  and Vs<sub>30</sub> as indicated in the title of each panel for the GM data set of Table A-2 (Appendix A).

Figure 4-4 plots clouds of the 611 data points along with the mean linear estimators of  $\alpha$  against the four considered properties obtained from linear regression analysis of the form (see also Appendix C for further technical details)

$$\hat{a} = C_0 + C_1 \cdot Y \quad (4.8)$$

where  $Y$  is the property under consideration (i.e., either PGA, PGV,  $T_m$ , or  $V_{s,30}$ ). Further, Table 4-1 collects the coefficient of determination  $R^2$ , the standard error of regression as well as the values and confidence intervals of the determined regression coefficients  $C_0$  and  $C_1$  (see Appendix C for mathematical definitions and significance of these quantities). The same Table reports p-values testing the likelihood of the hypotheses that  $C_0=0$  or  $C_1=0$  for all regression analyses undertaken. The p-value indicate the *minimum significance level of the test* for which the Hypothesis  $\mathcal{H}_0$  is falsified (rejected). In mathematical terms:

$$\mathcal{H}_0 : \text{the slope } C_0 = 0 ; \mathcal{H}_0 : \text{the intercept } C_1 = 0 \quad (4.9)$$

$$T(x): \text{Significance levels} = P[\text{reject } \mathcal{H}_0 \mid \mathcal{H}_0 \text{ correct}]$$

$$p_{value} = \inf \{ \gamma_I : T(x) \in D_C \} \quad (4.10)$$

where  $T(x)$  is the test statistic  $D_C$  is falsified region (critical region). Therefore, if there is a solid evidence against the hypothesis  $\mathcal{H}_0$  then  $p_{value}$  is small (appendix D).

It is deduced from Figure 4-4 that, on the average,  $\alpha$  is not significantly affected by the PGA as the mean fitted linear function to the  $(\alpha, \text{PGA})$  pairs of values is almost flat. Indeed, the fact that the p-value of the slope  $C_1$  coefficient of the regression analysis is relatively high in this case, confirms that the either way small value of the slope is not statistically significant with high probability (i.e., the null hypothesis of  $C_1=0$  is most likely valid). However, the average value of  $a$  increases appreciably as PGV increases in Figure 4-4 and slope coefficient  $C_1$  of the regression analysis is statistically significant as the p-value is very small (i.e.,  $C_1$  is not zero with high probability). These trends can be intuitively justified based on the following two simultaneously applicable considerations. The first is that GMs with larger PGV values tend to be richer in low frequencies because the velocity trace of GMs is derived by integration of the acceleration trace which is a low-pass filtering operation suppressing the higher frequency components and accentuating the lower frequencies (Worden 1990). The second is that lower frequency components in a typical GM usually appear at later times compared to the high frequencies due

to the early arrival of the p-waves (see e.g., Figures 2-5 and 4-2 for a typical examples). Therefore, it is natural to expect that the higher the PGV value in a typical GMs is, the more significantly the mean frequency content shifts in time from the higher to the lower frequencies. And if this shift is to be accommodated within roughly the same effective duration (note that in Table 4-1 most GMs considered are associated with a relatively narrow magnitude range,  $7 < M < 7.5$ , and hence with roughly the same effective duration as the latter correlates well with the magnitude (Kramer 1996), then the angle  $\alpha$  (i.e., rate of change of the mean frequency content from higher to lower frequencies for  $\alpha > 0$ ) attains higher values.

The validity of the above reasoning is further reinforced by examining the average  $\alpha$ - $T_m$  trend in Figure 4-4. Specifically, it is seen that  $\alpha$  increases with increasing mean frequency (averaged over all times). Hence, it is confirmed that the rate of change in time of the mean frequency content is, on the average, higher for GMs with rich mean low frequency content. The latter observation has also been reported by Rezaeian and Der Kiureghian (2010) in which the rate of change of the average frequency content was used as one of the parameters defining a non-stationary GM stochastic model but was extracted from a databank of recorded GMs based on the average zero-crossing rate of GMs: a very different time-domain approach from the wavelet-based one herein adopted. Turning the attention to the  $\alpha$ - $V_{s30}$  trend in figure 4-5 it is observed that  $\alpha$  decreases as local soil conditions becomes “stiffer” (Kramer 1996), that is, as the value of  $V_{s30}$  increases.

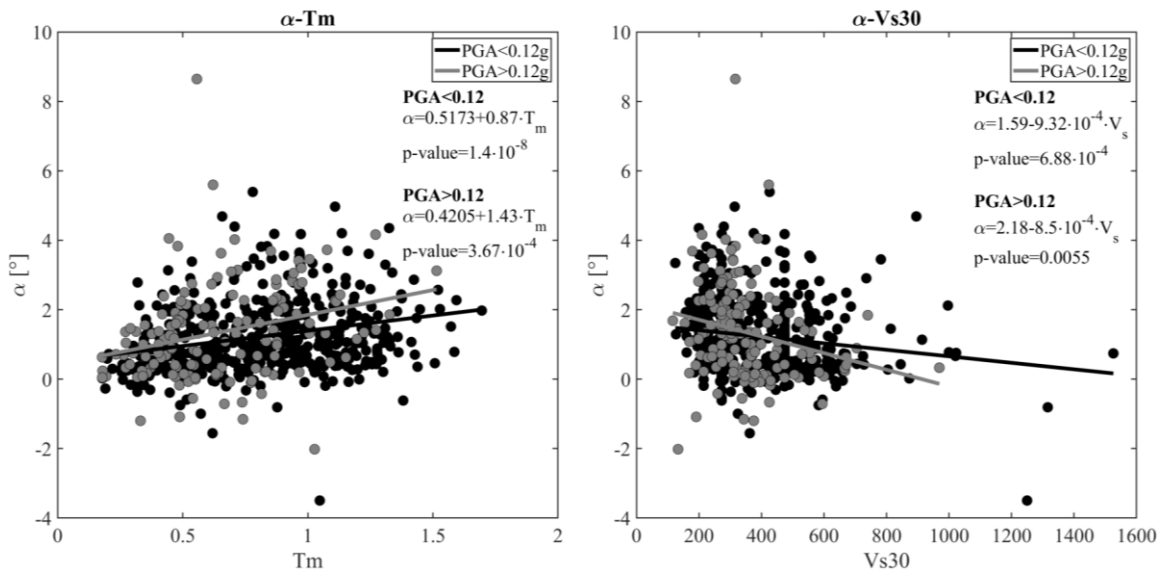


Figure 4-5 Linear regression analyses results of  $\alpha$  against  $T_m$  and  $V_{s30}$  as indicated in the title of each panel for the GM data set of Table A-2 (Appendix A) classified in 2 different PGA bins.

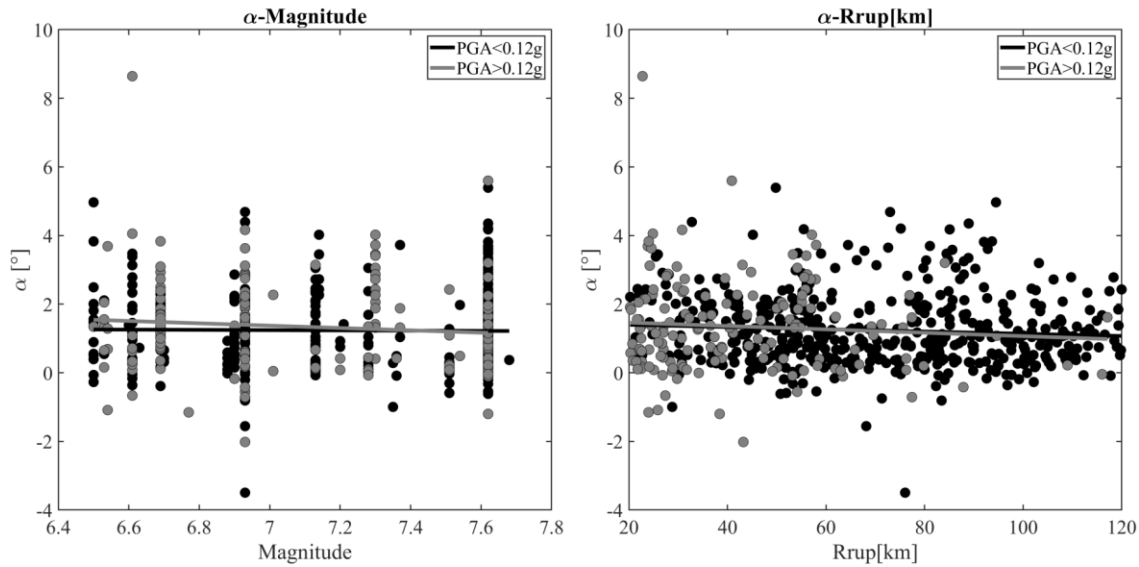


Figure 4-6 Linear regression analyses results of  $\alpha$  against magnitude  $M$  and fault distance  $Rup$  as indicated in the title of each panel for the GM data set of Table A-2 (Appendix A) classified in 2 different PGA bins.

This trend can be readily justified by taking as a fact that  $\alpha$  is higher for GMs with richer low frequency content and by considering that soft soils shifts the frequency content of the GMs towards lower frequencies (Kramer 1996). Alternatively, by reversing the above line of arguments, Figure 4-4 can be used as further evidence that the temporal rate of change of the mean frequency content is higher for GMs that are richer in low frequencies. Overall, the statistical data furnished in Table 4-1 and Figure 4-5 suggest that despite the large scattering/variability of the  $\alpha$  with all 4 considered scalars as evidenced by the small  $R^2$  values of the regression analyses, it is seen that  $\alpha$  is mostly related to the mean frequency content: GMs with lower frequency content tend to have larger  $\alpha$  values. To gain an insight on the potential dependency of the angle  $\alpha$  on the amplitude of the GM acceleration trace as captured by the PGA, further linear regression analyses are undertaken between  $\alpha - T_m$  and  $\alpha - V_{S30}$  upon dividing the GM dataset of Table A-2 (Appendix A2) into 2 different bins according to their PGA: (i)  $PGA \leq 0.12g$ ; low-to-medium intensity GMs, (ii)  $PGA > 0.12g$ ; medium-to-high intensity GMs. The mean regression lines between  $\alpha - T_m$  and  $\alpha - V_{S30}$  are plotted in Figure 4-5, respectively, for all bins on top of data points clouds mapped according to the considered PGA-based classification. It is observed that as PGA increases, the average value of  $\alpha$  becomes more sensitive to the values of both the  $T_m$  and  $V_{S30}$ . Indeed, the rate by which the mean estimated value of  $\alpha$  increases as the low frequency content of GMs becomes richer depends significantly on the PGA: the slope of the lighter coloured regression line corresponding to high intensity GMs is significantly steeper from the dark-coloured regression line. Note that the small p-values reported on the figures for the  $C_1$  regression slopes provide confidence about the statistical significance of

the reported data. This result indicates that although PGA is not well-correlated with  $\alpha$  directly (at least not as much as the PGV in Figure 4-4), it does influence the expected value of  $\alpha$  significantly for GMs rich in low frequency content. This trend can be attributed to the fact that typical GMs with relatively high PGA *and* PGV values are characterized by an early significant high frequency content, which drives the MIP towards high frequencies (short periods) at the beginning of the GM, *and* by rich low frequency content kicking in later in time, which shifts the MIP towards long periods at a fast rate (i.e., with a large  $\alpha$  value). The above observation is also verified by visual inspection of the Morlet CWT spectrograms and MIPs of GMs with  $\text{PGA} > 0.12\text{g}$ . Furthermore, Figure 4-5 suggests that the expected (average) value of  $\alpha$  is more sensitive to the soil conditions for high intensity GMs. Indeed, for the  $\text{PGA} \leq 0.12\text{g}$  bin, the average regression line of  $a$  with respect to the soil stiffness is flat: the expected value of  $\alpha$  is not sensitive to soil conditions. However, the average  $\alpha$  value increase as softer soils *and* higher PGA values are considered. This trend can be readily attributed to the fact that soft soils exhibit stronger non-linear behaviour under intense (high amplitude) seismic shaking compared to stiff soils (Kramer 1996), which reflects on the frequency content of GMs becoming richer in low frequencies. Lastly, the regression lines in Figure 4-6 suggest that the magnitude and the distance to rupture  $R_{\text{rup}}$  (at least within the considered ranges of  $6.5 < M < 8$  and  $20\text{km} < R_{\text{rup}} < 120\text{km}$ , respectively) do not influence  $a$  in a direct manner.

### 4.3 Non-sufficiency of PGA and PGV against $\alpha$ for Peak Inelastic Response Prediction

Having established statistical relationships/trends between  $\alpha$  and a number of well-established GM properties including PGA and PGV used as IMs in PBEE, attention is herein focused on providing statistical evidence on *the existence* of potential influence of  $\alpha$  to peak inelastic seismic demands of yielding structures, before embarking on quantifying this influence for different structures. To this aim, sufficiency testing of the two most widely used non-structure specific IMs in PBEE, namely PGA and PGV, to predict the most commonly adopted EDP, namely peak inter-storey drift ratio,  $\theta_{MAX}$ , against  $\alpha$  is herein pursued (see also Section 2.1.2). The adopted statistical test is interpreted as follows: if the adopted IM (i.e., PGA or PGV) is shown to be non-sufficient in predicting  $\theta_{MAX}$  against  $\alpha$ , then this means that  $\alpha$  “carries information” about  $\theta_{max}$  not included in PGA and PGV (see also discussion in Section 2.1.2). Indirectly, this further means that  $\alpha$  influences  $\theta_{MAX}$  in a statistical context. This can be better appreciated by noting that one way to rectify non-sufficiency of a specific scalar IM (say PGA or PGV) in establishing IM-EDP relationship against some other parameter (say  $\alpha$ ), is to include this parameter ( $\alpha$ ) in the specification of the IM resulting in a vector IM (see e.g., Baker and Cornell 2005).

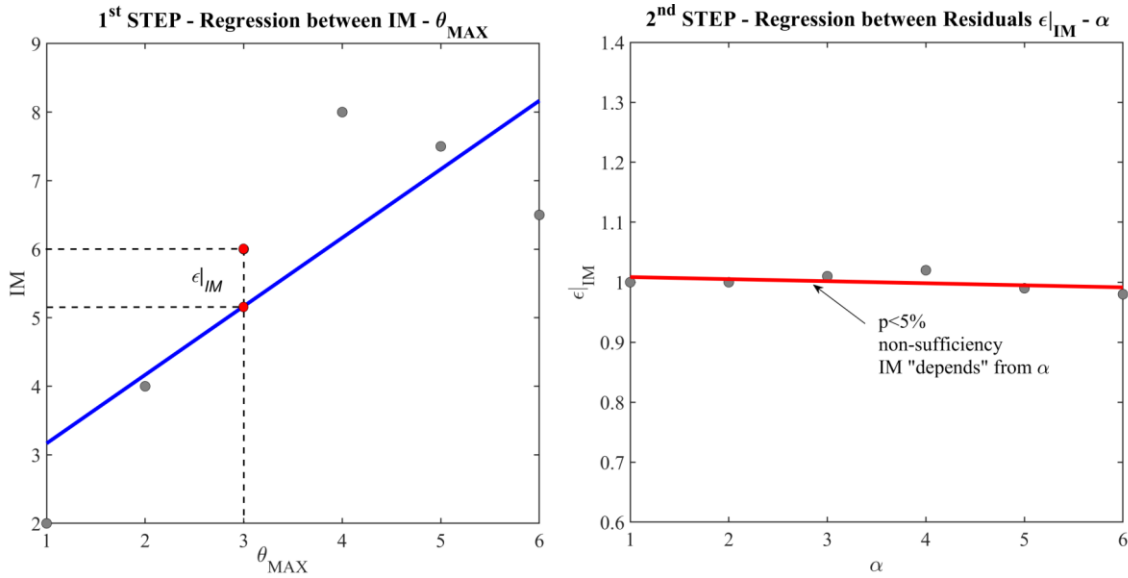


Figure 4-7 Adopted IM-EDP sufficiency testing.

In this context, a standard two-step sufficiency IM test is adopted which involves undertaking a different linear regression analysis at each step as delineated in Figure 4-7 (see also Tothong and Luco 2007, Mollaioli et al. 2013). In the first step, regression analysis between the IM and the engineering demand parameter EDP ( $\theta_{MAX}$ ) is undertaken (left panel of Figure 4-7) to obtain the residuals  $\epsilon_{|IM}$  as defined in Appendix C. Under the common assumption that IM-EDP relationship follows a power law, the linear regression model is written as

$$\ln(\theta_{max}) = \ln(C_0^*) + C_1^* \cdot \ln(IM) \quad (4.11)$$

where  $\ln(C_0^*)$  and  $C_1^*$  are the intercept and the slope regression coefficients of the  $\ln(\text{EDP})$ - $\ln(\text{IM})$  relationship, respectively. In the second step, regression analysis is undertaken between the residuals  $\epsilon_{|IM}$  and  $\alpha$  as in (right panel of Figure 4-7)

$$\epsilon_{|IM} = C_0' + C_1' \cdot \alpha. \quad (4.12)$$

Then, IM-EDP sufficiency is measured by the statistical significance of a non-zero slope in the last regression analysis,  $C_1'$ . If the p-value of the estimated slope coefficient between  $\epsilon_{|IM} - \alpha$  is adopted to test whether the null hypothesis  $C_1' = 0$  is true (see also Appendix D), then a relatively small p-value (typically <5%) in conjunction with an appreciably  $C_1'$  value different than 0 (non-flat regression line) indicate that the IM is non-sufficient in predicting the EDP ( $\theta_{MAX}$ ) against  $\alpha$

This is because a statistically significant non-zero trend in the regression in equation (4.12) shows that  $\alpha$  correlates with the residuals  $\varepsilon|IM$  and, hence, the adopted IM would benefit by the additional information carried by  $\alpha$  to improve its ability for EDP values prediction in the regression analysis in equation (4.11).

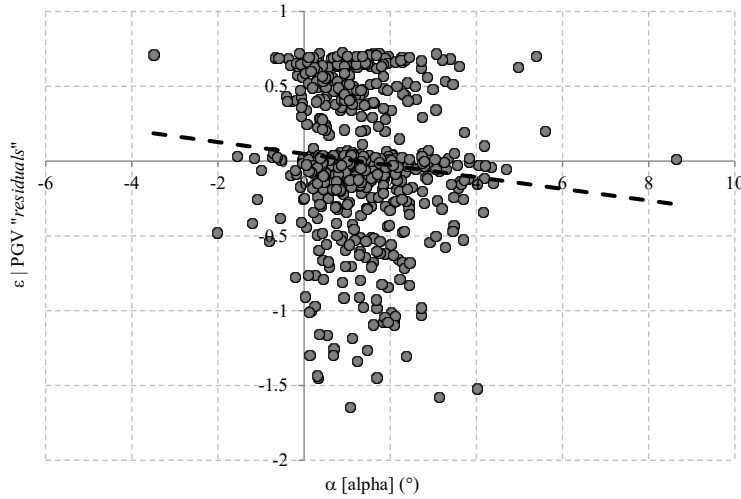


Figure 4-8 Regression analysis of  $\varepsilon|PGV$  residuals with  $\alpha$  (p-value=0.0186)

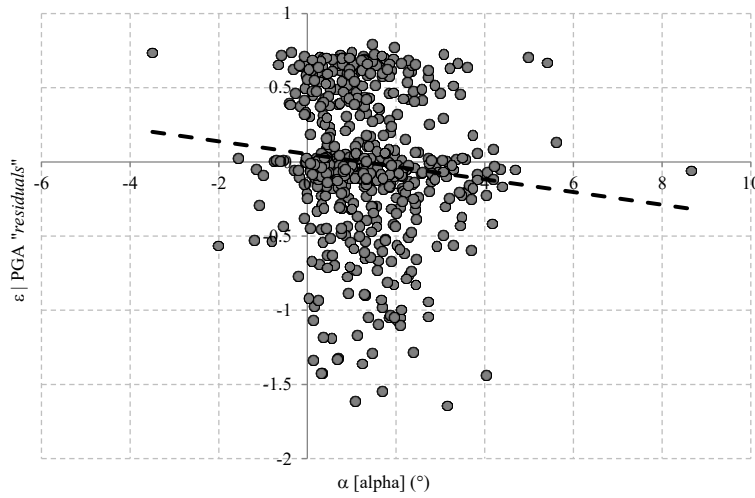


Figure 4-9 Regression analysis of  $\varepsilon|PGA$  residuals with  $\alpha$  (p-value=0.0096)

Following the above sufficiency testing approach, clouds of  $\varepsilon|PGV$  and  $\varepsilon|PGA$  residuals with  $\alpha$  are plotted in Figures 4-8 and 4-9, respectively (count: 611), along with the fitted linear regression lines. The EDP  $\theta_{max}$  values used in the regression analysis in equation (4.11) are obtained by performing IDA for the 611 GMs considered in the previous section (Table A-2 in Appendix A) to the SDOF hysteretic oscillator with strength and stiffness degradation presented in section 3.5 and implemented in OpenSees finite element platform. It is seen in Figures 4-8 and 4-9 that there is a non-negligible linear trend (slope  $C_1'$ ) in the fitted regression lines which is statistically

significant as indicated by *p-values* lower than 0.05 (Howell 2007). These low *p-values* demonstrate non-sufficiency of the IM considered (PGA, PGV) to predict peak seismic storey drift demands in the considered yielding structural system against  $\alpha$ . In this respect,  $\alpha$  has a statistically significant influence to peak inelastic demand and this effect is more prominent when adopting PGA as the IM as opposed to the PGV in the context of PBEE. Ultimately, the herein undertaken statistical tests demonstrate that the non-stationary average frequency content of GMs as captured by  $\alpha$  does influence the peak inelastic seismic demand in terms of  $\theta_{max}$ .

### 4.4 Concluding Remarks

A novel wavelet-based scalar quantity termed alpha,  $\alpha$ , has been introduced in this chapter to characterize the temporal evolution of the mean frequency content of recorded GMs. It is defined as the average slope (angle) of the time-varying mean instantaneous period (MIP) extracted from the wavelet coefficients of GMs bounded in time within the GM effective duration and bandlimited within the [0.25 25]Hz frequency range. Morlet wavelets were considered in the wavelet transformation of GMs as they yield relatively smooth MIPs in time. Pertinent linear regression analyses involving 611 GMs with no near-fault directivity effects was undertaken to quantify the relationship of  $\alpha$  with GM properties PGA, PGV, and mean frequency content  $T_m$ , with seismological parameters,  $M$ ,  $R_{rup}$ , and with the shear wave velocity  $V_s$ . No significant correlation was found between  $\alpha$  and  $M$ ,  $R_{rup}$ , or PGA. However, it was established that  $\alpha$  is well-correlated with the average frequency content of GMs as captured by  $T_m$  and by PGV: the lower the average frequency content, the larger  $\alpha$  tends to be, that is, the faster the time evolution (transition) of the average frequency content is from higher to lower frequencies. Further, the reported numerical data indicate that the level of the above correlation depends on the intensity of GMs in terms of PGA (conditional on PGA):  $\alpha$  is larger for fixed  $T_m$  as PGA increases and  $\alpha$  increases faster as  $T_m$  increases for larger PGA values. Moreover, GMs recorded on softer soils are more likely to have larger  $\alpha$  conditional on PGA, a phenomenon that is attributed to the fact that soft soils under strong seismic shaking exhibit strong non-linear behaviour that enriches the low frequency content of free field recorded GMs. Lastly, sufficiency statistical tests on  $\alpha$  with the residuals of regression analyses between peak inelastic drifts  $\theta_{max}$  of a hysteretic SDOF structure estimated through IDA for the previous 611 GMs with PGA and with PGV used as IMs were also conducted. The considered structure includes strength and stiffness degradation effects and is used as proxy of a 12-storey r/c frame. These statistical tests demonstrate that the non-stationary average frequency content of GMs as captured by  $\alpha$  influences the peak inelastic structural response at collapse, as captured by  $\theta_{max}$ . Overall, the herein furnished results establish the validity and usefulness of  $\alpha$  in characterizing the evolutionary frequency content of GMs and

suggests that  $\alpha$  should be considered as a record selection criterion in undertaking IDA using PGA and PGV as IMs. Note, however, that the adopted sufficiency testing has been only used as a tool to identify influence of  $\alpha$  to the hysteretic responses in establishing IM-EDP relationships when very loose GM record selection criteria were used. It does not quantify this influence. This is pursued in the next two chapters for SDOF and MDOF yielding structures adopting more straightforward statistical tools and using structure-specific IMs and/or more stringent record selection criteria.



## Chapter 5

Influence of Non-Stationary Frequency

Content of GMs to Seismic Demands of

Inelastic Single-Degree-of- Freedom

Systems

## 5 Preliminary Remarks

In the previous chapter, the usefulness of  $\alpha$  to represent time-evolving trends of the mean frequency content of recorded GMs has been established as well as statistical relationships of  $\alpha$  with seismological parameters,  $M$  and  $R$ , soil shear wave velocity  $V_{s30}$ , and GM properties PGA and PGV. It was further seen that  $\alpha$  does influence peak inelastic seismic response of SDOF systems by relying on sufficiency testing of PGA and PGV used as IMs in undertaking IDA. In this chapter, further numerical work is undertaken to quantify statistically the dependency of  $\alpha$ , and thus of the average non-stationary GM frequency content trends, to the response of SDOF inelastic oscillators widely used as proxies of yielding structures in undertaking seismic structural vulnerability and loss assessment within PBEE. This is pursued via gauging the change of the required IM to induce a specific EDP value (i.e., IM conditioned on EDPs) due to a change in the  $\alpha$  property of input GMs on the average (i.e., through regression analysis). Ultimately, tracing this change for SDOF oscillators with different properties, IMs and values of EDP, quantifies the influence/importance of GM non-stationary frequency content to hysteretic structural response statistically and in a phenomenological manner. In this regard, IMs and oscillators extensively used in pilot seismic vulnerability assessments (FEMA 2009, Kazantzi and Vamvatsikos 2015) are considered in the ensuing analyses aiming to conclude in which cases of practical interest to undertaking seismic vulnerability assessment studies using IDA this influence should be of concern. In this context, the use of an advanced IM accounting for the influence of spectral shape to period elongation, i.e., AvgSa, is studied vis-à-vis the most commonly used IM,  $S_a(T_1)$  which only carries information about the pre-yielding structural natural period. Further, two different benchmark SDOF systems corresponding to ductile and non-ductile structural inelastic behaviour are considered with varying pre-yielding natural periods. The comparison across SDOF systems with different properties in terms of IM|EDP is facilitated by considering a normalised IM as considered in FEMA P440A report. The presentation begins from the definition of the inelastic SDOF systems and their numerical modelling/implementation in OpenSees. Then, different IMs are discussed and results from IDA to a databank of 611 GMs are obtained. Lastly, regression analysis probing the statistical relationship of  $\alpha$  value to IMs conditioned on different values of EDP are reported with most focus given on the case of near collapse EDP values.

### 5.1 Description and modelling of adopted inelastic SDOF systems

The use of SDOF hysteretic oscillators/systems as proxies of detailed MDOF inelastic models of real-life structures is widely considered in undertaking IDA as it reduces computational cost, and accuracy, involved in NRHA. Properties of the SDOF systems are defined by means of a force-

displacement capacity curve and a hysteretic law which may or may not include strength and/or stiffness degradation. The latter defines a cyclic envelop which coincides with the capacity curve if no degradation is present or may be different if degradation is considered in the modelling as illustrated in Figure 5-1 (FEMA 2009). Force-deformation capacity boundary curve is thus an outer envelope in softening systems commonly derived from nonlinear static pushover analysis applied to MDOF structural models (see Section 3.5 for an example).

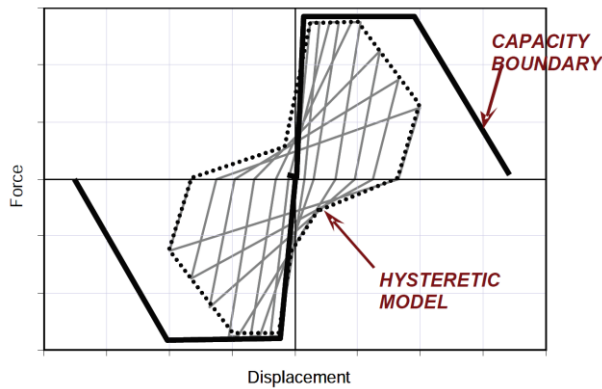


Figure 5-1 Force-Displacement capacity boundary and Hysteretic cycles with stiffness/strength degradation

Hysteretic law and degradation effects, either in-cycle or through-cycle, as depicted in Figure 5-2, are usually defined based on cyclic lab testing. The dynamic response between systems supporting cyclic strength degradation and in-cycle degradation are different with the first substantially stable and the latter presenting lateral instability to a state of collapse (FEMA 2009).

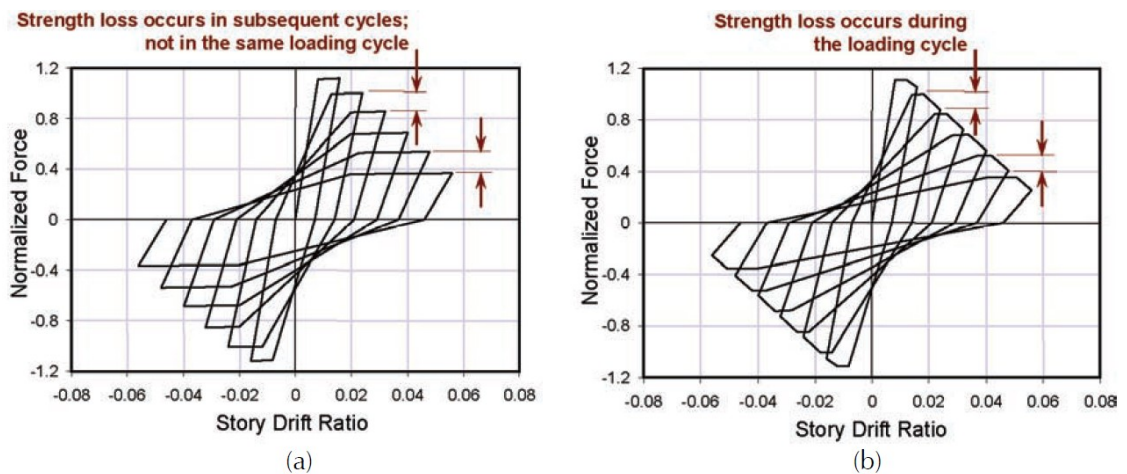


Figure 5-2 Hysteretic behaviour for models with: (a) cyclic strength degradation; and (b) in-cycle degradation (FEMA 2009)

Several such SDOF systems have been developed and generalised for wide classes of structures in FEMA P440A report consolidating results from 160 nonlinear degrading response of single-

spring systems and 600 multi-spring systems into eight different backbone curves. Herein, two of these backbone curves are adopted and taken as representatives of typical non-ductile and ductile structural systems. They are specified as follows:

- **Non-Ductile SDOF** – Proposed for modelling the behaviour of non-ductile moment frame system (e.g., steel or concrete). Their capacity boundary curve is characterized by a force-displacement envelope that includes strength and stiffness degradation and residual strength plateau at 15% of the yield strength, with an ultimate deformation capacity of 6%. The hysteretic behaviour considers the cyclic degradation.
- **Ductile SDOF** – Proposed for modelling the behaviour of ductile moment frame system (e.g., steel or concrete). Their capacity boundary curve is characterized by a force-displacement envelope that includes strength-hardening slope of 2% of the elastic stiffness, a strength degradation between 4% and 6%, with an ultimate deformation capacity of 8%. The hysteretic behaviour considers the cyclic degradation

The parameters of the force-displacement capacity boundary curves of the adopted models are defined in Table 5-1, and graphically showed in Figure 5-3.

**Table 5-1** Force-Displacement Capacity Boundary

Prototype		Quantity	Points of the force-deformation capacity boundary						
			A	B	C	D	E	F	G
Non-Ductile SDOF	Non-ductile moment	F/F <sub>y</sub>	0	1	0.15	0.15	0.15	0.15	0
		$\theta$	0	0.01	0.05	0.055	0.06	0.06	0.06
Ductile SDOF	Ductile moment frame	F/F <sub>y</sub>	0	1	1.05	0.8	0.8	0.8	0
		$\theta$	0	0.01	0.04	0.06	0.08	0.08	0.08

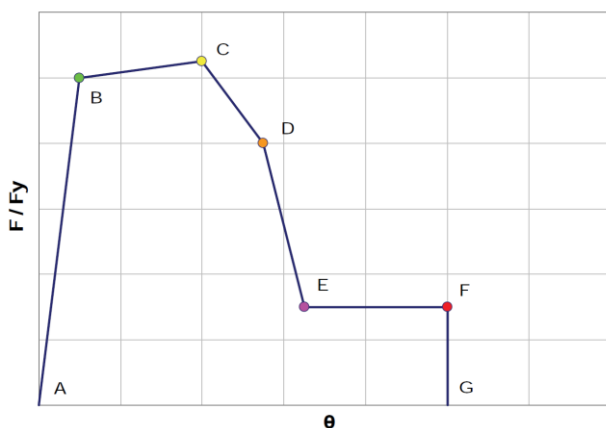


**Figure 5-3** Generic force-displacement capacity boundary - (FEMA P440A 2009).

To investigate the relation between the GMs alpha curves and the period of the systems, each spring were tuned to periods of 0.5s, 1.0s, 1.5s, and 2.0s. Further, the Hysteretic material used here reflects the uniaxial material implemented in OpenSEES that represents a 'pinched' one-dimensional hysteretic load-deformation relationship with stiffness and strength degradation under cyclic loading as detailed in Appendix E. Structural systems exhibit pinching behaviour when large difference in stiffness during reloading-unloading cycle associated with stiffness recovery when displacement is imposed in the opposite direction are noted (e.g., effect to opening and closing of cracks in concrete). The capacity boundary curve response specifies an unload-reload path which, in the cases considered, is multilinear and idealization of a load-deformation history predicted using this model as illustrated in Figure 5-4. The capacity boundary curves 1 and 2 account for load path changes to accommodate strength decreasing due to load-deformation history. The hysteretic model curves 3 and 4 are defined when the load-deformation level is entered and it is defined by two load-deformation points. These load-deformation points include the point reached once unloading or reloading occurred, which results to be a fraction of the minimum (or maximum) strength achievable.

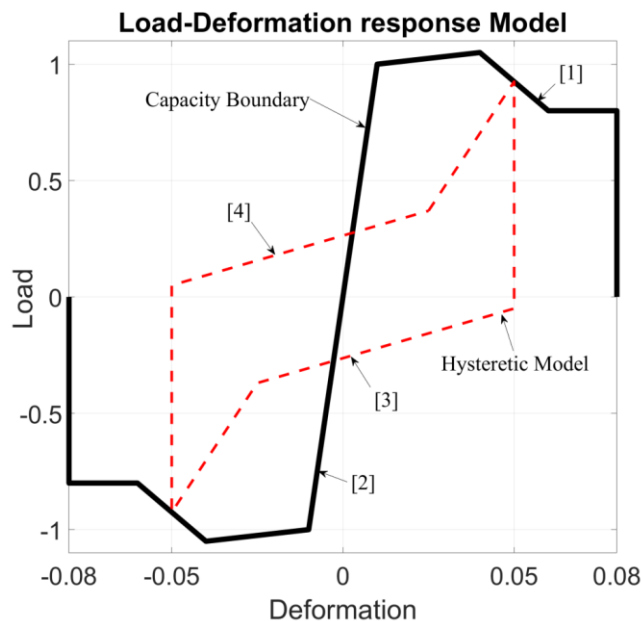


Figure 5-4 One-dimensional load-deformation response model (PEER 2003/10)

Cyclic degradation of strength and stiffness occurs in three ways: unloading stiffness degradation (see left panel of Figure 5-5 for illustration), reloading stiffness degradation (see right panel of Figure 5-5 for illustration), and strength degradation (see Figure 5-6 for illustration). The hysteretic damage therefore can be split in three components.

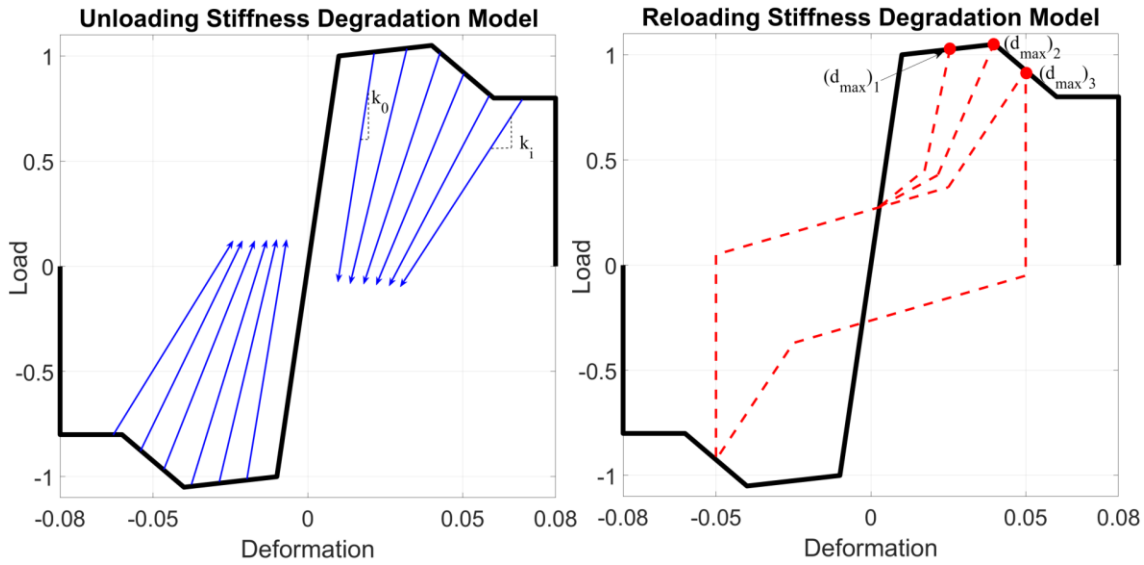


Figure 5-5 Unloading stiffness degradation and reloading stiffness degradation (PEER 2003/10)

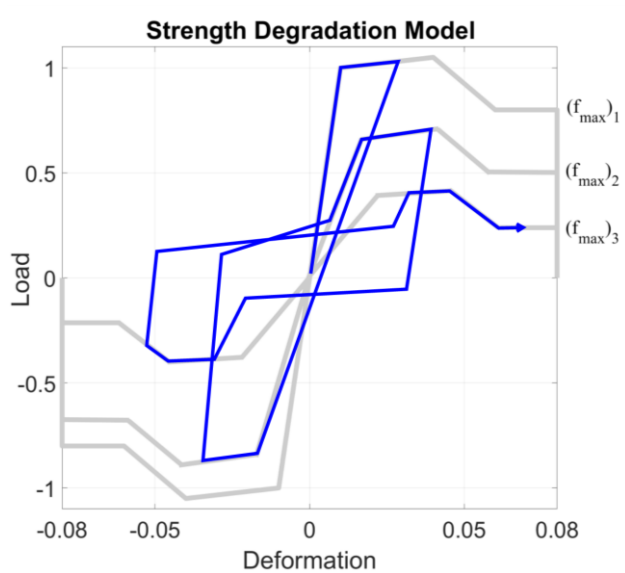


Figure 5-6 Strength degradation (PEER 2003/10)

Firstly, the capacity boundary curve section for the stiffness degradation is herein written as

$$k_i = k_0 \cdot (1 - \delta k_i) \tag{5.1}$$

where  $k_i$  and  $k_0$  are respectively the current and initial unloading stiffness and  $\delta k_i$  is the stiffness damage index associated to the current state  $t_i$ . Secondly, the capacity boundary curve section for the strength degradation is modelled as

$$d_{max,i} = d_{max,0} \cdot (1 + \delta d_i). \quad (5.2)$$

Here  $d_{max,i}$  and  $d_{max,0}$  are the current and initial deformation, respectively, and  $\delta d_i$  is the value of the reloading stiffness damage index associated to the current state  $t_i$ . Thirdly, the capacity boundary curve for the strength degradation is written as

$$f_{max,i} = f_{max,0} \cdot (1 - \delta f_i) \quad (5.3)$$

where  $f_{max,i}$  and  $f_{max,0}$  are the current and initial maximum strength, respectively, and  $\delta f_i$  is the strength damage index associated to the current state  $t_i$ .

The damage law adopted in modelling uses the damage index  $D$  proposed by Park et al. (1985) related to the displacement history and energy accumulation by

$$D = \frac{\delta_{max}}{\delta_u} + \beta_1 \int \left( \frac{\delta}{\delta_u} \right)^{\beta_2} \frac{dE}{E_c(\delta)} \quad (5.4)$$

where  $E_c(\delta)$  is the accumulate energy per loading cycle for the current displacement and  $\beta_1$  and  $\beta_2$  are two calibration parameters for cyclic damage. Making use of the notation adopted by OpenSees the last expression is rewritten as

$$D = A \cdot (\delta_{max})^C + B \cdot \left( \frac{E_i}{E_{U(mon)}} \right)^D \quad (5.5)$$

where

$$\delta_{max} = \max \left( \frac{\delta_{MAX}}{\delta_{u,MAX}}, \frac{\delta_{MIN}}{\delta_{u,MIN}} \right) \quad (5.6)$$

In equation (5.5),  $E_i$  is the hysteretic energy per cycle and  $E_{U(mon)}$  is the energy necessary, under monotonic loading, to reach the collapse deformation as illustrated in Figure 5-7, while parameters A, B, C and D are necessary to fit the model to experimental data. Further, in equation (5.6),  $\delta_{u,MAX}$ ,  $\delta_{u,MIN}$  are the positive and negative deformation which define the collapse and  $\delta_{MAX}$ ,  $\delta_{MIN}$  are the positive and negative historic deformation demands.

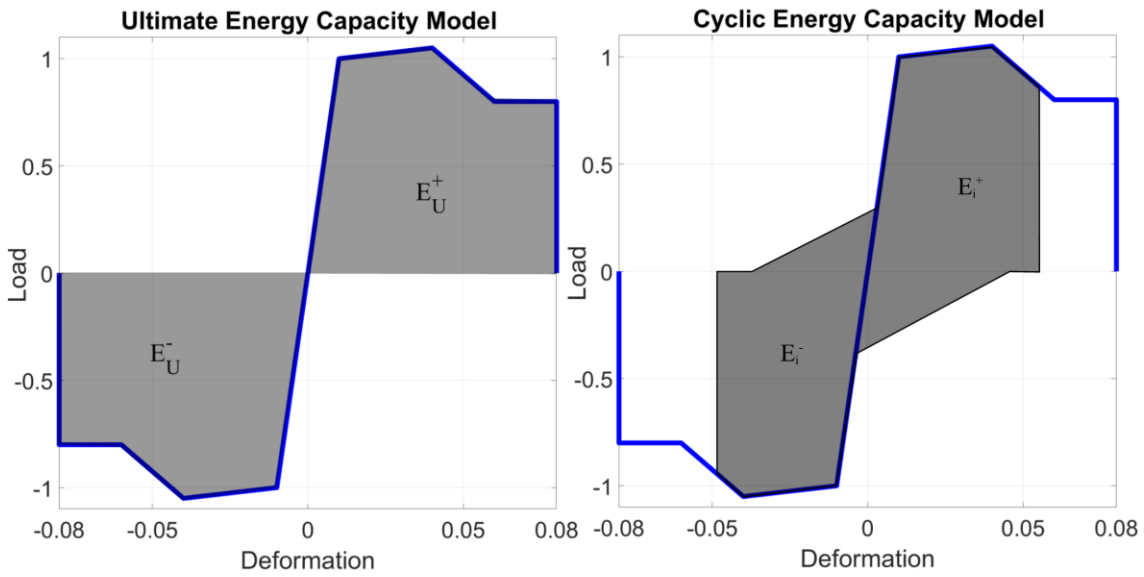


Figure 5-7 Illustration of energy calculation in the damage model adopted.

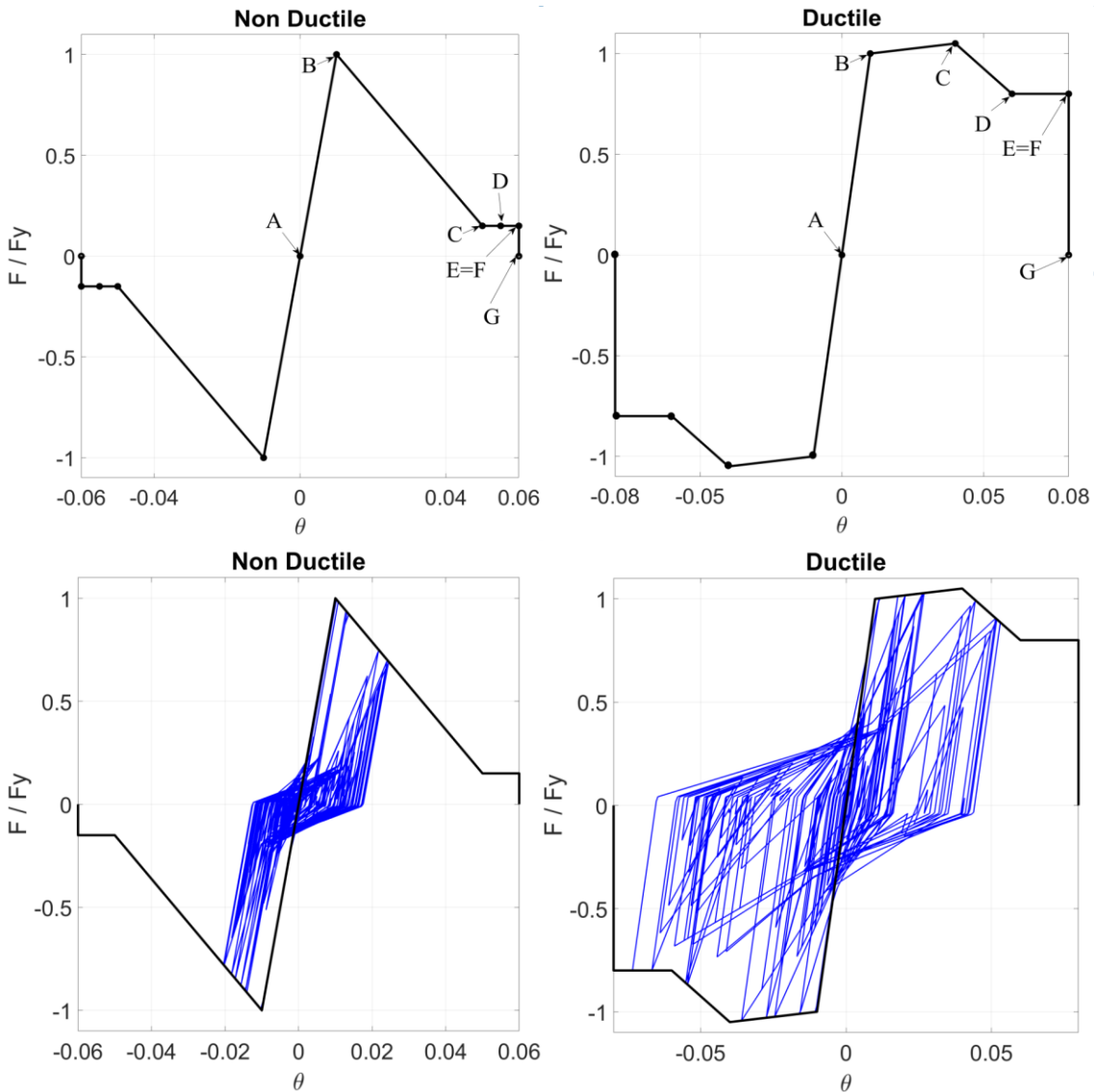


Figure 5-8 Force-Displacement capacity boundary and Hysteretic cycles with stiffness/strength degradation

Figure 5-8 plots the force-displacement boundary capacity curves for the two structural models adopted and illustrates numerically obtained hysteretic cycles with stiffness/strength degradation. The following section delineates briefly the numerical integration scheme adopted.

## 5.2 Numerical direct integration scheme

In Opensees the transient methods used to solve the dynamic integration are all single step methods and the Newmark method with average acceleration has been used in all numerical work. Since these algorithms, though stable for linear dynamical systems, are not necessary stable for nonlinear structures, the conservation of total energy within each integration step has been implemented. The Newmark method (Newmark, 1959) is the most widely used time integration algorithm for structural analysis. The discretization of the dynamic equations with a time step  $\Delta t = t_{k+1} - t_k$  are given as

$$\begin{cases} M\ddot{\mathbf{u}}_{k+1} + C\dot{\mathbf{u}}_{k+1} + K\mathbf{u}_{k+1} = \mathbf{f}(t_{k+1}) \\ \mathbf{u}(t_0) = \mathbf{u}_0, \dot{\mathbf{u}}(t_0) = \dot{\mathbf{u}}_0 \end{cases} \quad (5.7)$$

Further, the Interpolation equations are defined as (Newmark, 1959)

$$\begin{cases} \mathbf{u}_{k+1} = \mathbf{u}_k + \dot{\mathbf{u}}_k \Delta t + \ddot{\mathbf{u}}_k \left( \frac{1}{2} - \beta \right) \Delta t^2 + \ddot{\mathbf{u}}_{k+1} \beta \Delta t^2 \\ \dot{\mathbf{u}}_{k+1} = \dot{\mathbf{u}}_k + \ddot{\mathbf{u}}_k (1 - \gamma) \Delta t + \ddot{\mathbf{u}}_{k+1} \gamma \Delta t \end{cases} \quad (5.8)$$

where  $\beta$  and  $\gamma$  are the parameters of the time integration algorithm. Parameter  $\gamma = 1/2$  ensures second order accuracy while  $\beta = 0$  makes the algorithm explicit and equivalent to the central difference method. For  $\beta = 1/4$  the algorithm becomes implicit and equivalent to the trapezoidal rule (unconditionally stable). Lastly, for  $\gamma = 1/2, \beta = 1/6$  the algorithm becomes the well-known linear acceleration method which is adopted throughout this work.

## 5.3 Selection of Intensity Measures

One of the most used intensity measures (IM) is the spectral acceleration, of a given record, at the fundamental elastic natural period,  $S_a(T1,5\%)$ . This parameter is often chosen as the intensity measure (IM) in conducting IDA as it brings in structure-specific information in a straightforward

manner. However, as discussed in the previous chapter, field recorded strong ground motions (GMs) display a time-evolving frequency content which is difficult to capture with a single parameter and even more difficult if the IMs is based on the fundamental frequency only. Indeed a recognised deficiency of the intensity measure  $S_a(T_1, 5\%)$  is the case when SDOF oscillators exhibiting strong nonlinear behaviour, and  $T_1$  is no longer representative of the effective dynamic property this intensity measure is that it does not consider the inelastic elongation of the period as the structure as period elongation becomes significant, especially for oscillators with hysteretic laws accounting for softens under stiffness degradation.

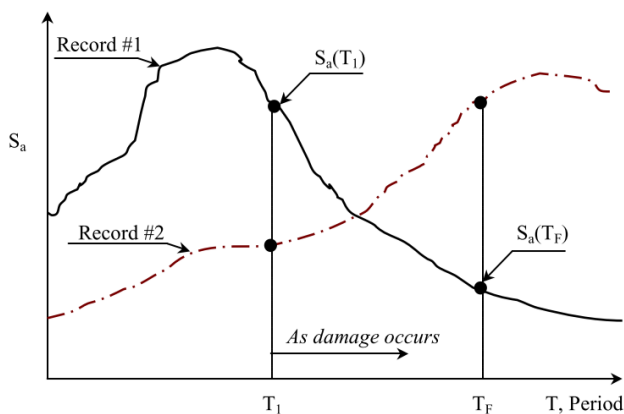


Figure 5-9 Response effects of structural softening (Cordova, et al. 2000 )

Two different ground motion records may induce responses which may be different between each other (Cordova, et al. 2000 ). With reference to the Figure 5-9 the first record induces a response (in terms of spectral accelerations  $S_a(T_1)$ ) which decreases with the increasing of the period as opposed to the second record where there is an effective increasing of  $S_a(T_1)$  with the increasing of the period. While first mode spectral acceleration is an accurate index for structures that respond elastically, this single parameter does not reflect many of the aspects of earthquake ground motions that affect inelastic stiffness and strength degradation. To account for that an additional structure-specific scalar IM was proposed by Cordova, et al. 2000. This parameter captures the period shift effect introducing a second intensity parameter at a longer delayed period to reflect the spectral shape. In addition, compared to  $S_a(T)$ , the choice of selecting  $AvgS_a$  as been observed to improve both efficiency and sufficiency (Kazantzi and Vamvatsikos 2015). The use of more elaborate indices, which seek to improve characterization of earthquake ground motions, have been the subject of continuing studies. For example, Housner in 1975 proposed combining spectral acceleration together with strong motion duration (Cordova, et al. 2000 ). The proposed parameter to do this is a ratio of spectral accelerations at two periods, defined as

$$AvgS_a(T_1, C, \beta) = S_a(T_1) \cdot \left( \frac{S_a(CT_1)}{S_a(T_1)} \right)^\beta \quad (5.9)$$

where  $C$  ( $C > 0$ ) accounts for period elongation which reflects softening due to inelastic behavior.

Herein, the values of  $C=2$  and  $\beta=0.5$  are adopted, and therefore the previous IM specialises as

$$AvgS_a\left(T_1, 1.5, \frac{1}{2}\right) = \sqrt{S_a(T_1) \cdot S_a(1.5T_1)} \quad (5.10)$$

The use of  $C=1.5$  was found to minimise on average the dispersion (standard deviation) of  $S_a$  derived by IDA curves (Cordova, et al. 2000). Further, it was found that the value of  $\beta=0.5$  (given  $C$ ) is relatively stable for  $C=1.5$  (Cordova, et al. 2000).

This property will be used as comparison to  $S_a(T_1)$  from now on, while a near collapse (or collapse prevention) limit state has defined in terms of the peak deflection (or drift  $\theta_{max}$ ).

Finally, the last IM is the normalised value of  $S_a(T_1)$  with respect its elastic value attained at first yielding  $S_{ay}(T_1)$ , that is,

$$R = S_a(T_1)/S_{ay}(T_1) \quad (5.11)$$

The latter IM represents the ratio of the demand elastic strength to the yielding strength of the structure and, as such, it can be used to compare the performance of structures with different properties including different  $T_1$  values.

## 5.4 Comparisons of IDA curves using different IMs

Seismic performance is assessed through nonlinear time history analyses. Acceleration components of the records are scaled and the resulting ground motion intensity is reported in terms of IMs (either spectral acceleration  $S_a$  or  $AvgS_a$ ) and summarized by plotting the scaled intensity measure versus maximum Interstory Drift Ratio (IDR), creating what are referred to herein as Incremented Dynamic Analysis (IDA) curves. Shome and Cornell (1997) have demonstrated that such scaling of records will not bias the results and is an appropriate technique for multi-level hazard analysis. The collection of data points (DM) (each data point corresponds to the peak IDR resulting from a single time history analysis) for a single ground record scaled to

multiple hazard levels (IM) forms the IDA curve (Cordova, et al. 2000 ). A Spline interpolation is used for constructing the IDA curves, where  $n$  cubic polynomial pieces are parametrised over  $n$  convergent runs/points including the default (0,0) (Vamvatsikos and Cornell, 2004). Consequentially it has been chosen to calculate the 16%, 50% and 84% fractiles curve's points which represent  $\mu \mp 1 \cdot \sigma$  ( $\mp 1$  standard deviation) which is typically used to summarise the limit-state capacity within central values (mean  $\mu$ ) and a measure of dispersion (the standard deviation  $\sigma$ ). From the set of 611 pairs of GM recordings, previously described, IDA curves have been processed using the analysis of Non-Ductile and Ductile systems. Plotting the spectral acceleration at the fundamental elastic natural period,  $S_a(T1,5\%)$  against the three levels of EDP chosen (peak deflection, or drift  $\theta_{max}$ ) it is possible to notice the influence of the period on the spectral acceleration value.

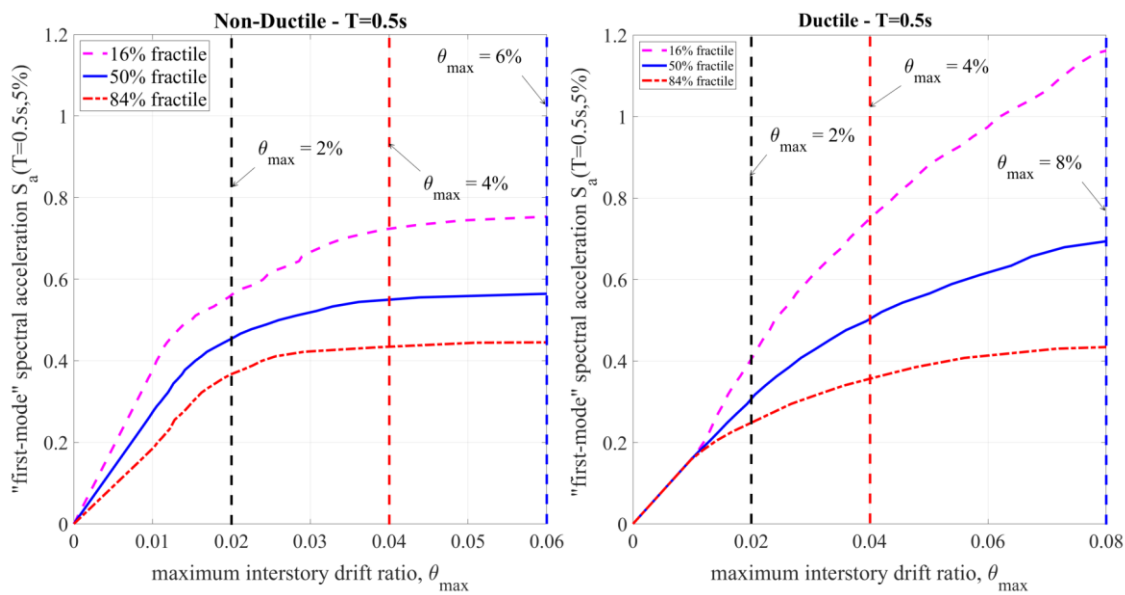


Figure 5-10 16, 50, 84% fractiles incremental dynamic analysis (IDA) curves for  $S_a(T1)$  – a) SDOF  $T=0.5s$  Non-Ductile SDOF, b) SDOF  $T=0.5s$  Ductile SDOF

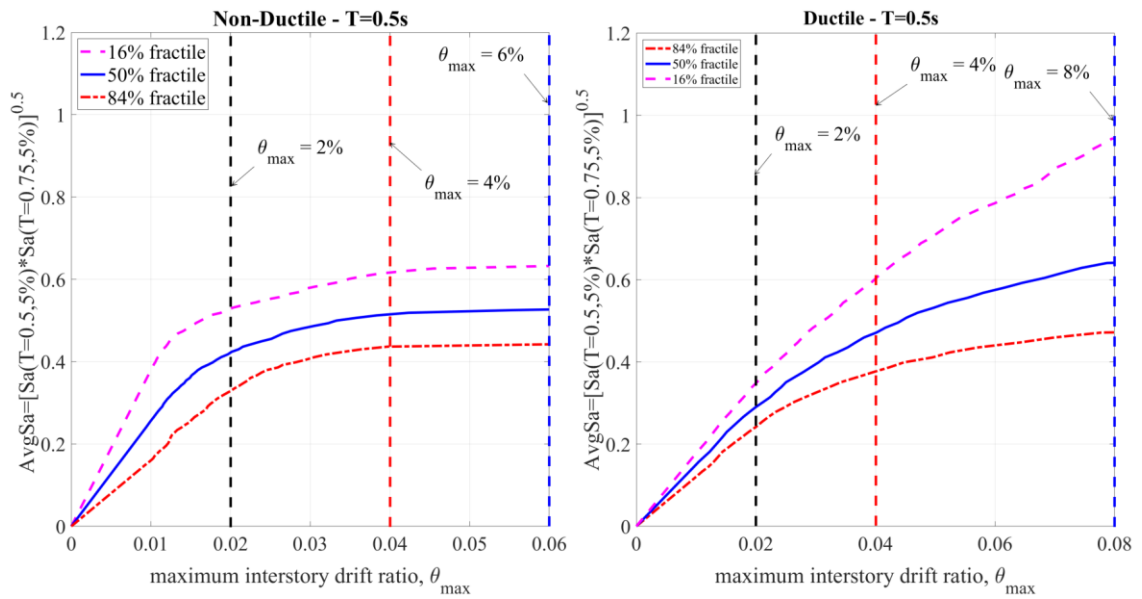


Figure 5-11 16, 50, 84% fractiles incremental dynamic analysis (IDA) curves for AvgSa(T1) – a) SDOF T=0.5s Non-Ductile SDOF, b) SDOF T=0.5s Ductile SDOF

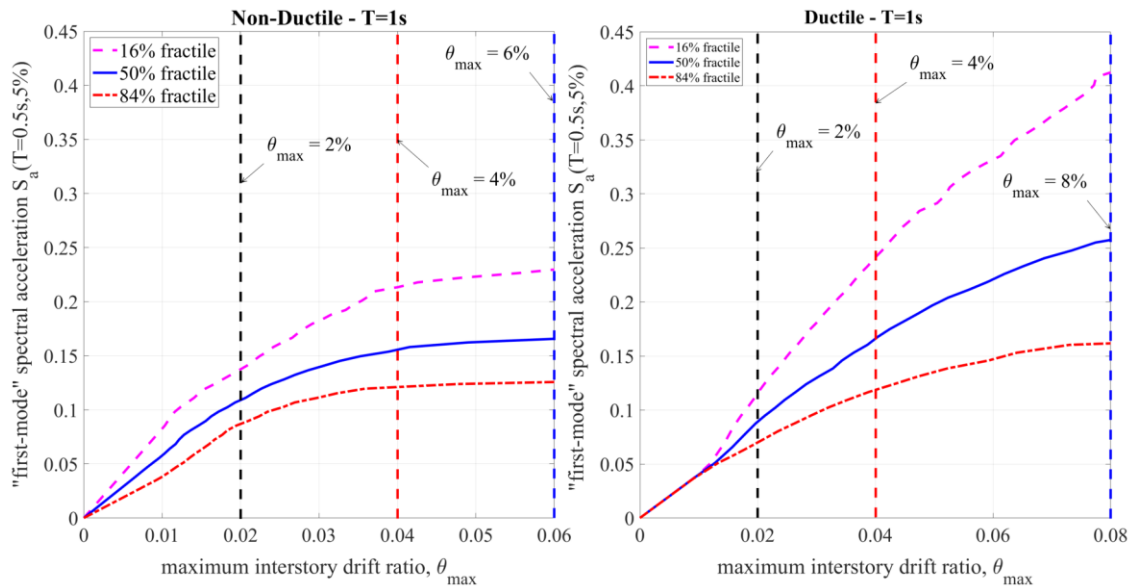


Figure 5-12 16, 50, 84% fractiles incremental dynamic analysis (IDA) curves for Sa(T1) – a) SDOF T=1s Non-Ductile SDOF, b) SDOF T=1s Ductile SDOF

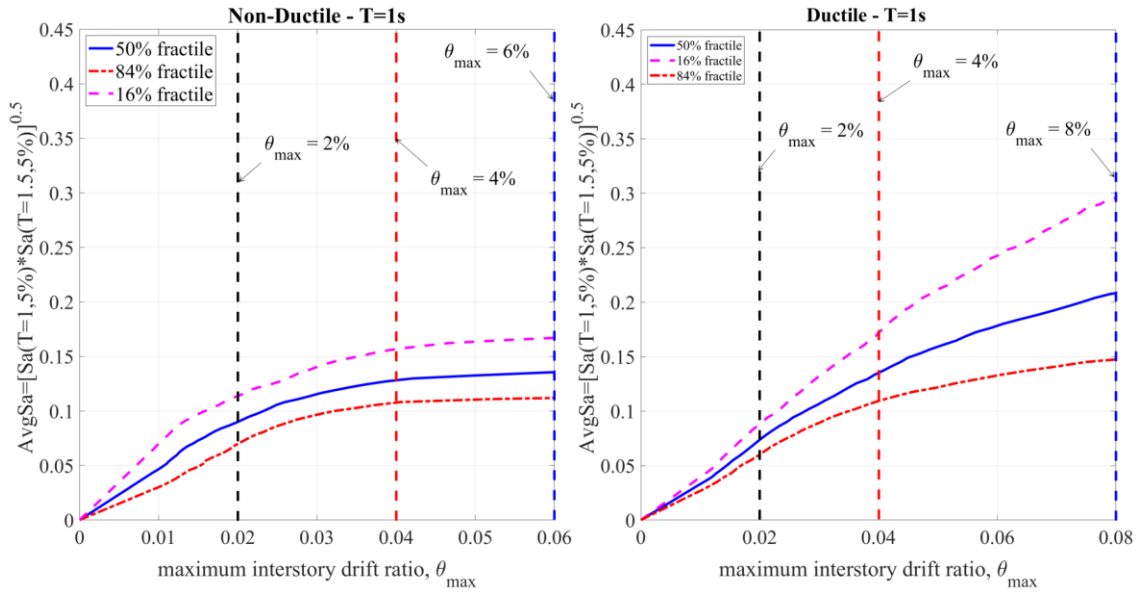


Figure 5-13 16, 50, 84% fractiles incremental dynamic analysis (IDA) curves for  $AvgSa(T1)$  – a) SDOF  $T=1s$  Non-Ductile SDOF, b) SDOF  $T=1s$  Ductile SDOF

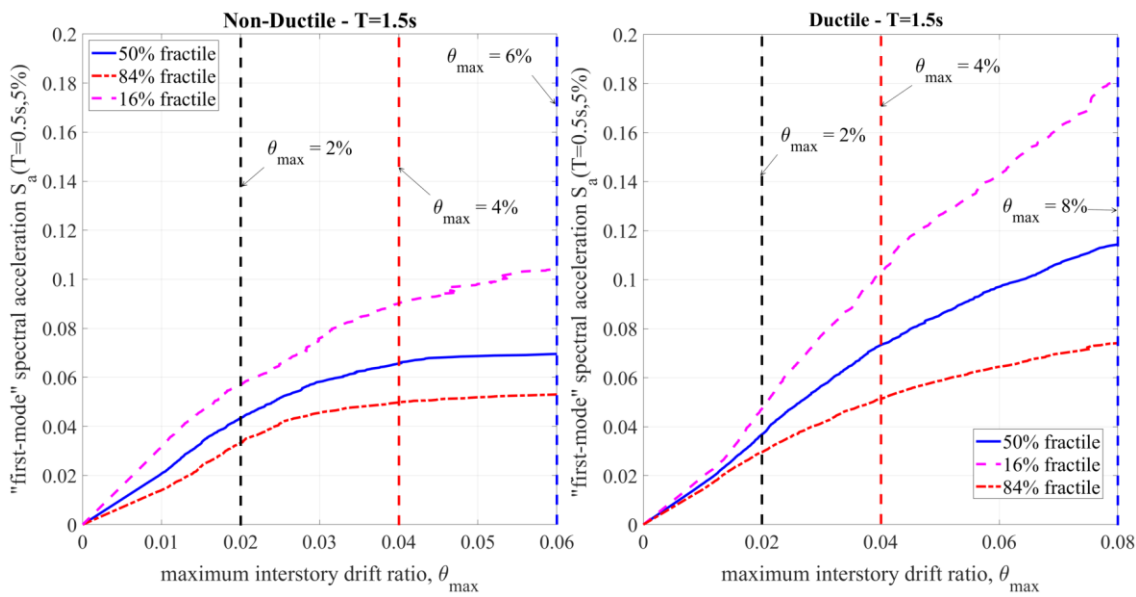


Figure 5-14 16, 50, 84% fractiles incremental dynamic analysis (IDA) curves for  $Sa(T1)$  – a) SDOF  $T=1.5s$  Non-Ductile SDOF, b) SDOF  $T=1.5s$  Ductile SDOF

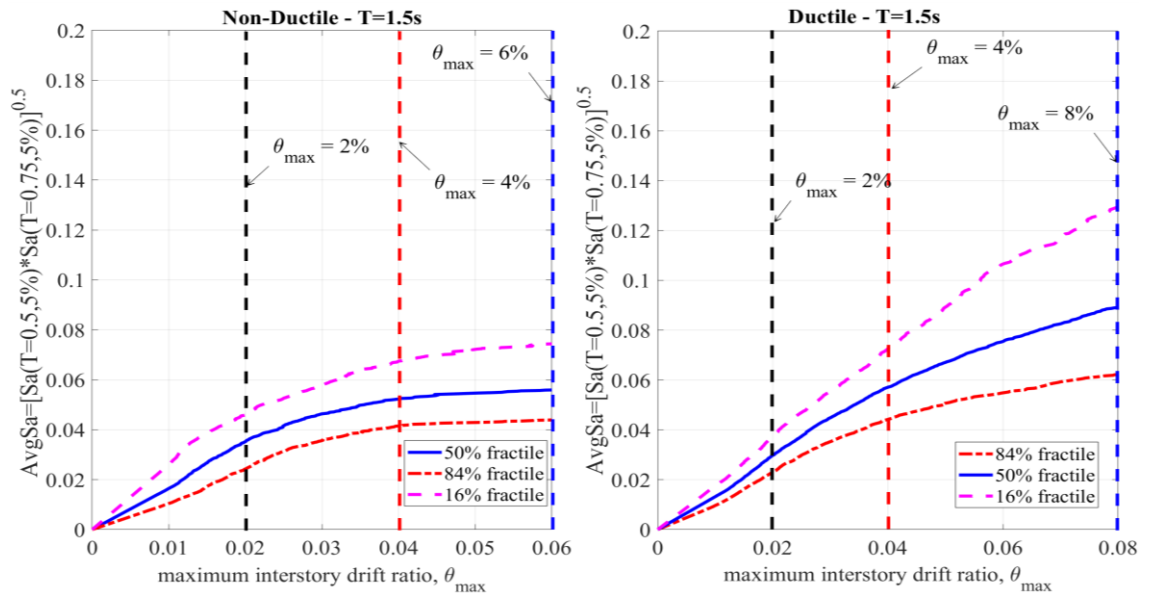


Figure 5-15 16, 50, 84% fractiles incremental dynamic analysis (IDA) curves for AvgSa(T1) – a) SDOF T=1.5s Non-Ductile SDOF, b) SDOF T=1.5s Ductile SDOF

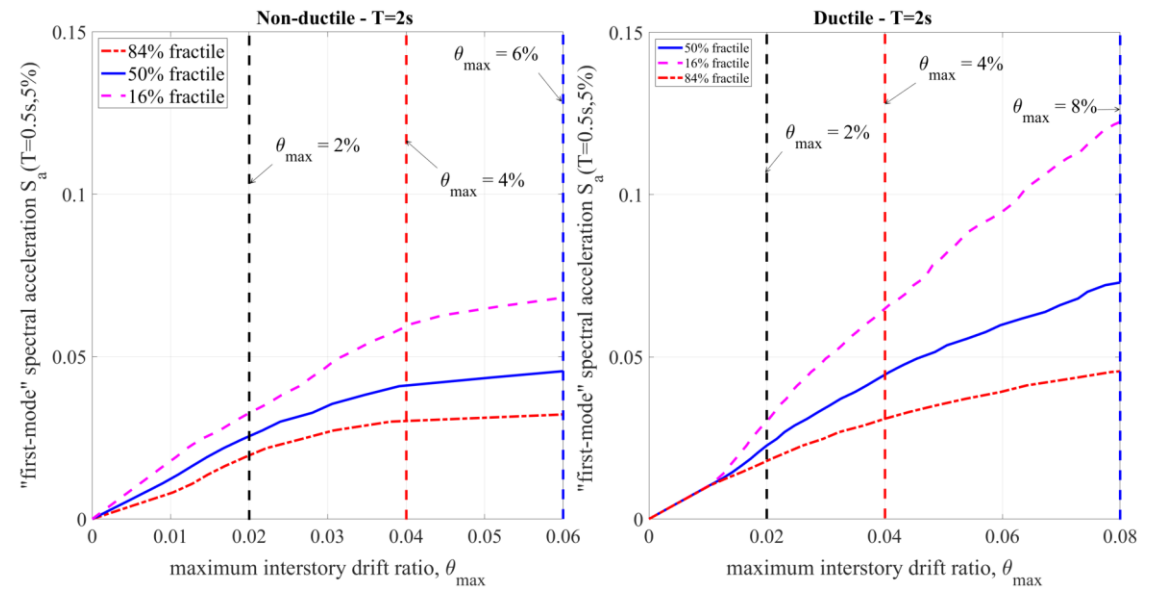


Figure 5-16 16, 50, 84% fractiles incremental dynamic analysis (IDA) curves for Sa(T1) – a) SDOF T=2s Non-Ductile SDOF, b) SDOF T=2s Ductile SDOF

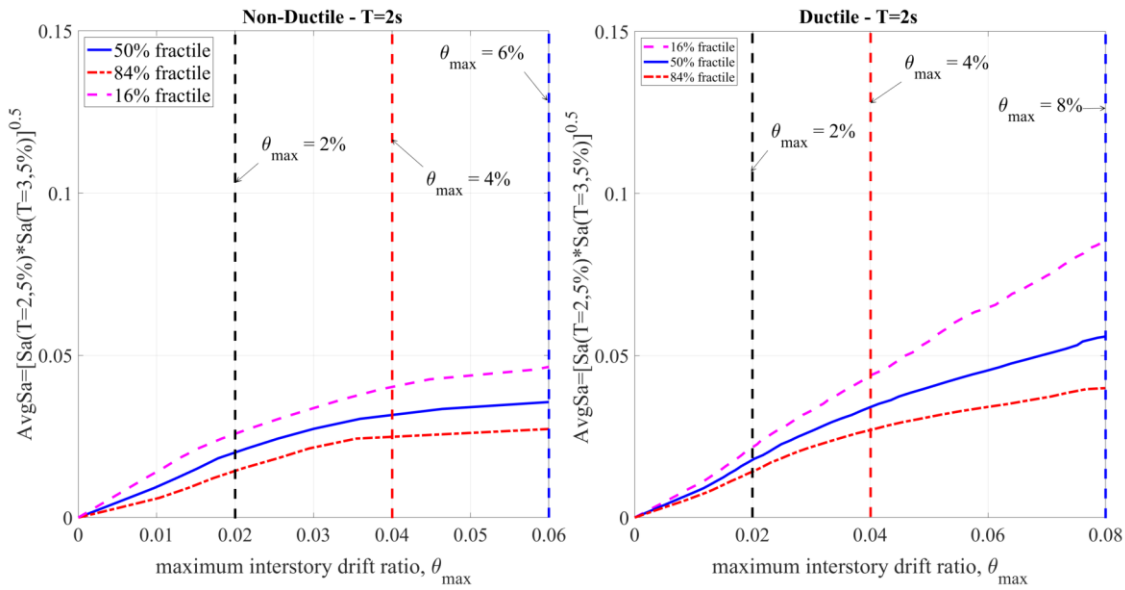


Figure 5-17 16, 50, 84% fractiles incremental dynamic analysis (IDA) curves for AvgSa(T1) – a) SDOF T=2s Non-Ductile SDOF, b) SDOF T=2s Ductile SDOF

Notably, each of the 6 different SDOF systems considered have different lateral strength and/or stiffness and, therefore, direct comparison between IDA curve fractiles among different systems is not straightforward. To facilitate such a comparison, it has previously introduced the normalised IM, in this manner, the IDA curves are re-scaled proportionally for each structural system. For this purpose it has been assumed that the value of the elastic strength  $S_{ay}(T, 5\%)$  is the one estimated to be at the (yield) drift of  $\theta_y = 0.01$  for both the Non-Ductile and ductile SDOF systems adopted (point B in Table 5-1)

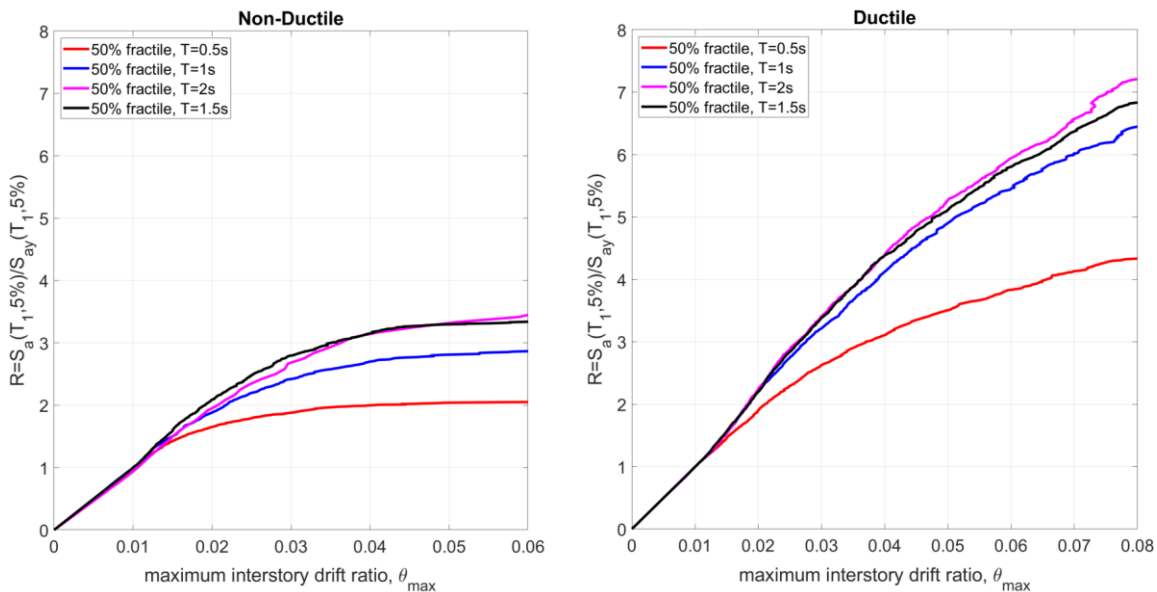


Figure 5-18 16, 50, 84% fractiles incremental dynamic analysis (IDA) curves for  $R = S_a(T, 5\%) / S_{ay}(T, 5\%)$  – a) SDOF T=0.5s,1s,1.5, 2s Non-Ductile SDOF, b) SDOF T=0.5s,1s,1.5s, 2s Ductile SDOF

It is important to note here (Figure 5-18) the dependence of the force reduction factor on the period of vibration of the structural system. In general, it is noted that the lowest the period of the structure the lowest its nonlinear capacity. Indeed, considering the inelastic response spectra basic principle it is well known that structures with fundamental period longer than about 1s follow the *equal-displacement* principle as strong as it is manifested their post-yield stiffness in the force-displacement capacity boundary. In this case the force reduction factor, mentioned above, is equivalent to the ductility of the system  $R = \mu = \frac{\Delta u_f}{\Delta u_y}$ . (Figure 5-19).

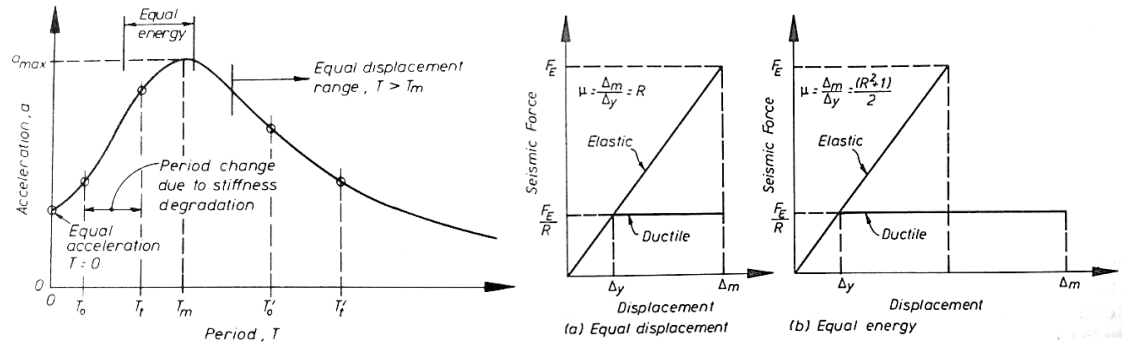


Figure 5-19 Influence of period on ductile force reduction and R definition (Paulay and Priestley 1992)

Conversely, for structures whose natural period is shorter the system follows the *equal-energy* principle and the force reduction factor is equivalent to  $R = \sqrt{2\mu - 1}$ . For very rigid systems where the period is  $T \cong 0$  the structural behaviour results independent from the ductility of the system and the force reduction factor is equivalent to  $R = 1$ . In this case the structure follows the *equal-acceleration* principle.

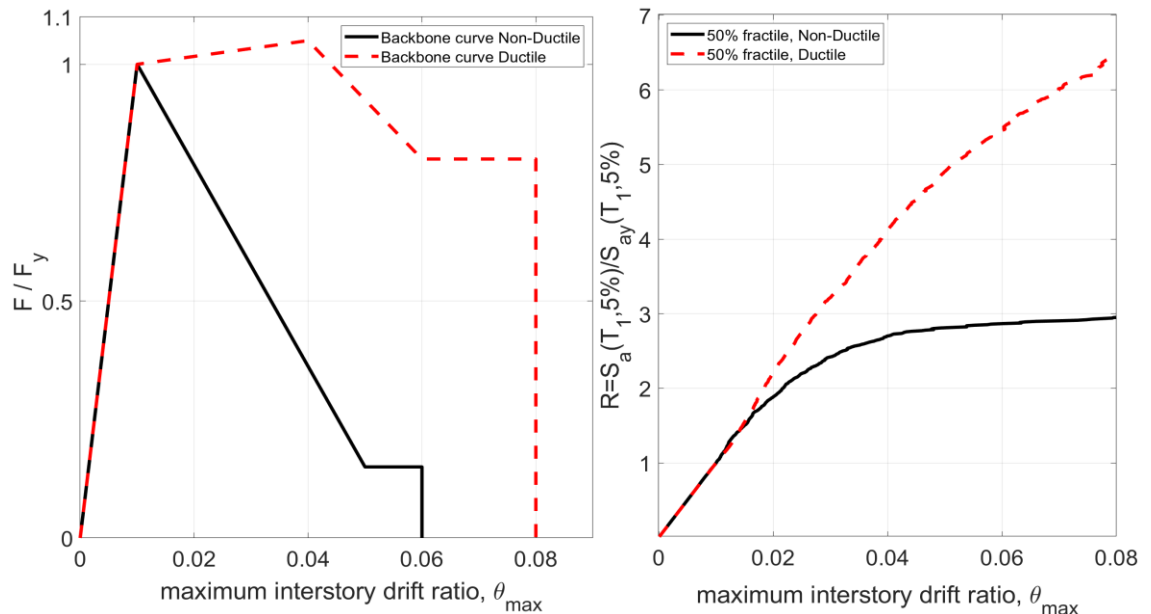


Figure 5-20 Post-yield behavior comparisons of SDOF T=1s Non-Ductile SDOF and 3b and the effect to the collapse capacity system

## 5.5 Regression Analysis of IMs against $\alpha$ and statistical quantification of the influence of $\alpha$

To quantify the influence of the rate of variation of the non-stationary GMs frequency content ( $\alpha$ ) to inelastic response a further study is herein undertaken using a linear regression analysis between the “scaled” spectral acceleration of a given record  $S_a(T_1)$  and  $\alpha$  and between the “scaled”  $AvgS_a(T_1)$  and  $\alpha$ . This investigation is motivated by the fact that  $S_a(T_1)$  and  $AvgS_a(T_1)$  are the most commonly adopted structure-specific intensity measures (IMs) to predict certain engineering demand parameters (EDPs) characterizing the seismic response of yielding structures within the PBEE framework (Vamvatsikos and Cornell, Incremental dynamic Analysis 2002) (Tothong and Luco 2007) (Bommer and Alarcon 2006) (Jalayer, Beck and Zareian, 2012). To quantify the influence of  $\alpha$  to the inelastic seismic demands, values of  $S_a(T_1)$  and  $AvgS_a(T_1)$  are statistically examined conditioned on pre-specified EDP corresponding to different limit states. These data sets of  $S_a(T_1)$  and  $AvgS_a(T_1)$  are obtained by taking “vertical strips” of points on IDA curves (IMs point at given EPD values) derived in the previous section for the 8 different structural systems. These vertical strips consist in cross sections of IDAs associated to 611 GM records for a given EDP (Kazantzi and Vamvatsikos 2015). For each EDP a set of IM capacity values have been selected, which corresponds to limit states associated to specific EDP levels. Moreover, for Ductile and Non-Ductile SDOF the following limit states have been set:

- Non-Ductile SDOF
  - $S_a(T_1)|(\theta_{max} = 0.02)$
  - $S_a(T_1)|(\theta_{max} = 0.04)$
  - $S_a(T_1)|(\theta_{max} = 0.06)$
  
- Ductile SDOF
  - $S_a(T_1)|(\theta_{max} = 0.02)$
  - $S_a(T_1)|(\theta_{max} = 0.04)$
  - $S_a(T_1)|(\theta_{max} = 0.06)$
  - $S_a(T_1)|(\theta_{max} = 0.08)$

To probe into dependency trends between IMs conditioned on different EDP values and  $\alpha$ , standard linear regression analyses using the "least squares" method is undertaken to fit a line (see Appendix C) through a set of observations obtained between  $\alpha$  of the 611 earthquake actions  $S_a(T_1)|\theta_{max}$ , and  $AvgS_a(T_1)|\theta_{max}$  for all 8 different structural systems (ductile and non-ductile and for 4 pre-yielding natural periods). The final linear regression equations (5.1) and (5.2),

establishes a statistical relationship between  $\alpha$  and  $S_a(T_1)|\theta_{max}$  for different limit states,  $S_a(T_1)|\theta_{max}$  (Kazantzi and Vamvatsikos 2015).

$$\alpha(S_a(T_1)|\theta_{max}) = A_0 + B_0 S_a(T_1) \quad (5.12)$$

$$\alpha(Avg S_a|\theta_{max}) = A_1 + B_1 Avg S_a \quad (5.13)$$

The above linear regression equations are represented below for different stiffness and periods. It should be noted that the above approach is based on “statistical sufficiency” via p-value which quantifies the significance of the regression coefficients and it is defined as the probability of rejecting the null hypothesis ( $H$ ) in order to measure the statistical significance of a set of data (“score”). The p-value approach, alone, implies significance or not significance in terms of influence of the IMs with respect to  $\alpha$  but it does not quantify this influence (Kazantzi and Vamvatsikos 2015). In order to provide quantitative information on the importance of the influence of  $\alpha$  on inelastic demands expressed as IMs conditioned on specific EDP levels, the following ratio (slope) of the linear regression curve is used (refer to Figure 5-21):

$$\eta = \frac{\Delta IMs}{\Delta \alpha} \quad (5.14)$$

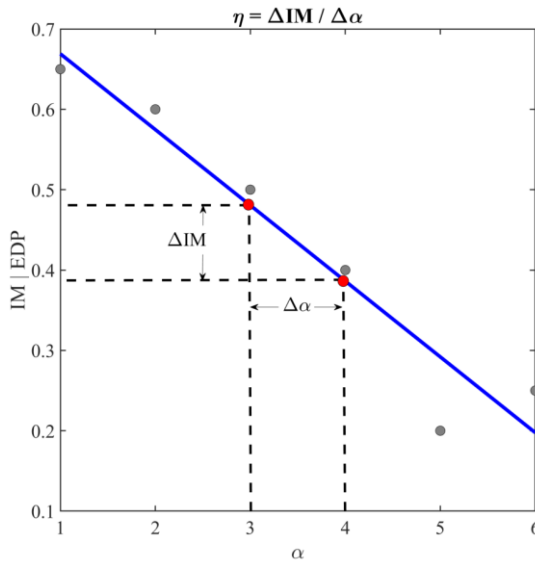
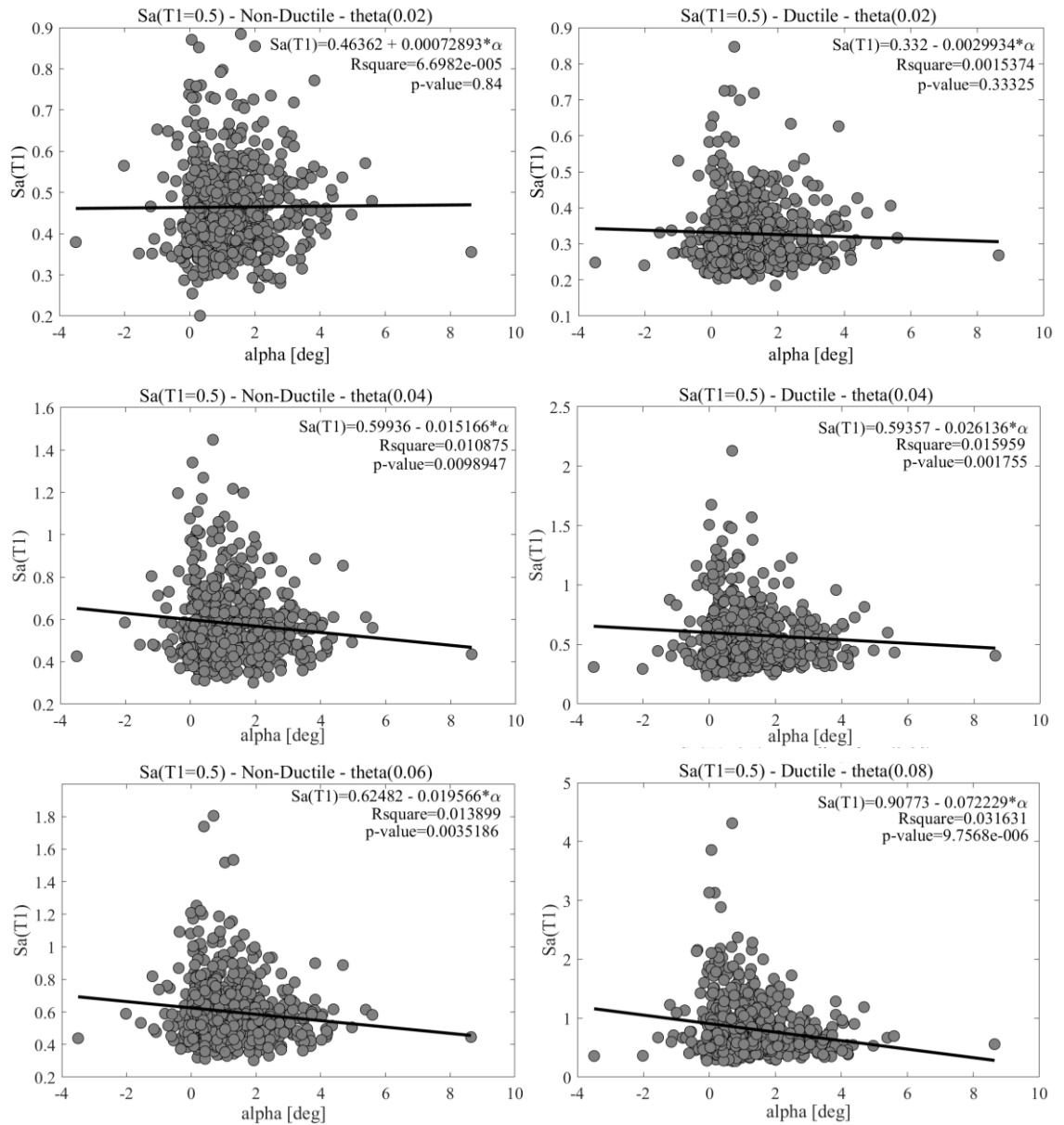


Figure 5-21  $\eta$  ratio (slope) of the linear regression curve

This information is herein used to quantify the influence of the GM predominant frequency’s variation in time ( $\alpha$ ) to the performance of a structure, which herein has been investigated varying its hysteretic behaviour and pre-yield natural period  $T_1$ .

Figure 5-19 plot results of linear regression analyses between  $\alpha$  and  $Sa(T_1)|\theta_{max}$  for all  $\theta_{max}$  values and for both inelastic systems with  $T_1=0.5s$ . It is seen both from the reported values of the slopes  $B$  (in Eqs.7.15) and from the p-values that the influence of  $\alpha$  becomes statistically more and more significant as  $\theta_{max}$  increases. Note that this is also true for  $T_1=1s$  and  $2s$ . These trends signify the increased statistical importance of the GM non-stationary frequency content as the level of nonlinear behaviour of inelastic oscillator increases. Intuitively, these trends can be explained by referring to the result presented in Figure 5-22 in which the average structural response  $\alpha$  approaches the average GM  $\alpha$  as the system is pushed closer to collapse. Ultimately, they indicate that  $\alpha$  may be an important GM record selection criterion for assessing collapse capacity of yielding structures.



v

Figure 5-22 Linear regressions between the  $Sa(T1)$  and  $\alpha$  of MIP for periods  $T=0.5s$  for Non-Ductile and Ductile.  $Sa(T1)$  is obtained interpolating the results at  $\theta_{max}=6\%$  for Non-Ductile and  $\theta_{max}=8\%$  for Ductile.

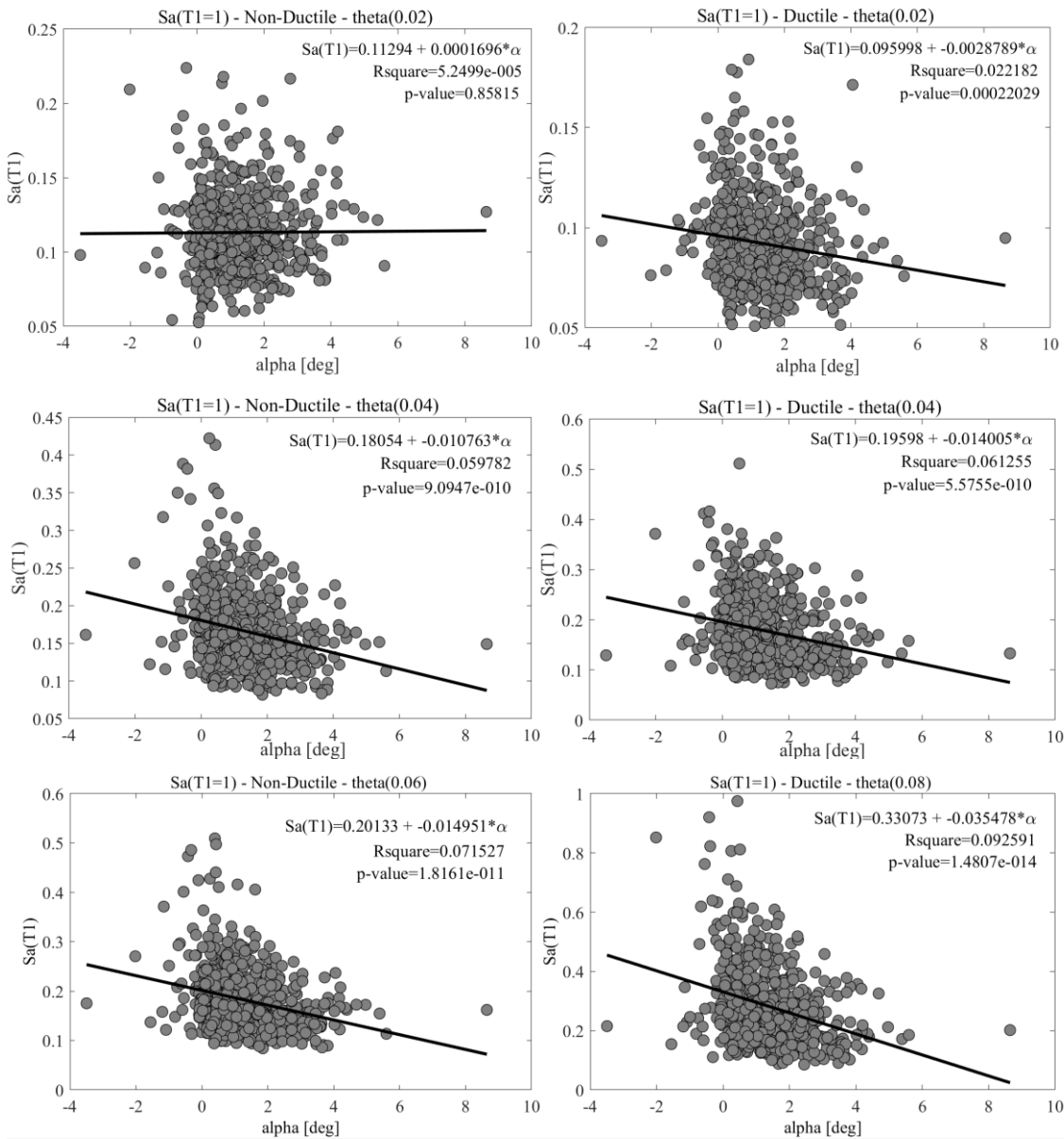


Figure 5-23 Linear regressions between the  $S_a(T1)$  and  $\alpha$  of MIP for periods  $T=1$ s for Non-Ductile and Ductile.  $S_a(T1)$  is obtained interpolating the results at  $\theta_{max}=6\%$  for Non-Ductile and  $\theta_{max}=8\%$  for Ductile.

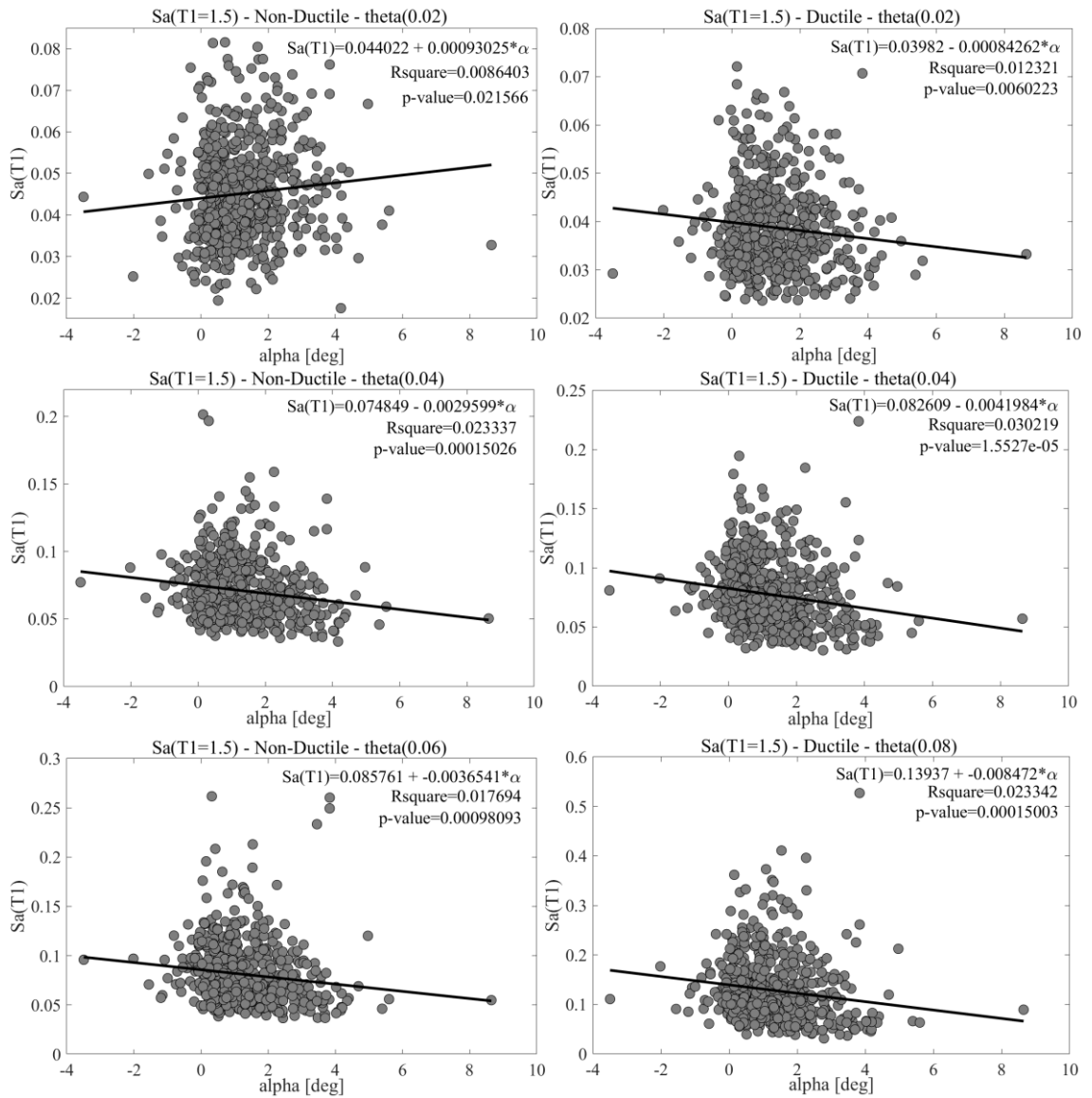


Figure 5-24 Linear regressions between the  $S_a(T1)$  and  $\alpha$  of MIP for periods  $T=1.5$ s for Non-Ductile and Ductile.  $S_a(T1)$  is obtained interpolating the results at  $\theta_{max}=6\%$  for Non-Ductile and  $\theta_{max}=8\%$  for Ductile.

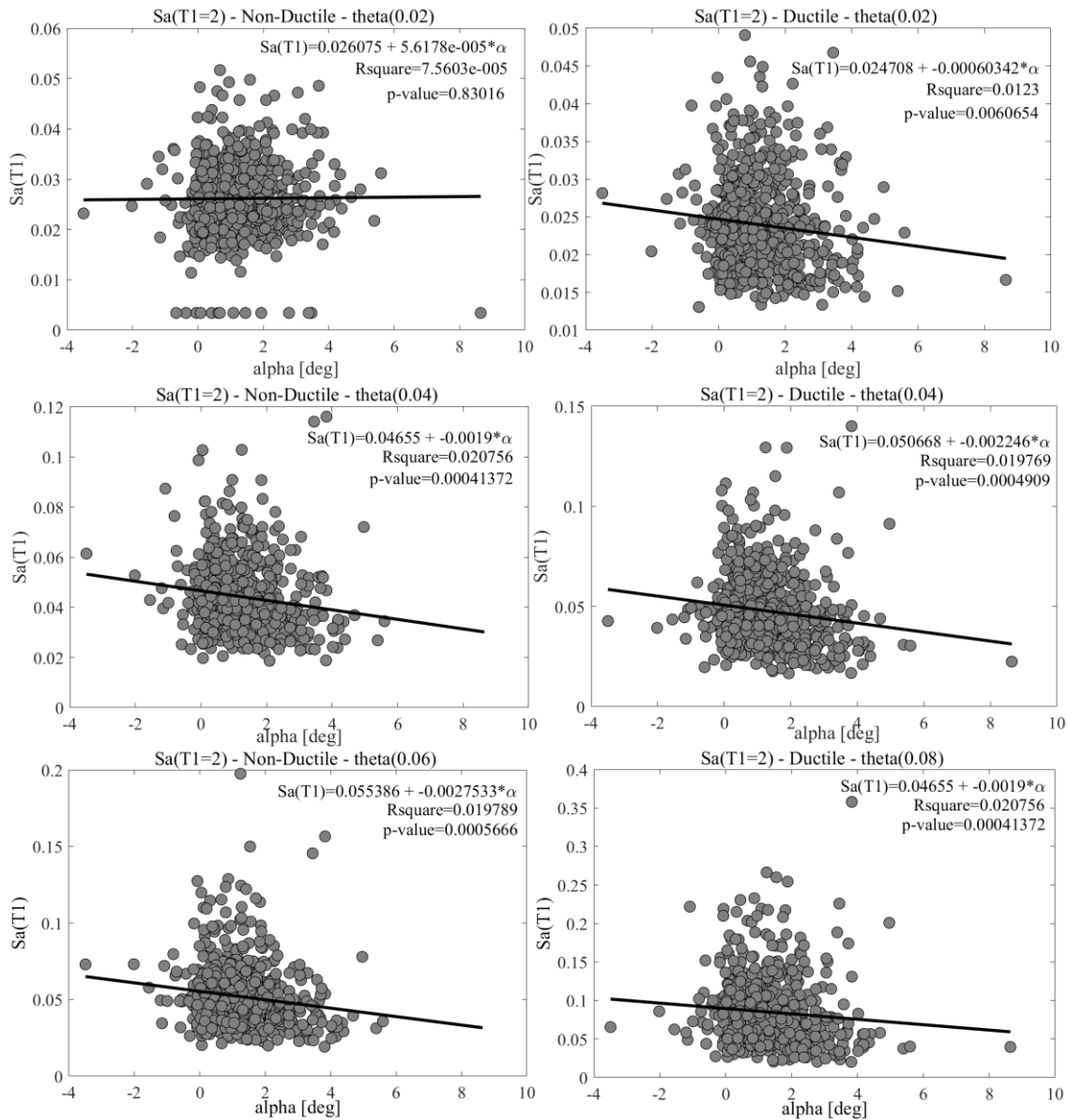


Figure 5-25 Linear regressions between the  $S_a(T1)$  and  $\alpha$  of MIP for periods  $T=2$  s for Non-Ductile and Ductile.  $S_a(T1)$  is obtained interpolating the results at  $\theta_{max}=6\%$  Non-Ductile and  $\theta_{max}=8\%$  for Non-Ductile and Ductile.

To quantify further, in practical terms, the significance of the influence of  $\alpha$  to the IM-EDP relationship at near collapse, the variation of  $IM|_{\theta_{max}}=0.06$  for the non-ductile system and of  $IM|_{\theta_{max}}=0.08$  for the ductile system for an assumed/imposed difference of  $\alpha$  ( $\Delta\alpha$ ) equal to  $2^\circ$  are reported in Table 5-2 for both  $Sa(T_1)$  and AvgSa considered and for all SDOF systems. It is clearly seen that the influence of  $\alpha$  is important across the board. Interestingly, it is observed that this influence is more important for the ductile structure which is, again, intuitively expected as ductile structures are more likely to act as band-pass filters near collapse thus preserving more faithfully input/output MIP resemblance. More importantly, it is seen that the influence of  $\alpha$  reduces through the use of AvgSa as opposed to  $Sa(T_1)$ : this reduction is reported as percentage in brackets in Table 5-2. This observation is also expected as AvgSa accounts for period elongation effects better than  $Sa(T_1)$  while these effects are well-related to  $\alpha$  as one appreciates by Fig.3-20. It also explains that the well-known improved efficiency of AvgSa over  $Sa(T_1)$  can be attributed to the fact that AvgSa appears to be more sufficient with respect to  $\alpha$  than  $Sa(T_1)$ .

Table 5-2  $\Delta Sa(T_1)$  results for  $\Delta\alpha = 2^\circ$

$\Delta\alpha$	$T$	Structural System			
		Non-Ductile SDOF		Ductile SDOF	
		$\Delta Sa(T_1)$	$\Delta Sa(T_1)/\Delta\alpha$	$\Delta Sa(T_1)$	$\Delta Sa(T_1)/\Delta\alpha$
$2^\circ$	0.5s	0.04 g	0.020 g/deg	0.14 g	0.07 g/deg
$2^\circ$	1s	0.030 g	0.015 g/deg	0.07 g	0.035 g/deg
$2^\circ$	1.5s	0.008 g	0.004 g/deg	0.016 g	0.008 g/deg
$2^\circ$	2s	0.006 g	0.003 g/deg	0.0038 g	0.0019 g/deg

Still, the dependence of  $AvgSa|_{\theta_{max}}$  on  $\alpha$  is significant especially since a difference of  $2^\circ$  in  $\alpha$  is not large given that the range of  $\alpha$  of about 90% of the GMs in the considered GM set is within  $[0^\circ 4^\circ]$ . One may be tempted to compare the influence of  $\alpha$  across oscillators with different  $T_1$  (varying stiffness) by looking at Table 5-2. However, it should be noted that these results may be misleading as they don't take into account that structures with different periods may have higher or lower elastic response spectra  $S_{ay}$ . To this end, Figure 5-26 to Figure 5-32 and Table 5-3 present the same IDA results as before but with re-scaled normalised IM  $R$  (FEMA 2009). It is found that the ratio between the force reduction and alpha ( $\Delta R/\Delta\alpha$ ) increases with the increase of the period, meaning that stiffer structures are less sensitive to a variation of the frequency content of GMs than more deformable ones. It is also interesting to note that this variation is influenced by the post-yield stiffness and the ductility. Notably, the same dependency from the fundamental period of the structure, has been found for the force-displacement capacity

boundaries from the IDA curves before documented and in accordance with FEMA 440a (FEMA P440A 2009).

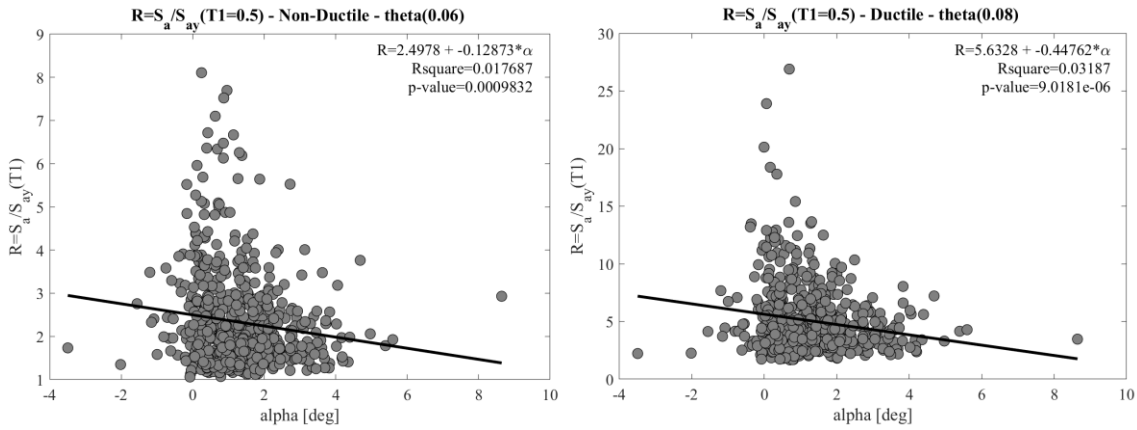


Figure 5-26 Linear regressions between the R and  $\alpha$  of MIP for periods  $T=0.5s$ , Non-Ductile and Ductile. R is obtained interpolating the results at  $\theta_{max}=6\%$  for Non-Ductile and  $\theta_{max}=8\%$  for Ductile.

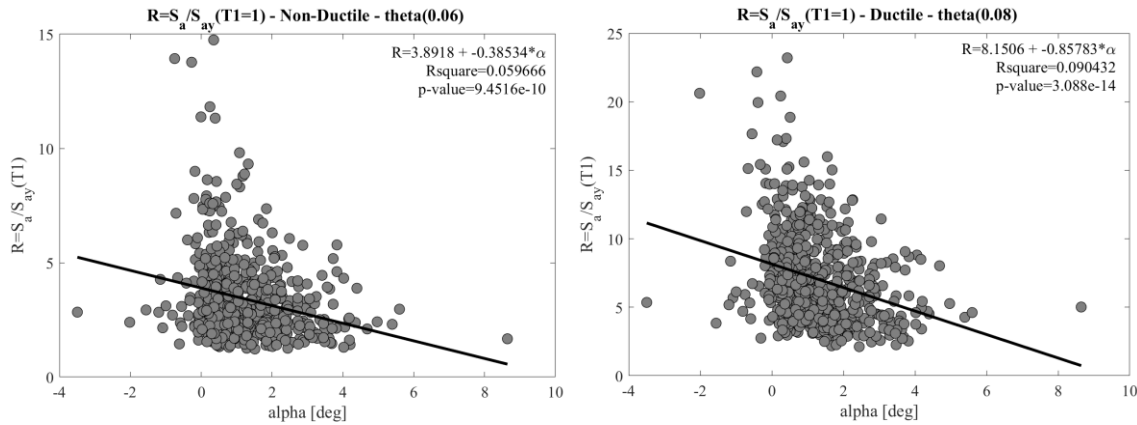


Figure 5-27 Linear regressions between the R and  $\alpha$  of MIP for periods  $T=1s$ , Non-Ductile and Ductile. R is obtained interpolating the results at  $\theta_{max}=6\%$  for Non-Ductile and  $\theta_{max}=8\%$  for Ductile.

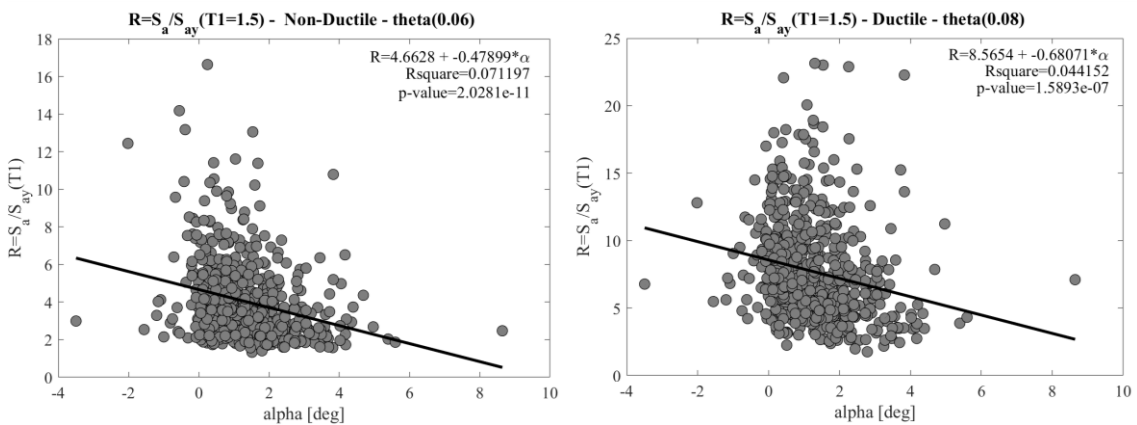


Figure 5-28 Linear regressions between the R and  $\alpha$  of MIP for periods  $T=1.5s$ , for Non-Ductile and Ductile. R is obtained interpolating the results at  $\theta_{max}=6\%$  for Non-Ductile and  $\theta_{max}=8\%$  for Ductile.

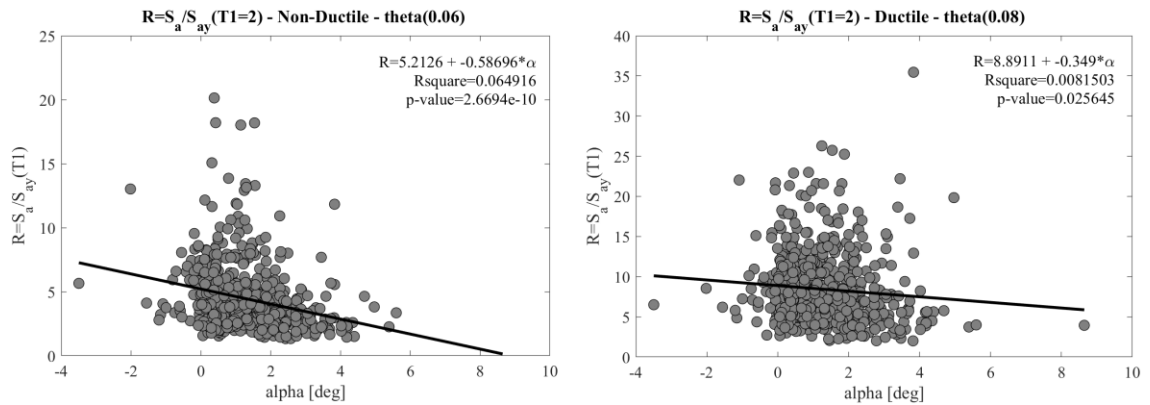


Figure 5-29 Linear regressions between the R and  $\alpha$  of MIP for periods T= 2s for Non-Ductile and Ductile. R is obtained interpolating the results at  $\theta_{max}=6\%$  for Non-Ductile and  $\theta_{max}=8\%$  for Ductile.

Table 5-3  $\Delta R$  results for  $\Delta\alpha = 2^\circ$

$\Delta\alpha$	T	System			
		Non-Ductile		Ductile	
		$\Delta R$	$\Delta R/\Delta\alpha$	$\Delta R$	$\Delta R/\Delta\alpha$
$2^\circ$	0.5s	0.26	0.13	0.90	0.45
$2^\circ$	1s	0.77	0.385	1.71	0.85
$2^\circ$	1.5s	0.96	0.479	1.36	0.68
$2^\circ$	2s	1.17	0.58	0.7	0.35

Indeed, it has been observed (Li et al, 2016) that low amplitudes components of GMs (normally present at the end of most earthquakes) may produce a relatively large response to elastic structures, especially for such structures whose fundamental frequency may tune in with the broadband frequency content of the GMs. As noted previously this phenomenon can play a significant role when considering non-linear systems whose natural periods varying overtime (elongated period). Such response is supported by the fact that the predominant periods (Fourier-based Mean period  $T_m$ ) of the GMs considered range between 0.2s to 1.5s with a large number of records between 0.3s to 0.9s (refer to Figure 4-4). This may imply a presence of a “resonant” effect which may magnify the influence of  $\alpha$  to the SDOF considered.

Comparison  $\beta$ -values, ductile - non-ductile SDOF

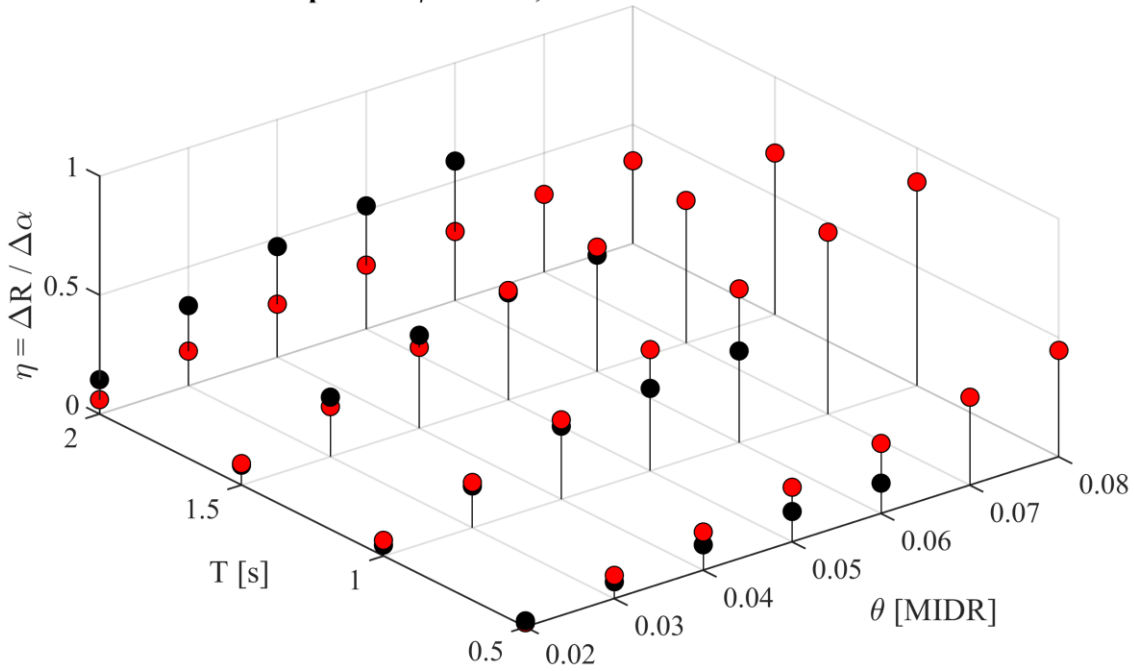


Figure 5-30 Comparison  $\eta$  slope values, for different condition of T (s) and  $\theta$  – 3D view

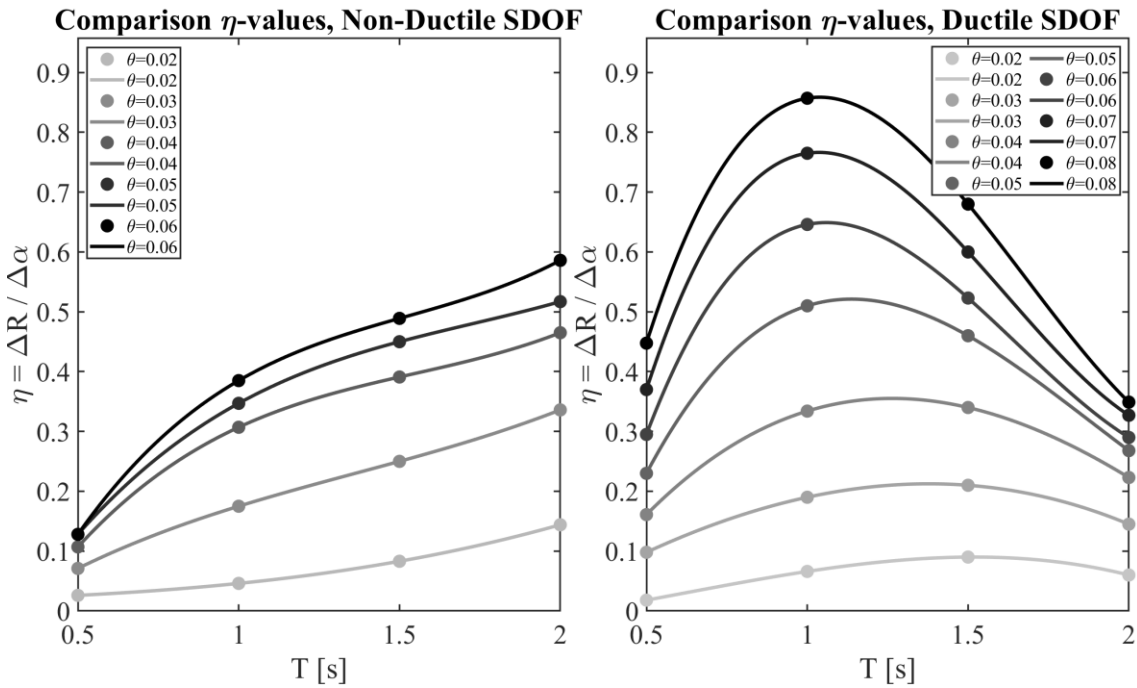


Figure 5-31 Comparison  $\eta$  slope values, for different condition of T (s) – 2D view

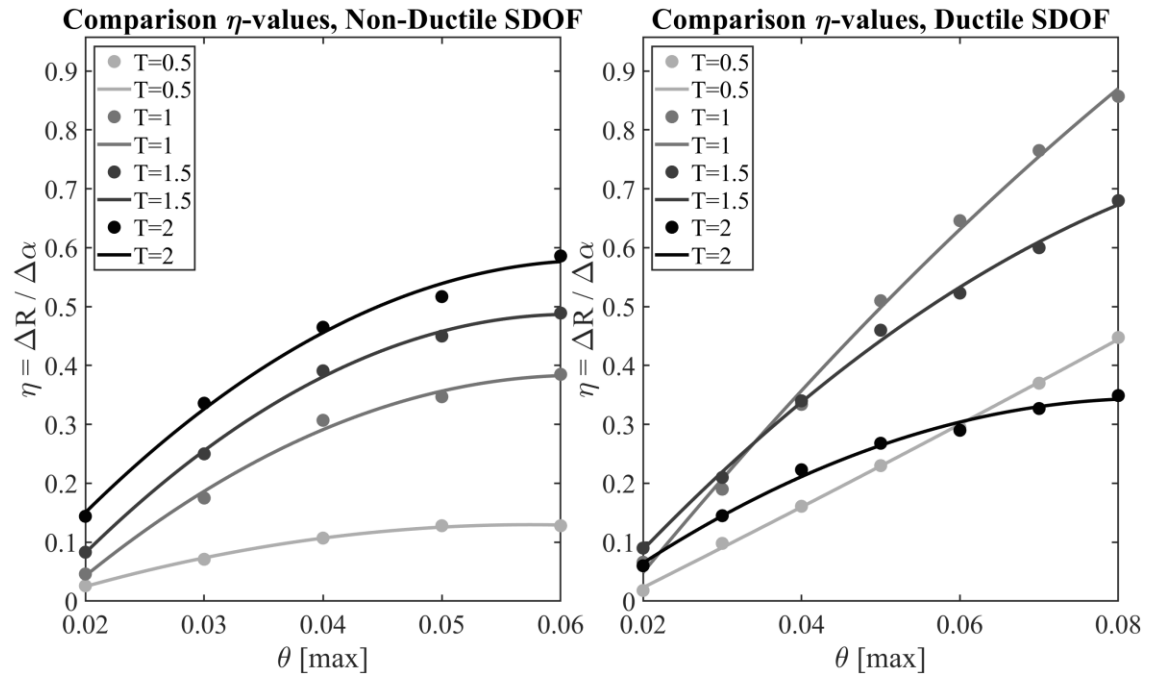


Figure 5-32 Comparison  $\eta$  slope values, for different condition of  $\theta$  – 2D view

From the slope values of the regression plots between  $\alpha$  and R, it appears evident that the influence of  $\alpha$  on the response of the system depends on the period of the structure and on the ductility/post stiffness as shown in Figure 5-27 and Figure 5-28. For the Non-Ductile SDOF the variation of the normalised intensity measure (R) with  $\alpha$  increases with its flexibility. However, for stiff structures ( $T_1=0.5s$ ) the rate of the variation of  $\alpha$  with R is statistically insignificant especially for limit states close to linear behaviour. On the contrary, for ductile structures the variation of R is substantial, even for short period structures (close to collapse limit state), and reach its maximum for intermediate period structures (between  $T_1=1s$  and  $T_1=1.5s$ ). Interesting to note is that the effect of  $\alpha$  on R for the ductile long period structure ( $T_1=2s$ ) is almost the same as for the stiff ductile structure ( $T_1=0.5s$ ). Meanwhile, for the non-ductile structures the influence of  $\alpha$  grows monotonically with period and, eventually, it becomes more important compared to the ductile structures for the long period ( $T_1=2s$ ).

## 5.6 Concluding Remarks

The capability of a single degree of freedom (SDOF) to “simply describe” complex phenomena has been proven, in this chapter, as key to describe the influence of the mean variation of GMs frequency content ( $\alpha$ ) to the collapse performance of “idealised” structures. These final plots have shown how the impact of  $\alpha$  varying with Period (T) and EDP ( $\theta$  [max]), investigating how post-yield behaviour and  $\alpha$  are correlated, comparing two SDOF with different ductility systems. The discussion was focused on how ductile and non-ductile, rigid and flexible structures, are influenced by  $\alpha$  introducing the variation of the normalised intensity measure (R) to quantify the behaviour of the systems. It has been seen that for ductile structures the variation of R is substantial, both for short and long period structures, attaining the peak for medium period structures which seemed to be more likely to be strongly affected by the mean variation of GMs frequency content. In addition, it has been investigated the effect of “elongated period” captured by a more sophisticated IM (AvgSa(T1)) to better take into account the influence of softens under seismic degradation and inelastic conducts. In the next chapter these behaviours will be investigated with MDOF systems to account for the correlation between higher modes and  $\alpha$  on the estimation of the structural collapse capacity of “real” structural systems.

The following Chapter extends the above analysis of the influence of  $\alpha$  to the IM-EDP relationship and, thus, of the non-stationary frequency content to hysteretic structural response in the context of PBEE by examining MDOF inelastic structures as well as considering significantly more rigorous record selection in order to isolate the potential influence of  $\alpha$  from spectral shape. The latter consideration is deemed important as it was observed in Table 6-4 that AvgSa, an IM that accounts for spectral shape to some extent, is less influenced by variations to  $\alpha$  compared to Sa(T<sub>1</sub>).



## Chapter 6

Influence of Non-Stationary Frequency

Content of GMs to Seismic Demands of

Inelastic Multi-Degree of Freedom System

## 6 Preliminary Remarks

The main aim of this Chapter is to quantify the influence of the average non-stationary GM frequency content, as captured by  $\alpha$ , to peak inelastic seismic demands of multi-degree-of-freedom (MDOF) inelastic models representing multi-storey building structures which yield under seismic excitation with progressively increasing intensity. In this regard, this chapter extends the numerical work of the previous Chapter by considering IDA results for MDOF inelastic systems as opposed to SDOF systems. Recognising the added complexity in demonstrating the influence of  $\alpha$  for MDOF systems due to the presence of several modes, a significantly more rigorous GM record selection procedure is herein employed which accounts for response spectral shape of GMs through the concept of spectrally equivalent GMs (Chamohandran et al. 2015). Selected records are also checked against a number of important GM properties, further to spectral shape, known to influence hysteretic structural response of MDOF structures including  $T_m$  (Rathje et al. 1998) and the effective duration (Chamohandran et al. 2015). Moreover, an extended version of AvgSa compared to the one used in the previous chapter is considered as IM to establish IM-EDP relationships through IDA which accounts for a large number of spectral acceleration values with periods longer and shorter than  $T_1$ . As in the previous Chapter, the presentation begins with a brief description of two benchmark inelastic (lumped plasticity) MDOF structural models representing a relatively flexible 7-storey reinforced concrete moment resisting frame structure and a stiffer 3-storey steel moment resisting frame. Then, record selection process and IMs considered in applying IDA to the two MDOF models are detailed. Finally, numerical results quantifying the influence of  $\alpha$  to peak inelastic demands for the MDOF systems are presented and discussed.

### 6.1 Description and modelling of adopted inelastic MDOF systems

Throughout this chapter two different inelastic MDOF models corresponding to buildings with different material properties and number of stories are considered to investigate the influence of  $\alpha$  on seismic structural response/performance of typical MDOF systems. The first relatively flexible model corresponds to a 7-storey reinforced concrete moment-resisting frame building (7RCMRF), developed as a benchmark structure by Kazantzi and Vamvatsikos (2015) to study seismic loss in large building stocks at the urban/city level. The second model is overall stiffer and corresponds to a benchmark low-rise 3-storey steel moment resisting frame (3CBF) developed as part of the EU-funded INNONSEIS project (INNONSEIS, 2017) investigating seismic structural response of buildings equipped with energy dissipation devices. Both structures are designed to contemporary (post-1980) seismic design provisions for high-seismicity regions. In

the following two sub-sections the overall geometry of the structures is provided together with some brief notes on assumptions made for their nonlinear finite element (FE) modelling.

### 6.1.1 Nonlinear modelling considerations of flexible benchmark 7-storey reinforced concrete building

A plan-symmetric 7-story reinforced concrete moment-resisting frame building shown in Figure 6-1 (Kazantzi and Vamvatsikos 2015) is herein employed as a case-study to illustrate the influence of the evolving GM frequency content as captured by  $\alpha$  to structural response of relatively flexible modern structures with good ductility capacity. The building does not correspond to any single structure, rather its features have been specified by Kazantzi and Vamvatsikos (2015) based on a statistical data from a large number (263) of actual post-1980 designed reinforced concrete moment-resisting frame buildings located in California gathered by Porter and Cho (2013). In this respect, it makes a benchmark structure representative of modern ductile flexible reinforced concrete buildings. The perimetric planar three-bay planar frame of the considered benchmark building indicated in Figure 6-1 is isolated from the structure and modelled by a nonlinear finite element (FE) model developed in OpenSees simulation platform (McKenna and Fenves 2001). The FE model represents nonlinear behaviour by lumped plasticity beam-column elements having hinge properties determined by the empirical equations proposed by Panagiotakos and Fardis (2001) for reinforced concrete members which account for geometric nonlinearity in the form of P- $\Delta$  effects. The moment  $M_y$  at yielding of the tension steel is computed from linear elastic analysis. Then, the corresponding chord rotation,  $\theta_y$ , is determined by the expression (Panagiotakos and Fardis 2001)

$$\theta_y = \frac{\phi_y L_s}{6} + 0.0025 + 0.25 \cdot d_b \cdot \frac{f_y^2}{E_s (d - d') \sqrt{f'_c}} \quad (6.1)$$

in which  $\phi_y$  is the yield curvature (computed from first principles),  $L_s$  is the length of the member,  $d_b$  is the mean diameter of tension reinforcement,  $(d - d')$  is the distance between the tension and compression steel and  $f_y$ ,  $E_s$  and  $f'_c$  (all in MPa) are the yield strength, elastic modulus of longitudinal steel and the concrete strength, respectively. Further, the ultimate chord rotation  $\theta_u$  is given as (Panagiotakos and Fardis 2001)

$$\theta_u = a_{st} a_{cyc} \left(1 + \frac{a_{s1}}{2.3}\right) (0.2^v) \left(\frac{\max(0.01, \omega_2)}{\max(0.01, \omega_1)} \cdot f'_c\right)^{0.275} \left(\frac{L_s}{h}\right)^{0.45} 1.1^{100\alpha\omega_{wx}} \cdot 1.3^{\rho_d} \quad (6.2)$$

where:

- $a_{st}$  and  $a_{cyc}$  are parameters related to the steel grade of longitudinal bars and to the type of loading, respectively, the first taken equal to 0.015 and the second taken equal to 0.6 for cyclic loading;
- $a_{s1}$  is a parameter for the slip of longitudinal bars taken equal to 0 for non-slippage;
- $\nu = \frac{N}{A_c f_c}$  is the axial load ratio taken positive for compression;
- $\omega_1, \omega_2$  are the mechanical reinforcement ratios;
- $f'_c$  is the uniaxial concrete strength in MPa;
- $\left(\frac{L_s}{h}\right) = \frac{M}{Vh}$  is the shear span ratio at the member end;
- $\omega_{wx} = \frac{A_{sx} f_{yw}}{b_w s_h f'_c}$  is the ratio of transverse steel parallel to the direction of loading;
- $\alpha$  is the confinement effectiveness ratio; and
- $\rho_d$  (%) is the steel ratio of any reinforcement placed in each diagonal direction of the member.

The secant-to-yield stiffness of a member in antisymmetric bending is determined by

$$EI = \frac{L_s}{6} \cdot \frac{M_y}{\theta_y} \quad (6.3)$$

The first pre-yield natural period of the FE model is  $T_1 = 1.60s$  and modal damping value of 5% for the first mode is set which is typical for concrete structures.

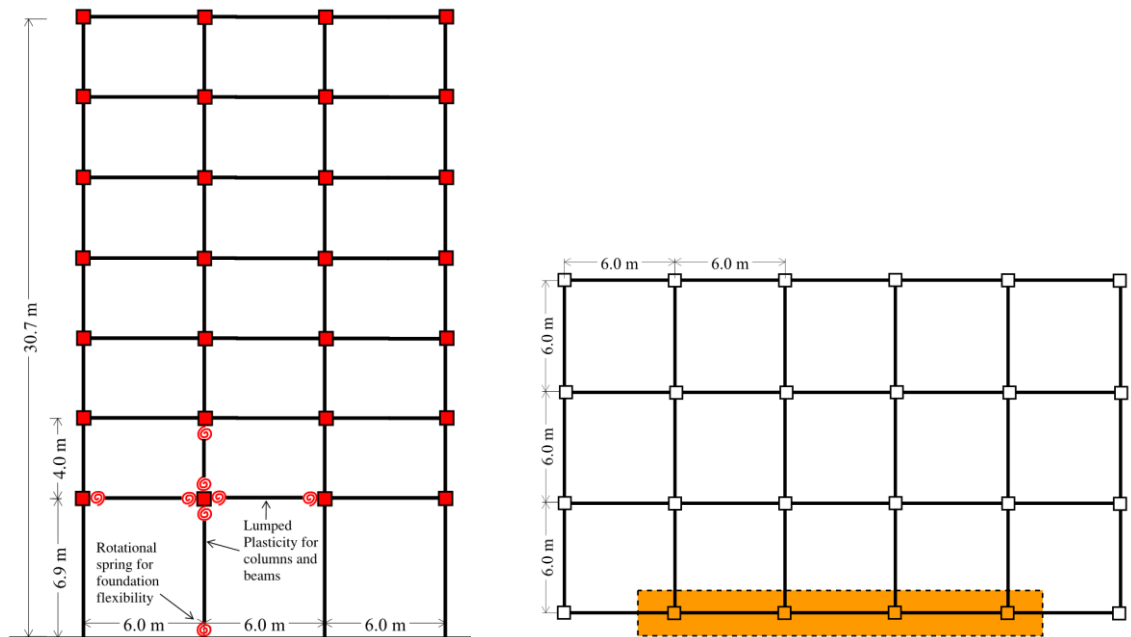


Figure 6-1 Generic model idealization of the perimeter RCMRFs with typical plan view with perimeter stability frames (Kazantzi and Vamvatsikos 2015)

### 6.1.2 3-storey Concentrically-Braced Frame Building

As a case-study of a relatively stiff modern structure, a symmetric 3-storey steel building with lateral load-resisting system consisting of concentrically X-braced frames with each brace extending between two consecutive floors is further adopted. The structure has been designed to the current European seismic code provisions (CEN 2004) for ductility class high,  $PGA=0.24g$  and ground type B (stiff soil) as part of the research programme INNOSEIS (2017). The geometric properties of the building are shown in Figure 6-2. A 3-storey 4-bay perimeteric planar frame of the structure is modelled with fundamental natural period of the structure is  $T_1=0.55s$ , that is, about three times shorter compared to the previous model of the 7-storey reinforced concrete frame structure.

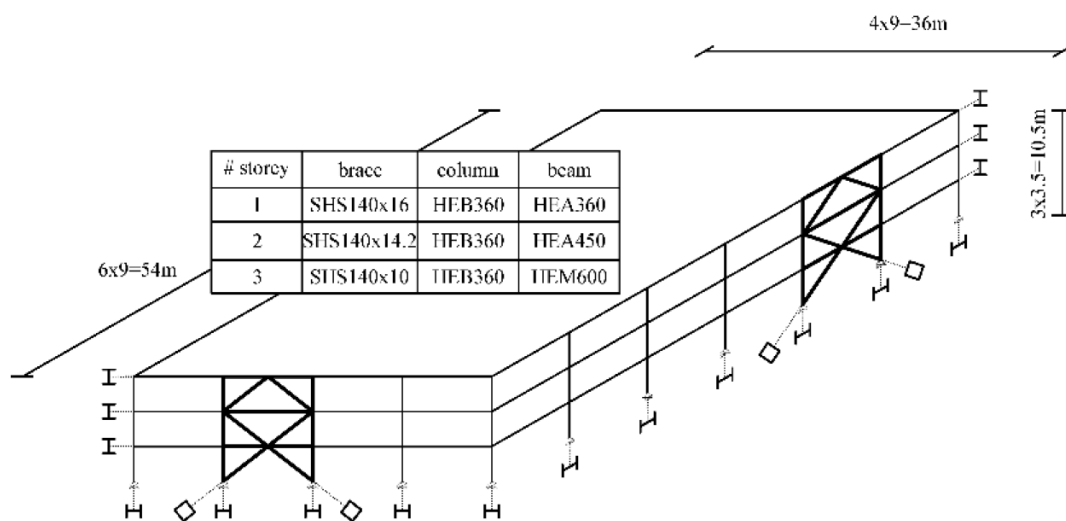


Figure 6-2 Case study 3-storey steel frame concentrically braced building (INNOSEIS, 2017)

Nonlinear fibre elements have been incorporated in the modelling of the 3-storey frame in OpenSees. For material specification the Steel02 material based on Menegotto Pinto (Menegotto and Pinto 1973) from the OpenSees (Steel02 n.d.) library is adopted with a steel Young's modulus  $E_0=210GPa$ , the yield strength  $f_y = 1.2 \cdot 355 = 426MPa$ , a strain-hardening ratio (ratio between post-yield tangent and initial elastic tangent)  $b=0.3\%$ . To control the transition curve and allow a good representation of pinching effects, the following functional curvature  $R$  is used to take into account strain reversal (Filippou, et al. 1983)

$$R(\xi) = R_0 - \frac{a_1 \cdot \xi}{a_2 + \xi} \quad (6.4)$$

where  $\xi$  is normalised strain as shown in Figure 6-3. The parameters appearing in the last equation are set to  $R_0 = 20, a_1 = 0.925, a_2 = 0.15$  based on experimental testing (INNOSEIS 2017). Then, the following stress-strain relationship is defined in terms of the functional  $R$  (Filippou, et al. 1983)

$$\sigma^* = b \cdot \varepsilon^* + \frac{(1 - b) \cdot \varepsilon^*}{[1 + \varepsilon^{*R}]^{\frac{1}{R}}} \quad (6.5)$$

where

$$\sigma^* = \frac{\sigma}{\sigma_y}, \quad \varepsilon^* = \frac{\varepsilon}{\varepsilon_y} \quad (6.6)$$

In the model, second-order P- $\Delta$  geometric transformation is considered for all beams and columns using a standard leaning column approach.

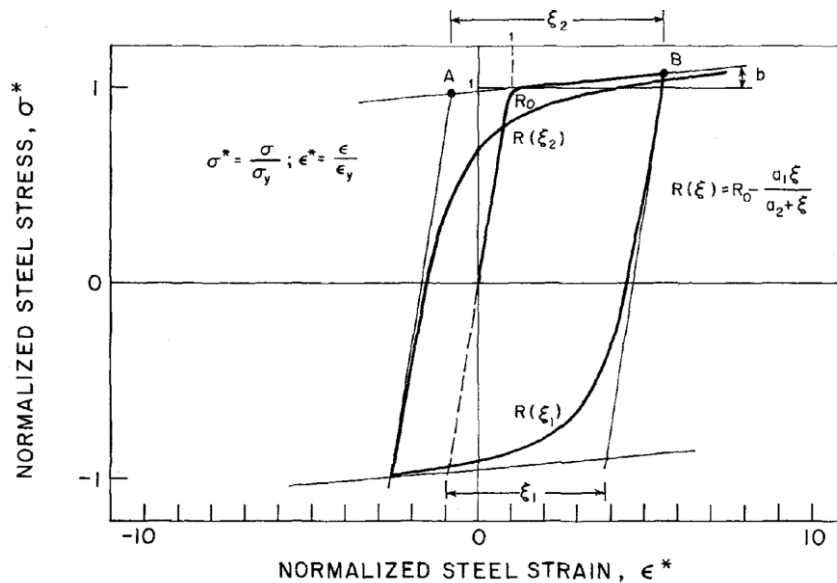


Figure 6-3 Definition of curvature parameter  $R(\xi)$  in Menegotto-Pinto Steel Model (Filippou, et al. 1983)

## 6.2 Construction of spectrally-equivalent GM ensembles with different range of $\alpha$ values

As extensively discussed in Chapters 2 and 5, an important issue in establishing IM-EDP relations and, ultimately, to predict reliably the structural collapse capacity using recorded GMs in the

context of IDA is to properly select GMs based on properties beyond seismological parameters (M,R) that affect highly nonlinear/hysteretic response behaviour. This is especially true in case of modelling real-life buildings through inelastic models with several DOFs. In this regard, it is well-known that the shape of GM linear response spectrum, hereafter spectral shape, influences significantly the peak inelastic response of yielding structures for fixed  $S_a(T_1)$  values (e.g., Baker and Cornell 2006), due to its influence to the multiple natural modes of MDOF systems. It is, therefore, deemed herein essential to separate, as much as possible, the GM spectral shape from  $\alpha$  during the record selection: a task which is intuitively feasible since the spectral shape is a “stationary metric” independent from non-stationary frequency content trends (i.e., it is possible that two recorded GMs with very different time-varying frequency content trends and, therefore,  $\alpha$  value attain the same or very similar spectral shape) To this aim, the concept of *spectrally equivalent* GM ensembles introduced by (Chandramohan, Baker and Deierlein 2015) is herein adopted having closely matched average response spectrum though potentially different GM properties not related to the spectral shape. In this regard, Chandramohan, et al. (2015) constructed spectrally equivalent GM ensembles with different average effective duration,  $D_{S5-95}$ , to study the effect of GM duration to the seismic response of structures.

Herein, the same record selection algorithm proposed by Chandramohan, et al. (2015) is used to construct two spectrally equivalent ensembles of 50 GMs each from a large GM database: one ensemble with relatively high average  $\alpha$  value, hereafter high- $\alpha$  set, and one with relatively low average  $\alpha$  value, hereafter low- $\alpha$  set. This is achieved by taking the following steps.

First, a set of 611 pairs of GM recordings (i.e. two horizontal components) from 30 different seismic events with magnitude range  $6.5 < M < 8$  and distance-to-rupture plane range  $20\text{km} < R_{\text{rup}} < 120\text{km}$  is retrieved from the PEER NGA-West2 Ground Motion Database (<http://ngawest2.berkeley.edu/>) listed in Table A-3 of the Appendix A. Then, the angle  $\alpha$  of each adjusted GM signal is computed using the MIP computed from Morlet CWT spectrograms as detailed in previous Chapters. It is found that 103 GMs (i.e., less than 9% of the total  $611 \times 2 = 1222$  GMs considered) attain a negative  $\alpha$ , that is, their average frequency content evolves from lower to higher frequencies in time. Careful examination of the Morlet wavelet spectra and the associated MIPs reveal that these GMs are characterized by the late arrival of significant bursts of energy with relatively high frequencies compared to the early mean frequency content observed. Such time-varying frequency content trends are non-typical. Consequently, the 103 GMs with  $\alpha < 0$  are regarded as “outliers” for the purposes of the current study and are discarded from the GM database.

Next, the high- $\alpha$  set is constructed by taking the 50 GMs with the highest  $\alpha$  values from the above GM database. Subsequently, the low- $\alpha$  set is constructed by choosing 50 GMs out of half the

GMs of the original database with the lowest positive  $\alpha$  value possessing equivalent spectral shapes with the GMs of the high- $\alpha$  set on an individual record-by-record basis. This is accomplished through a “greedy” matching-pursuit-like algorithmic process seeking to find for each GM of the high- $\alpha$  set a low- $\alpha$  GM that minimizes the sum of squared error differences of spectral ordinates for periods in the range of [0.1, 3.0]s (Chandramohan, et al. 2015) upon scaling of the low- $\alpha$  GM. In doing so, a scale factor of up to 5 is allowed, while it is ensured that no record appears twice in the low- $\alpha$  set. It is further important to recall that the  $\alpha$  index is *invariable to GM amplitude scaling* and thus the spectral matching algorithm retains the value of the unscaled  $\alpha$  GM property.

For illustration, Figure 6-4(a) plots the response spectra of a pair of spectrally equivalent GMs one belonging to the high- $\alpha$  set and one to the low- $\alpha$  set, while Figure 6-4(b) plots the ensemble mean response spectra of the two GM sets. The constructed sets achieve a quite satisfactory level of spectral equivalency across the targeted period range (i.e., 0.1s to 3s) and can be assumed to be “equal” on the average in terms of spectral shape, even though the quality of spectral equivalency of the individual pairs may not be consistently good at all periods within the targeted range.

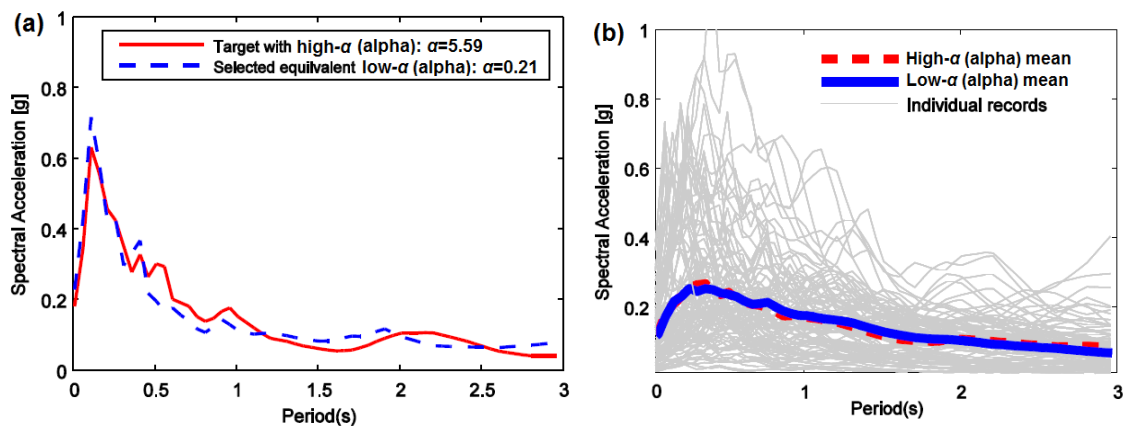


Figure 6-4 (a) Response Spectra of Two Spectrally Equivalent GMs (twins) with High And Low  $\alpha$  Values from San Fernando 1971 (Station: la Hollywood Stor Ff) and Landers 1992 (Station: Silent Valley, Poppet Flat) events, respectively: Low- $\alpha$  GM Scaled by 4.52, (b) Individual and Ensemble Mean Response Spectra of High- $\alpha$  and Low- $\alpha$  Sets.

Furthermore, Figure 6-5 provides  $\alpha$  value histogram of the GMs belonging to the high- $\alpha$  and to the low- $\alpha$  sets. It is seen that the two sets have significantly different  $\alpha$  values (the median  $\alpha$  of the high- $\alpha$  set is more than 5.5 times larger than the median  $\alpha$  of the low- $\alpha$  set) well-clustered together. It can be argued that the GMs of low- $\alpha$  set observe on average negligible change of frequency composition in time, while average frequencies in the high- $\alpha$  set vary at a fast rate from high to low frequencies. Clearly, the two sets lie at the two extreme ends of the range of  $\alpha$  values found in large database of as-recorded GMs putting aside negative  $\alpha$  values. Moreover, the

histogram of Figure 6-5 shows that the effective durations of the GMs in the two sets are not appreciably different and will not influence peak inelastic response of structures exhibiting insignificant cyclic degradation effects (Chandramohan, et al. 2015). Lastly, histograms of the GM mean period,  $T_m$ , computed by equation (2.5) are provided in Figure 6-6 for the two spectrally equivalent sets. It was deemed essential to probe into the statistics of  $T_m$  across the two sets since  $T_m$  and  $\alpha$  was shown to be statistically correlated in Section 4.2 while, as extensively discussed in Section 2.2,  $T_m$  is found to influence the response of yielding structures (Kumar et al. 2011, Katsanos et al 2014). Importantly, it is seen that although the two GM sets have significantly different  $\alpha$  their average in time stationary frequency content is very similar: the spread of the histograms in Figure 6-6 is comparable and the difference of the ensemble median values between the two sets is less than 15%.

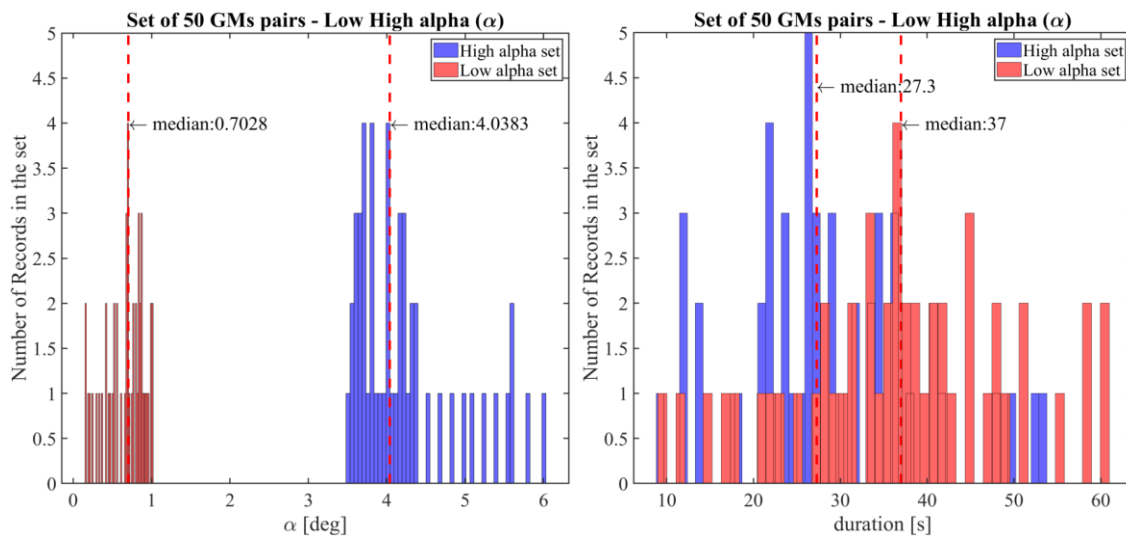


Figure 6-5 Histograms of the 50 high- $\alpha$  and 50 low- $\alpha$  sets for: (a) alpha,  $\alpha$ , values and (b) effective duration  $D_{S_{5-95}}$ .

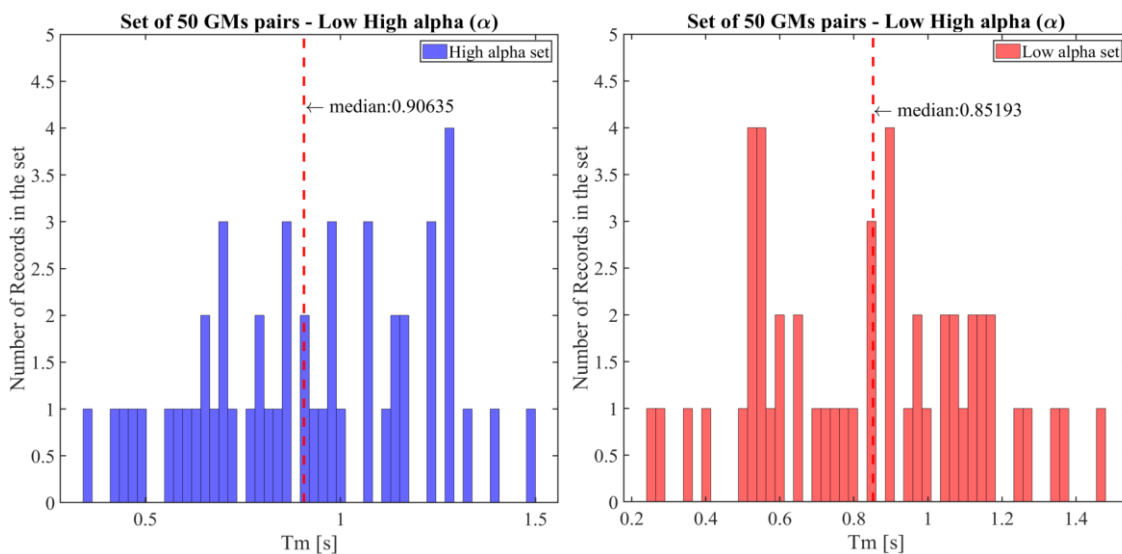


Figure 6-6 Histograms of the 50 high- $\alpha$  and 50 low- $\alpha$  sets for  $T_m$ , values.

Collectively, the numerical data in Figures 6-4 to 6-6 suggest that the two spectrally equivalent GM sets constructed as detailed in the previous section can be treated as “equal” in the mean/median sense in terms of spectral shape as well as  $T_m$  which are known to influence GM structural damage potential. Furthermore, it is noted that cyclic degradation is of little consequence for the two benchmark structures presented in Section 6.2. Thus, even though the median effective duration of the two GM sets show some differences in Figure 6-5, their effect on the response of the two benchmark structures is negligible (see also Chandramohan et al 2015). In this regard, if the two GM sets (high- $\alpha$  and low- $\alpha$ ) are used to conduct IDA for the two benchmark structures (results reported in the next sections) then  $\alpha$ , can be considered as the culprit for any differences found in the ensemble peak seismic response statistics. This is because the two sets are very different in terms of the rate by which their mean frequency content varies in time from high frequencies to lower frequencies as captured by  $\alpha$  (i.e., have been purposely and rigorously constructed to be quite biased in terms of  $\alpha$ ).

However, note that the above two GM sets comprise GMs that are spectrally similar in a *pairwise manner*. That is, each GM in one set has a “twin” GM, in terms of spectral shape, in the other set. Consequently, the difference of  $\alpha$  between twin GMs, though certainly significant as can be appreciated by the left-most histogram in Figure 6-5, is varying among twins/pairs. To this end, it is emphasised that, beyond ensemble IDA curves statistics, a more stringent statistical test to demonstrate the significance of the influence of  $\alpha$  is to probe into *pairwise statistics*. In the following section pertinent statistics and results interpretation for both ensemble-wise and pairwise statistics are furnished by post-processing IDA curves data obtained for the two benchmark structural models of Section 6.1 and for both high- $\alpha$  and low- $\alpha$  GM sets herein derived and discussed.

### 6.3 Quantification of $\alpha$ influence on IDA curves statistics from the spectrally-equivalent GM sets

#### 6.3.1 7-storey building: Numerical results

Standard IDA is applied to the case study 7-story building model discussed in Section 6.2.1 for the high- $\alpha$  and the low- $\alpha$  spectrally equivalent GM sets presented in Section 6.2. The standard Newmark time-integration algorithm with in-step average acceleration assumption presented in section 5.2 is used as implemented in Opensees. Figure 6-7 collects coloured-coded IDA curves obtained for the two GM sets using the  $Sa(T_1)$  as the IM and the max inter-storey drift (MIDR) along the height of the building frame as the EDP. Specifically, Figure 6-7(a) plots individual IDA curves, while Figure 6-7(b) summarizes these curves statistically. The high- $\alpha$  GM set

imposes significantly higher drift demands to the structure across a wide range of post-yield limit states. In particular, the high- $\alpha$  GM set induces a MIDR = 0.2 to the structure when scaled to 20% lower median  $Sa(T_1)$  compared to the low- $\alpha$  GM set. The difference of median  $Sa(T_1)$  between the two GM sets required to induce MIDRs  $\geq 0.4$  reaches up to 25%. Considering that the low- $\alpha$  GM set observes negligible evolution of the average frequency content compared to the high- $\alpha$  GM set, the numerical data in Figure 6-7 are in alignment with pertinent numerical results reported in the literature which compare stochastic GM models with and without non-stationarity in frequency content (e.g. Vetter and Taflanidis 2014).

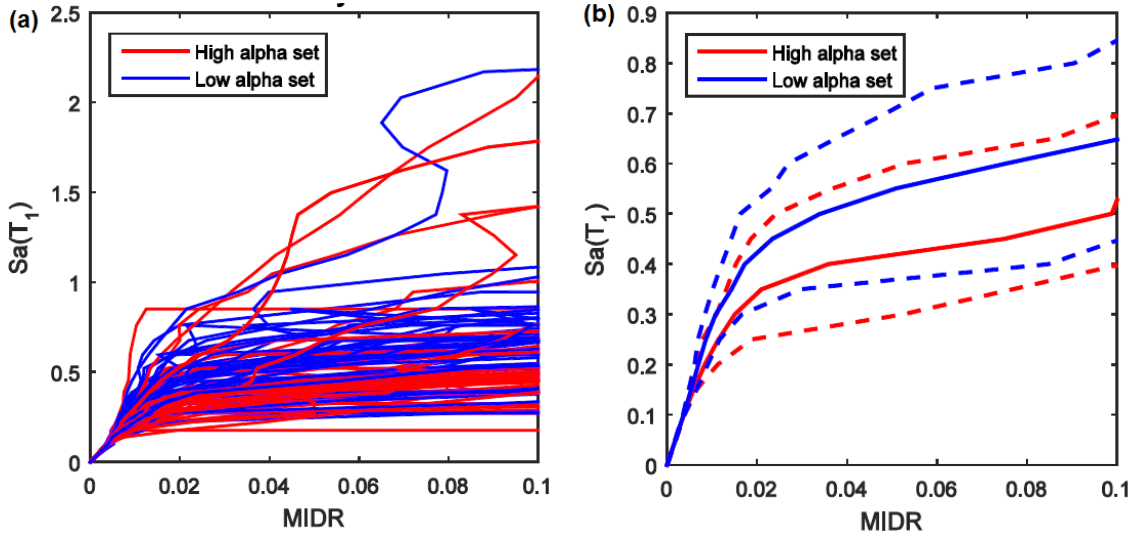


Figure 6-7 IDA Curves with respect to  $Sa(T_1)$  for High and Low  $\alpha$  Spectrally Equivalent Ensembles of 50 GMs: (A) Individual Curves; (B) Median (Solid Lines) and Median  $\pm 1$  Standard Deviation (Broken Lines) Ensemble Curves.

To further investigate the persistence of the influence of  $\alpha$  to the inelastic peak response demands in case one uses a more “advanced”, than the standard  $Sa(T_1)$ , IM in establishing IM-EDP relationship, the avgSa, whose capability to account for the effect of spectral shape to period elongation has been discussed in Section 5.3, is further considered. Herein, the avgSa IM is extended to encompass several different spectral ordinates as

$$\text{AvgSa} = \left( \prod_{j=1}^J Sa(T_j) \right)^{\frac{1}{J}}, \quad (6.7)$$

where  $J$  spectral ordinates are considered at  $T_j$  ( $j=1,2,\dots,J$ ) periods equally spaced in the range of [0.52s 2.4s] with an increment of 0.1s. Note that the lower bound of the considered range coincides with the second natural period of the structure (0.52s) while the upper bound is 50% larger from the fundamental structural natural period  $T_1=1.6s$ . In this respect, the IM in equation (6.7) was found to be more efficient and sufficient than  $Sa(T_1)$  as it accounts for period elongation phenomena not only in the first mode but also in higher modes of vibration (Kohrangi et al. 2016

and 2017). The IDA curves in Figure 6-7 are re-scaled in Figure 6-8 using the AvgSa in Eq.(6.7). It is seen by comparing Figure 6-7 and Figure 6-8 that the difference in the median IDA curves between the high- $\alpha$  and low- $\alpha$  sets remains significant from a seismic structural risk assessment perspective within the PBEE context. As discussed in Chapter 5 in view of results pertaining to SDOF structures, this observation manifests that the information on non-stationary frequency content trends carried by the  $\alpha$  index is not captured by the linear response spectral ordinates of GMs or by the spectral shape. In this case, this is confirmed for MDOF structures and it is verified by means of rigorously selected GMs based on the spectrally equivalency criterion.

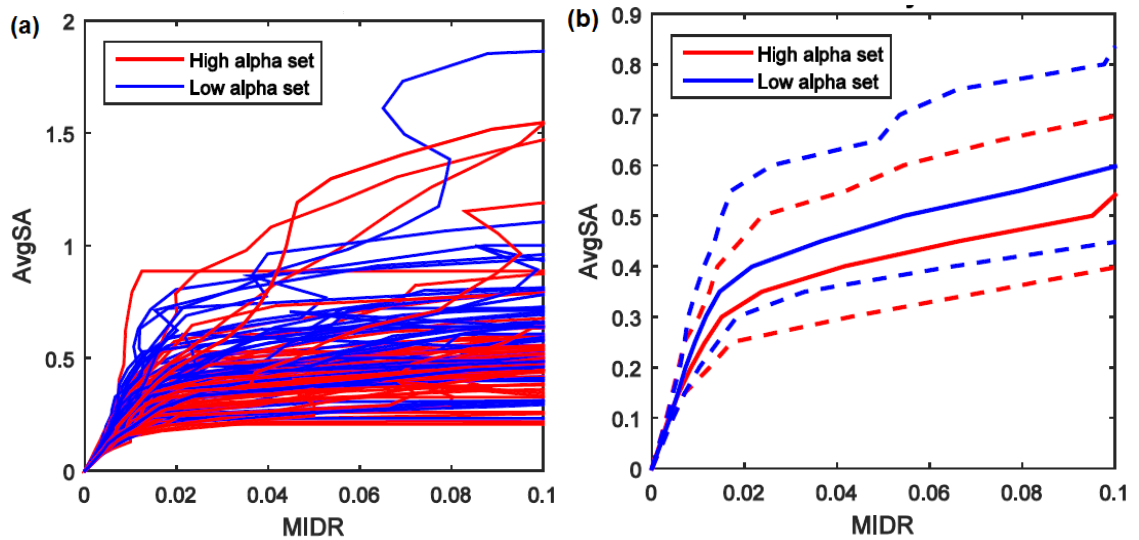


Figure 6-8 IDA Curves with respect to AvgSa for High and Low  $\alpha$  Spectrally Equivalent Ensembles of 50 GMs: (A) Individual Curves; (B) Median (Solid Lines) and Median  $\pm 1$  Standard Deviation (Broken Lines) Ensemble Curves.

Consequently, it is concluded that the time-evolving GM frequency content need be accounted for in undertaking IDA (and more generally NRHA) as it does influence the damage potential of GMs while the current state-of-art IMs cannot capture this influence for the considered structure. Further to the above results, *pairwise* boxplot statistics of IM|EDP (i.e.,  $Sa(T_1)|\theta_{max}$ ) ratios constructed between spectrally-equivalent GM twins coming from the high- $\alpha$  and low- $\alpha$  sets are computed in Figure 7-11. These have been constructed by taking ‘vertical stripes’ of IM values separately from the two GM sets at various interstorey drift levels (i.e., EDP or limit state values) all the way from (almost) linear behaviour to collapse. For each EDP, the ratio of IM|EDP values from each of the 50 twins (spectrally equivalent) GMs are computed to produce boxplot statistics.

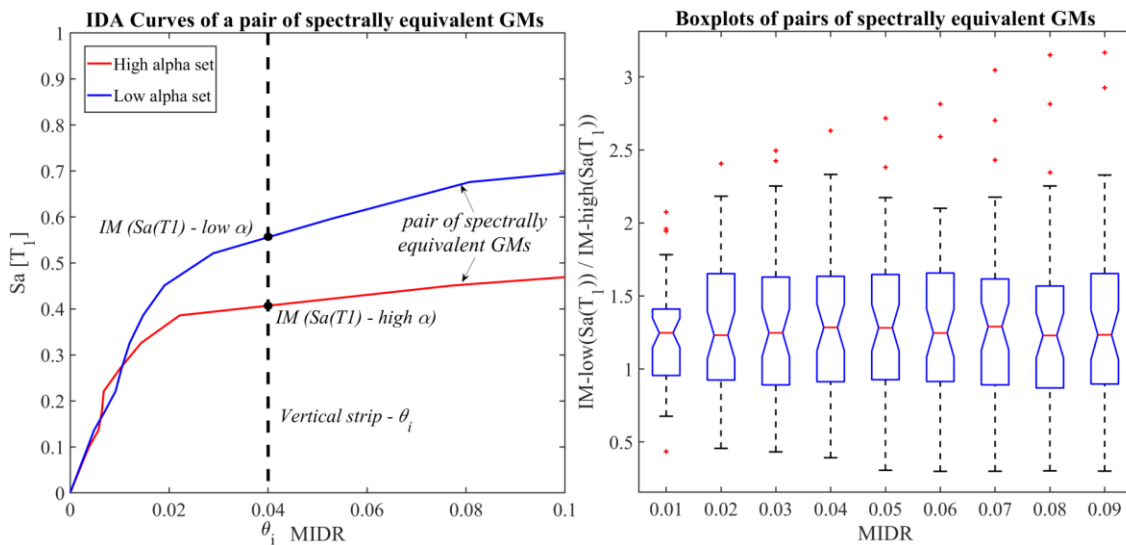


Figure 6-9 Vertical stripes on IDA curves and boxplots for 50 High and Low  $\alpha$  sets

In the boxplots, it is seen that the median of the ratios analysed is relatively constant with limit state MIDR values at about 1.25. In the median sense, the high- $\alpha$  member of the spectrally equivalent twin GMs induces 25% higher demand from the low- $\alpha$  across consistently across all limit states. Furthermore, the distribution/dispersion of these ratios (upper and lower quartiles indicated by the upper and lower limits of the boxes) is also generally consistent with EDP value except for ratios corresponding to the lowest value of  $\theta_{max}$  considered corresponding to elastic behaviour for which the ratios show significantly smaller dispersion. Most importantly, note that the lower quartile attains a value of about 1 suggesting that at least 75% of the GM spectrally equivalent twins with high  $\alpha$  have higher damaging potential than their low- $\alpha$  “brothers” with 95% confidence (statistically significance level). Note that, from a statistical viewpoint, the above boxplot-based results is the most stringent criterion that can be employed to demonstrate that the influence of  $\alpha$  to the IM-EDP statistics is significant with high confidence having “set aside”, statistically, all other known influencing factors: spectral shape,  $T_m$ , and effective duration as comparison is done against pairwise quantities rather than ensemble quantities.

Having established the importance of  $\alpha$  to IM-EDP relationship for the benchmark building considered, additional statistics are further provided in terms of IDA curves (i.e., without focusing onto spectral-equivalent GM twins statistics). This is done for a number of additional GM sets constructed from GM twins coming from the high- $\alpha$  and low- $\alpha$  sets based on different GM record selection criteria involving  $\alpha$ . The criteria are: (i) choice of 25 GMs from the high- $\alpha$  set with the *highest*  $\alpha$  and their twins from the low- $\alpha$  set; (ii) choice of 25 GMs from the high- $\alpha$  set and their twins from the low- $\alpha$  set with the *highest*  $\alpha$  difference; (iii) choice of 25 GMs from the high- $\alpha$  set and their twins from the low- $\alpha$  set with the *lowest*  $\alpha$  difference.

Table 6-1 Summary table of the GMs sets parameters

subset #	Description	Medians			Standard Deviations		
		Alpha	Duration	T <sub>m</sub>	Alpha	Duration	T <sub>m</sub>
1	50 Low alpha pairs, First 50 chosen with Highest Alphas	0.7028	37	0.856	0.2447	12.33	0.3005
2	50 High alpha pairs, First 50 chosen with Highest Alphas	4.0383	27.3	0.9065	0.6613	10.22	0.2833
3	25 Low alpha pairs, First 25 chosen with Highest Alphas	0.7730	36.1	0.8405	0.2467	10.79	0.8405
4	25 High alpha pairs, First 25 chosen with Highest Alphas	4.3945	26.7	0.9082	0.6168	10.01	0.9082
5	25 Low alpha pairs, First 25 chosen with Highest Difference between High Alphas and Low alphas	0.6128	36.10	0.8549	0.2693	12.18	0.3077
6	25 Low alpha pairs, First 25 chosen with Highest Difference between High Alphas and Low alphas	4.3945	26.4	0.9698	0.6721	11.07	0.3261

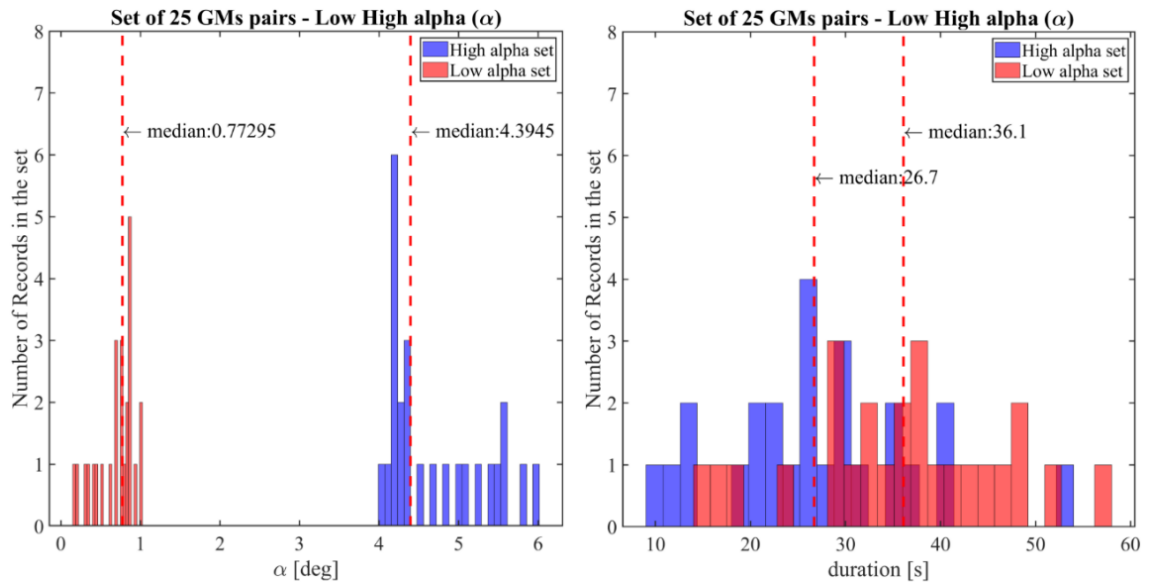


Figure 6-10 Histograms of the 25 high- $\alpha$  and 25 low- $\alpha$  sets for: (a) alpha,  $\alpha$ , values and (b) effective duration  $D_{S5-95}$ .

These sets are constructed from the subsets of GMs described in Table 6-1 in which set #1 is the low- $\alpha$  set and set #2 is the high- $\alpha$  set. Subset statistics with respect to important GM properties are included in the same table and relevant histograms are plotted in Figures 6-10 and 6-11.

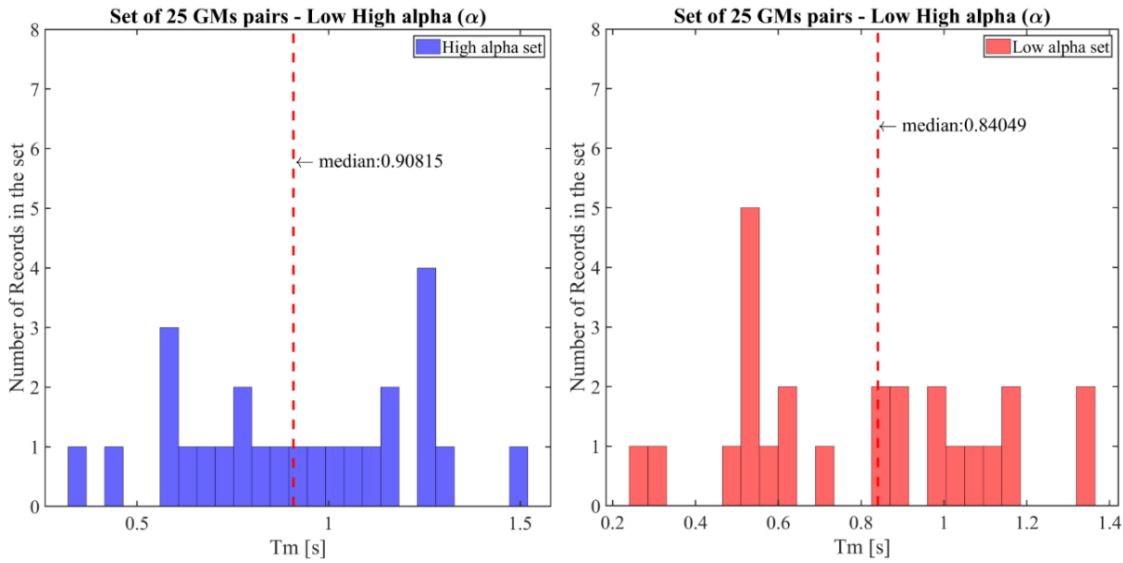


Figure 6-11 Histograms of the 25 high- $\alpha$  and 25 low- $\alpha$  sets for  $T_m$ , values.

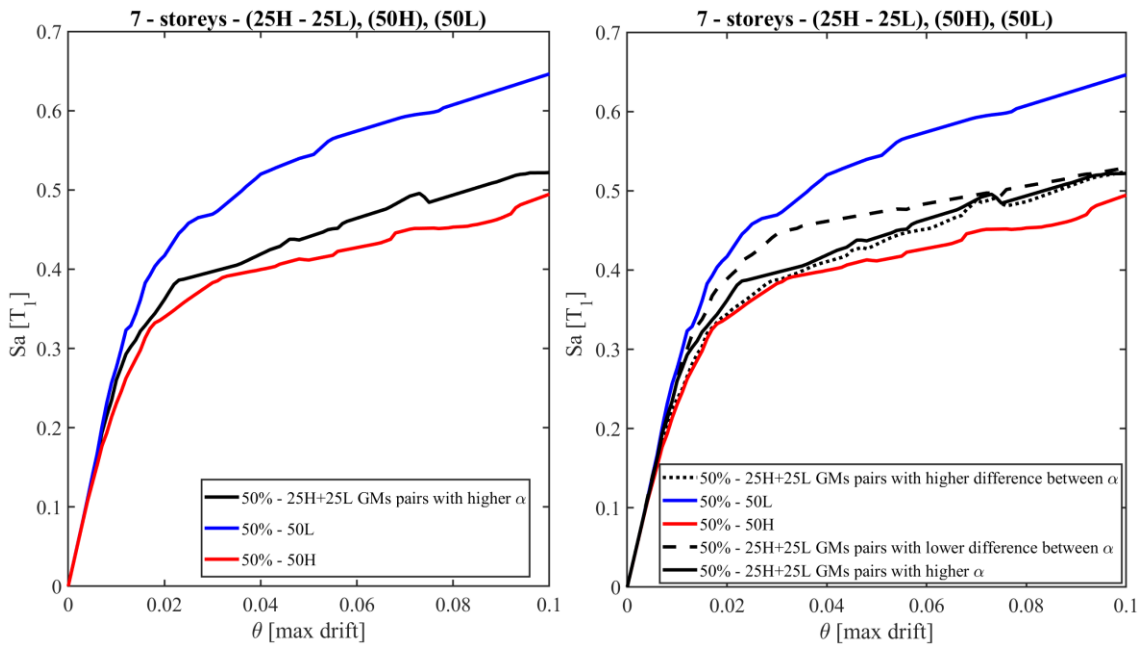


Figure 6-12 IDA curves comparisons for 25 High and Low  $\alpha$  sets (median curves)

Figure 6-12 plots median IDA curves for the three new mixed low- $\alpha$ /high- $\alpha$  GM sets based on the above selection criteria. Superimposed are the median IDA low- $\alpha$  and high- $\alpha$  curves. All three median IDA curves of the mixed GM sets lie always in between the median low- $\alpha$  and high- $\alpha$  curves with the mixed GM pairs set chosen on the basis of having higher  $\alpha$  difference being the closest to the low- $\alpha$  median curve. Lastly, Figures 6-13 and 6-14 probe into IDA curve statistics of the mixed GM sets vis-à-vis the high- $\alpha$  and low- $\alpha$  sets by examining the coefficient of variation (COV= standard deviation/mean). The variability of IDA curves of the mixed set based on the highest  $\alpha$  criterion lies in between the COV of the high- $\alpha$  and low- $\alpha$  sets (left panel of Figure 6-

13). Further the COV of mixed set based on the highest  $\alpha$  difference lies very close to COV of low- $\alpha$ . The smallest COV is observed based on the mixed GM set with criterion the lowest  $\alpha$  difference. Therefore, it appears that the last criterion reduces IDA curves variability significantly.

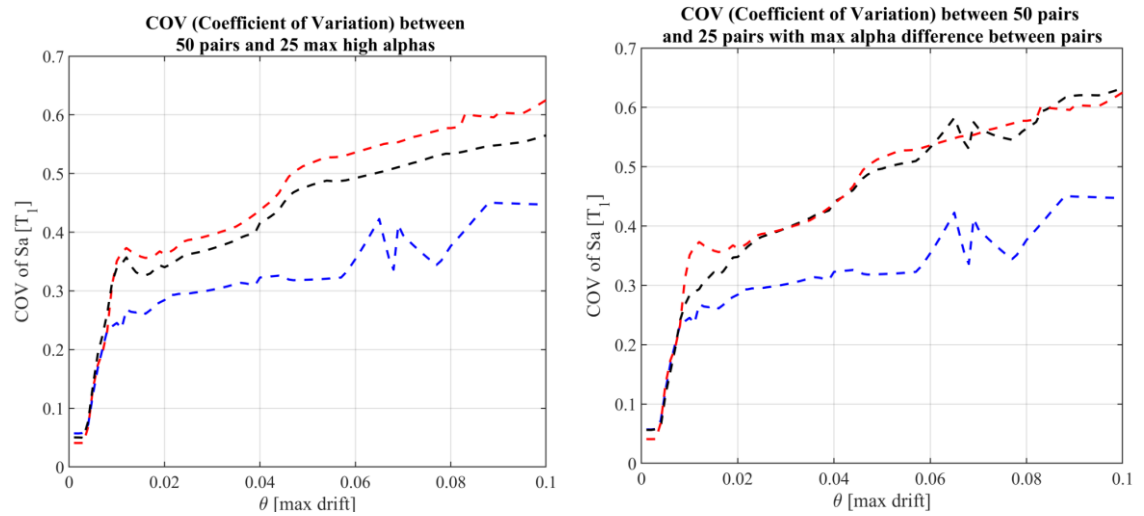


Figure 6-13 IDA COV (Coefficient of Variation) between 50 pairs and 25 max high alphas (two curves with 50L(red) and 50H(blue)), and one curve (25L+25H), black)

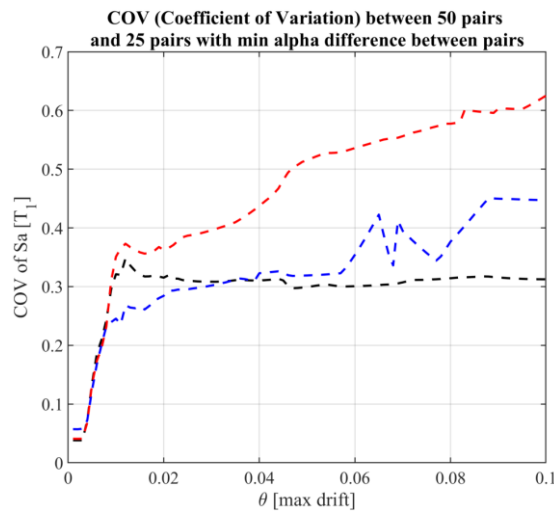


Figure 6-14 COV (Coefficient of Variation) between 50 pairs and 25 pairs with min alpha difference between pairs (two curves with 50L(red) and 50H(blue)), and one curve (25L+25H), black)

### 6.3.2 3-storey building: Numerical results

Similar as per the case of the 7-storey model, IDA are carried out the case study 3-story building model for the high- $\alpha$  and the low- $\alpha$  spectrally equivalent GM sets presented in the previous subsection. The same standard Newmark time-integration algorithm with in-step average acceleration assumption presented in section 5.2 is used in Opensees as before. Figure 6-15 collects coloured-coded IDA curves (GM ensemble statistics) while and Figure 6-16 provides boxplot statistics (GM pairwise statistics). Contrary to the 7-storey structure, median and dispersion of IDA curves obtained by the two different GM sets lie close to each other. This is further confirmed by examining the median boxplot (middle quartile), which is about 1.1 and remains relatively constant for all limit states. Dispersion of boxplot increase for near collapse limit states as well as the median increases but, overall, these trends are not statistically significant with similar level of confidence as in the case of the 7-storey structure. Note that unity is always within the notched part of the boxplot. These results suggest that  $\alpha$ , and therefore, the non-stationary frequency content of GMs does not influence much the seismic response of the 3-storey structure in terms of IM|EDP values. Noting that this structure is stiff with  $T_1=0.55s$  as opposed to  $T_1=1.6s$  for the 7-storey structure previously considered, the herein results verify trends observed in the case of stiff versus flexible inelastic SDOF oscillators seen in Chapter 5: the influence of  $\alpha$  is reduced for stiff structures.

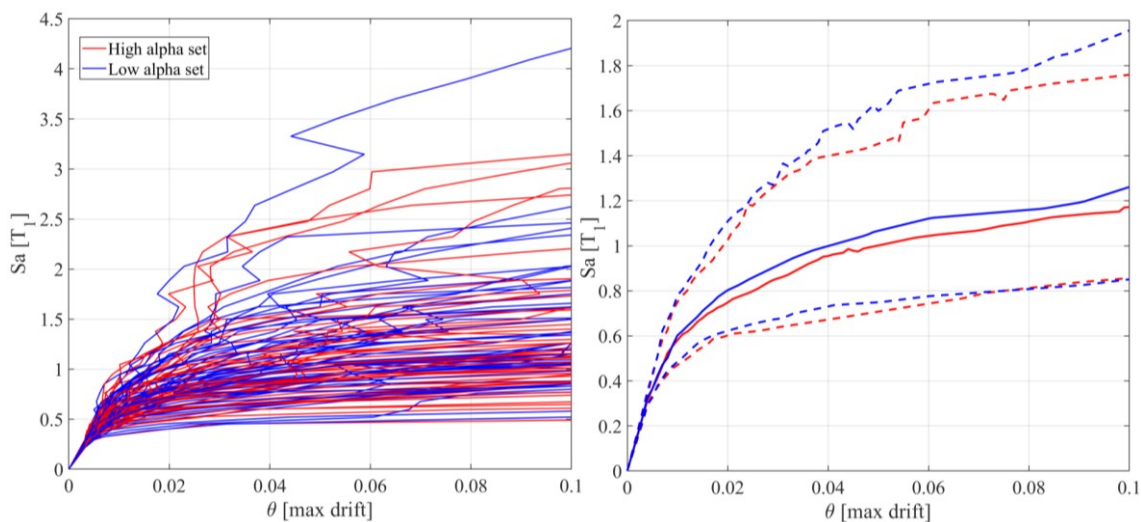


Figure 6-15 IDA curves for 50 High and Low  $\alpha$  sets (A) Individual Curves; (B) Median (Solid Lines) and Median  $\pm$  1 Standard Deviation (Broken Lines) Ensemble Curves.

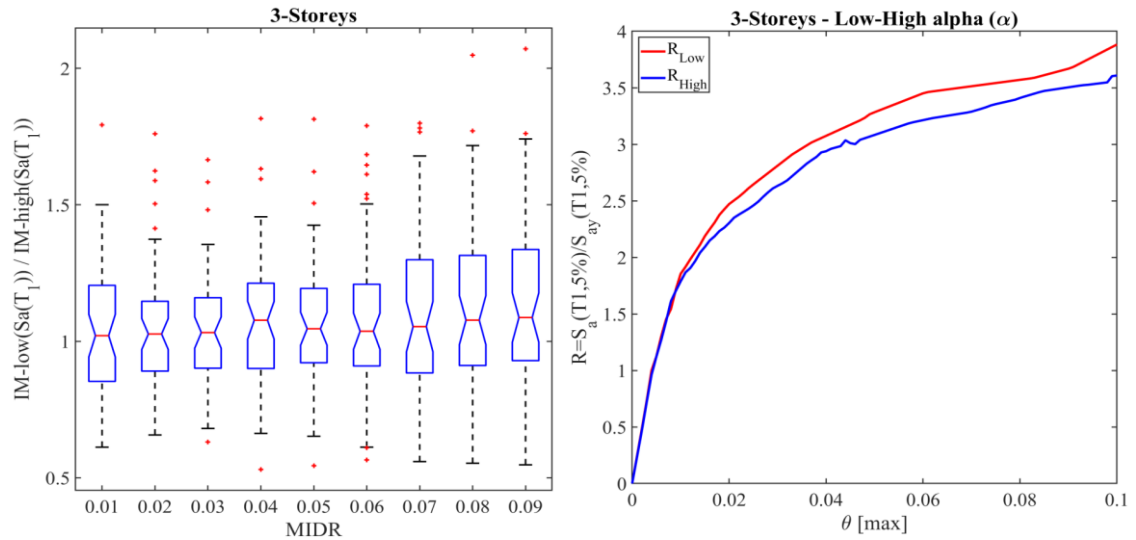


Figure 6-16 Boxplots and IDA curves of R for 50 High and Low  $\alpha$  sets for the 3-storey building

### 6.3.3 IDA curves comparison between 7-storey and 3-storey benchmark building models

To further appreciate the difference in IDA curves between the two 7-story and the latter 3-story structure, the IDA curves have been compared in Figure 6-17. In these plots the normalised to yielding strength demand IM, R in equation (5.11) is employed to enable a meaningful comparison of IDA curves for structures with different yielding and stiffness properties. Median IDA curves shown in Figure 6-17 demonstrate a significant difference in the deviation of IM|EDP values for the 7-storey structure vis-à-vis the 3-storey structure when estimated using the low- $\alpha$  GM set as opposed to the high- $\alpha$  set. It is seen that the low- $\alpha$  set brings median IDAs from the two structures much closer to each other than the high- $\alpha$  set.

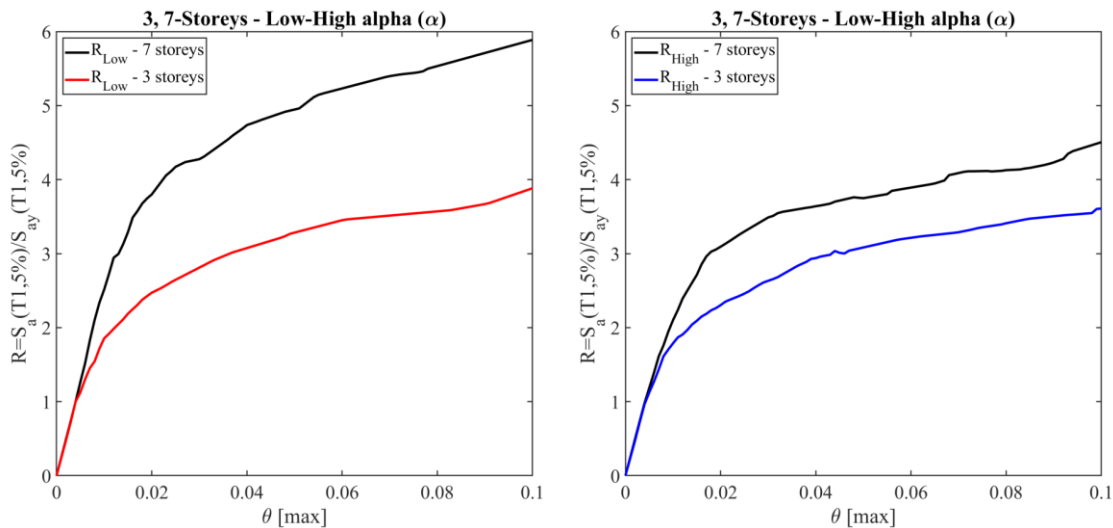


Figure 6-17 IDA curves comparisons of R for 50 High and Low  $\alpha$  sets for the 3 and 7 storey building

Moreover, the median pairwise ratios for the 3-storey structure in Figures 6-18 and 6-19 are significantly lower (around 1.05 on average and, thus, similar to median values shown in the boxplot of Figure 6-16) than the ratios for the 7-storey building which is up to more than 22% larger for the near collapse limit state. These final results and comparisons verify that the stiffer of the two benchmark structures is much less influenced by variations to the evolving frequency content as captured by  $\alpha$  compared to the more flexible benchmark structure.

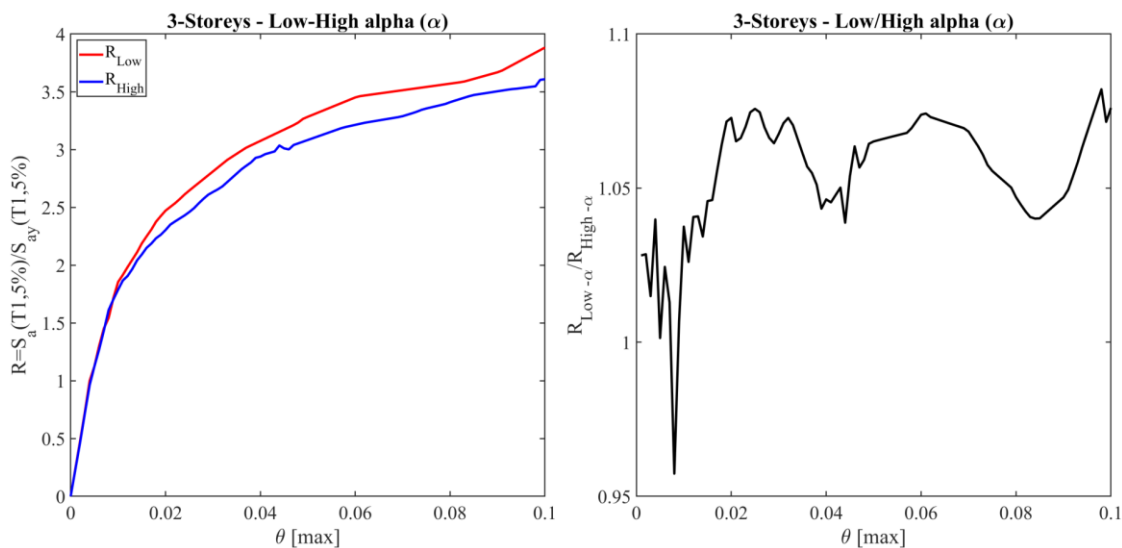


Figure 6-18 Median IDA curves comparison in terms of R for High- $\alpha$  and Low- $\alpha$  and ratio  $R_{Low}/R_{High}$  for the 3-storey building.

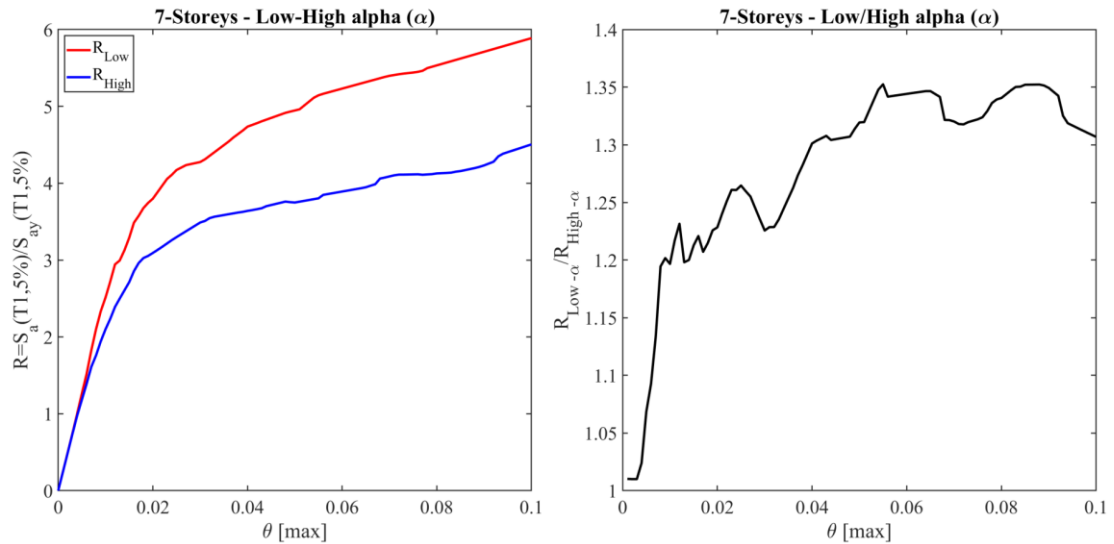


Figure 6-19 Median IDA curves comparison in terms of  $R$  for High- $\alpha$  and Low- $\alpha$  and ratio  $R_{Low}/R_{High}$  for the 7-storey building.

## 6.4 Concluding Remarks

The overarching conclusion of this chapter is that a proper treatment of the evolutionary frequency content of recorded GMs may be important for relatively flexible MDOF structural models. The evolutionary trend in time of the mean frequency content of GMs captured through  $\alpha$  has proven to be a practical and suitable metric for this purpose. The numerical evaluation of two realistic cases shed light on the phenomenological behaviour of different MDOF under a set of low- $\alpha$  and high- $\alpha$  pairs of spectrally equivalent GMs. Selecting ground motions with High and Low  $\alpha$  set of GMs has been shown to significantly influence the collapse performance of a structure. Low  $\alpha$  value set of GMs impact on structures in the sense of reduction of the collapse capability to 25% (in average) for moderate period structures. For low period MDOF the impact is less significant but still present with a percentage that varies between 5% to 10%.



## Chapter 7

### Concluding Remarks

## 7 Introduction

The quantification of the influence of time-varying average frequency content exhibited in typical far-field recorded GMs bearing no pulse-like signatures or forward directivity effects to the peak response of yielding structures has been pursued in this thesis. This need has been motivated by the fact that, despite previous work demonstrating the above influence for the case of stochastic GM models with and without accounting for non-stationary frequency content, the evolutionary frequency content trends of recorded GMs are not accounted for in the current state-of-practice of PBEE employing recorded GMs in undertaking NRHA (i.e., IDA). To this aim, the novel scalar index  $\alpha$ , has been defined representing the average in time rate of change of the mean frequency content of GMs. This is invariable to GM scaling and has been herein obtained from continuous wavelet transforming GMs using judiciously defined Morlet wavelets. Then,  $\alpha$  has been used as a proxy of the time-varying GM frequency content and statistical evidence were provided by post-processing IDA curve statistics of the influence of GM evolving frequency content to peak inelastic structural response demands of interest in PBEE (i.e., EDPs). This final section summarises the milestones reached in each chapter, highlights the main contributions and findings of the reported research work and concludes with recommendations for future work.

### 7.1 Summary of Work, Contributions and Major Findings

Following on a comprehensive literature review on the current state-of-art on using time-frequency analysis tools in earthquake engineering applications in Chapter 2, the continuous wavelet transform (CWT) was found rather advantageous for representing the time-varying frequency content in seismic response signals of hysteretic structures. Specifically, it was identified that ridge analysis on the CWT spectrogram as well as the mean instantaneous frequency (MIF) computed by the CWT spectrogram were successfully applied in previous studies for system identification of nonlinearly behaving structures under seismic excitation as well as for earthquake-induced damage detection.

In this regard, Chapter 3 focused on the presentation of all pertinent theoretical principles of CWT to underpin the use of CWT spectrogram for identifying salient time-varying frequency content features in recorded ground motion accelerograms (GMs). Specifically, a detailed discussion on analytic wavelets which lie at the heart of the wavelet ridge extraction method has been included focusing on Morlet wavelets which bears significant advantages in representing signal energy on the time-period plane. Pertinent numerical results were provided to underline advantages and limitations of CWT associated with the *ridge curves* approach. The latter approach supports the capability of CWT to trace the variation of frequency content of signals, even in the presence of

noise, by using appropriate filters, implemented in the ridge curve detection. Ultimately, a time-dependent CWT spectrogram-based mean instantaneous period (MIP) has been put forth as an advantageous alternative to CWT ridge analysis. This because it was seen, for the first time in the open literature, that the Morlet CWT spectrogram of typical recorded GMs provides for an impractically large number of simultaneous in time local ridges picking up the various different local frequency components out of the quite rich and inherently random frequency content. On the other hand, the herein proposed MIP, time-limited and band-limited to correspond to the effective duration of recorded GMs and to frequencies of interest to structural earthquake engineering, is a single time-history which was found to be capable of providing efficiently (visually as well as computationally) the evolution of the average frequency content of recorded GMs when coupled with Morlet analysis wavelets. In this regard, it was found that the herein developed MIP bears the same usefulness for characterising the evolution of the average frequency content of typical far-field recorded GMs as the MIF of CWT was found in the previous work of Spanos et al (2007a) to characterise the mean variation of natural frequencies of seismically excited yielding structures. This was achieved in Chapter 3 by considering the MIPs of a small benchmark suite of 20 GMs used by Vamvatsikos and Cornell (2002) to introduce IDA. Moreover,  $MIP = 2\pi/MIF$  of acceleration response signals were examined derived from IDA applied to a hysteretic oscillator representing a benchmark 12-storey r/c frame for the previous suite of 20 GMs. It was observed that the response signal MIPs tend to converge to the GM MIP in a point-wise manner as stronger inelastic behaviour is exhibited. This numerical evidence is the first in the literature to showcase phenomenologically moving resonance phenomena of yielding structures exposed to recorded GMs. More importantly, it has been shown that the slope of the ensemble average MIP for the near-collapse limit state lies close to the ensemble average GM MIP, while it may also be treated as indicator of the so-called “period elongation” phenomenon for degrading inelastic structures. Overall, the reported numerical data suggested that the time-varying frequency content is an important influence factor for hysteretic systems especially at the near collapse limit state since the average excitation MIP correlates with the average response MIP. This novel finding motivated considering the slope of the MIP as a useful proxy to account for the influence of the time-varying frequency content of GMs to structural response within the PBEE framework.

Chapter 4 introduced the novel scalar wavelet-based quantity termed alpha, “ $\alpha$ ”, defined by the average slope (angle) of the wavelet-based mean instantaneous period (MIP) to characterize the temporal evolution of the mean frequency content of recorded GMs. Consequently,  $\alpha$  captures the rate by which the mean frequency content of GMs changes in time. A rigorous mathematical definition of  $\alpha$  was provided based on linear regression analysis of discrete-time MIP data using mean least squares minimization criterion. Conveniently, the closed-form mathematical

expression of  $\alpha$  enables also its efficient numerical calculation. Linear regression analyses have been undertaken involving a dataset of 611 GMs from 30 seismic events of Magnitude  $6.5 < M < 8$  and distance to rupture plane  $20\text{km} < R_{rup} < 120\text{km}$  to quantify statistical/empirical correlation trends between  $\alpha$  and well-established GM properties, namely the peak ground acceleration (PGA), peak ground velocity (PGV), and the mean Fourier-based frequency ( $T_m$ ), oftentimes used as intensity measures (IMs) and record selection criteria in PBEE. Further, regression analyses have been carried out to probe into the relationships between  $\alpha$  and important seismological and local site characteristics. It is found that no significant correlation exists between  $\alpha$  and  $M$ ,  $R_{rup}$ , or PGA. However, it was established that  $\alpha$  is well-correlated with the average frequency content of GMs as captured by  $T_m$  and by PGV: the lower the average frequency content, the larger the value of  $\alpha$  tends to be, that is, the faster the time evolution (transition) of the average frequency content is from higher to lower frequencies. Further, the reported numerical data indicate that the level of the above correlation depends on the intensity of GMs in terms of PGA (conditional on PGA):  $\alpha$  is larger for fixed  $T_m$  as PGA increases and  $\alpha$  increases faster as  $T_m$  increases for larger PGA values. Moreover, GMs recorded on softer soils are more likely to have larger  $\alpha$  conditional on PGA, a phenomenon that is attributed to the fact that soft soils under strong seismic shaking exhibit strong non-linear behavior that enriches the low frequency content of free field recorded GMs. Lastly, the influence of  $\alpha$  in predicting the peak inelastic structural response is assessed within the PBEE framework through a standard sufficiency statistical test on PGA and PGV, treated as non-structure specific IMs in conducting IDA for a hysteretic oscillator with strength and stiffness degradation representing a benchmark 12-storey reinforced concrete frame exposed to the above set of 611 GMs. The considered statistical tests demonstrate that information of the non-stationary average frequency content of GMs as captured by  $\alpha$  is only partially included in the PGV and quite less in PGA when used as IMs to predict peak inelastic structural response.

The response of benchmark inelastic SDOF oscillators developed in the literature to represent different classes of archetype lateral load-resisting systems used in earthquake resistant building structures is considered in *Chapter 5* to demonstrate and quantify the influence of  $\alpha$  and, thus, of the mean variation of GMs frequency content, to different limit state performance of yielding structures. Pertinent numerical evidence was provided addressing ductile and non-ductile structures with different pre-yield stiffness relying on post-processing of IDA curves for the same 611 GM databank considered in *Chapter 6*. Important novel findings based on regression analyses to IDA curves derived by using the standard  $S_a(T_1)$  IM as well as the more advanced (efficient and sufficient)  $AvgS_a|IM$  which partly accounts for GM spectral shape showed that (1) both IMs values conditioned on near collapse limit state are significantly influenced by  $\alpha$ , though influence to  $AvgS_a$  is smaller; (2)  $\alpha$  becomes more influential to mean  $IM|EDP$  trends for larger EDP values (i.e., as limit states corresponding to more significant nonlinear behaviour from linear all the way

collapse) are considered; (3) influence of  $\alpha$  is more prominent for the ductile structures. Overall, the above three findings suggest that insufficient portion of information carried by  $\alpha$  (i.e., non-stationary frequency content trends as well as moving average and period elongation potential) is contained in the IMs considered and that IMs accounting for spectral shape (and thus for period elongation) are only partially able to capture some of the information in  $\alpha$ . Consequently,  $\alpha$  should be accounted for as a record selection criterion in establishing IM-EDP relationships especially when the routinely used  $Sa(T_1)$  is adopted as the IM and ductile structures (i.e., code-compliant/contemporary structures) and/or limit states close to collapse are studied. These recommendations are further supported/justified by results and discussion in Chapter 3 demonstrating that input/excitation  $\alpha$  correlates better with output/response  $\alpha$  in structures amenable to develop stronger period elongation through moving average phenomena (ductile and/or close to collapse limit states). Moreover, the use of a normalised to the yielding strength IM,  $R$ , was considered to enable meaningful comparisons among stiff versus flexible structures (based on their pre-yielding natural period). Here, it was found that for non-ductile structures the influence of  $\alpha$  increases monotonically with the flexibility of structures for all limit states. However, this is not the case for the ductile structures in which the influence of a relatively stiff structure ( $T_1=0.5s$ ) is almost the same with a relatively flexible structure ( $T_1=2s$ ) though much more important for intermediate structures ( $T_1=1s$  and  $1.5s$ ) for all limit states. Overall, it is found that  $\alpha$  is increasingly important for close to collapse limit states irrespective of structural ductility and stiffness. Further, as stiffness increases  $\alpha$  influences more substantially the ductile structure and it is mostly important for flexible ( $T_1=2s$ ) non-ductile structures and for intermediate stiffness ( $T_1=1s$  and  $1.5s$ ) ductile structures.

In *Chapter 6* rigorous GM record selection has been employed to examine the potential influence of  $\alpha$  to statistics of IMs conditioned on EDP values derived through IDA for a 7-storey flexible and 3-storey stiff benchmark structures modelled through detailed lumped-plasticity MDOF FE models. Record selection involved constructing two different GM sets of 50 GMs each chosen from a databank of 1222 GMs such that they are pair-wise spectrally equivalent (i.e., have similar spectral shapes in pairs) such that their average spectral shape is the same but have very different  $\alpha$  mean/median values. It was verified that the two GM sets, one high- $\alpha$  GMs and one with low- $\alpha$  GMs have similar  $T_m$  and effective duration distributions, thus, making them ideal to check the influence of  $\alpha$  to EDPs (maximum storey drift) of the benchmark structures in isolation from all other factors known to influence EDPs (spectral shape,  $T_m$ , effective duration). It was found that the evolving GM frequency content as captured by  $\alpha$  increases ensemble-wise median IDA curves by 20% or more across a wide range of post-yield limit states for the flexible 7-storey benchmark structure when adopting  $Sa(T_1)$  as the IM. This discrepancy in the mean sense does not reduce appreciably by adopting an advanced AvgSa|IM accounting for spectral shape effect to period

elongation and to higher modes influence since the two GM sets used are spectrally equivalent and response spectral ordinates cannot discriminate evolutionary trends of frequency content. Strictest possible pair-wise statistics provided in the form of boxplots of ratios of IM|EDP values for spectrally matched GM twins coming from the high- $\alpha$  and low- $\alpha$  sets were further considered demonstrating that the increased IM/EDP median values for low- $\alpha$  set is statistically important with very high confidence level. Ultimately, this compelling statistical evidence establishes the important influence of non-stationary frequency content in estimating fragilities and, eventually, seismic loss within the PBEE framework. On the antipode, the influence of  $\alpha$  to the hysteretic response of the stiffer 3-story benchmark structure was found to be insignificant which verifies findings and conclusions of Chapter 5 addressing inelastic SDOF structures.

## 7.2 Recommendations for Future Research

It is recognized that throughout this research work the number of hysteretic structural systems considered to appraise the influence of GM non-stationary frequency content was kept to a minimum. This was purposely done, through judicial selection of benchmark structures, aiming to explore structural behaviour lying towards the two ends of the spectrum of possible candidate structures. For example, in Chapter 5 only two different inelastic SDOF systems were considered, cherry-picked out of at least 8 different benchmarks inelastic SDOF systems representative of the structural behaviour of archetype structures included in FEMA P440A (2009), corresponding to ductile and to non-ductile moment resisting steel or r/c frames. The purpose was to examine whether and how systems with different ductility attributes are influenced by the non-stationary GM frequency content. Moreover, in Chapter 6, again only two benchmark structures were considered, a relatively flexible (7-storey r/c moment resisting frame) and a relatively stiff with fewer DOFs (3-storey steel braced frame), out of several possible, to explore the level of influence of non-stationary GM frequency content to flexible/mid-rise buildings versus stiff low-rise buildings. In all cases, it was found that the level of influence of the non-stationary GM frequency content as captured by the herein proposed  $\alpha$  to the inelastic structural response is governed by structural system properties such as stiffness and ductility. In this respect, it is recommended that further comprehensive research work is undertaken to study the effect of non-stationary GM frequency content to a wide variety of inelastic structural systems with different levels of stiffness, ductility, number of DOFs, capacity envelopes (backbone curve), and hysteretic laws (with and without and for different levels of stiffness and strength deterioration) representative of different materials and structural configurations (steel, r/c, composite, wood/timber, etc.). Along similar lines, the  $\alpha$  index as well as the methodology considered in Chapter 6 on record selection can be used to study the effects on non-stationary GM frequency content to structures protected by

various passive and semi-active devices and configurations against seismic hazard including energy dissipation devices (i.e., all types of dampers), tuned mass dampers, inerter-based vibration absorbers, base isolation, magnetorheological dampers. In fact, recent work showed that seismic protection effectiveness of tuned mass dampers and of base isolated structures does depend on non-stationary GM frequency content probed through wavelet analysis without however making use of the  $\alpha$  index (De Angelis, et al. 2019 ). Accordingly, further research is recommended to check the influence of non-stationary frequency content through  $\alpha$  for other types of important infrastructure facilities exposed to the seismic hazard, such as bridges and wind turbines.

From the engineering seismology viewpoint, numerical data in Chapter 4 indicate that further promising work can be undertaken to correlate trends of non-stationary GM frequency content as captured by  $\alpha$  against seismological and other key GM properties in different seismogenetic environments including near-fault, different types of faulting, different GM records orientation, etc. Moreover, given that  $\alpha$  was herein found to be a predictor of structural collapse capacity at least for certain types of structures at near collapse limit states, integrating site-specific seismic hazard characterisation of  $\alpha$  with structural collapse risk in a similar manner that this was undertaken by (Chandramohan, e al. 2015) for the case of effective duration, seems a promising and important further research to be undertaken.

Another aspect that sets the scene for promising future research is the consideration of the influence of GMs to structural response and collapse capacity with negative  $\alpha$ . It was seen in this research work that out of 2x611=1222 GMs of the set in Appendix A, 103 GMs (i.e., less than 9% of the total GMs considered) attain a negative  $\alpha$ , that is, their average frequency content evolves from lower to higher frequencies in time. Careful examination of the Morlet wavelet spectra and the associated MIPs reveal that these GMs are characterized by the late arrival of significant bursts of energy with relatively high frequencies compared to the early mean frequency content observed (Margnelli and Giaralis, 2017). However, such time-varying frequency content trends are non-typical and their influence to GM damage potential warrant separate treatment left for future work as highlighted in Chapter 6. Similarly, future research investigation is warranted to treat the case of pulse-like GMs which have not been considered at all in the present work. The use of wavelet-based procedure for classification of near-fault GMs is quite advanced (Baker 2007) but the use of a proxy like  $\alpha$  (or perhaps other more suitable proxies) and their effect to yielding structures or to structures equipped with passive/semi-active control devices is open to further investigation.

Finally, from the PBEE viewpoint, more research warranted to explore different and mostly practical ways to account for non-stationary frequency content through  $\alpha$  in performance-based

seismic design and/or seismic risk and loss assessments for structures expected to be mostly influenced by  $\alpha$ . Possible ways forward can be to use  $\alpha$  as an additional record selection criterion or the definition of alternative (vector) IMs that account for  $\alpha$ .

As closure, in view of the large number of items for recommended future work building on the current research and findings, it can be argued that a major contribution of this thesis, being mostly exploratory rather than conclusive, is that it opens up several new research directions in the field of earthquake engineering whose outcomes are expected to be fruitful from the scientific viewpoint and practically important from the practitioner viewpoint.



# Appendix A

## Ground Motions (GMs) sets

**A1 GMs SET 1 - 20 GMs**

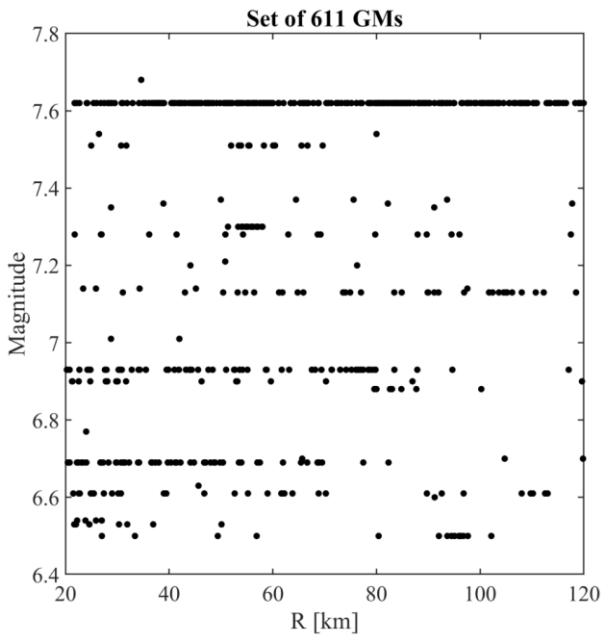
The 20 recorded GMs used in Sections 3.4 and 3.5 are listed in Table A-1 with some key properties. This suite of records has been constructed by Vamvatsikos and Cornell (2002) to represent a “scenario earthquake” and considers seismic events of magnitude range  $6.5 < M < 6.9$  recorded on firm soil conditions at moderate distances from the seismic fault.

Table A-1 Properties of the 20 ground motions considered by (Vamvatsikos and Cornell, Incremental Dynamic Analysis 2002)

<b>No.</b>	<b>Event (Year)</b>	<b>Station (Component)</b>	<b>M</b>	<b>R (km)</b>	<b>PGA (g)</b>	<b>T<sub>m</sub> (s)</b>
1	Loma Prieta (1989)	Agnews State Hospital (090)	6.9	28.2	0.159	0.957
2	Imperial Valley (1979)	Plaster City (135)	6.5	31.7	0.057	0.378
3	Loma Prieta (1989)	Hollister Diff. Array (255)	6.9	25.8	0.279	0.798
4	Loma Prieta (1989)	Anderson Dam Downstrm (270)	6.9	21.4	0.244	0.467
5	Loma Prieta (1989)	Coyote Lake Dam Downstrm (285)	6.9	22.3	0.179	0.538
6	Imperial Valley (1979)	Cucapah (085)	6.5	23.6	0.309	0.558
7	Loma Prieta (1989)	Sunnyvale Colton Ave (270)	6.9	28.8	0.207	1.502
8	Imperial Valley (1979)	El Centro Array #13 (140)	6.5	21.9	0.117	0.585
9	Imperial Valley (1979)	Westmoreland Fire Station (090)	6.5	15.1	0.074	0.849
10	Loma Prieta (1989)	Hollister South & Pine (000)	6.9	28.8	0.371	0.935
11	Loma Prieta (1989)	Sunnyvale Colton Ave (360)	6.9	28.8	0.209	1.380
12	Superstition Hills (1987)	Wildlife Liquefaction Array (090)	6.7	24.4	0.180	0.854
13	Imperial Valley, 1979	Chihuahua (282)	6.5	28.7	0.254	0.701
14	Imperial Valley, 1979	El Centro Array #13 (230)	6.5	21.9	0.139	0.470
15	Imperial Valley, 1979	Westmoreland Fire Station (180)	6.5	15.1	0.110	0.985
16	Loma Prieta (1989)	WAHO (000)	6.9	16.9	0.370	0.275
17	Superstition Hills (1987)	Wildlife Liquefaction Array (360)	6.7	24.4	0.200	1.137
18	Imperial Valley (1979)	Plaster City (045)	6.5	31.7	0.042	0.361
19	Loma Prieta (1989)	Hollister Diff. Array (165)	6.9	25.8	0.269	0.890
20	Loma Prieta (1989)	WAHO (090)	6.9	16.9	0.638	0.271

**A2 GMs SET 2 - 611 GMs**

A set of 611 of GM recordings (i.e. one direction horizontal component) from 30 different seismic events with magnitude range  $6.5 < M < 8$  and distance-to-rupture plane range  $20\text{km} < R_{\text{rup}} < 120\text{km}$  is retrieved from the PEER NGA-West2 Ground Motion Database (<http://ngawest2.berkeley.edu/>) as shown in Table A-2. Table A2 lists the seismic events, number of GMs considered per event, magnitude, and faulting mechanism while Figure A-2 shows the spread of the seismic events on the magnitude (M)- rupture distance (R) plane. Unscaled and unfiltered GMs along the “as-recorded” direction are considered and no filter was applied on the faulting type, while “pulse-like” GMs are excluded. This GM dataset attains a relatively uniform spread on the M- $R_{\text{rup}}$  plane as shown in Figure A-1. The same base-line adjustment is applied to each horizontal component of the dataset by acausal high-pass filtering using a 4-order Butterworth filter with 0.13Hz cut-off frequency (see e.g., Giaralis and Spanos 2009 and references therein).



**Figure A-1** Magnitude vs distance for the set of 611 GMs

**Table A-2** Properties of the 611 ground motions considered

<b>Event</b>	<b>Date</b>	<b>Number of components</b>	<b>Magnitude</b>	<b>Faulting</b>
Northwest California	02/09/1941	2	6.6	strike slip
Borrego Mtn, El Centro Array	04/09/1968	2	6.5	strike slip
San Fernando	02/09/1971	32	6.6	Reverse

Appendix A2 – GMs Set 2 – 611 GMs

<b>Event</b>	<b>Date</b>	<b>Number of components</b>	<b>Magnitude</b>	<b>Faulting</b>
Friuli, Italy	05/06/1976	4	6.5	Reverse
Imperial Valley-06	10/15/1979	9	6.5	strike slip
Irpinia, Italy	11/23/1980	8	6.9	Normal
Ierissos, Greece	08/06/1983	1	6.7	strike slip
Taiwan SMART1(25)	09/21/1983	9	6.5	Reverse
Borah Peak ID-01	10/28/1983	8	6.9	Normal
Superstition Hills-02	11/24/1987	4	6.5	strike slip
Spitak Armenia	12/07/1988	1	6.8	Reverse Oblique
Loma Prieta	10/18/1989	62	6.9	Reverse Oblique
Cape Mendocino	04/25/1992	2	7.0	Reverse
Northridge-01	01/17/1994	55	6.7	Reverse
Kobe, Japan	01/16/1995	8	6.9	strike slip
Nenana Mountain Alaska	10/23/2002	2	6.7	strike slip
Kern County	07/21/1952	3	7.4	Reverse
Tabas, Iran	09/16/1978	2	7.4	Reverse
Trinidad	11/08/1980	3	7.2	strike slip
Taiwan SMART1	11/14/1986	15	7.3	Reverse
Landers	06/28/1992	16	7.3	strike slip
Gulf of Aqaba	11/22/1995	1	7.2	strike slip
Duzce, Turkey	11/12/1999	5	7.1	strike slip
Caldiran, Turkey	11/24/1976	1	7.2	strike slip
Manjil, Iran	06/20/1990	4	7.4	strike slip
Hector Mine	10/16/1999	34	7.1	strike slip
Kocaeli, Turkey	08/17/1999	13	7.5	strike slip
Chi-Chi, Taiwan	09/20/1999	302	7.5	Reverse Oblique

Appendix A2 – GMs Set 2 – 611 GMs

---

<b>Event</b>	<b>Date</b>	<b>Number of components</b>	<b>Magnitude</b>	<b>Faulting</b>
Sitka, Alaska	07/30/1972	1	7.7	strike slip
St Elias, Alaska	02/28/1979	2	7.5	Reverse

### A3 GMs SET 3 – 2 x 611 GMs

A set of 611 pairs of GM recordings (i.e. two horizontal components) from 30 different seismic events with magnitude range  $6.5 < M < 8$  and distance-to-rupture plane range  $20\text{km} < R_{\text{rup}} < 120\text{km}$  is retrieved from the PEER NGA-West2 Ground Motion Database (<http://ngawest2.berkeley.edu/>) as shown in Table A-3. Unscaled and unfiltered GMs along the “as-recorded” direction are considered and no filter was applied on the faulting type, while “pulse-like” GMs are excluded. This GM dataset attains a relatively uniform spread on the M- $R_{\text{rup}}$  plane as shown in Figure 2(a). The same base-line adjustment is applied to each horizontal component of the dataset by acausal high-pass filtering using a 4-order Butterworth filter with 0.13Hz cut-off frequency (see Giaralis and Spanos 2009 and references therein).

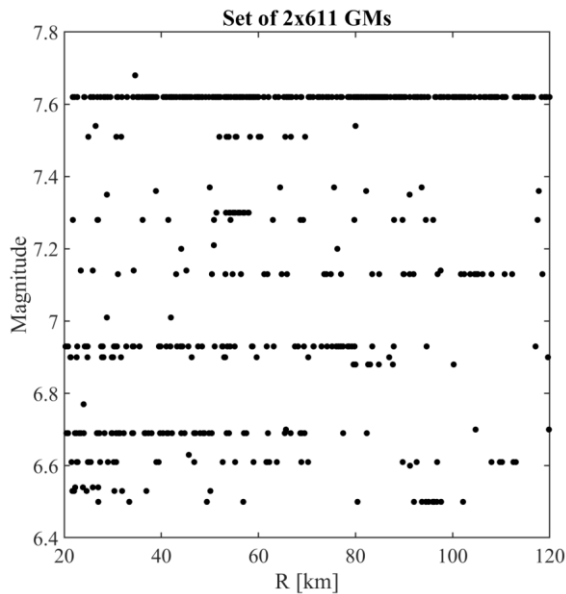


Figure A-2 Magnitude vs distance for the set of 611 GMs

Table A-3 Properties of the 611 ground motions considered

Event	Date	Number of components	Magnitude	Faulting
Northwest California	02/09/1941	2	6.6	strike slip
Borrego Mtn, El Centro Array	04/09/1968	2	6.5	strike slip
San Fernando	02/09/1971	32	6.6	Reverse
Friuli, Italy	05/06/1976	4	6.5	Reverse
Imperial Valley-06	10/15/1979	9	6.5	strike slip
Irpinia, Italy	11/23/1980	8	6.9	Normal

Appendix A3 – GMs Set 3 – 2 x 611 GMs

<b>Event</b>	<b>Date</b>	<b>Number of components</b>	<b>Magnitude</b>	<b>Faulting</b>
Ierissos, Greece	08/06/1983	1	6.7	strike slip
Taiwan SMART1(25)	09/21/1983	9	6.5	Reverse
Borah Peak ID-01	10/28/1983	8	6.9	Normal
Superstition Hills-02	11/24/1987	4	6.5	strike slip
Spitak Armenia	12/07/1988	1	6.8	Reverse Oblique
Loma Prieta	10/18/1989	62	6.9	Reverse Oblique
Cape Mendocino	04/25/1992	2	7.0	Reverse
Northridge-01	01/17/1994	55	6.7	Reverse
Kobe, Japan	01/16/1995	8	6.9	strike slip
Nenana Mountain Alaska	10/23/2002	2	6.7	strike slip
Kern County	07/21/1952	3	7.4	Reverse
Tabas, Iran	09/16/1978	2	7.4	Reverse
Trinidad	11/08/1980	3	7.2	strike slip
Taiwan SMART1	11/14/1986	15	7.3	Reverse
Landers	06/28/1992	16	7.3	strike slip
Gulf of Aqaba	11/22/1995	1	7.2	strike slip
Duzce, Turkey	11/12/1999	5	7.1	strike slip
Caldiran, Turkey	11/24/1976	1	7.2	strike slip
Manjil, Iran	06/20/1990	4	7.4	strike slip
Hector Mine	10/16/1999	34	7.1	strike slip
Kocaeli, Turkey	08/17/1999	13	7.5	strike slip
Chi-Chi, Taiwan	09/20/1999	302	7.5	Reverse Oblique
Sitka, Alaska	07/30/1972	1	7.7	strike slip
St Elias, Alaska	02/28/1979	2	7.5	Reverse



## Appendix B

### Brief notes on Energy-Based methodology

## B1 Introduction

The present section is to describe methods based on the estimation of input energy and other energy parameters in order to investigate the inelastic behaviour for a SDOF. Since these parameters have been used in the previous chapters frequently it seemed necessary to prepare an introduction in this appendix. Recent studies have advised the use of energy concepts as an alternative way to the traditional strategies for the identification of seismic demand parameters. The possibility of defining a rational approach based on energy concepts required the understanding of the effects that energy and other relevant parameters both external (magnitude, soil type and distance to the causative fault) and internal (ductility, hysteric behaviour, damping), can have on the response of earthquake-resisting structures. There are interesting and unexplored ways to relate energy indexes (such as the ratio of hysteretic energy to input energy or the ratio of kinetic energy to input energy) with the Performance Based Seismic Design parameters (such as IM and DM of the IDA curves).

### B1.1 Energy Based methodology

For an elastic single degree of freedom, the input energy is dissipated by the damping energy only whereas for an inelastic SDOF the yielding is acting an important role. The energy terms are normally derived by integrating the equation of motion (Uang and Bertero 1990):

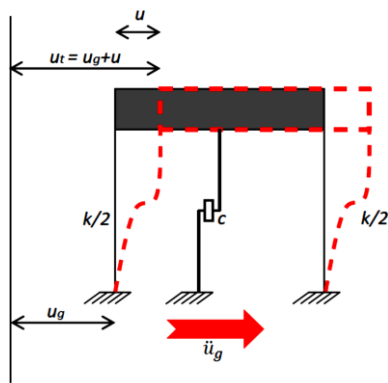


Figure B-1 Diagram of a SDOF

$$\int_0^u m \ddot{u}(t) du + \int_0^u c \dot{u}(t) du + \int_0^u f_s(u, \dot{u}) du = - \int_0^u m \ddot{u}_g(t) du$$

Clearly the previous equation is based on an inelastic system in which  $f_s$  is the restoring force depending on velocity and displacement of the system. This equation is also called Energy Balance Equation. The energy supplied to the structure by the external seismic force  $-m\ddot{u}_g(t)$  is called energy input and is equal to the right term of the energy balance equation:

$$E_I(t) = - \int_0^u m\ddot{u}_g(t)du$$

The first term of the energy balance equation is the Kinetic energy (relative motion to the ground):

$$E_K(t) = \int_0^u m\dot{u}(t)du = \int_0^{\dot{u}} m\dot{u}(t)du = \frac{m\dot{u}^2(t)}{2}$$

The second term is the energy dissipated by damping:

$$E_D(t) = \int_0^u c\dot{u}(t)du$$

The third term is the restoring strain energy:

$$E_S(t) = \frac{[f_s(t)]^2}{2k}$$

Where k is the initial stiffness of the nonlinear system. Therefore, the hysteretic energy (energy dissipated by yielding) is:

$$E_Y(t) = \int_0^u f_s(u, \dot{u})du - E_S(t)$$

Summarizing the energy balance equation for an inelastic system can be rewritten as:

$$E_I(t) = E_K(t) + E_D(t) + E_S(t) + E_Y(t)$$

The input energy relation proposed by (Uang and Bertero 1990) were based on absolute and relative motions supported recently by studies (Kalkan and Kunnath 2007) that corroborate the theory of important meanings of absolute input energy. In this section everything will be based on the input energy based on relative motion as it is the most meaningful approach (Chopra 2007) (Kalkan and Kunnath 2007).

Based on the previous equation it has been developed a Matlab-OpenSees platform (McKenna and Fenves 2001) that can derive all the energy terms before described and the energy ratio time-histories.

## B1.2 Elasto-Perfectly Plastic material and the effect on the Energy Actions

The Elasto-Perfectly Plastic material used is described below:

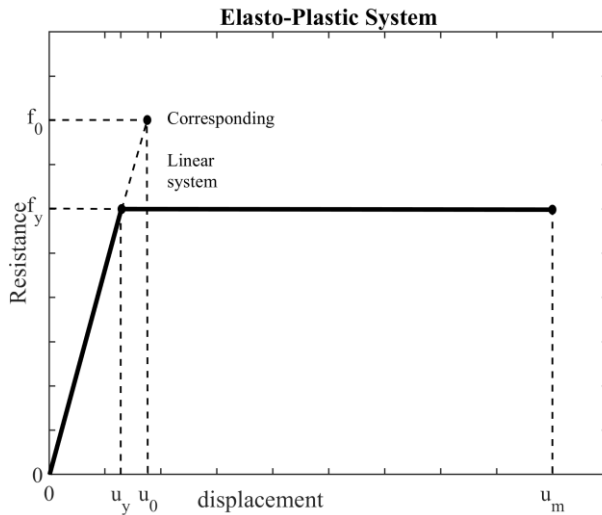


Figure B-2 Force Deformation Curve (Elastoplastic Behaviour) (Chopra 2007)

Following the same approach as per (Chopra 2007) and using the *normalized yield strength*:

$\bar{f}_y = \frac{f_y}{f_0} = \frac{u_y}{u_0}$  where  $f_0$  and  $u_0$  are the peak value of the earthquake-induced resisting force and deformation,

respectively, in the correspondent linear system. For example, a  $\bar{f}_y = 0.5$  implies that the yield strength of the system is half of the minimum strength required for the system to remain elastic during the ground motion. Another important factor has been introduced that is the inverse of the normalized yield strength and it is called the *yield strength reduction factor*  $R_y$ :

$$R_y = \frac{f_0}{f_y} = \frac{u_0}{u_y}$$

In this case for  $R_y = 1$  the system is elastic,  $R_y = 2$  implies that the yield strength of the system is the minimum strength required for the system to remain elastic divide by 2. Introducing also the *ductility factor*  $\mu$  as:

$$\mu = \frac{u_m}{u_y}$$

It is simple to obtain  $\frac{u_m}{u_y} = \mu \bar{f}_y = \frac{\mu}{R_y}$

Considering ElCentro seismic action:

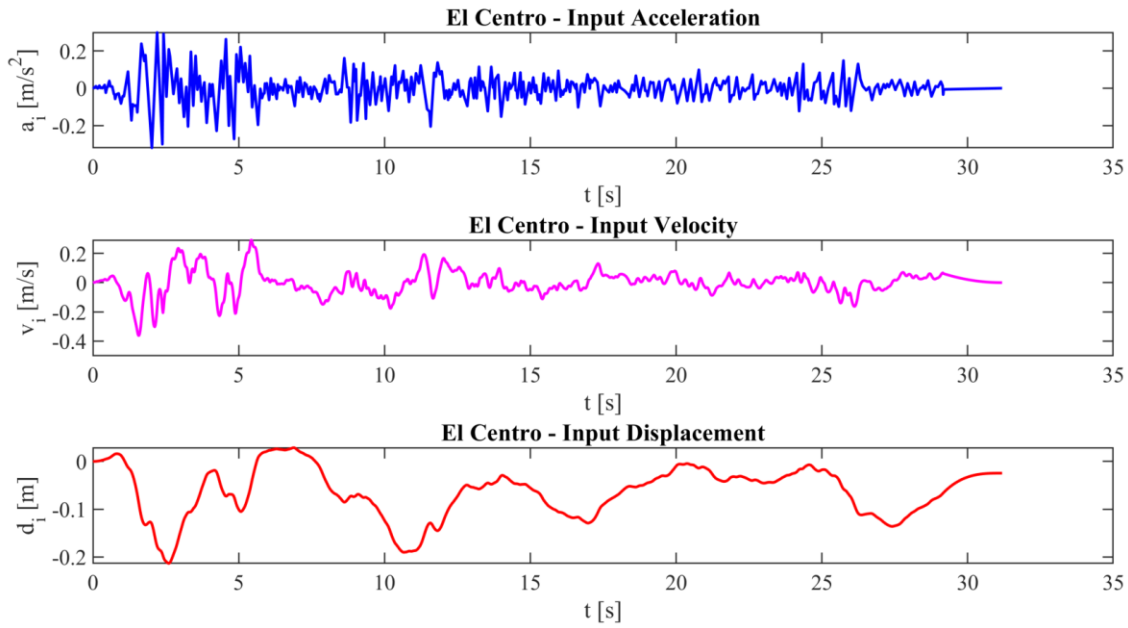


Figure B-3 ElCentro seismic action (Chopra 2007)

For different levels of normalized yield strength, it is possible to explore the effect of yielding in the response history. For a SDOF with a natural period of  $T=0.5s$ , damping of  $\xi=5\%$  and the elastic max response of  $u_0=0.05693m$  with a resisting force value  $\frac{1}{4}$  of the yielding value  $\bar{f}_y = 0.25$ . In the Figure B-4 it is described the response for an elastic system ( $\bar{f}_y = 1$ ) (no yield) and in the figures below a comparison between various levels of normalized yield strength

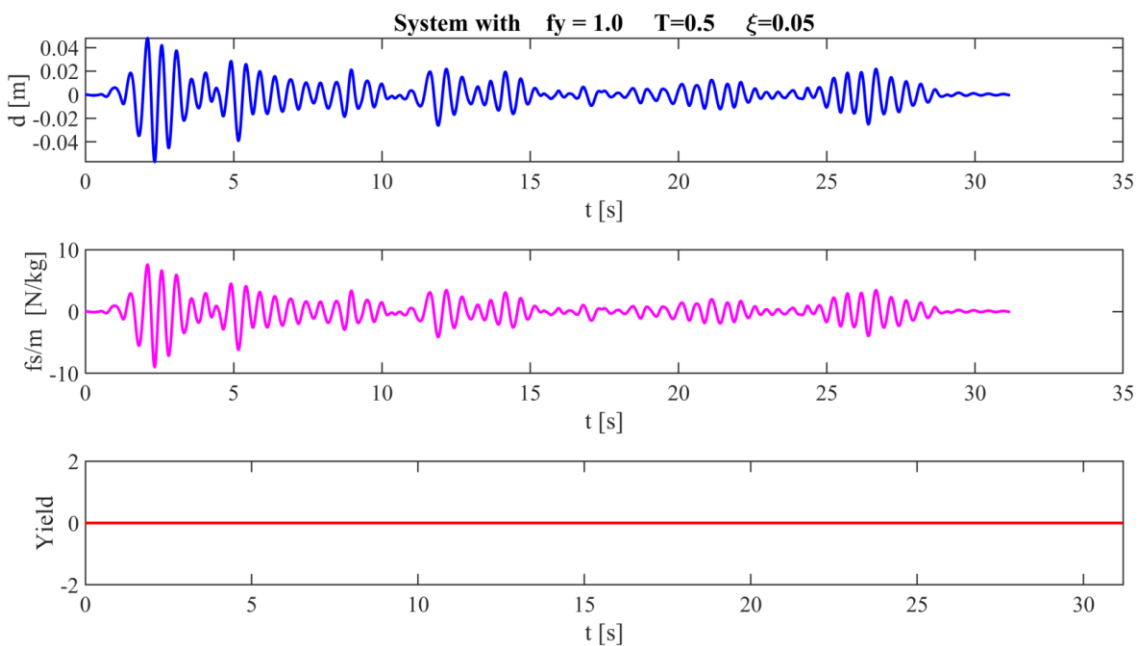


Figure B-4 Elastic response ( $\bar{f}_y = 1$ )

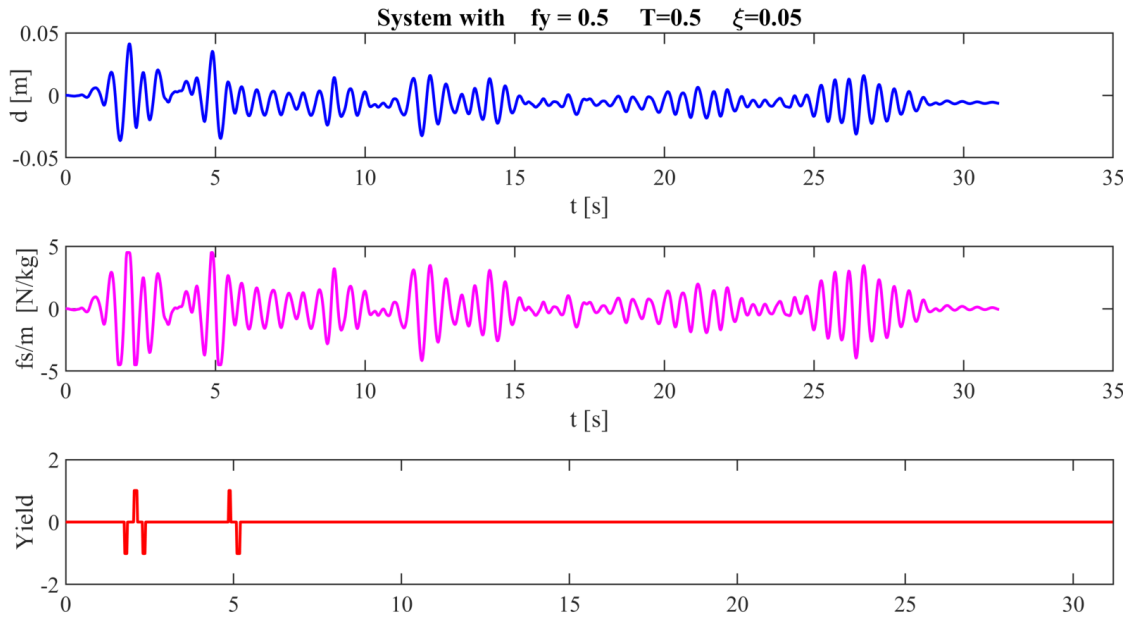


Figure B-5 Elastic response ( $\bar{f}_y = 0.5$ )

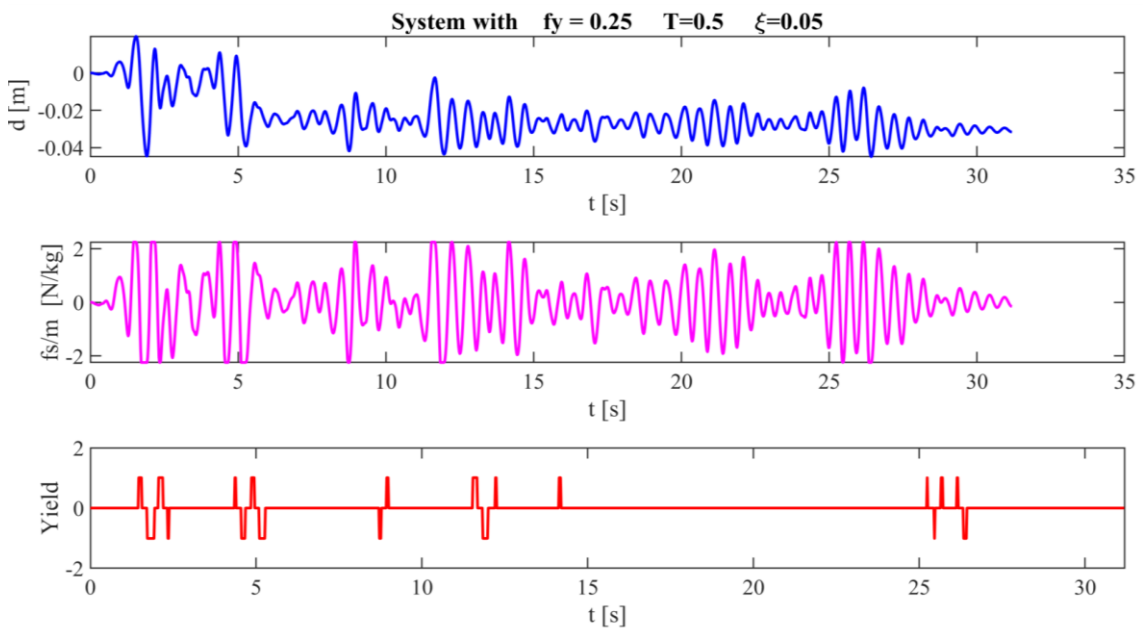


Figure B-6 Elastic response ( $\bar{f}_y = 0.25$ )

As expecting, from the plots above, with the decreasing of  $\bar{f}_y$  there is an increasing of residual displacements and an increasing on the number of yielding levels reached. In those plots it has been developed an additional plot called Yield. If we introduce the number ( $N_Y$ ) and the amplitude ( $A_Y$ ) of the yield excursion of the SDOF, we can use them as indicators of the time spent by the SDOF to yield and looking at the above plots the time spent with  $\bar{f}_y = 0.5$  is  $t_Y = \frac{0.4}{31.2} = 1.28\%$ ,

where with  $\bar{f}_y = 0.25$   $t_y = 5.32\%$  and with  $\bar{f}_y = 0.125$   $t_y = 15.2\%$ . Clearly very interesting considering that, reducing the normalized yield strength by 2 times from  $\bar{f}_y = 0.5$  to  $\bar{f}_y = 0.25$  (with the number of yield excursion passing from  $N_y=5$  to  $N_y=18$  (360%)) the time spent is increased of 415% whereas with an additional reduction of normalized yield strength of 2 times from  $\bar{f}_y = 0.25$  to  $\bar{f}_y = 0.125$  (with the number of yield excursion passing from  $N_y=18$  to  $N_y=44$  (244%)) the time spent is increased of 285%. The history of yielding is clearly very significant as much as the amount of energy absorbed by the system which leads to the cumulative yielding, a concept still at early stages of study.

The force-deformation relation becomes larger and larger clearly showing an increasing of area and therefore an increasing of energy dissipated by yielding (as describe in the plots below).

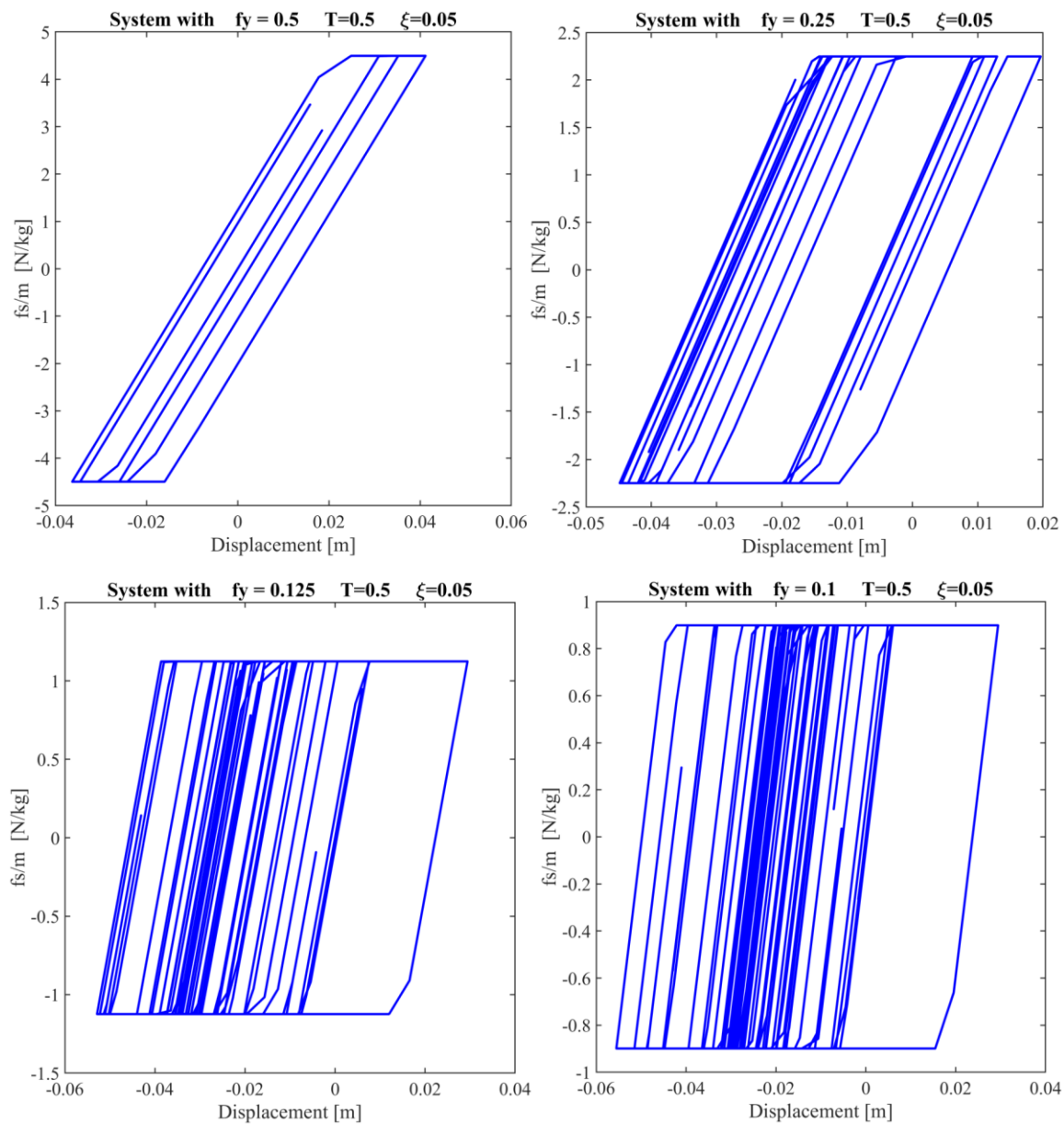
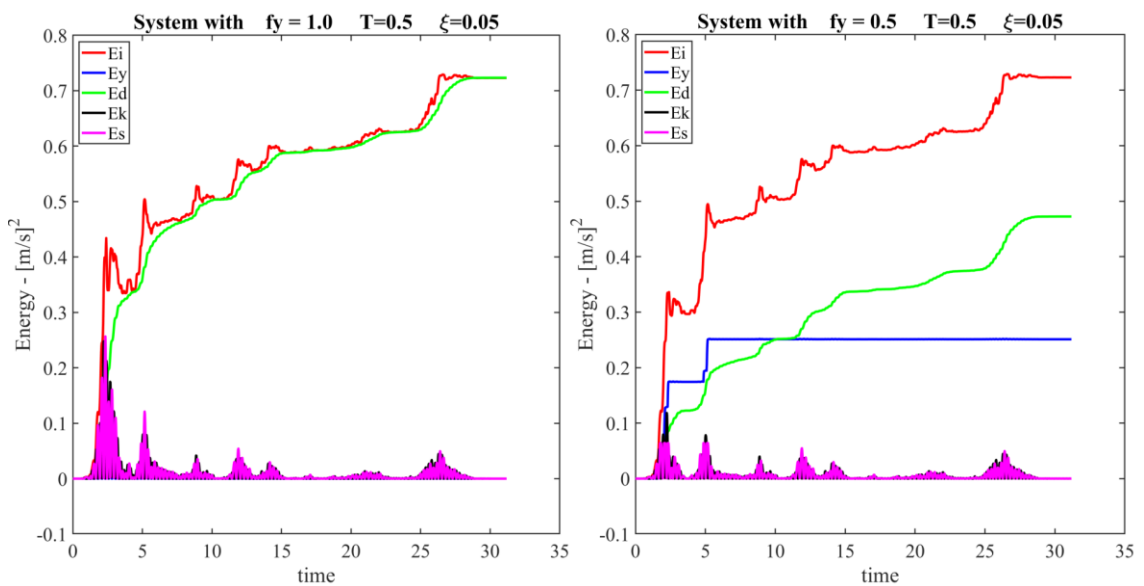


Figure B-7 Comparison between various levels Force-deformation relations

Figure B-7 shows, in addition to the enlargement of the force-displacement areas, the reduction in the resisting force with the decreasing of the normalized yield strength. This is even clearer looking at the energy plots at Figure B-8. As shown the amount of relative input energy ( $E_I$ ) that is absorbed by the SDOF is decreasing with the reduction of the levels of normalized yield strength. The first plot shows the elastic SDOF ( $f_{y\_} = 1$ ) which has also the highest value of energy dissipated by damping ( $E_D$ ), kinetic ( $E_K$ ) and strain ( $E_S$ ). Is interesting to see how the amount of dissipated energy by damping, changes (decrease) at every level of  $\bar{f}_y$  and from the elastic SDOF to the first Elasto-plastic SDOF ( $\bar{f}_y = 0.5$ ) the damping energy is decreasing substantially leaving a big part of dissipated energy to the yielding energy which was clearly absent in the elastic phase. The increasing of yielding energy along with the reduction of normalized yield strength is a proof that the yielding is absorbing energy to the detriment of all the other energies such as kinetic, strain and damping, being the system less stiff as the number of yield excursion increased (cumulative yield excursion). As discussed also the strain and kinematic energies have their peaks at the initial part of the graphs, where the structure is stiffer and  $N_y$  is minimal or zero, and then display relative peaks between the yield excursions.



**Figure B-8** Comparison between various levels Energies (time variation of energy): a) Elastic SDOF  $f_y=1$ , b) Elasto-plastic SDOF with  $f_y=0.5$

As mentioned before there are a few ratios which can be used to describe the energy process and that are representative of the SDOF behaviour as well. Those ratios are plotted against the time history and are essentially four (based on the relative input energy) plus one based on the yield values. The main two are the ratio between the hysteretic energy and the input energy ( $\eta = \frac{E_y}{E_I}$ )

and the ratio between the hysteretic energy and the maximum hysteretic energy ( $\lambda = \frac{E_y}{E_{ym}}$ ). The

Figure B-9 indicates values of the above ratios with different levels of normalized yield strength. Analysing the first two figures, where the normalized yield strength is about  $f_y=0.5$ , it can be noted that the kinetic and strain energy ratios dissipate quickly as soon as the structure starts to yield (as consequence of loss of stiffness), whereas the yield energy presents the maximum peak just right after the first group of yields and then it gradually decreases with the time showing less dissipation capacity at the end (clearly because there are presence of plastic residual displacements that reduce the ductility and therefore the yield energy capacity). On the contrary, the damping energy rises along the timescale until a point where intersects the yielding energy and exceed it becoming the biggest dissipative energy after 10s. This is very interesting because is happening for stiffer systems and is not happening for the others ( $f_y=0.25, f_y=0.125$ ) where the yielding energy is the biggest dissipative energy.

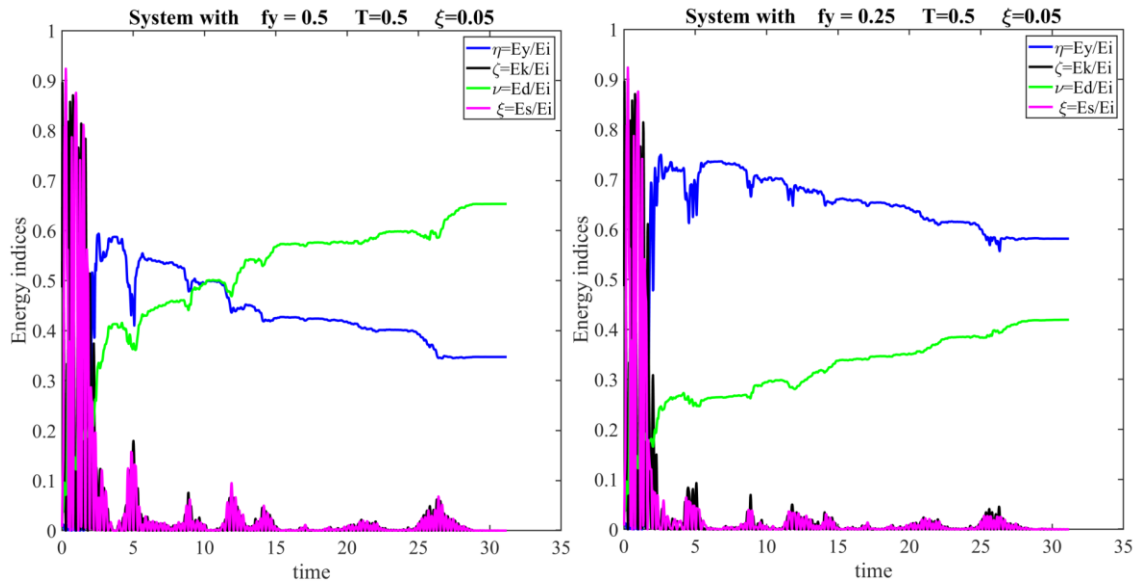


Figure B-10 Comparison between various levels Energy indices (time variation of energy): a) Elasto-plastic SDOF  $f_y=0.5$ , b) Elasto-plastic SDOF with  $f_y=0.25$

In addition for system with low normalized yield strength the ratio  $\eta$  is almost constant after the first step of yielding and at limit for  $\lim_{f_y \rightarrow 0} \eta = \frac{E_y}{E_i} \rightarrow const$ . Furthermore the system with  $f_{y-} = 0.5$  shows (Figure B-11 at the right) a 70% of dissipated energy, for hysteretic process, during the first 2.5s of the entire process where the first hinges are formed and then to reach 100% at the 2<sup>nd</sup> hinges, whereas the maximum ratio of  $\eta = \frac{E_y}{E_i}$  is about 60%, leaving also no possibility to have other yielding dissipation having reached the maximum quickly.

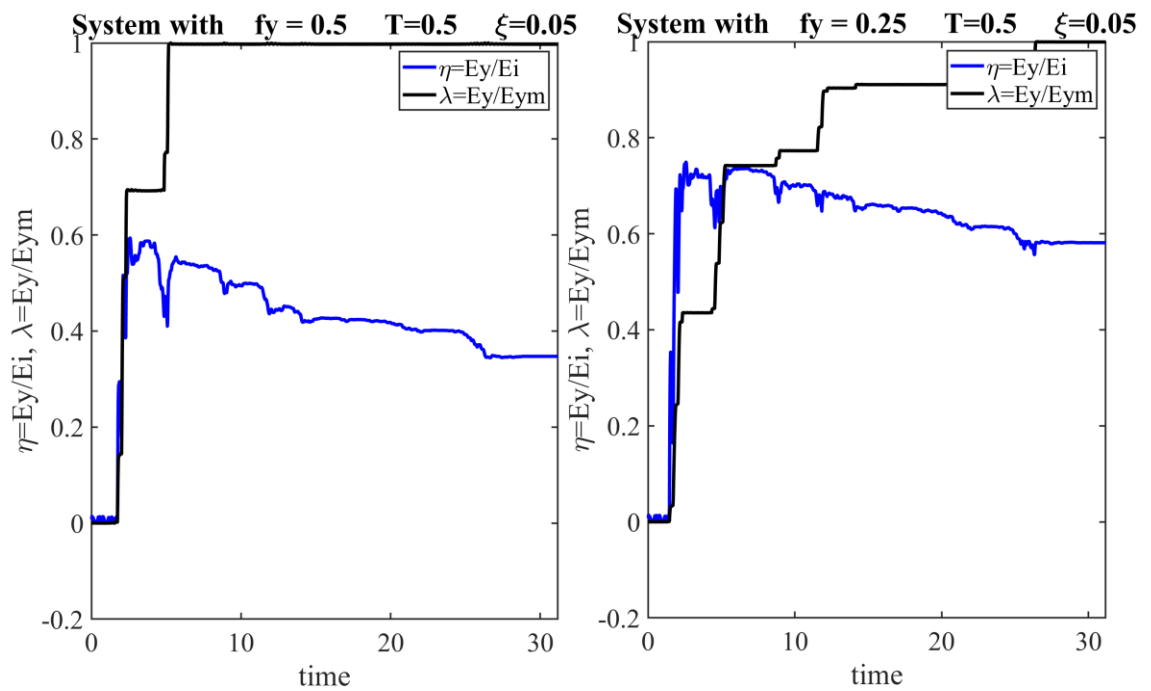


Figure B-12 Comparison between various energy indices  $\eta$  and  $\lambda$  (time variation of energy): a) Elasto-plastic SDOF  $f_y=0.5$ , b) Elasto-plastic SDOF with  $f_y=0.25$



# Appendix C

## Brief notes on Regression Analysis

## C1 Regression Analysis

The past three decades have witnessed exponential increase in the use of linear regression models as quantitative tool for both theoretical and applied science. The popularity of this tool is attributable to its intuitive credibility and its low computational cost (Benjamin and Cornell 1970). Linear regression is a power statistical procedure that explores and utilize the relation among data (variables) to produce a prediction model in order to foresee an outcome variable from the data investigated.

Suppose we collected a series of observations on a data pairs  $x, y$ . A linear model assumes the law which relates the mean of a random variable  $y$  with a non-random variable  $x$  is linear, such as

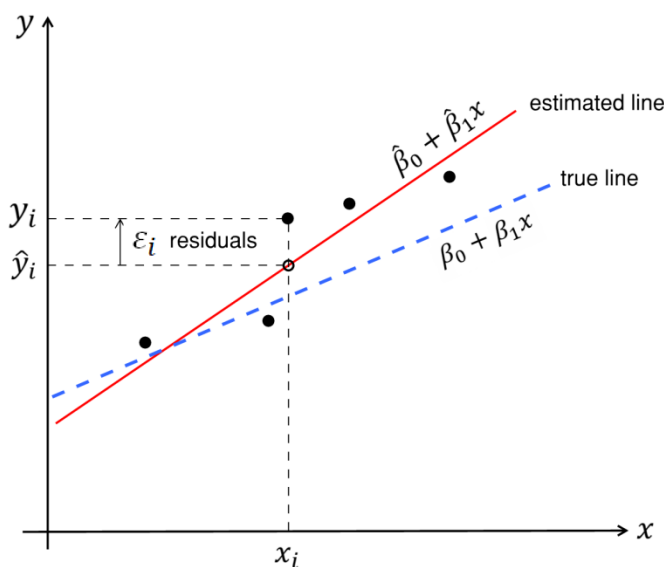


Figure C-1 Concepts of Regression Analysis

$$y_i = \beta_0 + \beta_1 x_i \quad \text{where } \varepsilon_i \text{ are called residuals}$$

The task of estimation is to obtain parameter estimators,  $\hat{\beta}_0$  and  $\hat{\beta}_1$  which *minimise* the vertical distance (residuals) between the data points and the estimator line

$$y_i = \hat{\beta}_0 + \hat{\beta}_1 x_i + \varepsilon_i \Rightarrow \varepsilon_i = y_i - (\hat{\beta}_0 + \hat{\beta}_1 x_i)$$

where  $\varepsilon_i$  are called residuals. It is assumed that the residuals are zero mean random variables with constant variance:

$$E(\varepsilon_i) = 0, E(\varepsilon_i^2) = \sigma_\varepsilon^2$$

To minimise the residuals, the *least square method* is commonly used

$$\min \left\{ \varepsilon_i^2 = \sum_{i=1}^n [y_i - (\hat{\beta}_0 + \hat{\beta}_1 x_i)]^2 \right\} \text{ residuals sum of squares}$$

The solution gives: (Benjamin and Cornell 1970)

$$\hat{\beta}_1 = \frac{\sum_{i=1}^n x_i y_i - \bar{y} \bar{x}}{\sum_{i=1}^n x_i^2 - n \bar{x}^2} \Rightarrow \hat{\beta}_1 = \frac{s_{x,y}}{s_x^2} \text{ is the first parameter estimator}$$

where:

$$\bar{x} = \frac{1}{n} (\sum_{i=1}^n x_i) \text{ is the sample mean of } x$$

$$\bar{y} = \frac{1}{n} (\sum_{i=1}^n y_i) \text{ is the sample mean of } y$$

$$s_{x,y} = \frac{1}{n} \sum_{i=1}^n x_i y_i - n \bar{x} \bar{y} \text{ is the sample covariance}$$

$$s_x^2 = \frac{1}{n} (\sum_{i=1}^n x_i^2 - n \bar{x}^2) \text{ is the sample standard deviation of } x$$

$$s_y^2 = \frac{1}{n} (\sum_{i=1}^n y_i^2 - n \bar{y}^2) \text{ is the sample standard deviation of } y$$

and

$$\hat{\beta}_0 = \bar{y} - \hat{\beta}_1 \cdot \bar{x} \text{ is the second parameter estimator}$$

$$\sigma_\varepsilon^2 = \frac{\varepsilon_i^2}{(n-2)} = \frac{\sum_{i=1}^n [y_i - (\hat{\beta}_0 + \hat{\beta}_1 x_i)]^2}{(n-2)} \text{ is the variance of the residuals}$$

$\sigma_\varepsilon$  is called the standard error of regression

$$R^2 = 1 - \frac{\varepsilon_i^2}{s_y^2} \text{ is the coefficient of determination}$$

$$c_v = \frac{\sigma_x}{\bar{x}} \text{ is the Coefficient of variation}$$



# Appendix D

## Significance Testing

## D1 Hypothesis testing

A conventional method, called *significance testing* (Benjamin and Cornell 1970), uses statistics to verify the validity of some hypothesis  $\mathcal{H}$ : a hypothesis is *falsified* or *rejected* by the significance test based on the statistics of observed empirical data acquired or generated to test the validity of the hypothesis. This process known as *falsification* was introduced by the philosopher Sir Karl Popper in 1934, in “*Logik der Forschung*“ (The Logic of Scientific Discovery).

In this setting, a statistical hypothesis is an estimation of the distribution of one or more random variables and a hypothesis testing is the process for establishing the validity of the hypothesis via statistical testing. If we assume that a distribution of a random vector  $\mathbf{x} = (x_1, x_2, \dots, x_n)$  of a density function  $f(\mathbf{x}, \theta)$  depends on a parameter  $\theta$ , then the hypothesis testing is to test the assumption where  $\theta = \theta_0$  or  $\theta \neq \theta_0$  (Papoulis and Pillai 2002). We define *null hypothesis* in the event of  $\theta = \theta_0$  denoted by  $\mathcal{H}_0$ , and *alternative hypothesis* in the event of  $\theta \neq \theta_0$  denoted by  $\mathcal{H}_a$ . The aim of the hypothesis testing is to establish whether statistical data may support the falsifiability of the null hypothesis. Mathematically this can be represented in the following way:

$$\text{if } \mathbf{x} = (x_1, x_2, \dots, x_n) \in \begin{cases} D_c \rightarrow \mathcal{H}_0 \text{ is falsified (rejected)} \\ \bar{D}_c \rightarrow \mathcal{H}_a \text{ is not falsified (accepted)} \end{cases}$$

where  $D_c$  is called the *falsified region* (or *critical region*).

Typically, the falsified region (critical region)  $D_c$  is of the form (Benjamin and Cornell 1970)

$$D_c := \{x := (x_1, x_2, \dots, x_n) : T(x) > c\}$$

where,  $T(x)$  is the test statistic and  $c$  is the *critical value*. Therefore, operatively the problem of finding the region  $D_c$  is reduced to that of finding appropriate  $T(x)$  and  $c$ . The outcome of any hypothesis test can be summarised as in the following table

	Not falsify <i>null hypothesis</i> $\mathcal{H}_0$	falsify <i>null hypothesis</i> $\mathcal{H}_0$
$\mathcal{H}_0$ is True	$(1 - \alpha_I)$ correct	Type I error
$\mathcal{H}_1$ is True	Type II error	$(1 - \beta_I)$ correct

## D2 Confidence interval

Confidence intervals (Mood et al. 1974, Chapra 2012) contains the exact value of  $\mu$  to be examined with a certain level of significance. The *significance level of the test* is called  $\alpha_I$  and it is chosen, normally, to have a value of 10%, 5% or 1%.

Then the confidence interval has to contain the parameter with a *confidence levels* (probability) of  $p = 1 - \alpha$ .

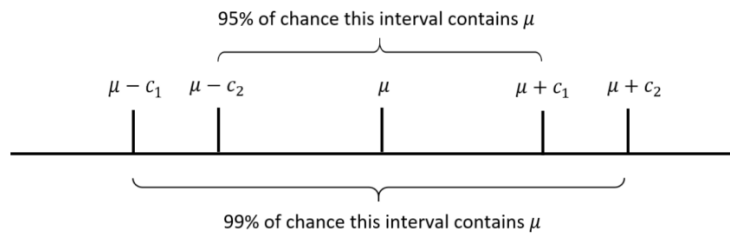


Figure D-1 Example of confidence intervals at significance levels  $\alpha_I = 5\%$  and  $\alpha_I = 1\%$

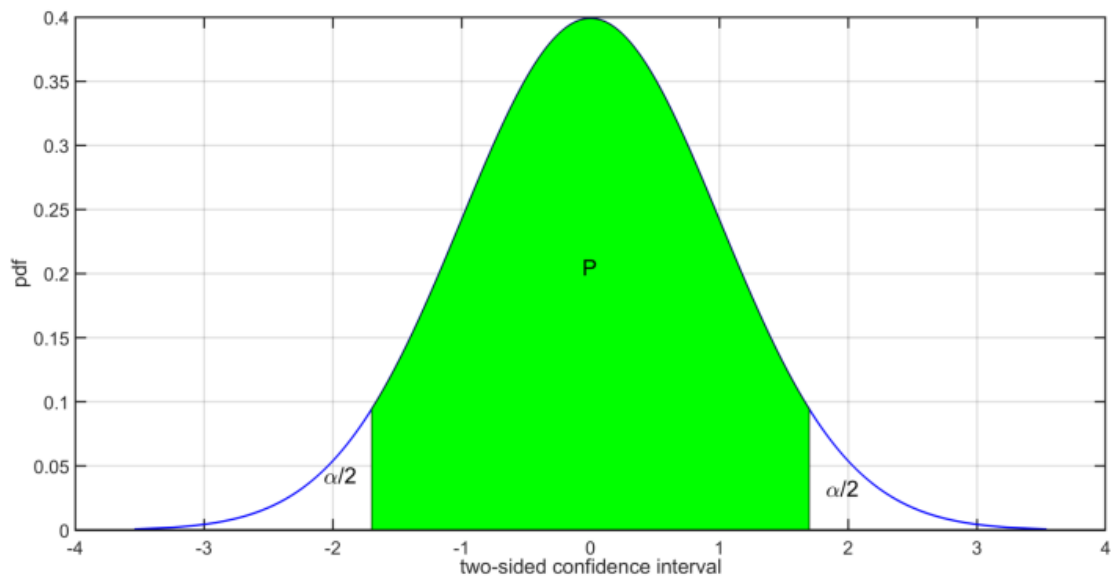


Figure D-2 Example of two-sided confidence intervals at significance levels  $\alpha_I/2$

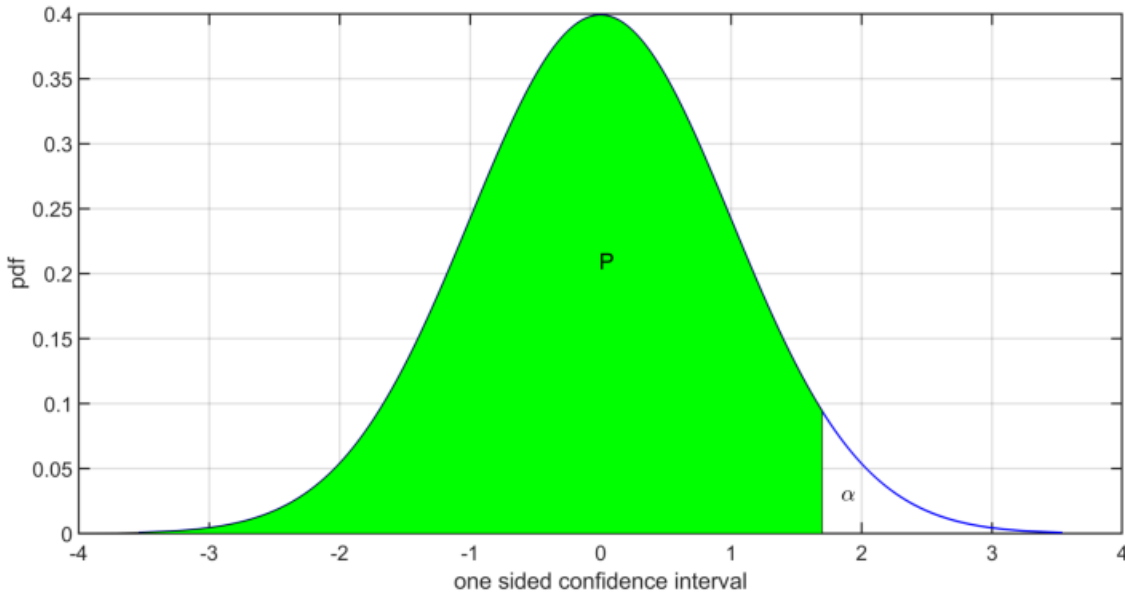


Figure D-3 Example one-sided confidence intervals at significance levels  $\alpha_I$

### D3 Type I and II errors

This is the error we make by choosing a critical value

$$P[\mu_0 - c \leq x \leq \mu_0 + c \mid \mathcal{H}_0] = 1 - \alpha_I$$

If the significant level's value is  $\frac{\alpha_I}{2} = 5\%$ , and assuming a standard normal distribution  $Z\left(\frac{\alpha_I}{2}\right) = \frac{\mu - \mu_0}{\sigma_0}$ , then the confidence interval  $c$  has to be equal to  $c = 1.65\sigma$  where  $\sigma$  is the standard deviation and  $\mu = \mu_0 - c$ .

In principle, therefore, on assuming a value of  $\alpha = 5\%$  eventually we will commit a so-called Type I error 5% of the time (Benjamin and Cornell 1970), (Mood, Graybill and Boes 1974).

Assuming instead that we accept the hypothesis  $\mathcal{H}_0$  when it is not true, then we are encountering in a type II error.

### D4 P-value of a Hypothesis test

The p-value indicate the *minimum significance level of the test*  $\alpha_I$  for which the Hypothesis  $\mathcal{H}_0$  is falsified (rejected). In mathematical terms:

$$p_{value} = \inf \{ \alpha_I : T(x) \in D_C \}$$

where  $T(x)$  is the test statistic  $D_C$  is falsified region (critical region).

Therefore, if there is a solid evidence against the null hypothesis  $\mathcal{H}_0$  then  $p_{value}$  is small.

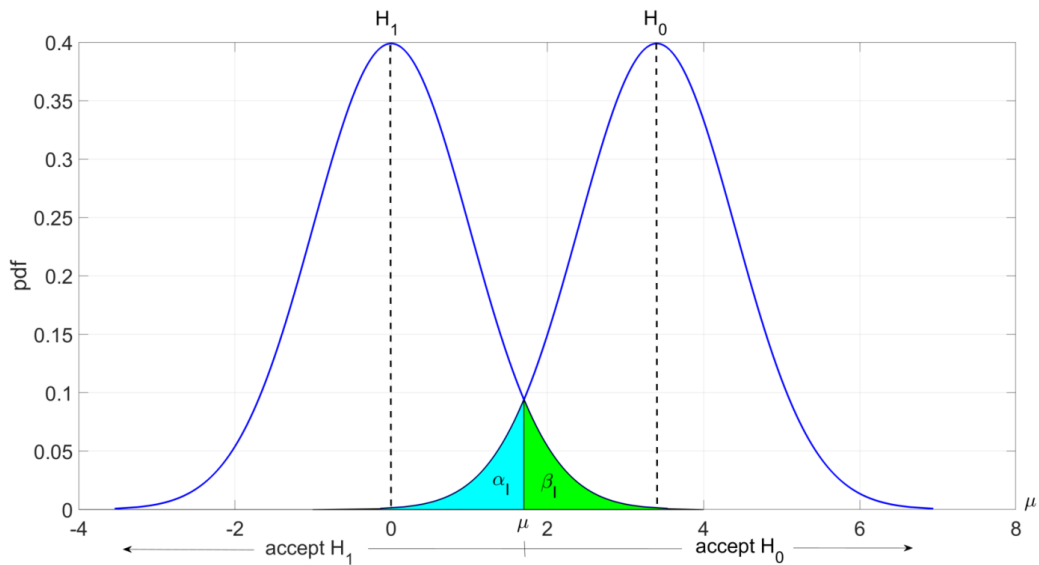


Figure D-4 Example of one-sided hypothesis testing

Smaller  $p_{value}$  suggests that the null hypothesis  $\mathcal{H}_0$  is likely to be falsified, but it is never completely negated. On using  $p_{value}$  we are not assessing any validity of the null hypothesis but rather how significant the evidence are against it (i.e., it is unlikely that  $\mathcal{H}_0$  is true but not impossible).

## D5 Regression analysis and Hypothesis test

Having established the rules for significance testing and determined the parameter estimators we have completed all we need for a statistical analysis of a dataset. As per Appendix C, if we assume a linear model (where the law which relates the mean of a random variable  $y$  with a non-random variable  $x$  is linear), such as

$$y_i = \beta_0 + \beta_1 x_i,$$

the question of most practical relevance to this thesis is how significantly different from zero the first parameter estimator  $\beta_1$  (i.e., the slope) is. To answer this question, we introduce the concept of p-value (as defined above p-values indicate the *minimum significance level of the test*  $\alpha_1$  for which the Hypothesis  $\mathcal{H}_0$  is falsified), which in mathematical terms can be seen as:

$$\mathcal{H}_0 : \text{the slope } \beta_1 = 0 ; \mathcal{H}_1 : \text{the intercept } \beta_0 = 0 \tag{0.1}$$

$$T(x): \text{Significance levels} = P[\text{reject } \mathcal{H}_0 \mid \mathcal{H}_0 \text{ correct}]$$

## Appendix D – Significance Testing

---

$$p_{value} = \inf \{ \alpha_I : T(x) \in D_C \} \quad (0.2)$$

where  $T(x)$  is the test statistic  $D_C$  is falsified region (critical region).



# Appendix E

## Implementation of Hysteretic Material in OpenSees

## E1 Hysteretic models

The Hysteretic models have been implemented in the OpenSees, finite element platform, using the Pinching4\_material property:

[[http://opensees.berkeley.edu/wiki/index.php/Pinching4\\_Material](http://opensees.berkeley.edu/wiki/index.php/Pinching4_Material)]

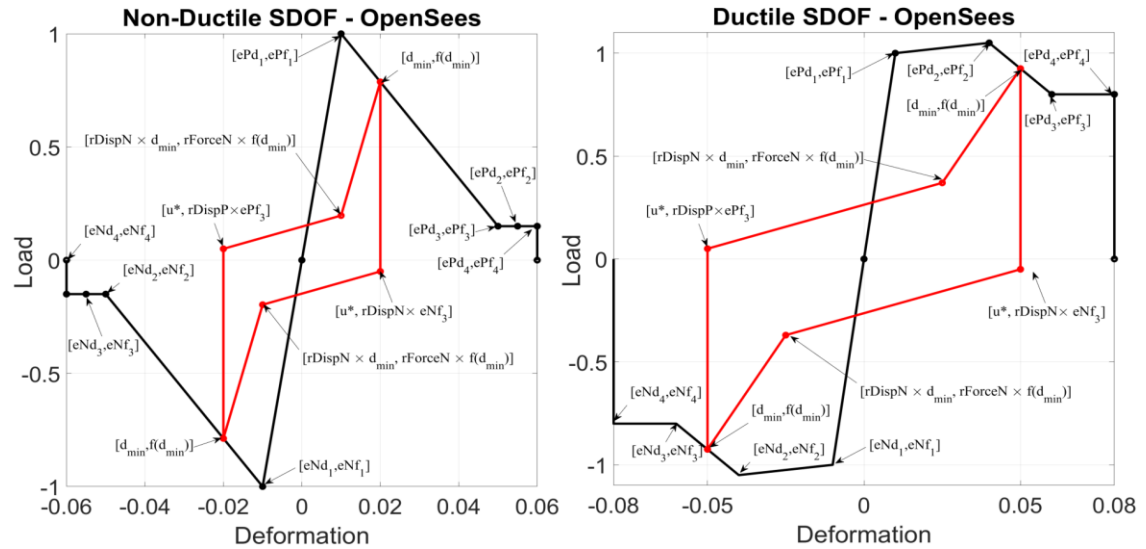


Figure E-1 Force–Displacement capacity boundary and Hysteretic cycles principles as adopted in OpenSees

The following tables describes the parameters, with their values, used as input in the settings of the material class:

Table E-1 Non-ductile SDOF Properties

uniaxialMaterial Pinching4		Non-Ductile SDOF
\$matTag	10	integer tag identifying material
\$ePf1 \$ePd1	1, 0.01	floating point values defining force points on the positive response envelope
\$ePf2 \$ePd2	0.15, 0.05	floating point values defining force points on the positive response envelope
\$ePf3 \$ePd3	0.15, 0.055	floating point values defining force points on the positive response envelope
\$ePf4 \$ePd4	0.15, 0.06	floating point values defining force points on the positive response envelope
\$eNf1 \$eNd1	-1 -0.01	floating point values defining force points on the negative response envelope
\$eNf2 \$eNd2	-0.15, -0.05	floating point values defining force points on the negative response envelope
\$eNf3 \$eNd3	-0.15, -0.055	floating point values defining force points on the negative response envelope
\$eNf4 \$eNd4	-0.15, -0.06	floating point values defining force points on the negative response envelope

Appendix E – Implementation of Hysteretic Material in Opensees

<b>\$rDispP \$rForceP \$uForceP</b>	0.5, 0.25, 0.05	floating point value defining the <b>ratio of the deformation</b> at which reloading occurs to the <i>maximum</i> historic deformation demand, the <b>ratio of the force</b> at which reloading begins to force corresponding to <i>the maximum</i> historic deformation demand and the <b>ratio of strength</b> developed upon unloading from negative load to the <i>maximum</i> strength developed under monotonic loading
<b>\$rDispN \$rForceN \$uForceN</b>	0.5, 0.25, 0.05	floating point value defining the <b>ratio of the deformation</b> at which reloading occurs to the <i>minimum</i> historic deformation demand, the <b>ratio of the force</b> at which reloading begins to force corresponding to the <i>minimum</i> historic deformation demand, and the <b>ratio of strength</b> developed upon unloading from negative load to the <i>minimum</i> strength developed under monotonic loading
<b>\$gK1 \$gK2 \$gK3 \$gK4 \$gKLim</b>	0, 0, 0, 0, 0	floating point values controlling cyclic degradation model for unloading stiffness degradation
<b>\$gD1 \$gD2 \$gD3 \$gD4 \$gDLim</b>	0, 0, 0, 0, 0	floating point values controlling cyclic degradation model for unloading stiffness degradation
<b>\$gF1 \$gF2 \$gF3 \$gF4 \$gFLim</b>	0, 0, 0, 0, 0	floating point values controlling cyclic degradation model for strength degradation
<b>\$gE</b>	10	floating point value used to define maximum energy dissipation under cyclic loading. Total energy dissipation capacity is defined as this factor multiplied by the energy dissipated under monotonic loading.
<b>\$dmgType</b>	"energy"	string to indicate type of damage

Table E-2 Ductile SDOF Properties

<b>uniaxialMaterial Pinching4</b>		<b>Ductile SDOF</b>
<b>\$matTag</b>	11	integer tag identifying material
<b>\$ePf1 \$ePd1</b>	1, 0.01	floating point values defining force points on the positive response envelope
<b>\$ePf2 \$ePd2</b>	1.05, 0.04	floating point values defining force points on the positive response envelope
<b>\$ePf3 \$ePd3</b>	0.8, 0.06	floating point values defining force points on the positive response envelope
<b>\$ePf4 \$ePd4</b>	0.8, 0.08	floating point values defining force points on the positive response envelope
<b>\$eNf1 \$eNd1</b>	-1 -0.01	floating point values defining force points on the negative response envelope
<b>\$eNf2 \$eNd2</b>	-1.05, -0.04	floating point values defining force points on the negative response envelope
<b>\$eNf3 \$eNd3</b>	-0.8, -0.06	floating point values defining force points on the negative response envelope
<b>\$eNf4 \$eNd4</b>	-0.8, -0.08	floating point values defining force points on the negative response envelope
<b>\$rDispP \$rForceP \$uForceP</b>	0.2, 0.4, 0.05	floating point value defining the <b>ratio of the deformation</b> at which reloading occurs to the <i>maximum</i> historic deformation demand, the <b>ratio of the force</b> at which reloading begins to force corresponding to <i>the maximum</i> historic deformation demand and the <b>ratio of strength</b> developed upon unloading from negative load to the <i>maximum</i> strength developed under monotonic loading

Appendix E – Implementation of Hysteretic Material in Opensees

<b>\$rDispN \$rForceN \$uForceN</b>	0.2, 0.4, 0.05	floating point value defining the <b>ratio of the deformation</b> at which reloading occurs to the <i>minimum</i> historic deformation demand, the <b>ratio of the force</b> at which reloading begins to force corresponding to the <i>minimum</i> historic deformation demand, and the <b>ratio of strength</b> developed upon unloading from negative load to the <i>minimum</i> strength developed under monotonic loading
<b>\$gK1 \$gK2 \$gK3 \$gK4 \$gKLim</b>	0, 0, 0, 0, 0	floating point values controlling cyclic degradation model for unloading stiffness degradation
<b>\$gD1 \$gD2 \$gD3 \$gD4 \$gDLim</b>	0, 0, 0, 0, 0	floating point values controlling cyclic degradation model for unloading stiffness degradation
<b>\$gF1 \$gF2 \$gF3 \$gF4 \$gFLim</b>	0, 0, 0, 0, 0	floating point values controlling cyclic degradation model for strength degradation
<b>\$gE</b>	10	floating point value used to define maximum energy dissipation under cyclic loading. Total energy dissipation capacity is defined as this factor multiplied by the energy dissipated under monotonic loading.
<b>\$dmgType</b>	"energy"	string to indicate type of damage



# Bibliography

- Aguiar-Conraria, L., and M.J. Soares. 2011. *The Continuous Wavelet Transform: A Primer*. NIPE WP 16-2011, Lisbon, Portugal: NIPE – Núcleo de Investigação em Políticas Económicas - Portugal - Lisbon.
- Akkar, S., and O. Ozen. 2005. “Effect of peak ground velocity on deformation demands for SDOF systems.” *Earthquake Engineering and Structural Dynamics* 34: 1551–1571.
- Amin, M., and A. H.S. Ang. 1968. “Nonstationary stochastic model of earthquake motions.” *ASCE Journal of Engineering Mechanical Division* 94: 559-583.
- Avramidis, I., A. Athanatopoulou, K. Morfidis, A. Sextos, and Giaralis A. 2016. *Eurocode-compliant seismic analysis and design of r/c buildings: Concepts, commentary and worked examples with flowcharts*. London: Springer International Publishing.
- Baker, J W, and C A Cornell. 2006. “Spectral shape, epsilon and record selection.” *Earthquake Engineering and Structural Dynamics* 35: 1077–1095.
- Baker, J. W. 2007. “Quantitative Classification of Near-Fault Ground Motions Using Wavelet Analysis.” *Bulletin of the Seismological Society of America* 97 (5): 1486-1501.
- Baker, J.W., and C.A. Cornell. 2005. “A vector-valued ground motion intensity measure consisting of spectral acceleration and epsilon.” *Earthquake Engineering and Structural Dynamics* 34: 1193–1217.
- Baraniuk, R.G., and D.L. Jones. 1996. “Wigner- based formulation of the chirplet transform.” *IEEE Transactions on Signal Processing* 44: 3129–3135.
- Basu, B., and B.K. Gupta. 1998. “Seismic Response Of Sdof Systems By Wavelet Modeling Of Nonstationary Processes.” *Journal Of Engineering Mechanics* 124 (10): 1142–1150.
- Basu, B. 2005. “Identification of stiffness degradation in structures using wavelet analysis.” *Construction and Building Materials* 19: 713–721.
- Beck, J.L., and C. Papadimitriou. 1993. “Moving resonance in nonlinear response to fully nonstationary stochastic ground motion.” *Probabilistic Engineering Mechanics* 8: 157–167.
- Benjamin, J.R, and C.A. Cornell. 1970. *Probability, Statistics. and Decision for Civil Engineers*. McGraw Hill, Inc.
- Boashash, B. 1992a. “Estimating and Interpreting The Instantaneous Frequency of a Signal-Part 1: Fundamentals.” *Proceedings of the IEEE* 80 (4): 520–538.
- Boashash, B. 1992b. “Estimating and Interpreting the Instantaneous Frequency of a Signal-Part 2: Algorithms and Applications.” *Proceedings of the IEEE* 80 (4): 540–568.

- Bojorquez, E, and I Iervolino. 2011. "Spectral shape proxies and nonlinear structural response." *Soil Dynamics and Earthquake Engineering* 996–1008.
- Bommer, J.J., and J.E. Alarcon. 2006. "The Prediction and Use Of Peak Ground Velocity." *Journal of Earthquake Engineering* 10: 1-1.
- Boore, D.M. 2003. "Simulation of ground motion using the stochastic method." *Pure and Applied Geophysics* 160: 635–676.
- Bracewell, R.N. 1999. *The Fourier Transform and Its Applications. Third Edition*. Mc-Graw Hill, New York.
- Brincker, R. and C.E. Ventura. 2015. *Introduction to Operational Modal Analysis.*: John Wiley & Sons, Ltd, Chichester.
- Bycroft, G. N. 1960. "White noise representation of earthquakes." *White noise representation of earthquakes" ASCE Journal of Engineering Mechanical Division* 86: 1–16.
- Carmona, R, W L Hwang, and B Torresani. 1997. "Characterization of Signals by the Ridges of Their Wavelet Transforms." *IEEE Transactions on Signal Processing* 45 (10): 2586–2590.
- Carmona, R, W L Hwang, and B Torresani. 1999. "Multiridge detection and time–frequency reconstruction." *IEEE Transactions on Signal Processing* 47 (2): 480–492.
- Castellanos, F., and M. Ordaz. 2013. "Damage severity estimation of an elastoplastic single-degree-of-freedom oscillator from its ground and response accelerations." *Structural Control and Health Monitoring* 21 (1): 1–22.
- CEN: Eurocode 8 - EN 1998-1. 2004. *Design of structures for earthquake resistance - Part 1: General rules, seismic actions and rules for buildings*. Brussels, Belgium: European Committee for Standardization.
- Çelebi, M., Y. Hisadab, R. Omranic, S.F. Ghaharic, and E. Taciroglu. 2016. "Responses of two tall buildings in Tokyo, Japan, before, during, and after the M9.0 Tohoku Earthquake of 11 March 2011." *Earthquake Spectra* 32: 463–495.
- Chandramohan, R., J.W. Baker, and G.G. Deierlein. 2015. "Quantifying the influence of ground motion duration on structural collapse capacity using spectrally equivalent records." *Earthquake Spectra* 32: 927–950.
- Chapra, S.C. 2012. *Applied Numerical Methods with Matlab*. New York, NY, USA: McGraw Hill.

- Chopra, A. K. 2007. *Dynamics Of Structures: Theory And Applications To Earthquake Engineering*. 3rd. Upper Saddle River, New Jersey, USA: Pearson Prentice Hall.
- Cohen, L. 1995. *Time- Frequency Analysis*. New Jersey: Prentice-Hall.
- Conraria, L A, and M J Soares. 2011. *The Continuous Wavelet Transform: A Primer*. WP 16/2011, NIPE.
- Conte, J.P, and B.F. Peng. 1997. "Fully Nonstationary Analytical Earthquake Ground-Motion Model." *Journal of Engineering Mechanics* 123 (1): 15–24.
- Cordova, P.P, G.G. Deierlein, S.S.F Mehanny, and C.A. Cornell. 2000 . "Development of A Two-Parameter Seismic Intensity Measure and Probabilistic Assessment Procedure." *2nd U.S.-Japan Workshop on Performance-Based Earthquake Engineering for Reinforced Concrete Building Structures*. Sapporo, Japan.
- Daubechies, I. 1988. "Orthogonal Bases of Compactly Supported Wavelets." *Communications on Pure and Applied Mathematics* 41: 909–996.
- De Angelis, M., A. Giaralis, F. Petrini, and D. Pietrosanti. 2019 . "Optimal tuning and assessment of inertial dampers with grounded inerter for vibration control of seismically excited base-isolated systems." *Engineering Structures* 196: 109250.
- Deierlein, G.G. 2004. "Overview of a Comprehensive Framework for Earthquake Performance Assessment." *Performance-Based seismic Design Concepts and Implementation - Proceedings of an International Workshop*. Bled, Slovenia: PEER 2004/05. 15-26.
- Der Kiureghian, A., and O. Ditlevsen. 2009. "Aleatory or epistemic? Does it matter?" *Structural Safety* 31 (2): 105–112.
- DiPasquale, E., and A. S. Cakmak. 1990. "Detection of seismic structural damage using parameter-based global damage indices." *Probabilistic Engineering Mechanics* 5 (2): 60–65.
- Ebrahimian, H., F. Jalayer, A. Lucchini, F. Mollaioli, and G. Manfredi. 2015. "Preliminary ranking of alternative scalar and vector intensity measures of ground shaking." *Bulletin of Earthquake Engineering* 13: 2805–2840.
- Failla, Giuseppe, and Pol D Spanos. 2005. "Wavelets: Theoretical Concepts and Vibrations Related Applications." *The Shock and Vibration Digest* 5 (37): 359–375.
- Fajfar, P, and H Krawinkler. 2004. "Performance-Based Seismic Design - Concepts and Implementation." *PEER Report 2004/05*. Bled, Slovenia: Proceedings of the International Workshop.

- Fajfar, P. 2000. "A Nonlinear Analysis Method for \performance Based Seismic Design." *Earthquake Spectra* 16: 573–592.
- Fan, F.G., and G. Ahmadi. 1990. "Nonstationary Kanai-Tajimi models for El Centro 1940 and Mexico City 1985 earthquake." *Probabilistic Engineering Mechanics* 5: 171–181.
- FEMA 349. 2000. *Action Plan for Performance Based Seismic Design*. Washington, D.C., USA: Federal Emergency Management Agency.
- FEMA P440A. 2009. *Effects of Strength and Stiffness Degradation on Seismic Response*. Washington, D.C., USA: Federal Emergency Management Agency.
- FEMA P-58-1. 2012. *Seismic Performance Assessment of Buildings Volume 1 – Methodology*. Washington, D.C., USA: Prepared by the Applied Technology Council for the Federal Emergency Management Agency.
- FEMA-273. 1997. *NEHRP guidelines for the seismic rehabilitation of buildings*. Washington, D.C.: Federal Emergency Management Agency.
- Filippou, F. C., E. P. Popov, and V. V. Bertero. 1983. *Effects of Bond Deterioration on Hysteretic Behavior of Reinforced Concrete Joints*. EERC 83-19, Berkeley, CA USA: Earthquake Engineering Research Center, University of California.
- Flandrin, P. and P. Gonçaves. 2004. "Empirical mode decompositions as data-driven wavelet-like expansions." *International Journal of Wavelets, Multiresolution & Information Processing* 2: 477–496.
- Gabor, Dennis. 1946. "Theory of communication." *IEEE* 429-457.
- Giaralis, A. 2008. "Wavelet based response spectrum compatible synthesis of accelerograms and statistical linearization based analysis of the peak response of inelastic systems." Ph.D. Thesis. Dept of Civil and Environmental Engineering, Rice University, Houston.
- Giaralis, A., and P. D. Spanos. 2009. "Wavelet-based response spectrum compatible synthesis of accelerograms Eurocode application (EC8)." *Soil Dynamics and Earthquake Engineering* 29 (1): 219–235.
- Giaralis, A. and P.D. Spanos. 2012. "Derivation of response spectrum compatible non-stationary stochastic processes relying on Monte Carlo peak factor estimation." *Earthquake and Structures* 3: 581–609.
- Gkoktsi, K., and A. Giaralis. 2015. "Effect of frequency domain attributes of wavelet analysis filter banks for structural damage localization using the relative wavelet entropy index." *International Journal of Sustainable Materials and Structural Systems (IJSMSS)* 2 (1/2): 134–160.

- Giaralis, A., I.A. Kougioumtzoglou, and K. Dos Santos. 2017. “Non-stationary stochastic dynamics response analysis of bilinear oscillators to pulse-like ground motions.” *Proceedings of the 16th World Conference on Earthquake Engineering- 16WCEE*, paper #3401, p.12.
- Gkoktsi, K., and A. Giaralis. 2020. “A compressive MUSIC spectral approach for identification of closely-spaced structural natural frequencies and post-earthquake damage detection.” *Probabilistic Engineering Mechanics* 60: 103030.
- Goupillaud, P., A. Grossmann, and J. Morlet. 1984. “Cycle-octave and related transforms in seismic signal analysis.” *Geoexploration* 85–102.
- Grossmann, A, and J Morlet. 1984. “Decomposition of Hardy functions into square integrable wavelets of constant shape.” *SIAM J. Math.* 15: 723–736.
- Haselton, C.B., A.B. Liel, G.G. Deierlein, B.S. Dean, and J.H. Chou. 2011. “Seismic Collapse Safety of Reinforced Concrete Buildings. I: Assessment of Ductile Moment Frames.” *Journal of Structural Engineering, ASCE* 137: 481–491.
- Haselton, C.B., and G.G. Deierlein. 2007. *Assessing seismic collapse safety of modern reinforced concrete frame buildings*. Berkeley, CA, USA: PEER Rep. 2007/08, PEER Center, Univ. of California.
- Housner, G.W. 1947. “Characteristics of strong motion earthquakes.” *Bulletin of the Seismological Society of America* 37: 19–31.
- Housner, G.W. 1955. “Properties of strong motion earthquakes.” *Bulletin of the Seismological Society of America* 45: 197–218.
- Housner, G.W., and P.C Jennings. 1964. “Generation of artificial earthquakes.” *Generation of artificial earthquakes” ASCE Journal of Engineering Mechanical Division* 90: 113–150.
- Howell, D.C. 2007. *Statistical methods for psychology*. Belmont, CA, USA: Thompson Wadsworth.
- Hsu, T I, and M C Bernard. 1978. “A random process for earthquake simulation.” *Earthquake Engineering and Structural Dynamics* 6: 347–362.
- Huang, N.E., Z., Shen, S.R. Long, M.C. Wu, H.H. Shih, Q. Zheng, N.C. Yen, C.C. Tung, and H.H. Liu. 1998. “The empirical mode decomposition and the Hilbert spectrum for nonlinear and non-stationary time series analysis.” *Proceedings of the Royal Society of London, Series A*, 454: 903–995.
- Ibarra, L. F., R. Medina, and H. Krawinkler. 2005. “Hysteretic models that incorporate strength and stiffness degradation.” *Earthquake Engineering Structural Dynamics* 34: 1489–1511.

- INNOSEIS - Valorization of innovative anti-seismic devices. 2017. *Recommended procedure for EN1998-compatible behaviour factor evaluation of new structural systems*. Brussels, Belgium: European Commission - Research Programme of the Research Fund for Coal and Steel.
- Iwan, W D, and Z K Hou. 1989. "Explicit solutions for the response of simple systems subject to non stationary random excitation." *Structural Safety* 6: 77–86.
- Iyama, Jun, and Hitoshi Kuwamura. 1999. "Application of wavelets to analysis and simulation of earthquake motions." *Earthquake Engineering & Structural Dynamics* 28 (3): 255–272.
- Jalayer F., De Risi R., Manfredi G. 2015. "Bayesian Cloud Analysis: efficient structural fragility assessment using linear regression." *Bulletin of Earthquake Engineering* 1183–1203.
- Jalayer F., Ebrahimian H., Miano A., Manfredi G., Sezen H. 2017. "Analytical fragility assessment using unscaled ground motion records." *Earthquake Engineering and Structural Dynamics* 2639–2663.
- Jalayer, F., and J.L. Beck. 2008. "Effect of the alternative representations of ground motion uncertainty on seismic risk assessment of structures." *Earthquake Engineering and Structural Dynamics* 37 (1): 61–79.
- Jalayer, F., J.L. Beck, and F. Zareian. 2012. "Analyzing the sufficiency of alternative scalar and vector intensity measures of ground shaking based on information theory." *Journal of Engineering Mechanics ASCE* 138: 307-316.
- Jennings, P C, G W Housner, and N C Tsai. 1968. *Simulated Earthquake Motions*. Report, Earthquake Engineering Research Lab. Calif. Inst. Tech.
- Jian, F., Z. Yanping, and L. Xiaohong. 2014. "Establishment of a time-varying modified Kanai-Tajimi non stationary stochastic model of seismic records based on the S-transform." *Journal of Earthquake Engineering* 18: 876-890.
- Kalkan, E., and S. K. Kunnath. 2007. "Effective cyclic energy as a measure of seismic demand." *Journal of Earthquake Engineering* 11: 725–751.
- Kanai, K. 1957. "Semi-empirical formula for the seismic characteristics of the ground." *University of Tokyo, Bulletin of the Earthquake Research Institute* 35: 309–325.
- Katsanos, E. I. and A. G. Sextos. 2015. "Inelastic spectra to predict period elongation of structures under earthquake loading." *Earthquake Engineering and Structural Dynamics* 44: 1765–1782.

- Katsanos, E. I., A. G. Sextos, and A. S. Elnashai. 2014. "Prediction of inelastic response periods of buildings based on intensity measures and analytical model parameters." *Engineering Structures* 71 (15): 161-177.
- Katsanos, E.I., A.G. Sextos, and G.D. Manolis. 2010. "Selection of earthquake ground motion records: A state-of-the-art review from a structural engineering perspective." *Soil Dynamics and Earthquake Engineering* 30: 157-169.
- Kazantzi, A.K., and D. Vamvatsikos. 2015. "Intensity measure selection for vulnerability studies of building classes." *Earthquake Engineering and Structural Dynamics* 44: 2677–2694.
- Kijewski-Correa T and Kareem A. (2006). Efficacy of Hilbert and wavelet transforms for time-frequency analysis. *Journal of Engineering Mechanics*, ASCE, 132: 1037-1049.
- Kohrangi, M, Bazzurro, P., D Vamvatsikos, and A. Spillatura. 2017. "Conditional spectrum-based ground motion record selection using average spectral acceleration." *Earthquake Engineering and Structural Dynamics* 46: 1667-1685.
- Kohrangi, M., P. Bazzurro, and D. Vamvatsikos. 2016. "Vector and scalar IMs in structural response estimation: part II—building demand assessment." *Earthquake Spectra* 32: 1525–1543.
- Kramer, Steven L. 1996. *Geotechnical Earthquake Engineering*. New Jersey: Prentice Hall.
- Krawinkler, H., and E. Miranda. 2004. "Performance-Based Earthquake Engineering." In *Engineering Seismology to Performance-Based Engineering*, by Y. Bozorgnia and V.V. Bertero, 9-1,9-59. Chapman and Hall/CRC.
- Kumar, M., J. M. Castro, P. J. Stafford, and A. Y. Elghazouli. 2011. "Influence of the mean period of ground motion on the inelastic dynamic response of single and multi degree of freedom systems." *Earthquake Engineering And Structural Dynamics* 40: 237–256.
- Li, Y., J.P. Conte, and M. Barbato. 2016. "Influence of time-varying frequency content in earthquake ground motions on seismic response of linear elastic systems." *Earthquake Engineering and Structural Dynamics* 45: 1271-1291.
- Liel, . A.B., C.B. Haselton, G.G. Deierlein, and Baker J.W. 2009. "Incorporating modeling uncertainties in the assessment of seismic collapse risk of buildings." *Structural Safety* 31 (2): 197–211.
- Liel, A.B., C.B Haselton, G.G. Deierlein, and J.W. Baker. 2009. "Incorporating modeling uncertainties in the assessment of seismic collapse risk of buildings." *Structural Safety* 31 (2): 197-211.

- Lilly, J. M., and S. C. Olhede. 2009. "Higher-Order Properties of Analytic Wavelets." *IEEE Transactions on signal processing* 57 (1): 146–160.
- Lilly, J M, and S C Olhede . 2010. "On the Analytic Wavelet Transform." *IEEE Transactions on Information Theory* 56 (8): 4135–4156.
- Luco, N., and C.A. Cornell. 2007. "Structure-Specific Scalar Intensity Measures for Near-Source and Ordinary Earthquake Ground Motions." *Earthquake Spectra* 23: 357–392.
- Mallat, S G. 1989. "A Theory for Multiresolution Signal Decomposition: The Wavelet Representation." *IEEE Transactions on Pattern Analysis and Machine Intelligence* 11 (7): 674-693.
- Mallat, S G. 1998. *A Wavelet Tour of Signal Processing*. 3rd. San Diego, CA, USA: Academic Press.
- Margnelli, A., and A. Giaralis. 2017. "Non-stationary frequency content characterization of seismic accelerograms via the slope "alpha" of the wavelet-based mean instantaneous period." *16th World Conference on Earthquake Engineering*. Santiago, Chile. paper #4106.
- Margnelli, A., and A. Giaralis. 2015. "Wavelet-based mean instantaneous period (MIP) of ground motions and time-varying period elongation of earthquake excited hysteretic structures." *Proceedings of the SECED 2015 Conference on Earthquake Risk and Engineering towards a Resilient World*. Cambridge, UK.
- Margnelli, A., M. Kohrangi, A. Giaralis, and D. Vamvatsikos. 2018. "Influence of Non-Stationary Frequency Content of Recorded Ground Motions to Seismic Demand of Multi-Storey Structures via the vavelet-based alpha index." *16th European Conference on Earthquake Engineering*. Thessaloniki, Greece.
- Mann, S., and S. Haykin. 1995. "The chirplet transform: Physical considerations." *IEEE Transactions on Signal Processing*, 43: 2745–2761.
- MATLAB version R.2019a. . 2019. Natick, Massachusetts, USA: The MathWorks Inc., 2010.
- McGuire, R.K. 1995. *Seismic Hazard and Risk Analysis*. Monograph MNO-10, Oakland: Earthquake Engineering Research Institute.
- McKenna, F., and G. Fenves. 2001. *The OpenSees Command Language Manual: version 3.0.3*. Berkeley, CA, USA: Pacific Earthquake Engineering Center.
- Menegotto, M., and P.E. Pinto. 1973. "Method of analysis for cyclically loaded R.C. plane frames including changes in geometry and non-elastic behaviour of elements under combined normal force and bending." *Preliminary Report IABSE*, 13.

- Michel, C. and P. Gueguen. 2011. "Time-frequency analysis of small frequency variations in civil engineering structures under weak and strong motions using a reassignment method." *Structural Health Monitoring* 9(2):159–171.
- Minas, S., and C. Galasso. 2019. "Accounting for spectral shape in simplified fragility analysis of case-study reinforced concrete frames." *Soil Dynamics and Earthquake Engineering* 119: 91–103.
- Moehle, J., and G.G. Deierlein. 2004. "A Framework Methodology for Performance-Based Earthquake Engineering." *13th World Conference on Earthquake Engineering*. Vancouver, B.C., Canada.
- Mollaioli, F., A. Lucchini, Y. Cheng, and G. Monti. 2013. "Intensity measures for the seismic response prediction of base-isolated buildings." *Bulletin of Earthquake Engineering* 11: 1841–1866.
- Mollaioli, F., S. Bruno, L. Decanini, and R. Saragoni. 2011. "Correlations between energy and displacement demands for performance-based seismic engineering." *Pure and Applied Geophysics* 168: 237–259.
- Montejo, L. A., and M. J. Kowalsky. 2008. "Estimation of frequency-dependent strong motion duration via wavelets and its influence on nonlinear seismic response." *Computer-Aided Civil and Infrastructure Engineering* 23 (4): 253-264.
- Mood, A.M., F.A. Graybill, and D.C. Boes. 1974. *Introduction to the Theory of Statistics*. New York, NY, USA: McGraw Hill International Editions.
- Mucciarelli, M., A. Masi, M.S. Gallipoli, P. Harabaglia, M. Vona, F. Ponso, and M. Dolce. 2004. "Analysis of RC building dynamic response and soil building resonance based on data recorded during a damaging earthquake (Molise, Italy, 2002)." *Bulletin of the Seismological Society of America* 94(5): 1943–53.
- Muscolino, G. 2002. *Dinamica delle strutture*. 1st, in italian. Milano: McGraw-Hill.
- Mwafy, A.M., and A.S. Elnashai. 2001. "Static pushover versus dynamic collapse analysis of RC buildings." *Engineering Structures* (23): 407–424.
- Newland, D. E. 1994. "Harmonic and musical wavelets." *Proceedings of Royal Society of London* 605-620.
- Noh, H. Y., K. K. Nair, D. G. Lignos, and A. S. Kiremidjian. 2011. "Use of Wavelet-Based Damage-Sensitive Features for Structural Damage Diagnosis Using Strong Motion Data." *Journal of Structural Engineering* 137 (10): 1215-1228.

- Noh, H Y, D G Lignos, K K Nair, and A S Kiremidjian. 2012. "Development of fragility functions as a damage classification/prediction method for steel moment-resisting frames using a wavelet-based damage sensitive feature." *Earthquake Engineering Structure Dynamics* 41: 681–696.
- Omori, F. 1922. "The semi-destructive earthquake of April 26." *Seismological Notes* (Imperial Earthquake Investigation Committee), 3:1-30, 1922.
- Pampanin, S., C. Christopoulos, and M.J.N. Priestley. 2002. *Residual Deformations in the Performance-Seismic Assessment of Frame Structures*. Research Report No. ROSE-2002/02, Pavia, Italy: European School for Advanced Studies in Reduction of Seismic Risk.
- Pan, T.-C., and C. L. Lee. 2002. "Application of wavelet theory to identify yielding in seismic response of bi-linear structures." *Earthquake Engineering Structural Dynamics* 31: 379–398.
- Panagiotakos, T.B., and Fardis M.N. 2001. "Deformations of reinforced concrete members at yielding and ultimate." *ACI Structural Journal* 2 (98): 135–148.
- Papoulis, A. 1997. *Signal Analysis*. McGraw-Hill, New York.
- Papoulis, A., and S.U. Pillai. 2002. *Probability, Random Variables and Stochastic Process*. New York, NY, USA: McGraw Hill Higher Education.
- Park, Y.-J., A.H.-S. Ang, and Y.K. Wen. 1985. "Seismic Damage Analysis of Reinforced Concrete Buildings." *Journal of Structural Engineering, ASCE* 111: 740-757.
- Paulay, T., and M.J.N. Priestley. 1992. *Seismic Design of Reinforced Concrete and Masonry Buildings*. New York, NY, USA: John Wiley & Sons, inc.
- PEER 2003/10. 2004. *A Beam-Column Joint Model for Simulating the Earthquake Response of Reinforced Concrete Frames*. Berkeley, CA, USA: Pacific Earthquake Engineering Research Center.
- PEER Report 2007/08. 2008. *Assessing Seismic Collapse Safety of Modern Reinforced Concrete Moment-Frame Buildings*. Berkeley: Pacific Earthquake Engineering Research Center.
- Pinto, P.E., R. Giannini, and Franchin P. 2004. *Seismic Reliability Analysis of Structures*. Pavia, Italy: IUSS Press.
- Porter, K.A. 2003. "An Overview of PEER's Performance-Based Earthquake Engineering Methodology." *Conference of Applications of Statistics and Probability in Civil Engineering (ICASP9)*. San Francisco, CA, USA: Civil Engineering Risk and Reliability Association (CERRA).

- Porter, K., and I. Cho. (2013). Characterizing a building class via key features and index buildings for class-level vulnerability functions. *Proceedings of the 11th International Conference on Structural Safety & Reliability (ICOSSAR)*, Columbia University, New York.
- Priestley, M.J.N., G.M. Calvi, and M.J. Kowalsky. 2007. *Displacement-Based Seismic Design of Structures*. Pavia, Italy: IUSS Press.
- Qian S. 2001. *Introduction to time-frequency and wavelet transforms*. Prentice-Hall, New Jersey.
- Rathje, E.M., N. A. Abrahamson, and J. D. Bray. 1998. "Simplified frequency Content Estimates of Earthquake Ground Motions." *Journal of Geotechnical and Geoenvironmental Engineering* 124 (2): 150–159.
- Rathje, E.M., F. Faraj, S. Russel and J.D. Bray. 2004. "Empirical relationships for frequency content parameters of earthquake ground motions." *Earthquake Spectra* 20: 119–144.
- Regnier, J. Michel C, Bertrand E, Gueguen P (2013) Contribution of ambient vibration recordings (free-field and buildings) for post-seismic analysis: The case of the Mw 7.3 Martinique (French Lesser Antilles) earthquake, November 29, 2007. *Soil Dynamics and Earthquake Engineering*, 50:162-167.
- Rezaeian, S., and Der Kiureghian A. 2008. "A stochastic ground motion model with separable temporal and spectral nonstationarities." *Earthquake Engineering and Structural Dynamics* 37: 1565-1584.
- Rezaeian, S.; Der Kiureghian, A. - PEER 2010/02. 2010. *Stochastic Modeling and Simulation of Ground Motions for Performance-Based Earthquake Engineering*. Berkeley, C.A., USA: Pacific Earthquake Engineering Research.
- Roberts, J B, and P D Spanos. 1999. *Random Vibration and Statistical Linearization*. 1st. New York: Dover Publications inc.
- Ruiz-Garcia, J., and E. Miranda. 2003. "Inelastic displacement ratio for evaluation of existing structures." *Earthquake Engineering and Structural Dynamic* 32: 1237-1258.
- Ruzzene, M., A. Fasana, L. Garibaldi, and B. Piombo. 1997. "Natural Frequencies and Dampings Identification using Wavelet Transform: Application to Real Data." *Mechanical Systems and Signal Processing* 2 (11): 207-218.
- Saragoni, G.R., and G.C. Hart. 1974. "Simulation of artificial earthquakes." *Earthquake Engineering and Structural Dynamics* 2: 249-267.
- SEAOC Vision 2000. 1995. *Performance based seismic engineering of buildings*. Sacramento, California, USA: Structural Engineers Association of California.

- Shinozuka, M, and Y Sato. 1967. "Simulation of nonstationary random processes." *ASCE J. Eng. Mech. Div.* 93: 11-40.
- Shome, N, and C,A Cornell. 1999. *Probabilistic seismic demand analysis of nonlinear structures*. Reliability of Marine Structures Report, Stanford, CA USA: Dept. of Civ. and Envir. Engrg. Stanford University.
- Smerzini, C., C Galasso, I Iervolino, and R. Paolucci. 2014. "Ground motion record selection based on broadband spectral compatibility." *Earthquake Spectra* 30 (4): 1427-1448.
- Spanos, P.D., and L.M. Vargas Loli. 1985. "A statistical approach to generation of design spectrum compatible earthquake time histories." *Soil Dynamics and Earthquake Engineering* 4: 2-8.
- Spanos, P. D., and G. Failla. 2005. "Wavelets: Theoretical Concepts and Vibrations Related Applications." *The Shock and Vibration Digest* 37 (5): 359-375.
- Spanos, P.D., A. Giaralis, and N.P. Politis. 2007a. "Time-frequency representation of earthquake accelerograms and inelastic structural response records using the adaptive chirplet decomposition and empirical mode decomposition." *Soil Dynamics & Earthquake Engineering* 27: 675- 689.
- Spanos, P.D., A. Giaralis, N.P. Politis, and J.M. Roessett. 2007b. "Numerical treatment of seismic accelerograms and of inelastic seismic structural responses using harmonic wavelets." *Computer-Aided Civil & Infrastructure Engineering* 22: 254-264.
- Staszewski WJ. (1998a). Structural and mechanical damage detection using wavelets. *The Shock and Vibration Digest*, 30: 457-472.
- Staszewski WJ. (1998b). Identification of non-linear systems using multi-scale ridges and skeletons of the wavelet transform. *Journal of Sound and Vibration*, 214: 639-658.
- Steel02, Opensees. n.d. "[http://opensees.berkeley.edu/wiki/index.php/Steel02\\_Material\\_-\\_Giuffr%C3%A9-Menegotto-Pinto\\_Model\\_with\\_Isotropic\\_Strain\\_Hardening](http://opensees.berkeley.edu/wiki/index.php/Steel02_Material_-_Giuffr%C3%A9-Menegotto-Pinto_Model_with_Isotropic_Strain_Hardening)."
- Stewart, J P, S J Chiou, J D Bray, R W Graves, P G Somerville, and N A Abrahamson. 2001a. *Ground Motion Evaluation Procedures for Performance-Based Design*. Report No. PEER-2001/09, Berkeley, CA, USA: PEER Report 2001/09, University of California, 229.
- Taflanidis, A.A., and G. Jia. 2011. "A simulation-based framework for risk assessment and probabilistic sensitivity analysis of base-isolated structures." *Earthquake Engineering and Structural dynamics* 40: 1629-1651.

- Tajimi, H. 1960. "A statistical method of determining the maximum response of a building structure during an earthquake." *Tokyo and Kyoto* 781–797.
- Thomson, W.T. 1959. "Spectral aspect of earthquakes," *Bulletin of the Seismological Society of America* 49: 91–98.
- Todorovska, M.I. and M.D. Trifunac. 2010. "Earthquake damage detection in the Imperial Country Services Building I: The data and time-frequency analysis." *Soil Dynamics and Earthquake Engineering* 27: 564–576.
- Torrence, C, and G P Compo. 1997. "A Practical Guide to Wavelet Analysis." *Bulletin of American Meteorological Society* 61–78.
- Tothong, P, and C. A Cornell. 2007. *Probabilistic Seismic Demand Analysis Using Advanced Ground Motion Intensity Measures, Attenuation Relationships, and Near-Fault Effects*. PEER Report 2006/11, Berkeley, CA USA: Pacific Earthquake Engineering Research Center.
- Tothong, P., and N. Luco. 2007. "Probabilistic seismic demand analysis using advanced ground motion intensity measures." *Earthquake Engineering and Structural Dynamics* 36: 1837–1860.
- Trevlopoulos, K., and P. Guéguen. 2016. "Period elongation-based framework for operative assessment of the variation of seismic vulnerability of reinforced concrete buildings during aftershock sequences." *Soil Dynamics and Earthquake Engineering* 84: 224–237.
- Trifunac, M.D., and A.G. Brady. 1975. "A study on the duration of strong earthquake ground motion." *Bulletin of the Seismological Society of America* 65: 581–626.
- Tsioulou, A., A.A Taflanidis, and C. Galasso. 2019. "Validation of stochastic ground motion model modification by comparison to seismic demand of recorded ground motions." *Bulletin of Earthquake Engineering* 17 (6): 2871–2898.
- Uang, C. M., and V. V. Bertero. 1990. "Evaluation of seismic energy in structures." *Earthquake Engineering and Structural Dynamics* 19: 77–90.
- Ubertini, F., N. Cavalagli, A. Kita, and G. Comanducci. 2017. "Assessment of a monumental masonry bell-tower after 2016 Central Italy seismic sequence by long-term SHM." *Bulletin of Earthquake Engineering* 16: 775–801.
- Vamvatsikos, D., and C. A. Cornell. 2004. "Applied incremental dynamic analysis." *Earthquake Spectra* 20 (2): 523–553.
- Vamvatsikos, D., and C. A. Cornell. 2002. "Incremental dynamic Analysis." *Earthquake Engineering and Structural Dynamics* 31: 491–514.

- Vamvatsikos, D., and M. Fragiadakis. 2009. "Incremental dynamic analysis for estimating seismic performance sensitivity and uncertainty." *Earthquake Engineering and Structural Dynamics* 39 (2): 141–163.
- Vetter, C., and A.A. Taflanidis. 2014. "Comparison of alternative stochastic ground motion models for seismic risk characterization." *Soil Dynamics and Earthquake Engineering* 58: 48–65.
- Vidal, F., M. Navarro, C. Aranda, and T. Enomoto. 2013. "Changes in dynamic characteristics of lorca rc buildings from pre-and post-earthquake ambient vibration data." *Bulletin of Earthquake Engineering*, 12: 2095–2110.
- Ville, J. 1948. "Theorie et application de la notion de signal analytique." *Cables et Transmission* 2: 61-74.
- Wang, C., W.-X. Ren, Z.-C. Wang, and H.-P. Zhu. 2013. "Instantaneous frequency identification of time-varying structures by continuous wavelet transform." *Engineering Structures* 52: 17–25.
- Wang, J, L Fan, S Qian, and J Zhou. 2002. "Simulations of non-stationary frequency content and its importance to seismic assessment of structures." *Earthquake Engineering & Structural Dynamics* 31: 993–1005.
- Worden, K. 1990. "Data processing and experiment design for the restoring force surface method, part I: integration and differentiation of measured time data." *Mechanical Systems and Signal Processing* 4: 295–319.
- Yen, C.H., and Y.K. Wen. 1990. "Modeling of nonstationary ground motion and analysis of inelastic structural response." *Structural Safety* 8 (1-4): 281–298.